DISSERTATION

Ground state properties and thermoelectric features of multinary cage based structures

ausgeführt zum Zwecke der Erlangung des akademischen
Grades eines Doktors der technischen Wissenschaften
unter der Leitung von

a.o. Univ. Prof. Dr. Ernst Bauer

E138
Institut für Festkörperphysik

eingereicht an der Technischen Universität Wien
Technisch-Naturwissenschaftliche Fakultät
von

DI Christoph Paul
Matr.-Nr. 9425166
Vorgartenstr. 129-143/2/28
1020 Wien

Wien, im Dezember 2003

Kurzfassung

Gegenstand dieser Arbeit ist die Unteruchung der Grundzustandseigenschaften und der thermoelektrischen Leistungsfähigkeit mit Pr gefüllter Skutterudite $Pr_yFe_{4-x}(Co,Ni)_xSb_{12}$, auf Si/Ge basierender Typ I Clathrate und der Zn Germanide $RE_2Zn_6Ge_3$ mit RE=La, Ce, Pr, Nd, Sm und Gd mittels magnetischen, thermodynamischen und transport-orientierten Methoden, wobei letztere die Berechnung der thermoelektrischen Figure of Merit aus elektrischem Widerstand, Thermokraft und thermischer Leitfähigkeit ermöglichen.

Die magnetischen Eigenschaften der Randphase $Pr_{0.73}Fe_4Sb_{12}$ (kubische Raumgruppe $Im\bar{3}$, Nr. 204), die unterhalb von 4.5 K langreichweitige magnetische Ordnung zeigt, sind stark von Kristallfeldeffekten beeinflußt. Basierend auf einer Neuberechnung des Hamilstonoperators für die kubischen Raumgruppen T und T_h, wird erfolgreich versucht, experimentelle Werte der magnetischen Suszeptibilität und inelastische Neutronenspektren theoretisch zu beschreiben. Dabei werden die Resultate auch mit dem bis dato verwendeten Hamiltonoperator für kubische Symmetrie verglichen. Der neu berechnete Hamiltonoperator liefert den magnetischen Triplettzustand Γ_4^2 als Grundzustand und weiters ein nicht verschwindendes Matrixelement zwischen Γ_4^2 und dem ersten angeregten Zustand Γ_1. Dieser Übergang wird in der Tat im inelastischen Neutronenspektrum beobachtet. Berechnung der magnetischen Entropie und des Spin-Disorder Anteils zum elektrischen Widerstand aus der modellierten Kristallfeldaufspaltung ermöglichen anschließend einen weiteren Vergleich mit dem Experiment. Durch sukzessive Substitution von Fe durch Co oder Ni wird die magnetische Ordnung unterdrückt. Isotherme Magnetisierungsmessungen zeigen im Zuge dessen auch eindeutige Änderungen der Kristallfeldaufspaltung. Im Weiteren kommt es zur Reduktion des elektronischen Anteils zur spezifischen Wärme, der für die Randphase $Pr_{0.73}Fe_4Sb_{12}$ einige hundert $mJ/molK^2$ beträgt und somit auf Schweres-Fermionen-Verhalten hinweist. Die thermoelektrische Güte von mit Pr gefüllten Skuteruditen kommt durch die experimentell beobachteten sehr hohen Seebeckkoeffizienten zum Ausdruck, die für die Verbindung $Pr_{0.21}Fe_{2.5}Ni_{1.5}Sb_{12}$ in Werten um 220 $\mu V/K$ bei einer Temperatur von etwa 450 K ihr Maximum erreichen. Darüberhinaus ergeben die Experimente Gitteranteile der thermischen Leitfähigkeit in einer Größenordnung, die von amorphen Materialien oder Gläsern bekannt sind. Thermokraft und thermische Leitfähigkeit werden in Abhängigkeit von der Probenzusammensetzung untersucht. Die Änderung der thermischen Leitfähigkeit mit abnehmendem Fe-Gehalt wird modellhaft durch die Streuung von Gitterschwingungen an einer 'festen Lösung' bestehend aus einem mit Pr gefüllten-, und einem leeren Untergitter verursacht.

Die Verbindungen $RE_2Zn_6Ge_3$ (RE=La, Ce, Pr, Nd, Sm und Gd) konnten mit Hilfe von Röntgenbeugungsuntersuchungen der hexagonalen Raumgruppe $P\bar{6}2m$, Nr. 189, zugeordnet werden, wobei weiters die Zusammensetzung durch Eletronenstrahlmikroanalyse überprüft wurde. Sämtliche Verbindungen zeichnen sich durch magnetische Ordnung aus, die höchste Übergangstemperatur wird mit 28.8 K in $Gd_2Zn_6Ge_3$ beobachtet. Aus isothermen Magnetisierungsmessungen wird antiferromagnetische Ordnung bestimmt, mit Ausnahme der Probe $Ce_2Zn_6Ge_3$, für die eine Art von Ferrimagnetismus angenommen werden kann. Aus den Daten elastischer Neutronenbeugung unter- und oberhalb der Ordungstemperaturen ergeben sich die magnetischen Strukturen von $Nd_2Zn_6Ge_3$ und $Pr_2Zn_6Ge_3$. Alle Verbindungen zeigen metallisches Verhalten im gesamten experimentell zugänglichen Temperaturbereich, weiters relativ kleine negative Thermokräfte, die auf Elektronen als primäre Ladungsträger hinweisen, und mäßig niedrige thermische Leitfähigkeiten. Kondowechselwirkungen, welche oft in intermetallischen Ce Verbindungen und eher selten auch in Pr enthaltenden Materialien beobachtet werden, scheinen von untergeordneter Bedeutung in $Ce_2Zn_6Ge_3$ und $Pr_2Zn_6Ge_3$ zu sein.

Typ I Clathrate $Ba_8Al_xSi_{42-3/4x}\square_{4-1/4x}$ und $Ba_8Ga_xSi_{42-3/4x}\square_{4-1/4x}$ mit $x=8$, 12, 16, wobei $\square$ Defekte in der Struktur bezeichnet, als auch $Ba_8Cu_4Si_{42-x}Ga_x$ ($x=0$, 4, 6, 8), $Ba_8In_{16}Ge_{30}$ und $Eu_{2-x}(Sr,Ba)_{6-x}M_ySi_{46-y}$ mit M=Cu, Al und Ga kristallisieren in der standardisierten Typ I-$Ba_8Al_{16}Ge_{30}$ Struktur (Raumgruppe $Pm\bar{3}n$, Nr. 223). Aus geometrischen Überlegungen wird ein Stammbaum für alle bekannten intermetallischen Clathratphasen erstellt, der sich auf einem simplen Untergitter aus Si/Ge Atomen begründet. Während Ba und Sr in Abwesenheit von Eu beiderseits 2a und 6c Gitterpositionen besetzen, führt die teilweise Substitution durch Eu zu einer neuen quarternären geordneten Variante der $Ba_8Al_{16}Ge_{30}$ Struktur, in der Eu exklusiv auf 2a Positionen zu finden ist und sich die Verteilung von Ba bzw. Sr auf die 6c Gitterplätze reduziert. Magnetische Untersuchungen wurden für die auf Eu basierenden Proben durchgeführt, welche alle langreichweitige Ordnung zeigen. Bestätigung hiefür liefern Röntgenuntersuchungen an den L_{III} Absorptionskanten von Eu, die eindeutig auf divalentes magnetisches Eu hinweisen. Widerstandsmessungen unter Druck liefern Erkenntnisse über die RKKY Wechselwirkung, die für die magnetische Kopplung der seltenen Erden via Leitungselektronensystem verantwortlich ist. Alle hergestellten Proben sind Metalle mit geringer elektrischer Leitfähigkeit und Seebeckkoeffizienten, die -75 $\mu V/K$, in den meisten Fällen -30 $\mu V/K$ nicht übertreffen. Jedoch ergeben sich thermische Leitfähigkeiten, deren Größenordnung durch die starke Phononstreuung an Ba, Sr und Eu, welche anharmonischen, lokalisierten Schwingungen unterworfen sind, zu erklären ist.

Abstract

Physical ground state properties and thermoelectric performance of Pr filled skutterudites $Pr_yFe_{4-x}(Co,Ni)_xSb_{12}$, Si/Ge based clathrate I type structures as well as ternary Zn germanides according to the chemical formula $RE_2Zn_6Ge_3$ with RE=La, Ce, Pr, Nd, Sm and Gd were studied by means of magnetic, thermodynamic and transport investigations. The latter allow for the calculation of the thermoelectric figure of merit from electrical resistivity, thermopower and thermal conductivity data.

The magnetic behavior of parent $Pr_{0.73}Fe_4Sb_{12}$ (cubic space group $Im\bar{3}$, No. 204) exhibiting long range magnetic order below about 4.5 K is revealed to be significantly influenced by crystal electric field (CEF) effects. Magnetic susceptibility as well as inelastic neutron scattering data are modeled with a recently re-calculated point charge model based Hamiltonian for the cubic point groups T and T_h and compared with the commonly used cubic Hamiltonian. According to the new Hamiltonian, the magnetic triplet Γ_4^2 as ground state has a non-vanishing matrix element to first excited singlet Γ_1 state, which is indeed found in the inelastic neutron spectra. Evaluation of magnetic entropy associated with CEF effects and spin-disorder resistivity additionally serves to probe the derived level scheme. Upon rising the (Co,Ni) content long range magnetic order vanishes. From isothermal magnetization measurements a change in the CEF level splittings can be concluded accompanied by a decrease of the electronic contribution of the specific heat, which amounts to several hundred $mJ/molK^2$ for parent $Pr_{0.73}Fe_4Sb_{12}$ pointing to heavy fermion behavior. Strongly enhanced Seebeck coefficients culminating at roughly 220 $\mu V/K$ around 450 K in $Pr_{0.21}Fe_{2.5}Ni_{1.5}Sb_{12}$ and lattice thermal conductivities with a magnitude in the range of those of amorphous or glassy materials indicate the thermoelectric potential of Pr filled skutterudites. The evolution of thermopower as well as of thermal conductivity upon lowering Fe content is examined and the latter property is successfully explained in the scope of a model assumption relating diminished lattice thermal conductivities to phonon scattering due to solid solution formation between a Pr filled and an empty sublattice.

The structure of $RE_2Zn_6Ge_3$ with RE=La, Ce, Pr, Nd, Sm and Gd was determined by means of x-ray diffraction (hexagonal space group $P\bar{6}2m$, No. 189), compositions were controlled employing electron probe micro analyses. All Zn germanides under investigation exhibit long range magnetic order with a maximum transition temperature of $T_N = 28.8$ K in $Gd_2Zn_6Ge_3$. Isothermal magnetization data reflect antiferromagnetic order with the exception of $Ce_2Zn_6Ge_3$, where some type of ferrimagnetism is assumed. The magnetic structures of $Nd_2Zn_6Ge_3$ and $Pr_2Zn_6Ge_3$ are resolved on the basis of elastic neutron powder diffraction performed below and above the respective transi-

tion temperature. Transport properties are characterized by metallic behavior and moderate thermal conductivities. Relatively low negative thermopower values evidence electrons as primary charge carriers. Signs of Kondo type of interactions frequently found in Ce and more rarely also in Pr containing compounds seem to be absent completely.

Framework-deficient solid solutions $Ba_8Al_xSi_{42-3/4x}\square_{4-1/4x}$ and $Ba_8Ga_xSi_{42-3/4x}\square_{4-1/4x}$ with x=8, 12, 16 as well as $Ba_8Cu_4Si_{42-x}Ga_x$ (x=0, 4, 6, 8), $Ba_8In_{16}Ge_{30}$ and rare earth substituted clathrates $Eu_{2-x}(Sr,Ba)_{6-x}M_ySi_{46-y}$ with M=Cu, Al and Ga could be identified to adopt the standardized clathrate I-$Ba_8Al_{16}Ge_{30}$ type of structure, space group $Pm\bar{3}n$, No. 223. Following structural considerations an intermetallic clathrate family tree is proposed from a geometrical analysis of clathrate crystal structures rooting at a simple Si/Ge sublattice. Whereas Ba and Sr are randomly distributed at the 2a and 6d lattice positions in clathrates solely containing Ba or Sr, in Eu substituted clathrates, the rare earth exclusively occopies the 2a position, while Ba or Sr are found at the 6c positions only. Eu substituted samples thus represent new quartenary ordered versions of the $Ba_8Al_{16}Ge_{30}$ structure type. Magnetism is investigated in the case of the rare earth containing compounds and long range magnetic order for all samples is found. This is in accordance with L_{III} absorption edge studies performed indicating Eu to adopt the magnetic divalent oxidation state. RKKY interactions among rare earth ions mediated by the conduction electron system are studied in terms of pressure dependent electrical resistivity. All samples are metals with rather low electrical conductivities and Seebeck coefficients below -75 μV/K, in most cases even below -30 μ V/K pointing to unoptimized electronic properties and thermoelectric capability. However, thermal conductivities are strongly reduced due to phonon scattering by the inclusion atoms performing anharmonic, localized vibrations.

Ich danke...

... meinem Betreuer Prof. Dr. Ernst Bauer, der mir die Durchführung dieser Dissertation ermöglicht, mich immer unterstützt und in vieler Hinsicht uneingeschränktes und freies Arbeiten mit eigenen Ideen und Vorstellungen zugelassen hat. Die freundschaftliche Atmosphäre und das sehr angenehme Klima in unserer Arbeitsgruppe möchte ich besonders hervorheben.

... den Kollegen von der Arbeitsgruppe Magnetismus & Supraleitung Prof. Dr. Gerfried Hilscher und Dr. Herwig Michor unter anderem für Messungen der spezifischen Wärme und Suszeptibilität, aber vor allem für ihre ständige uneingeschränkte Bereitschaft zur Hilfestellung bei jeglichen Fragen und Problemen, was Fortschritte an der hier durchgeführten Arbeit immens beeinflußt hat.

... Prof. Dr. Peter Rogl, Dr. Andriy Grytsiv und Dr. Yaroslav Mudryk vom Institut für Physikalische Chemie der Universität Wien für die Präparation und Strukturanalyse der untersuchten Probenserien und zum Teil für die grafisch so ansprechenden Bilder der Kristallstrukturen.

... meinem Freund und Kollegen Dr. Stefan Berger für das angenehme Arbeitsklima, die gute Zusammenarbeit und seine vielfache Hilfsbereitschaft während der letzten Jahre.

... vor allem meinen Eltern für ihre Unterstützung seit Beginn meines Studiums, ohne sie wäre vieles in keinster Weise möglich gewesen.

Contents

Introduction

The last twenty years were adumbrated by massive interest in alternative energy generation. This lead to a new flaming up of certain research areas dealing with the exploration and synthetization as well as characterization of materials that since then have been considered to provide higher efficiencies in thermoelectric power generation and thermoelectric cooling than state of the art commonly used bismuth, antimony lead tellurides and silicon/germanium based materials. Within this thesis three groups of intermetallic compounds, each belonging to material classes considered potential candidates for thermoelectric applications, are presented, namely filled skutterudite-, clathrate- and ternary germanide compounds. Structural considerations for each class of materials are followed by detailed descriptions of magnetic, electronic and transport properties allowing the calculation of the thermoelectric figure of merit ZT, which is the principal parameter in thermoelectric materials. In increasing this thermoelectric quantity several physical properties have to be taken into account, low electrical resistivities and thermal conductivities and primarily elevated Seebeck coefficients are required. The difficulties in achieving high ZT values is illustrated best when considering electrical resistivity and thermopower. High electrical conductivity and high thermopower are two physical quantities of opposite requirements, since a greater number of free charge carriers lowers electrical resistivity but on the other hand gives rise to diminishing Seebeck coefficients and vice versa, leading to the need of electronically optimized materials.

The series of filled skutterudites $Pr_yFe_{4-x}(Co,Ni)_xSb_{12}$, type I Si and Ge clathrates as well as novel Zn_9-cluster compounds $RE_2Zn_6Ge_3$ (RE=La, Ce, Pr, Nd, Sm, Gd) are of particular interest not only with respect to possible thermoelectric applicability or enhanced thermoelectric performance, rather physical ground state properties mainly determined by the unique behavior of the particular rare earth elements may lead to fascinating electronic and magnetic phenomena such as long range magnetic order, intermediate valence, superconductivity, heavy fermion behavior or even heavy fermion superconductivity, metal to insulator transitions and also structural phase transitions just to name a few. Pr filled skutterudites have indeed attracted much attention in recent years, since $PrOs_4Sb_{12}$ was discovered to exhibit su-

perconductivity mediated by heavy quasi-particles below $T_c = 1.85$ K [1, 2, 3], whereas $PrFe_4P_{12}$ is characterized by the coexistence of anti-quadrupolar ordering and quadrupolar Kondo coupling [3, 4]. In both cases, elucidation of the respective crystal electric field CEF level splitting was essential for latter conclusions. Thus, special emphasis is drawn to magnetic and electronic ground state properties of $Pr_yFe_{4-x}(Co,Ni)_xSb_{12}$ significantly influenced by CEF effects.

Type I clathrates have been subject of numerous publications essentially pointing to enhanced thermoelectric potential due to the viability of the phonon-glass electron-crystal (PGEC) approach [5] describing the decoupling of electronic and vibrational degrees of freedom within materials characterized by open structures with large cavities or voids, that may be occupied by electropositive elements. Within this thesis Ba, Sr and eu were chosen, where the latter carries a magnetic moment giving rise to RKKY interactions among Eu spins via conduction electron system and possibly to long range magnetic order. This part of the thesis is meant to present a rigorous physical picture considering both thermoelectric and general solid state-physical properties also dealing with structural relations among the various intermetallic clathrate structures. A universal clathrate structure tree rooting at a simple Si/Ge sublattice is therefore proposed.

Since only a few compounds belonging to the ternary Zn germanides such as $YbZn_2Si_2$ and $YbZn_2Ge_2$ [6] or $EuZn_2Ge_2$ [7] have been reported so far, little information is available in literature as far as ground state and thermoelectric performance are concerned. Full characterization of novel Zn_9-cluster compounds $RE_2Zn_6Ge_3$ (RE=La, Ce, Pr, Nd, Sm, Gd) thus provides further information on ternary Zn germanides.

In order to account for the large variety of phenomena expected within these three classes of materials, various measurements were carried out, the techniques employed together with aspects of sample preparation are shortly outlined in chapter 2. Theoretical considerations of thermoelectricity as well as of transport, magnetic and thermodynamic properties of solids are presented prior within chapter 1. Thereafter, each chapter provides a detailed summary of literature data already available and structural features of each class of intermetallic compounds investigated within this thesis followed by illustration and interpretation of the experimental results obtained.

Chapter 1

Theoretical overview

1.1 Historical thermoelectrics

The discovery of thermoelectric effects first dates back to 1823, when Thomas Johann Seebeck (1770-1831) published results on experiments with two dissimilar conductors forming a closed loop. He observed a compass needle, placed in the vicinity of this loop, to be deflected if one of the junctions of the conductors was heated [8]. Although this phenomenon was not interpreted correctly by Seebeck, who related the deflection of the needle to magnetism, he managed to find it to occur in a lot of materials including also semiconductors, he thus unwittingly discovered the thermoelectric effects.

Although directly utilizing the Seebeck effect in his experiments as a current source, Jean Charles Althanase Peltier (1785-1845) failed to relate this effect to the observations he had made himself leading to the Peltier effect describing temperature changes of a junction of dissimilar metals passed through by a current [9]. 1838 Heinrich Friedrich Emil Lenz (1804-1865) managed to give a physically correct explanation for these experimental findings [10].

Not before 1851, due to increased interest in other fields over the intervening years (this was the time of electromagnetism with outstanding investigations by Oersted, Ampere, Laplace or Faraday), William Thomson (1824-1907) succeeded in establishing a relationship between Seebeck and Peltier effect combined with the prediction of the existence of a third thermoelectric effect later named the Thomson effect [11]. It describes heating or cooling of one homogeneous conductor, when a current passes through it in the presence of a temperature gradient along it.

A satisfactory theory of thermoelectric power generation and refrigeration was finally formulated by Altenkirch in 1909 and 1911 [12, 13]. Since then it has been 'axiomatic', that materials used for thermoelectric applications should possess large Seebeck coefficients S and low thermal conductivities λ to retain the heat at the junction as well as low electrical resistivities ρ in

12

order to minimize Joule heating. The thermoelectric figure of merit $ZT = S^2/\rho\lambda$ mentioned in the introduction should represent the unification of these quantities into one characteristic material dependent constant.

Within the following period of about 40 years with research mainly focusing on metals and metal alloys, interest in the field of thermoelectrics stagnated. This can be ascribed to the fact, that simple metals and their alloys do neither exhibit Seebeck coefficients substantially above 10 μV/K, nor was it possible to optimize thermal conductivity, since in metals, lattice and electronic part of the thermal conductivity are linked to each other via the Wiedemann-Franz law, their ratio being constant. Thus minimizing one quantity maximizes the other and vice versa.

Driven by the development of new synthetic semiconductors possessing thermopower values of up to 100 μV/K, Ioffe developed a theory of semiconductor thermoelements [14] followed by a report by Goldsmid and Douglas on the possibility of thermoelectric cooling from ambient temperatures to temperatures below 0°C [15]. Starting at this time of the last century also military aspects and interests gained importance leading to tremendous surveys of materials by U.S. laboratories and the discovery of a few semiconductors with a ZT greater than 1.5 (ZT of 1 is considered to be a prerequisite for thermoelectric materials).

With the discovery and possible synthetization of new complex materials several new approaches to achieve enhanced figures of merit have been reported over the last 2 centuries mainly focusing on reducing thermal conductivity down to the theoretically lowest possible values. Amongst others, these attempts resulted in the type of compounds investigated within this work. Filled skutterudites and clathrate compounds were identified to be possibly well suited for future thermoelectric energy conversion.

1.2 Macroscopic transport equations, Onsager relations

Transport theory represents the physical basis for any thermoelectric concepts and applications, a rigorous derivation of the presented quantities as well as details and remarks on thermoelectrics in general can be found elsewhere [16, 17, 18, 19].

Irreversible processes can be thermodynamically described by constructing a relation among forces and thereby caused fluxes:

$$J_i = \sum_{k=1}^{n} L_{ik}X_k. \tag{1.1}$$

L_{ii} represent elementary transport coefficients such as electrical conductivity,

whereas L_{ik} with $i \neq k$ resemble superposed effects. If forces and fluxes are suitably chosen, the coefficients in equation 1.1, L_{ik}, are symmetric. Therefore

$$L_{ik} = L_{ki} \qquad (1.2)$$

holds, a relation known as the Onsager Theorem or as the Onsager Reciprocal Relations. Although this theorem links macroscopic quantities to each other, its origin is of microscopic nature: the reversibility of time in the fundamental equations of mechanics. It is important to note, that these reciprocal relations are invariant as to linear transformations of forces and fluxes as well as that linear dependencies among both forces and fluxes do not affect their validity. There are two different kinds of forces, the electrical force on the one hand and a force originating from concentration gradients resulting in diffusive fluxes on the other. Considering an electric field $\vec{E}$ and a temperature gradient $\mathrm{grad}T$ as present forces and taking into account basic energy arguments including setting up mass-, energy- and charge current densities in combination with entropy production, which is a result of the irreversibility of such processes, the macroscopic transport equations can be derived:

$$\vec{E} = \rho \vec{I} + S \mathrm{grad}T \qquad (1.3)$$

and

$$\vec{J} = \Pi \vec{I} - \lambda \mathrm{grad}T, \qquad (1.4)$$

with $\vec{I}$ and $\vec{J}$ denoting the modified charge and heat current densities, respectively. Recalling equation 1.1, the macroscopic transport coefficients correspond to the elementary coefficients in the following way:

$$\text{specific electrical resistance}: \rho = \frac{T}{L_{11}},$$

$$\text{Seebeck coefficient}: S = \frac{L_{12}}{L_{11}},$$

$$\text{Peltier coefficient}: \Pi = T\frac{L_{21}}{L_{11}},$$

$$\text{thermal conductivity}: \lambda = L_{22} - \frac{L_{12}L_{21}}{L_{11}}. \qquad (1.5)$$

The Onsager Theorem (equation 1.2) guarantees the simple relation $\Pi = TS$ between Peltier and Seebeck coefficient. Note that the Onsager Theorem is only valid in the case of isotropic homogeneous materials, in general the transport coefficients will have to be treated as tensors. In this case the Onsager Reciprocal Relation has to be modified, if a magnetic field is applied, e.g. with respect to resistivity under the influence of magnetic fields.

$$\vec{L}_{ij}(\vec{B}) = \vec{L}_{ji}^{\mathrm{T}}(-\vec{B}) \qquad (1.6)$$

1.3   Thermoelectric effects

If assumed constants, electrical resistivity as well as thermal conductivity coefficients can be easily obtained in a measurement when specifying the conditions in equations 1.3 and 1.4 ($\mathrm{grad}T = 0$ on the one hand for resistivity in equation 1.3 and $\vec{I} = 0$ on the other for thermal conductivity in equation 1.4) leading to

$$\vec{E} = \rho\vec{I} \quad \text{and} \quad \vec{J} = -\lambda\mathrm{grad}T. \tag{1.7}$$

As for the Seebeck coefficient, also a unique material specific constant can be derived under the condition $\vec{I} = 0$ in equation 1.3:

$$\vec{E} = S\mathrm{grad}T. \tag{1.8}$$

The determination of this coefficient yet is generally based on an open thermoelectric circuit shown in figure 1.1, where a temperature difference is built up between the junctions of two dissimilar conductors. The thermoelectric voltage $\Delta V_{AB} = V_B - V_A$ developed, defines the thermoelectric power for this couple by

$$S_{AB} = \lim_{\Delta T \to 0}(\Delta V/\Delta T) \quad \text{or} \quad S_{AB} = S_A - S_B = \frac{dV}{dT}, \tag{1.9}$$

where S_A and S_B denote the absolute thermopowers of materials A and B, respectively. In contrast, if a current is imposed, the Peltier effect causes liberation or absorption of heat at the junctions depending on the direction of the current. The rate of heat exchange

$$Q = \Pi_{AB}I \tag{1.10}$$

provides the relative Peltier coefficient related to the absolute Peltier coefficients via

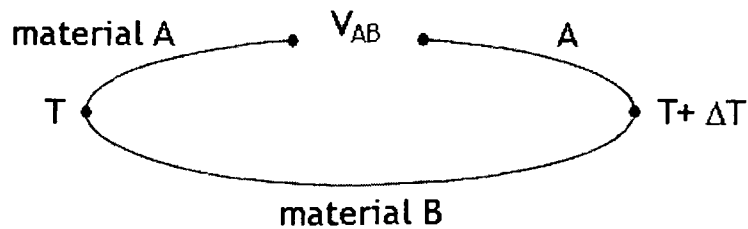$$\Pi_{AB} = \Pi_A - \Pi_B. \tag{1.11}$$

Figure 1.1: Thermoelectric circuit.

The Peltier effect is not to be confused with Joule heat, since it is reversible in the sense, that if the direction of the current is changed, Peltier heat will be either evolved or absorbed, whereas produced Joule heat is independent of the current's direction passing through the conductors.

The third thermoelectric effect observable in a thermoelectric circuit is the Thomson effect. It is a measure for the reversible liberation or absorption of heat in a homogeneous conductor, which carries an electrical current as well as which a temperature gradient is maintained in. The rate of heat production then equals

$$Q = -\kappa I \mathrm{grad} T \qquad (1.12)$$

with κ representing the Thomson coefficient, which can be expressed as

$$\kappa = T\frac{dS}{dT} \qquad (1.13)$$

and is understood to arise from energy conservation. Together with

$$\Pi = ST, \qquad (1.14)$$

given by the Onsager Theorem, these relations are known as the Kelvin relations.

It is important to point out, that neither of these thermoelectric effects are the consequence of the external contact potential. The Seebeck voltage generated is a direct result of the charge carriers at hot and cold end possessing different Fermi distributions and thus also varying in their chemical potential giving rise to the measurable voltage drop in the open circuit. The Peltier effect originates from the entropy change of the charge carriers when crossing a junction between the conductors, whereas the Thomson heat is produced due to increase or decrease of the charge carriers' potential energy when, driven by the applied current, the direction is along or opposite to a thermal gradient [20].

1.4 Energy conversion, the thermoelectric figure of merit

Figure 1.2 depicts a thermocouple consisting of a 'p' branch with positive- and an 'n' branch with negative thermopower. Connected thermally parallel and electrically in series, the two branches are joined together by a good conductor with supposedly vanishing electrical resistance and thermopower. Assuming no thermal resistance between conductor and both thermocouple branches and neglecting heat losses due to radiation or convection and temperature dependencies of transport coefficients electrical resistivity ρ, thermal conductivity λ and thermopower S, the coefficient of performance for refrigeration can be obtained.
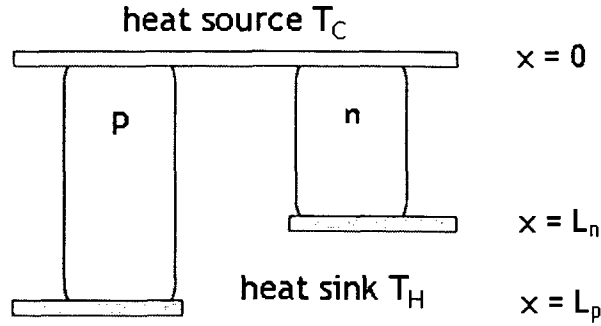
Figure 1.2: Thermocouple for heat pumping or power generation.

$$Q_p = S_p IT - \lambda_p A_p \frac{dT}{dx} \quad \text{and} \quad Q_n = -S_n IT - \lambda_n A_n \frac{dT}{dx} \tag{1.15}$$

represent the total heat flows in 'p' and 'n' branch originating from transport of heat by an applied electrical current (Peltier effect). A denotes the cross-sectional area of each branch. Since S_n is negative per definition, heat flow is positive, resulting overall in heat removal from the source at a rate

$$Q_C = (Q_p + Q_n)|_{x=0}. \tag{1.16}$$

The Peltier coefficients were substituted by ST according to the second Kelvin relation.

To compensate for the heat generated by $I^2 \rho / A$, the Joule heat, a non-constant thermal gradient exists given by

$$-\lambda_{p,n} A_{p,n} \frac{d^2 T}{dx^2} = \frac{I^2 \rho_{p,n}}{A_{p,n}}. \tag{1.17}$$

Owing to the assumption of S being temperature independent, the Thomson effect does not enter the equations (compare equation 1.13). Applying boundary conditions of $T = T_C$ at the source $(x = 0)$ and $T = T_H$ at the heat sink $(x = L_{p,n})$, equation 1.17 reads as

$$\lambda_{p,n} A_{p,n} \frac{dT}{dx} = -\frac{I^2 \rho_{p,n}(x - \frac{L_{p,n}}{2})}{A_{p,n}} + \frac{\lambda_{p,n} A_{p,n} \Delta T}{L_{p,n}} \tag{1.18}$$

with $\Delta T = (T_H - T_C)$. Substituting in equation 1.15 and using 1.16 results in the net heat pumping rate

$$Q_C = (S_p - S_n)IT_C - K\Delta T - \frac{1}{2}I^2 R, \tag{1.19}$$

where K and R denote total thermal conductance and electrical resistance, respectively:

$$K = \frac{\lambda_p A_p}{L_p} + \frac{\lambda_n A_n}{L_n}, \qquad R = \frac{L_p \rho_p}{A_p} + \frac{L_n \rho_n}{A_n}. \qquad (1.20)$$

By setting $dQ_C/dI = 0$, the maximum cooling power

$$Q_{Cmax} = \frac{(S_p - S_n)^2 T_C^2}{2R} - K \Delta T \qquad (1.21)$$

is obtained corresponding to the current

$$I_{max} = \frac{(S_p - S_n) T_C}{R}. \qquad (1.22)$$

Obviously, a temperature difference greater then that defined by $Q_{Cmax} = 0$, will not result in a positive cooling effect, which implies the suitable derivation of a figure of merit as a measure for the maximum temperature difference achievable with a certain thermocouple. With $Q_{Cmax} = 0$ and

$$Z = \frac{(S_p - S_n)^2}{KR}, \qquad (1.23)$$

equation 1.21 leads to

$$\Delta T_{max} = (T_H - T_C)_{max} = \frac{1}{2} Z T_C^2. \qquad (1.24)$$

The figure of merit, the way it is defined in equation 1.23, itself depends on dimensions of both 'p' and 'n' branch, a fact, that makes it only reasonable to talk about a pair of thermocouples rather than a pair of materials. Circumventing this permits the minimization of the RK ratio resulting in

$$\frac{L_n A_p}{L_p A_n} = \left(\frac{\rho_p \lambda_n}{\rho_n \lambda_p} \right)^{1/2}, \qquad (1.25)$$

and thus leading to the figure of merit of a pair of materials:

$$Z = \frac{(S_p - S_n)^2}{[(\lambda_p \rho_p)^{1/2} + (\lambda_n \rho_n)^{1/2}]^2}. \qquad (1.26)$$

From this relation it is clear, which properties a material designed for thermoelectric application should possess. Large Seebeck coefficients directly implying a large Peltier effect as well as low electrical resistivity and thermal conductivity to limit irreversible effects such as heat conduction and Joule

heat. A convenient way to label a certain material is simplifying equation
1.26 and relating it just to one particular material:

$$Z_{p,n} = \frac{S_{p,n}^2}{\rho_{p,n}\lambda_{p,n}}.$$ (1.27)

Although only correctly referable to the true figure of merit, if both n and p
type materials possess the same S and $\lambda\rho$, meaning

$$S_p = -S_n \quad \text{and} \quad \rho_p\lambda_p = \rho_n\lambda_n,$$ (1.28)

expression 1.27 provides an estimate of the thermoelectric properties of the
material itself. Of course application requires a second material of appropriate
and matching attributes.

To receive the coefficient of performance for refrigeration, given by Q_C/W,
in which Q_C represents the net heat pumping rate (compare equation 1.19),
the amount of external electrical power W consumed follows from the as-
sumption that W not only consists of the Joule heat but also of a factor
accounting for overcoming of the Seebeck voltage:

$$W = I(S_p - S_n)\Delta T + I^2 R.$$ (1.29)

Thus the coefficient of performance ϕ is

$$\phi = \frac{Q_C}{W} = \frac{(S_p - S_n)IT_C - K\Delta T - \frac{1}{2}I^2 R}{I[(S_p - S_n)\Delta T + IR]}.$$ (1.30)

By setting $d\phi/dI = 0$ the optimum current leading to the maximum coefficient
of performance is obtained, see equation 1.31. T_M is the mean temperature
and ω is defined as $\omega = (1 + ZT_M)^{1/2}$.

$$\phi_{max} = \frac{T_C\omega - T_H}{(T_H - T_C)(\omega + 1)}$$ (1.31)

As for thermoelectric power generation, the efficiency η is determined by
W, the power provided by the couple:

$$W = \left[\frac{(S_p - S_n)(T_C - T_H)}{(R_L + R)}\right]^2 R_L,$$ (1.32)

where $(S_p - S_n)(T_C - T_H)$ is the Voltage generated and R_L denotes the re-
sistance of a load supplied with energy. Furthermore, with the rate at which
heat is provided by the source

$$Q_H = K(T_C - T_H) + (S_p - S_n)IT_C - \frac{1}{2}I^2 R,$$ (1.33)

η_{max} follows again with T_M, the mean temperature and $\omega = (1 + ZT_M)^{1/2}$:

$$\eta_{max} = \frac{(T_C - T_H)(\omega - 1)}{T_H + \omega T_C}. \tag{1.34}$$

If irreversible effects were absent, the coefficient of performance and the efficiency for power generation could reach the theoretical Carnot limit. Further details can be found in reviews by Goldsmid and Nolas et al. [21, 22].

1.5   Transport properties

Returning to transport theory, the theoretical derivation of transport coefficients such as electrical resistivity or thermal conductivity defined in equation 1.5 generally requires solution of the Boltzmann equation

$$\left(\frac{\partial}{\partial t} + \dot{\mathbf{r}} \cdot \nabla_r + \mathbf{k} \cdot \nabla_k\right) f(\nu, \mathbf{r}, t) = \left(\frac{\partial f(\nu, \mathbf{r}, t)}{\partial t}\right)_{coll}, \tag{1.35}$$

which assumes, that a distribution function for the conduction electrons $f(\gamma, \mathbf{r}, t)$ can be defined depending on position and the wave vector $\mathbf{k}$, both incorporated in the parameter ν, a combined abbreviation for $\mathbf{k}$, the band index and the direction of spin. In the case of the free electron gas this distribution function transforms into the Fermi-Dirac distribution

$$f_0(\varepsilon_\nu) = \left[\exp\frac{\varepsilon_\nu - \mu}{k_B}T + 1\right]^{-1} \tag{1.36}$$

describing the occupation of electronic states as a function of temperature with ϵ_ν denoting the energy of the electrons corresponding to the quantum number ν. Note, that the chemical potential μ equals the Fermi energy at $T = 0$. The distribution results in only a certain number of free states near the Fermi Energy depending on temperature, thus only electrons in this range contributing to charge or mass transport. The Boltzmann equation itself represents a balance between effects of forces such as electric fields (left hand side of equation 1.35) and scattering processes always present in real crystals due to interactions of conduction electrons with impurities, lattice imperfections, phonons and magnetic moments (collision term, right hand side). Solving the equation, however, relies on some simplification: essentially the assumption, that the unknown distorted distribution function $f(\nu, \mathbf{r})$ shows only slight deviations from the local Fermi distribution $f_0(\epsilon_\nu, \mathbf{r})$. This leads to the linearized Boltzmann equation, which, under the influence of both uniform electric field and thermal gradient, reads as

$$Q = (e\mathbf{E} \cdot \mathbf{v}_\nu + \frac{(\epsilon_\nu - \mu)}{T} \nabla T \cdot \mathbf{v}_\nu)\frac{\partial f_0(\epsilon_\nu)}{\partial \epsilon_\nu}, \tag{1.37}$$

where

$$Q = \sum_{\nu'} \frac{f_0(\epsilon_\nu)}{k_B T} [1 - f_0(\epsilon_{\nu'})] \mathbf{P}_{\nu\nu'}(\Phi_\nu - \Phi_{\nu'}) \qquad (1.38)$$

denotes the linear collision operator. $P_{\nu\nu'}$ is the equilibrium transition probability per unit time for a transition from state ν to state ν'. The simplest method available to solve the linearized Boltzmann equation is the relaxation-time approximation assuming an exponential fade-out of the distorted distribution function towards equilibrium conditions given by $f_0(\epsilon_\nu)$ in a time τ_ν, the collision term is replaced by

$$\left(\frac{\partial f(\nu)}{\partial t}\right)_{coll} = \frac{f(\nu) - f_0(\epsilon_\nu)}{\tau_\nu}. \qquad (1.39)$$

While the application of this ansatz considers one relaxation time corresponding to one particular scattering process, it is generally possible to define an average relaxation time τ combining all scattering processes present, if these processes can be treated independently from each other according to Matthiessen's rule

$$\frac{1}{\tau} = \sum_i \frac{1}{\tau_i}. \qquad (1.40)$$

In the scope of a single band model, where one parabolic conduction band contains just one type of charge carriers and neglecting significant effects of charge carrier-phonon interactions on the distribution function of the charge carriers, in other words, considering phonons simply as scattering centers, the linearized Boltzmann equation results in following expressions for the transport coefficients:

$$\rho = \frac{1}{K_0} \frac{T}{e^2}, \qquad (1.41)$$

$$S = \pm \frac{1}{eT}\left(\mu - \frac{K_1}{K_0}\right) \quad \text{and} \qquad (1.42)$$

$$\lambda_e = \frac{1}{T^2}\left(K_2 - \frac{K_1^2}{K_0}\right). \qquad (1.43)$$

The sign of the Seebeck coefficient S depends on the type of charge carriers as illustrated by $\pm$ in equation 1.42 accounting for electrons or holes as primary charge carriers. With the tabulated Fermi-Dirac integrals [23, 24, 25]

$$F_n(\xi) = \int_0^\infty \xi^n f_0(\xi) d\xi, \qquad (1.44)$$

($\xi = \epsilon_\nu/k_B T$), the K_s' can be calculated according to the relation

$$K_s = \frac{8\pi}{3}\left(\frac{2}{h^2}\right)^{\frac{3}{2}} (m^\star)^{\frac{1}{2}} T\tau_0 \left(s + r + \frac{3}{2}\right)(k_B T)^{s+r+\frac{3}{2}} F_{s+r+\frac{1}{2}}, \qquad (1.45)$$

in which the constants r and τ_0 relate to the relaxation time via $\tau_\nu = \tau_0 \epsilon_\nu^r$, $m^\star$ is the charge carriers' effective mass.

1.5.1 Electrical resistivity

Mentioned in the previous section, an average relaxation time for the various scattering processes within a solid applies (compare equation 1.40), if the total collision operator can be treated as the sum of the collision operators for the different scattering mechanisms. These processes are thus assumed independent from each other and the electrical resistivity can then also be divided into three basic components:

$$\rho(T) = \rho_0 + \rho_{ph} + \rho_{spd}. \tag{1.46}$$

While ρ_0 represents the elastic potential scattering of charge carriers by impurities, lattice imperfections or grain boundaries revealing no net energy transfer from carriers to scatterers, ρ_{ph} denotes scattering of conduction electrons by lattice vibrations. The former contribution to the total electrical resistivity results in a temperature independent behavior (at very high temperatures diffusion processes may still influence this part), the latter is usually accounted for in terms of the Bloch-Grüneisen law with $z = \hbar\omega/k_B T$, Θ_D, the Debye temperature and C, a measure for the electron-phonon interaction strength containing ion mass, electron density etc.

$$\rho_{ph} = \frac{C}{\Theta_D}\left(\frac{T}{\Theta_D}\right)^5 \int_0^{\Theta_D/T} \frac{z^5 dz}{(e^z - 1)(1 - e^{-z})}. \tag{1.47}$$

This equation is derived from the linearized Boltzmann equation employing a variational method within the Debye approximation neglecting Umklapp processes (coupling of electrons with longitudinal phonons exclusively) and a Fermi surface other than of spherical form [26, 27]. Low ($T \ll \Theta_D$) and high temperature ($T \geq \Theta_D$) approximations of equation 1.47 yield

$$\rho_{ph} \propto T^5 \quad \text{and} \quad \rho_{ph} \propto T, \tag{1.48}$$

respectively. Note, that the Bloch-Grüneisen formula usually holds just in the case of 'simple' compounds. In the case of alloys containing transition and f elements, deviations from the proposed behavior can occur. These commonly observed deviations of the electrical resistivity from ordinary Bloch-Grüneisen curvature especially at higher temperatures were ascribed to s-d (s-f) scattering of the conduction electrons by Mott [28, 29], who proposed an additional term BT^3, where B as well as the sign of the latter depend on the density of d states at the Fermi level, in $4f$ or $5f$ compounds presumably dominated by $N_f(E_F)$, the density of f states at the Fermi energy.

ρ_{spd} denotes the interaction between conduction electrons and disordered localized spins referring to compounds with atoms carrying magnetic moments. In the absence of crystal electric field (CEF) splitting, long range

magnetic order and any kind of short range correlations, the spin-disorder resistivity is constant and amounts to [30]

$$\rho_{spd} = \frac{3\pi N m^\star}{2\hbar e^2 E_F} \mid \Gamma \mid^2 (g-1)^2 J(J+1). \tag{1.49}$$

Γ is the exchange interaction constant between electrons and localized spins, $m^\star$ the effective charge carrier mass and $(g-1)^2 J(J+1)$ represents the de Gennes factor. Relation 1.49 is directly obtained when a Hamiltonian similar to that in expression 1.81 in section 1.6.3 forms the basis of the calculation.

Taking crystal field splitting into account, which at least partly lifts the $(2J+1)$-fold degeneracy of the groundstate, equation 1.49 has to be replaced by [31]

$$\rho_{spd} = \frac{3\pi N m^\star}{2\hbar e^2 E_F} \mid \Gamma \mid^2 (g-1)^2 \sum_{m_s,m'_s,i,i'} \langle m'_s i' \mid \vec{s}\vec{J} \mid m_s i \rangle^2 p_i f_{ii'}, \tag{1.50}$$

where m_s and m'_s correspond to the spins of the charge carriers in initial and final state i and i'.

$$p_i = \frac{e^{E_i/k_B T}}{\sum_j e^{-E_j/k_B T}} \tag{1.51}$$

yields the thermal population of a particular CEF level with the energy E_i, while $f_{ii'}$ reads as

$$f_{ii'} = \frac{2}{1 + e^{-(E_i - E'_i)/k_B T}}. \tag{1.52}$$

The matrix elements are between the simultaneous eigenstates for the local moment-conduction electron system.

At low temperatures, due to the interaction of conduction electrons with spin-waves, which tends to dominate magnetically ordered compounds, different temperature dependencies are expected for ferro- and antiferromagnetic order. While the former is related with a T^2 behavior, the latter is supposed to give rise to a T^4-law, although very rarely observed in antiferromagnetic materials [32, 33]. Generally electron scattering on spin-waves can be described by a

$$\rho(T) = \rho_0 + A T^n \exp -\Delta/k_B T \tag{1.53}$$

dependence with A, a constant, and Δ an energy gap in the spin-wave energy spectrum, the latter being at least required in order to excite a spin-wave [34].

Magnetoresistance

The effect of external magnetic fields on the conduction electron orbits of nonmagnetic metals and alloys is understood in terms of the classical mag-

netoresistance, which is defined as

$$\frac{\Delta\rho}{\rho} = \frac{\rho(T, B) - \rho(T, 0)}{\rho(T, 0)}. \tag{1.54}$$

In the low-field limit the mean free path expressed in terms of a relaxation time τ, is much smaller than the induced circular movement of the conduction electrons perpendicular to the applied magnetic field, in other words, in between two collision events, suffered by an electron, only a small arc is delineated by the latter. With the cyclotron frequency ω_c these prerequisites can be summarized by $\omega_c\tau \ll 1$ and the magnetic field can be treated as a small perturbation. In the high field limit ($\omega_c\tau > 1$) conduction electrons are able to complete full circular orbits before being scattered into an other orbital state, the external magnetic field thus has to be accounted for in terms of a quantum-mechanical treatment. In any case the conduction electron system should actually only be affected by the magnetic field in a plane perpendicular to $\mathbf{B}$, however, also longitudinal effects are observed in practice originating from deviations of the conduction bands from parabolic- as well as of the energy surface from a spherical form. Materials with exceptionally complex shapes of the Fermi surface are known to give rise to a longitudinal response of the order of the expected transverse signal, compare e.g. YAl_2 exhibiting transverse and longitudinal magnetoresistance of equal magnitude [35]. The latter has indeed been pointed out to be characterized by a very complicated Fermi surface [36]. Summarizing, classical magnetoresistance is always positive due to the field dependent frequency increase of electrons being subject to scattering events.

In the case of materials containing magnetic moment carrying elements, externally applied magnetic fields result in different temperature and field variations depending on the magnetic state of the material considered. Calculations based on the molecular-field approximation were carried out by Yamada et al. [37] for ferro- and antiferromagnetic spin arrangements. In the paramagnetic temperature range the right-hand denominator in equation 1.54 simply has to replaced by a factor proportional to $(g-1)^2 J(J+1)$ accounting for the spin-disorder resistivity (compare equation 1.49). In the ferromagnetic case the external magnetic field suppresses the fluctuations of localized spins due to a change in effective field leading to negative magnetoresistance. On the other hand, $\rho(B)/\rho(0)$ of an antiferromagnetic spin structure is sensitively dependent on the orientation of the external field relative to the sublattices' magnetizations. It is greater than 1 and proportional to B^2, if $\mathbf{B}$ is parallel to one of the sublattices' magnetization, and equal to 1 in the perpendicular case. $\rho(B)/\rho(0) < 1$ can be expected, if, above a critical field, complete spin alignment is induced (field induced ferromagnetic order).

1.5.2   Thermopower

Theoretical calculations or predictions concerning thermopower are subject to the 'disadvantage' of this effect being a result of higher order transport processes. While electrical resistivity can in most cases be separated into different parts stemming from the various scattering mechanisms, charge carriers are subject to within a solid, the situation in the case of thermopower is by far less simple. Nevertheless, attempts were made in the scope of variational procedures leading to the Kohler rule for the diffusion thermopower S_e (equation 1.55) originating from the interaction of the conduction electron system with randomly distributed scattering centers.

$$S_e(T) = \sum_i \frac{\lambda_{e,i}}{\lambda_e} S_{e,i} \qquad (1.55)$$

λ_e, $\lambda_{e,i}$ and $S_{e,i}$ represent total electronic thermal conductivity, thermal conductivity and Seebeck coefficient due to a particular scattering mechanism i, respectively. If the Wiedemann-Franz law holds (compare equation 1.60), the so-called Nordheim-Gorter rule applies resulting in

$$S_e(T) = \sum_i \frac{\rho_i}{\rho} S_{e,i}. \qquad (1.56)$$

As for the variation of the Seebeck coefficients with temperature, Mott's expression for the diffusion thermopower [28]

$$S_e(T) = \frac{\pi^2 k_B^2 T}{3e} \left(\frac{\partial \ln \sigma}{\partial E} \right)_{E_F} \qquad (1.57)$$

with $\sigma = 1/\rho$ in most cases tends to be too simple to be able to describe the observed temperature dependencies often characterized by change of sign as well as by pronounced minima or maxima. Even binary non-magnetic compounds are known to exhibit significantly more complicated curvatures than understood by means of this equation. The situation becomes even more non-transparent, if transition or f elements are present. Only rather crude generalizations of the possible $S(T)$ dependencies can be made such as the speculation of a linear dependence of the thermopower due to spin-disorder scattering in the paramagnetic temperature range of magnetically ordering materials as e.g. proposed by Bauer et al. [38]. What can, however, be asserted is the fact that $S(T)$ is sensitive to the density of states at the Fermi energy and moreover to its derivative $dN(E)/dE$ at E_F illustrated by the relation for the diffusion thermopower of a two-band s-d conductor [18],

$$S_e^{s-d} = -\frac{\pi^2 k_B^2 T}{3e} \left(\frac{3}{2E_F} - \frac{1}{N_d(E)} \frac{dN_d(E)}{dE} \right)_{E_F}. \qquad (1.58)$$

The first term in the large brackets represents the normal (s-type) band contribution, while the overall variation is dominated by the second term caused by s-d scattering of the charge carriers explaining the elevated values of $S(T)$ in transition metal containing alloys due to their large values of $[dN(E)/dE]_{E_F}$. The same arguments apply for s-f scattering in materials containing rare earth or actinide elements (compare [39, 40] for examples). The latter are also known to be responsible for unusually large minima and maxima in the low temperature region of $S(T)$ around the characteristic temperature related to Kondo-type of interactions and heavy- fermion behavior due to instabilities of their electronic configurations connected with hybridization of f electrons with the conduction band. Further details are found in [17].

Besides diffusion of the conduction electron system, so-called 'drag' effects contribute to the total Seebeck effect primarily at low temperatures, they are presumably simply additive. The phonon drag effect, observed e.g. in pure gold as slight hump in $S(T)$ [41], is the result of the material being subject to a thermal gradient. When the phonon system is in equilibrium no net momentum can be imparted to the electrons, whereas this balance is disturbed when phonon flow takes place and a net phonon current along the temperature gradient establishes. The flowing phonons will thus 'drag' electrons with them tending to pile up at the colder end resulting in the constitution of a new contribution to the total thermoelectric field. A similar explanation can be given for the magnon drag effect in magnetically ordered materials [19].

1.5.3   Thermal conductivity

The thermal conductivity of solids can in general be expressed as a combination of heat conduction by electrons λ_e and by lattice vibrations λ_{ph}

$$\lambda_{tot} = \lambda_e + \lambda_{ph}, \tag{1.59}$$

which explains the non-vanishing thermal conductivity of insulators. In magnetic insulators, metals as well as semiconductors effects due to heat transport by spin-waves at low temperatures are expected, whereas in the latter additional contributions can be of importance for λ_{tot}, namely bipolar, photon and exciton contributions (details are found in the review article by Smirnov et al. [42]).

The Wiedemann-Franz law

$$\lambda_e = L_0 \frac{T}{\rho}, \tag{1.60}$$

with the Sommerfeld value of the Lorenz number $L_0 = (\pi^2/3)(k_B e)^2 = 2.45 \times 10^{-8} \text{W}\Omega\text{K}^{-2}$, establishes a relation between electrical conduction and

electronic thermal conductivity [43]. Although derived in the scope of the free electron model, this equation is frequently used in analyzing experimental thermal conductivity data of metals, since the deviation of the real temperature dependent Lorenz number L from L_0 is somewhat negligible. L was shown to be constant and not differing from L_0 for metals of any purity at temperatures $T \gg \Theta_D$ and for metals with imperfections and lattice defects, as is the case for polycrystalline materials, also at $T \ll \Theta_D$. Significantly influenced by the purity of a metal, any deviation of L from L_0 with temperature is usually associated with the presence of some new elastic or inelastic scattering mechanisms for the heat carriers. Expression 1.60 should hold in the case of metals, too in the intermediate temperature range since in any case the ratio L/L_0 should stay above 0.8 [44, 45]. Note that semiconductors and materials with strong interband scattering can exhibit significantly different behaviors of the Lorenz number compared to 'simple' compounds.

If one again assumes Mathiessen's rule to be valid, electronic thermal resistivity can be expressed by

$$\frac{1}{\lambda_e} \equiv W_e = \sum_i W_{e,i}. \tag{1.61}$$

While $W_{e,0}$ can simply be calculated from residual resistivity values in terms of the Wiedemann-Franz law resulting in a dependence of λ proportional to T, the contribution due to electron scattering by phonons $W_{e,ph}$ is approximated by following expression

$$W_{e,ph} = B\left(\frac{T}{\Theta_D}\right)^2 \left[I_5\frac{\Theta_D}{T} + \frac{D}{E_F}\frac{\Theta_D}{T}\left(\frac{2\pi^2}{3}I_5\frac{\Theta_D}{T} - \frac{1}{3}I_7\frac{\Theta_D}{T}\right)\right], \tag{1.62}$$

where B and D are constants and I_5 and I_7 abbreviate integrals of the type

$$I_n(x) = \int_0^x \frac{z^n dz}{(e^z - 1)(1 - e^{-z})}. \tag{1.63}$$

In the low and high temperature case, equation 1.62 successfully explains the experimentally observed temperature dependence due to electron-phonon scattering:

$$\lambda_{e,ph}(T) \propto T^{-2} \quad \text{for} \quad T \ll \Theta_D,$$
$$= \text{const.} \quad \text{for} \quad T \geq \Theta_D. \tag{1.64}$$

Equation 1.65 corresponds to the spin-disorder contribution to the electronic thermal resistivity in the paramagnetic region in the absence of CEF effects (see ρ_{spd} in equation 1.49) proposed by Bauer et al. [46]. It was deduced via comparison of the electronic thermal resistivity of nonmagnetic YAl_2 with magnetic $REAl_2$ compounds (RE ... rare earth).

$$W_{e,spd}(T) = 1/\lambda_{e,spd} = \frac{9m^\star N}{2\pi\hbar k_B^2 E_F} \mid S \mid^2 (g - 1)^2 J(j + 1)\frac{1}{T} \tag{1.65}$$

Taking CEF effects into consideration further complicates the evaluation of $W_{e,spd}$. Conceptional attempts were made to theoretically account for the thus expected temperature variation, however, until now the calculations have been limited to rather simple model assumptions [47].

Besides the electronic contribution to the total thermal conductivity of a solid, a thermal heat flow is carried by the lattice itself. A T^3 increase in insulators as well as semiconductors and a T^2 dependence in metals are found at temperatures $T \ll \theta_D$ due to strong phonon-electron interactions followed by a maximum of λ_{ph} and a decrease proportional to T^{-1} for $T > \Theta_D$. Different three-phonon scattering mechanisms determine the variation of λ_{ph} to a great extent, normal (N) processes, in which the total momentum is conserved, and Umklapp (U) processes, where the sum of the wave vectors is not conserved leading to a sharp change of the wave vector and consequently of the direction of the flow. By definition, N processes alone would lead to infinite thermal conductivities. This increase and subsequent decrease of λ_{ph} generally observed is the result of the possible excitation of phonons able to participate in U processes only at elevated temperatures due to the necessity of phonon wave vectors with dimensions large enough in a way, that the resulting vector may cross the first Brioullin zone. Processes involving four or more interacting phonons are also possible.

Analyses of the lattice thermal conductivity are usually based on the Debye model and the assumption all phonon scattering mechanisms to be incorporable into a frequency-dependent relaxation time:

$$1/\tau_c = \sum_i \tau_i^{-1}. \tag{1.66}$$

Besides above mentioned phonon-electron and phonon-phonon interactions these include scattering of lattice vibrations by point defects and grain boundaries. The calculated total lattice thermal conductivity then reads [48]

$$\lambda_{ph} = \frac{k_B}{2\pi^2 v_s}\left(\frac{k_B T}{\hbar}\right)^3 \left[\int_0^{\Theta_D/T} \tau_c \frac{x^4 e^x}{(e^x - 1)^2} dx + \frac{I_2}{I_1}\right] \tag{1.67}$$

with v_s denoting the velocity of sound and x abbreviating $\hbar\omega/k_B T$. I_1 and I_2 represent

$$I_1 = \int \frac{\tau_c}{\tau_N}\frac{x^4 e^x}{(e^x - 1)^2} dx \qquad \text{and}$$

$$I_2 = \int \frac{1}{\tau_N}\left(1 - \frac{\tau_c}{\tau_N}\right)\frac{x^4 e^x}{(e^x - 1)^2} dx, \tag{1.68}$$

respectively. Note, that $\tau_i = \tau_i(x)$. The first term within the large brackets of equation 1.67 is usually a good approximation for the lattice thermal conductivity, however, only as long as normal three-phonon interactions are not

of distinct importance. If this, in contrast, is the case, it must be corrected by the term I_1/I_2 explicitly taking into account the conservation of the total wave vector of the phonon system by the normal processes, recognizable by τ_N, the relaxation time for normal processes, also included in τ_c, the combined relaxation time [49].

1.6 Magnetic and thermodynamic properties

Two opposite approaches to the theoretical understanding of magnetism in metals and alloys have been developed over the last 80 years relating the origin of magnetic phenomena to either local magnetic moments or itinerant, moments, respectively. While the former, adopted by Heisenberg in 1928 [50], assumes the electrons to remain localized on an atom resulting in large intraatomic electron-electron interactions determining the magnetic moments of each lattice site, the latter starting point, established by Bloch, Mott, Stoner and further by Wohlfarth [51, 53, 52, 54], considers the electrons to form energy bands due to free movement in an average field of charge carriers and ions. Magnetic order is stabilized via electron-electron interactions leading to an energy gain by unequal occupation of spin-up and spin-down band under compliance with Pauli's exclusion law.

Applicability of the respective model is generally determined by the electron wave functions' mutual extent of overlap. Small overlap corresponding to large intraatomic interaction and consequently small electron band widths favors the localized picture, whereas the opposite would be associated with itinerant magnetism. Distinguishing between both cases in practice, however, is only possible in limited cases, since both localized and itinerant components are commonly observable. Besides, each model fails to explain certain characteristics accounted for emphasizing the other picture, e.g. while low temperature behavior of ferromagnetic materials is successfully treated within the band model, this model fails to reconstruct the experimentally observed Curie-Weiss susceptibility derived in the scope of the localized picture.

Nevertheless, attention is drawn to the localized model within this thesis due to the local moment behavior of the rare earth elements' 4f electrons mainly responsible for magnetic ground state properties in the compounds under investigation, although in skutterudite compounds the transition metals may carry magnetic moments of itinerant character. A rigorous description of itinerant phenomena are found e.g. in [55].

1.6.1 Crystal electric field effects

In a solid, electrons in open shells are subject to a variety of interactions with their surroundings giving rise to an electrostatic field. Two-ion interactions

couple the electron clouds at pairs of ions. While this crystal electric field CEF is usually strong for 3d-electrons in transition metals resulting in a decoupling of angular and spin momentum, it can be treated in first order perturbation theory in the case of 4f-electrons since spin-orbit coupling exceeds CEF effects by at least one order of magnitude due to the screening of the 4f electrons by the outer fully occupied 5s and 5p shells. Describing ground states of rare earth compounds in the scope of Russel-Saunders coupling to the total angular momentum J in combination with Hund's rule is therefore suitable.

The electric field originating from the charge distribution around an ion contributes to the potential energy, at least partly lifting the rotational degeneracy of the free ion multiplet according to the values of the projections of the total angular momentum J. The potential energy contribution

$$V_{CEF}(\mathbf{r}) = \int \frac{e\rho(\mathbf{R})}{|\mathbf{r} - \mathbf{R}|} d\mathbf{R}, \qquad (1.69)$$

where $\rho(\mathbf{R})$ denotes the charge density of the surrounding electrons and nuclei, is a solution of the Laplace equation, it can be expanded in terms of spherical harmonics as

$$V_{CEF}(\mathbf{r}) = \sum_{lm} A_l^m r^l Y_{lm}(\hat{\mathbf{r}}) \qquad (1.70)$$

with

$$A_l^m = (-1)^m \frac{4\pi}{2l+1} \int \frac{\rho(\mathbf{R})}{R^{l+1}} Y_{l-m}(\hat{\mathbf{R}}) d\mathbf{R}. \qquad (1.71)$$

The multipoles $r^l Y_{lm}(\hat{\mathbf{r}})$ of the 4f electrons thus interact with the appropriate components of the electric field [56, 57]. Besides the fact, that terms with $l > 6$ vanish for 4f electrons, the spherical harmonics reflect the local point symmetry of the ion under consideration leading to additional simplifications of the corresponding Hamiltonian. Furthermore, pointed out by Stevens [58], the matrix elements of functions of the angular coordinates ($Y_{l-m}(\hat{\mathbf{R}})$ in equation 1.71) are proportional to so-called operator equivalents given in terms of J operators if remaining in the manifold of constant J. Expression 1.70 is then be replaced by the Hamiltonian

$$H_{CEF} = \sum_{i=0}^{l} \sum_{j=0}^{i} B_i^j O_i^j(J), \qquad (1.72)$$

where $O_i^j(J)$ denote Stevens operator equivalents and B_i^j crystal field parameters. While the parameters B_i^j are usually determined experimentally, since calculations would require rigorous knowledge of the charge distribution in the compound, the operator equivalents are tabulated as functions of J operators and can be found e.g. in [57]. The number of non-vanishing terms in

H_{CEF} is generally strongly restricted by the local symmetry, in the case of cubic and hexagonal point groups equation 1.72 reads as

$$H_{cub} = B_4^0(O_4^0 + 5O_4^4) + B_6^0(O_6^0 - 21O_6^4) \tag{1.73}$$

and

$$H_{hex} = B_2^0 O_2^0 + B_4^0 O_4^0 + B_6^0 O_6^0 + B_6^6 O_6^6, \tag{1.74}$$

respectively. Equation 1.73 has just recently been annotated to result in Eigenvalues and consequently in Eigenvectors slightly deviating from their exact values for the cubic point groups T_h and T, nevertheless the correct degeneracy of each sub level is well reproduced. To account for these discrepancies, a term $(O_6^2 - O_6^6)$ has to be added to H_{cub} [59].

Construction and diagonalization of the energy matrix

$$V_{CEF} = \langle J'M_J' \mid H_{CEF} \mid JM_J \rangle \tag{1.75}$$

yields the particular CEF scheme in terms of new Eigenvalues and Eigenfunctions in general composed of mixed states of the unperturbed Eigenfunctions $\mid JM_J \rangle$ of the free ion.

1.6.2 Localized magnetic moments

Within the molecular field theory, where magnetic interactions are incorporated into an internal molecular field, the high temperature limit magnetic susceptibilities of rare earth metals and compounds usually follow a Curie-Weiss law:

$$\chi = \frac{N\mu_{eff}^2}{k_B T} \frac{1}{T - \theta_p}. \tag{1.76}$$

Herein $k_B T \gg \Delta_{CEF}$ (Δ_{CEF} ... crystal field splitting) is assumed guaranteeing thermal population of all excited CEF levels and thus free alignment of the magnetic moments in direction of the magnetic field. N represents the number of magnetic moments per unit volume and μ_{eff} denotes the effective paramagnetic moment

$$\mu_{eff} = \mu_B g_J \sqrt{J(J+1)} \tag{1.77}$$

with the total angular momentum J corresponding to the multiplet $^{2S+1}L_J$ of the free atom and g_J, the Landé factor. θ_p, the paramagnetic Curie temperature is considered a measure for the magnetic interaction strengths within a metal, substances with strong (weak) interactions exhibit high (low) Curie temperatures. Besides, a positive θ_p is associated with ferromagnetic interactions between neighboring moments, whereas antiferromagnetic interactions give rise to negative paramagnetic Curie temperatures. Appearance of a negative paramagnetic Curie temperature does not necessarily indicate presence

of any type of long range magnetic order, it is simply a parameter arising from the deviation of the inverse magnetic susceptibility from linearity at temperatures determined by the particular CEF level scheme.

In the temperature range $k_B T \leq \Delta_{CEF}$ equation 1.76 has to be upgraded, since thermally induced population of the appropriate CEF levels is of importance and may alter magnetic susceptibility (as well as other physical properties, compare e.g. spin-disorder scattering of conduction electrons in the presence of CEF effects as illustrated by equation 1.50 in section 1.5.1). With a magnetic field applied along the direction α, χ^α_{CEF} follows from the Van Vleck formula [60]

$$\chi^\alpha_{CEF} = \frac{N(g_J \mu_B)^2 \sum_{j,i}^{E_i \neq E_j} |\langle j \mid J_\alpha \mid i \rangle|^2}{E_j - E_i}(n_i - n_j), \qquad (1.78)$$

n_p denotes the population factor of the pth CEF state and is defined by the relation

$$n_p = \frac{e^{(-E_p/k_B T)}}{\sum_n e^{(-E_n/k_B T)}}. \qquad (1.79)$$

The total magnetic susceptibility is then calculated with the molecular field parameter λ using

$$\frac{1}{\chi} = \frac{1}{\chi_{CEF}} - \lambda. \qquad (1.80)$$

To account for the experimentally derived magnetic susceptibilities, in any case, a temperature independent contribution χ_0 needs to be included incorporating diamagnetic susceptibility proportions as well as Pauli and Landau contribution arising from the conduction electron system.

1.6.3   Long range magnetic order

Due to the strong localization of the 4f electron wave functions no direct overlaps exist, consequently prohibiting direct interactions between magnetic moments situated at different lattice sites. In order to comprehend long range magnetic order of frequently very complex structure, yet commonly observed in various rare earth element containing compounds, one has to examine interactions between 4f electrons and the conduction band, namely s-f interactions.

Coupling between 4f shell (localized spins $\vec{S}_i$) and conduction band with spin $\vec{s}(\vec{r})$ is mainly governed by spin-spin interaction according to

$$H_{c4f} = -\sum_i \Gamma(\vec{r} - \vec{R}_i)\vec{S}_i \cdot \vec{s}(\vec{r}), \qquad (1.81)$$

where the interaction constant Γ is a function of distance and of conduction electron wavevectors. This coupling mechanism leads to a maximum
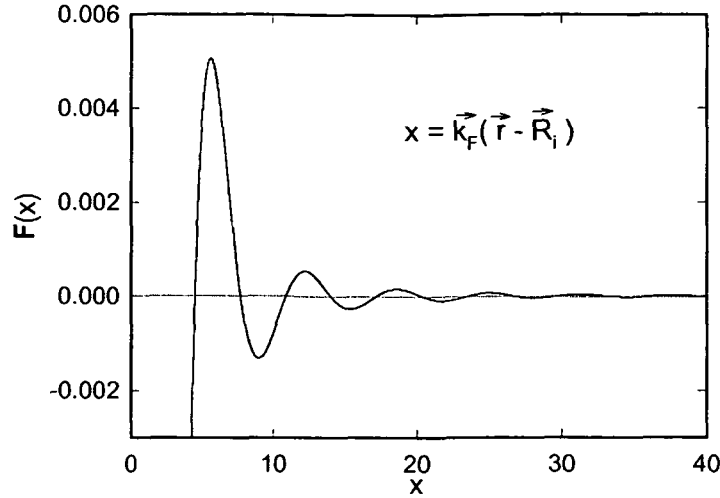
Figure 1.3: Rudermann-Kittel function $\mathbf{F}(x) = \frac{x\cos x - \sin x}{x^4}$.

polarization of the conduction electrons in the vicinity of a magnetic moment situated at a particular ion and to an oscillating decrease of this polarization with increasing distance. Treated in second order perturbation theory, Ruderman, Kittel, Kasuya and Yosida proposed the neighboring magnetic moments to be influenced by the thus polarized conduction electron spins - a type of Heisenberg Hamiltonian was established describing the indirect exchange interactions between localized magnetic moments [61, 62, 63]:

$$H_{RKKY} = -\frac{1}{2}\frac{(3n)^2\pi}{2E_F}\Gamma^2(g_J - 1)^2 \sum_{i\neq j} \mathbf{F}(x)\vec{J_i}\vec{J_j}. \qquad (1.82)$$

As suggested by De Gennes [64], the local spins $\vec{S_i}$ in equation 1.81 were replaced by their projection $(g_J - 1)\vec{J_i}$ on the total angular momentum inside the ground state multiplet of the ion. The oscillating spin density of the conduction electrons at a distance $x = 2\vec{k_F}(\vec{r} - \vec{R_i})$ from the magnetic moment located at $\vec{R_i}$, is proportional to $\mathbf{F}(x)$, the RKKY function (compare figure 1.3):

$$\mathbf{F}(x) = \frac{x\cos x - \sin x}{x^4}. \qquad (1.83)$$

It is obvious from these latter relations, that the formation of often complex types of magnetic order in a certain compound is highly dependent on the distribution of 4f ions in the different crystallographic directions of the lattice and on their respective distances.

Provided, magnetic interactions among an ensemble of magnetic ions are governed by the RKKY mechanism, the following expression for the param-

agnetic Curie temperature in equation 1.76 is derived:

$$\theta_p = -\frac{(3n)^2\pi}{4E_F}\Gamma^2(g_J - 1)^2 J(J+1)\sum F(2k_F r). \tag{1.84}$$

1.6.4   Specific heat

The heat capacity of solids is composed of various contributions, each of importance within different temperature ranges:

$$C(T) = \gamma T + C_{ph} + C_{mag} + C_{nuc}. \tag{1.85}$$

γT describes the linear specific heat of the conduction electron system, which is directly proportional to the density of states at the Fermi energy since γ, the Sommerfeld coefficient, equals $\frac{\pi^2}{3}N_A N(E_F)$ with N_A, the number of atoms per formula unit and $N(E_F)$, the density of states at the Fermi energy. Although derived in the scope of the free electron model and thus possibly deviating in practice due to interaction of band electrons with quasi-particles, the Sommerfeld coefficient allows for estimations of band characteristics via experimental data analyses. Whereas pure metals are known to exhibit electronic contributions in the order of 0.1 to 10 mJ/molK^2, the γ values of materials with strong electron-electron interactions or magnetic correlations exceed those of the former by far, e.g. observable in intermediate valence compounds, spin fluctuation systems and most prominently in heavy fermion compounds with a γ of up to some J/molK^2 [65].

The second term in equation 1.85 represents the phonon contribution to the specific heat, which, according to the Debye model, meets a $C_{ph} = \beta T^3$ dependence at low temperature with $\beta = \frac{12\pi^4}{5}N_A k_B \Theta_D^{-3}$. This variation with temperature is yet only valid up to $T \approx \Theta_D/24$. The overall temperature dependence of the lattice specific heat in terms of the Debye model is approximated by following expression ($z = \hbar\omega/k_B T$):

$$C_{ph}(T) = 9N_A k_B \left(\frac{T}{\Theta_D}\right)^3 \int_0^{\Theta_D/T} \frac{z^4 e^z}{(e^z - 1)^2}dz. \tag{1.86}$$

At temperatures $T \gg \Theta_D$, C_{ph} becomes temperature independent approaching $c_{ph} = 3N_A k_B$ as predicted by classical statistical mechanics' Dulong-Petit law.

In magnetic materials the contribution C_{mag} emerges, the variation with temperature of which depending sensitively on magnetic order and thermally induced excitations of electrons populating certain CEF levels. Since the entropy of a system is connected to the specific heat by the relation

$$S(T) = \int_0^T \frac{C(T')}{T'}dT', \tag{1.87}$$

magnetic order is reflected by C_{mag} at the magnetic ordering temperature. First order transitions should thus lead to a divergence of the magnetic heat capacity due to a jump of the magnetic entropy proportional to the latent heat consumed by the transition, whereas second order magnetic transitions are characterized by a change of slope in $S_{mag}(T)$ at T_{mag} in turn causing a jump of the heat capacity. In this case, the magnetic entropy released at T_{mag} amounts to $S_{mag} = R \ln(2J + 1)$. CEF effects on the other hand give rise to so-called Schottky anomalies at temperatures resembling the respective energy splitting of the CEF states. The Schottky contribution to the specific heat is regarded employing following expression, where n_i is defined by equation 1.79:

$$C_{CEF} = \frac{N_A}{k_B T^2} \left[\sum_i n_i E_i^2 - (\sum_i n_i E_i)^2 \right]. \tag{1.88}$$

The magnetic entropy associated with CEF effects can thus be also calculated with respect to equation 1.89 from its statistical definition and used such as to verify or exclude CEF level splittings proposed from experimental results.

$$S(T) = k_B \sum_i g_i n_i \ln[g_i n_i] \tag{1.89}$$

Herein g_i denotes the degeneracy of a CEF level with energy E_i [56].

The last term in equation 1.85 is connected with the nuclear specific heat, only contributing to the total heat capacity at very low temperatures, typically below $T = 1$ K. It originates from the fact, that electrons with open shells in direct core-proximity produce an effective magnetic hyperfine field at the nucleus due to their rotational degrees of freedom, thus interacting with the core magnetic moment. This strong intrasite coupling causes a lifting of the nuclear state's degenerated total angular momentum resulting in a significant very-low temperature upturn of the heat capacity proportional to T^{-2} (nuclear Schottky term C_{nuc}) [66].

Chapter 2

Experimental

2.1 Sample preparation

2.1.1 $Pr_yFe_{4-x}(Co,Ni)_xSb_{12}$ and $Pr_{0.5}Co_4Sb_{10}Sn_2$

Starting materials for this series of filled skutterudites were ingots of Pr and La of a mass purity of 99.9% ($LaFe_4Sb_{12}$ was used as an isomorphous non-magnetic reference compound), pieces of iron, powders of nickel, cobalt and tin and rods of antimony, all of which also of 99.9% minimum purity. The samples were synthesized by argon arc melting on a water cooled copper hearth under a current as low as possible in order to counteract the high vapor pressures of Sb and Sn at elevated temperatures. Additional Sb was added when compensation of losses due to evaporation was noticed. Repeated arc melting interrupted by flipping of the samples, fragmenting into pieces and moving of the outer parts to inside positions resulted in dense products, that afterwards were sealed under vacuum in silica capsules, slowly heated to 650°C at a rate of about 50°C/h followed by quenching in water. The Sn containing sample was annealed at 300°C.

2.1.2 $RE_2Zn_6Ge_3$

Due to the low melting and boiling points of zinc (T_m =419.6°C, T_b =907.3°C [67]) and thus the lack of applicability of usually adopted preparation techniques such as high-frequency or arc melting, the following method was chosen and successfully used to produce $RE_2Zn_6Ge_3$ compounds with RE=La, Ce, Pr, Nd, Sm and Gd, whereas attempts with RE=Eu and Yb only lead to the formation of $EuZn_2Ge_2$ and $YbZn_2Ge_2$. Starting with zinc granules, ingots of RE and pieces of Ge at least of 99.9% mass purity, Zn powder was admixed to arc melted master alloys with the nominal compositions RE_2Ge_3, that had been powdered under cyclohexane before, were then compacted, sealed in evacuated silica ampoules and kept at 350-400°C for 4-7 days resulting in

36

nearly single-phase $RE_2Zn_6Ge_3$ powders. Recompacting and resintering improved quality and reduced secondary phases (Zn and Ge) to an amount of below 3-5 vol% confirmed by x-ray powder refinement.

Single crystals of $Ce_2Zn_6Ge_3$ were produced applying a technique based on the Lebeau method [68]. As it was shown in the case of e.g. $EuZn_2Si_2$ and $EuZn_2Ge_2$, where the low melting and boiling points of Eu and Zn prohibited application of other techniques, employing low-melting flux solvents, sizeable single-crystal material can be obtained [6, 69, 70, 71]. In our case the single-crystals were grown from 60In-40Zn (at.%) flux taken in a mass ratio of 12:1 with an elemental mixture of 33.3Ce-66.7Ge (at.%). Pieces of elements, vacuum sealed within thick-walled quartz tubes and put in Al_2O_3 crucibles, were treated in the following manner: starting from room temperature up to 1100°C with a heating speed of 75°C/h and an intermediate hold of 1 hour at 450°C, a soaking period of 24 hours was then followed by cooling to 500°C at a rate of 25°C/h and remaining at this temperature for another 12 hours, before the crucibles were simply taken out of the furnace. The indium-zinc flux was finally dissolved in an ultrasonic-agitated bath of mercury at room temperature.

2.1.3 Clathrate I Si and Ge phases

Clathrate I Si and Ge phase samples, namely novel compounds of the framework-deficient solid solutions $Ba_8Al_xSi_{42-3/4x}\square_{4-1/4x}$ and $Ba_8Ga_xSi_{42-3/4x}\square_{4-1/4x}$ with $x = 8, 12, 16$ ($\square$ represents lattice vacancies) as well as $Ba_8Cu_4Si_{42-x}Ga_x$ ($x = 0, 4, 6, 8$), $Ba_8In_{16}Ge_{30}$ and rare earth substituted clathrates $Eu_{2-x}(Sr,Ba)_{6-x}M_ySi_{46-y}$ with M=Cu, Al and Ga were also prepared by argon arc melting of the constituent metal pieces of minimum 99.9% mass purity. To account for the evaporation of Ba in the highly exothermic reaction of the synthetization of Ba containing clathrates, a precalculated extra amount of Ba was added before melting. Additionally the barium pieces were placed on top of the components' mixture in order to avoid an unconditional reaction process. Following these requirements weight losses could be minimized below 1.5 mass%. All compounds except $Ba_8Al_{16}Si_{30}$, $Ba_8Al_{12}Si_{33}$ and $Ba_8In_{16}Ge_{30}$ formed directly from the melt, however, were still undertaken heat treatment to improve homogeneity. Latter three compounds due to only incongruent melting were only received via annealing in sealed quartz capsules for 10-14 days at 600°C in the case of $Ba_8In_{16}Ge_{30}$ and 1-2 weeks at 850°C in the case of the two former compounds. Generally, samples with high Ga content were heat treated at 800°C. After quenching in water the samples appeared to be quite stable in air, forming shiny solids, nevertheless, the quality of the generally brittle samples was affected by cracks complicating preparation for measurements of physical properties. Furthermore, iodine containing single crystals $I_8Sb_8Ge_{38}$ were obtained by transport

reactions, the procedure of which is outlined in [72]. Attempts to synthesize $Ba_8Ni_4Ge_{42}$, $Ba_8Ga_{16}Ge_{30}$ and $Ba_8Al_{16}Ge_{30}$ were in general also successful, however, these samples fragmented into powders within several hours. The resulting powders still contained the main phase, no traces of decomposition were observed. Fragmentation may thus be attributed to hydrolysis of small amounts of impurities concentrated at the grain boundaries.

2.2 Physical and chemical investigations

2.2.1 Structural chemistry

Single-phase conditions of the samples were checked at room temperature by means of x-ray powder diffraction patterns using a Huber-Guinier powder camera supplied with an image plate recording system applying $CuK\alpha1$ radiation on flat powder specimens in the range of $8° \leq 2\theta \leq 100°$ with a step of 0.005 in 2θ. Considering the three different types of material systems investigated lattice parameters were calculated by least-squares fits with the program package STRUKTUR [73] on base of available single crystal data of $YbFe_4Sb_{12}$ [74] for the series of filled skutterudites and with respect to Si and Ge standards in the case of clathrates and $RE_2Zn_6Ge_3$. X-ray intensities were analyzed in terms of quantitative refinement employing the FULLPROF program [75].

Some samples were also inspected using a 57.3 mm radius Gandolfi camera additionally enabling preliminary unit cell dimension determinations, whereas Weissenberg photographs assured single crystal quality and revealed crystal symmetry. A four-circle Nonius Kappa diffractometer equipped with a CCD area detector employing graphite monochromatic $MoK\alpha$ radiation (λ =0.071073 nm) collected single-crystal x-ray data, that were analyzed in terms of orientation matrix and unit cell parameters with the program DENZO [76]. Absorption correction was taken from the program SORTAV [76] and structural refinement was performed using SHELXS-97 [77].

Additionally electron probe micro analyses (EPMA) were carried out for some of the compounds in order to control the correct composition. In the case of Pr filled skutterudite compounds, EPMA also served to monitor the particular rare earth filling fraction.

In the case of $Nd_2Zn_6Ge_3$ and $Pr_2Zn_6Ge_3$ elastic neutron diffraction measurements, carried out on the DMC spectrometer of the PSI spallation source SINQ, served to further validate crystal structure and to elucidate the magnetic structures. At a neutron wavelength of λ =0.255924 nm diffraction data were collected covering a scattering angle of $4° \leq 2\theta \leq 95°$. Details concerning the Double-Axis Multi-Counter Powder Diffractometer DMC can be found in [78]. Analysis of the retrieved data was also accomplished by application of

FULLPROF [75].

Inelastic neutron scattering investigations were performed for $Pr_{0.73}Fe_4Sb_{12}$ on the HET spectrometer at the pulsed neutron source of ISIS, Rutherford Appleton Laboratory, Chilton, UK, which is optimized to measure high energy magnetic excitations in the energy range of meV with an energy resolution of 2-6% upon an incident beam of variable energy between 15 to 2000 meV. For further information see [79].

2.2.2 Temp.-, magn. field- and pressure dependent electrical resistivity

Temperature dependent electrical resistivity measurements were performed in terms of a standard 4 point dc method from 4.2 K to room temperature in a conventional nitrogen pre-cooled and shielded ^4He bath cryostat and from room temperature to 600 K in an evacuated furnace, respectively. The samples of bar-shaped geometry (sample length about 5 mm, cross sectional area between 1 and 3 mm^2) were mounted on an electrically isolated brass panel and contacted by four gold needles of well defined distance pressed down by springs in the former and fixed on an A_2O_3 plate and contacted with W26% Re pins in the latter case. The outer two of which applied the current, whereas the inner ones were used to measure the corresponding voltage along the sample. Control of temperature was assured via a Au+0.07at% Fe vs. Chromel thermoelement (for $T \leq 300K$) and a NiCr vs. Ni thermoelement (for $T \geq 300K$), respectively.

Electrical resistivity down to 300 mK as well as in external magnetic fields up to 12 T was measured in a *Cryogenics* nitrogen-coated ^3He cryostat, sample geometry and contacting resembling those in the ^4He cryostat setup. Temperature was determined using a calibrated *Cernox* temperature sensor supplied by *Lakeshore Cryogenics*. A detailed summary of sample holder as well as measurement setup and equipment is given in [80, 81].

Additional lowest temperature electrical resistivity measurements for $Pr_{0.73}Fe_4Sb_{12}$ down to 20 mK were performed in a $^3He/^4He$ dilution refrigerator system at the Institute of Physics, University of Augsburg, Germany, where external magnetic fields of up to 5 T were applied.

In the case of the $Pr_{0.73}Fe_4Sb_{12}$ as well as for selected clathrate samples investigations were extended by studying the electrical resistivity under the influence of quasi-hydrostatic pressure. A piston-cylinder (liquid pressure) cell embodying four samples, that were pressed against by guitar strings made of stainless steel as contacts, served to apply pressure up to 16 kbar with a paraffin mixture as pressure transmitter. Determination of absolute pressure was realized by observation of the superconducting transition temperature of lead [82]. For further information see [83, 84, 85]

2.2.3 Thermopower

Thermopower measurements were carried out at low (5-300 K) and high temperatures (315-600 K). The technique corresponding to the low temperature regime is based on the so-called differential seesaw-heating method [86]. Spot welded junctions of two thermocouple pairs of Chromel and Constantan residing within A_2O_3 tubes were pressed against the surface of the sample by springs. Two heaters underneath the sample maintained a temperature gradient of about 0.2 K along the specimen, successively in both directions providing seesaw heating conditions. At high temperatures samples were placed in between two platinum plates of about 1 mm thickness contacted via PtRh vs. Pt thermocouples welded onto them. A gradient was kept up during measurement by a thermo coax situated underneath one of the plates. Absolute Seebeck coefficients were calculated based on the following equations:

$$S_x = S_{Ch} - \frac{V_{Ch}}{V_{Ch} - V_{Co}}(S_{Ch} - S_{Co}) \quad \text{for } T \leq 300K, \quad (2.1)$$

where S_{Ch} and S_{Co} represent the absolute thermopowers of Chromel and Constantan and V_{Ch} and V_{Co}, the voltages along Chromel and Constantan circuits, respectively. Due to different setup this relation simplifies for high temperature evaluation of the absolute Seebeck coefficient:

$$S_x = S_{Pt}(T) - V_{Pt,x}/\Delta T. \quad (2.2)$$

S_{Pt} denotes the absolute thermopower of platinum and $V_{Pt,x}$ the thermally induced voltage across the sample depending on a temperature difference ΔT.

2.2.4 Thermal Conductivity

Measurements of thermal conductivity from 3.5 to 300 K were performed in an evacuated flow cryostat on cuboid-shaped samples of about 1 cm length and 2 mm^2 cross section surrounded by three radiation shields. The innermost of which was kept on the sample's temperature to reduce heat losses due to radiation at temperatures above about 150 K. One end of the samples was anchored onto a thick copper panel mounted on the heat exchanger of the system, whereas the other end a strain gauge was glued onto electrically establishing the necessary temperature gradient. Temperature evolution along the sample was controlled by means of Au+0.07at% Fe vs. Chromel differential thermocouples [87].

2.2.5 Magnetic investigations

Evaluation of magnetic ground state properties, in some cases rounded up by a.c. susceptibility investigations, were performed in a commercial 6 T three-axis *CryogenicsS*603 Squid magnetometer covering temperatures between 2

and 300 K, where the flux change in a superconducting pick-up coil induced by movement of the sample, gave magnetization with a resolution in the order of 10^{-9} emu/g. The simultaneously recorded signals of the three orthogonal second-order gradiometer coils served to calculate the magnetization vector, additionally enabling separation of magnetic dipol moment from moments of higher order [88]. For $Pr_{0.73}Fe_4Sb_{12}$ magnetization measurements were extended up to a magnetic field of 15 T using a vibration magnetometer.

To moreover confirm magnetic ordering temperatures, above mentioned a.c. susceptibility measurements were conducted for certain compounds in the temperature range of 1.8-300 K in a commercial *Lakeshore*7000 ac susceptometer with a resolution of about 10^{-7} m^3/kg. The measured voltage, provided by a sensing coil surrounding the sample and caused by flux changes due to the sample being exposed to a small alternating magnetic field, exhibits direct proportionallity to the desired magnetic susceptibility [89].

Eu L_{III} x-ray absorption edge investigations revealing the rare earth valence in Eu containing material were conducted at the french synchrotron radiation facility LURE in Orsay employing the x-ray beam of the DCI storage ring operated at 1.85 Gev and 320 mA. To cut off energies higher than about 10 keV, two parallel mirrors were adjusted also rejecting third order harmonics, the monochromator was made up of a double Si 311 crystal. Powdered samples arranged on adhesive Kapton tapes, four of which stacked in a row to guarantee signal intensity, were exposed to radiation of energies between 6900 and 7080 eV, the energy range containing the L_{III} edge of Eu. Spectra were obtained at 10 and 300 K respectively and analyzed in terms of a standard deconvolution technique [90].

2.2.6 Specific heat

Two automated calorimeters were used to derive the specific heat of skutterudites, selected clathrate and $Re_2Zn_6Ge_3$ compounds between 1.5 and 100 K in external magnetic fields up to 11 T employing a quasi-adiabatic step heating technique. By means of a design originating from a quasi-adiabatic Nernst setup [91], a sapphire plate fixed by nylon wires and surrounded by a radiation shield, in a bore of which a temperature sensor was placed, accommodated the sample. Details concerning implemented algorithms as well as calibration are found in [92, 93, 94].

The $^3He/^4He$ dilution refrigerator system also used for extended very low temperature electrical resistivity measurements, compare above, served to investigate specific heat of $Pr_{0.73}Fe_4Sb_{12}$ down to temperatures of about 20 mK under the influence of magnetic fields of up to 5 T.

Chapter 3

Ground state and thermoelectric properties of $Pr_yFe_{4-x}T_xSb_{12}$ with T=Co, Ni

3.1 Introduction to skutterudites

The structure of binary skutterudites was identified in 1928 by Oftedal [95]. The name stems from the small mining town Skutterud, Norway, where this type of materials was first discovered in the form of the mineral $CoAs_3$ at the beginning of the last century. During the late 1980's filled skutterudites, ternary derivatives of the $CoAs_3$ type material systems, have become subject of extensive work especially in the field of thermoelectric material research due to prospective and promising properties such as strongly enhanced Seebeck coefficients and low thermal conductivities. Besides, a large variety of ground state properties such as superconductivity, long range magnetic order or heavy fermion behavior, just to name a few, too led to numerous investigations in the field of solid state physics and chemistry. A detailed review on skutterudites both from a thermoelectric as well as a general physical point of view can be found e.g. in [96].

3.1.1 Crystal structure and bonding

Binary skutterudites are structures with the chemical formula TX_3, where T represents one of the group 9 transition metals Co, Rh or Ir and X denotes P, As or Sb. All nine combinations of latter elements exist crystallizing in a body centered cubic type of structure, space group $Im\bar{3}$, No. 204, without Umklappung and fourfold symmetry axis [59]. 32 atoms in the unit cell, arranged in eight groups of TX_3 blocks, are distributed in the way, that the crystallographic c sites are occupied by 8 transition metal atoms, while the
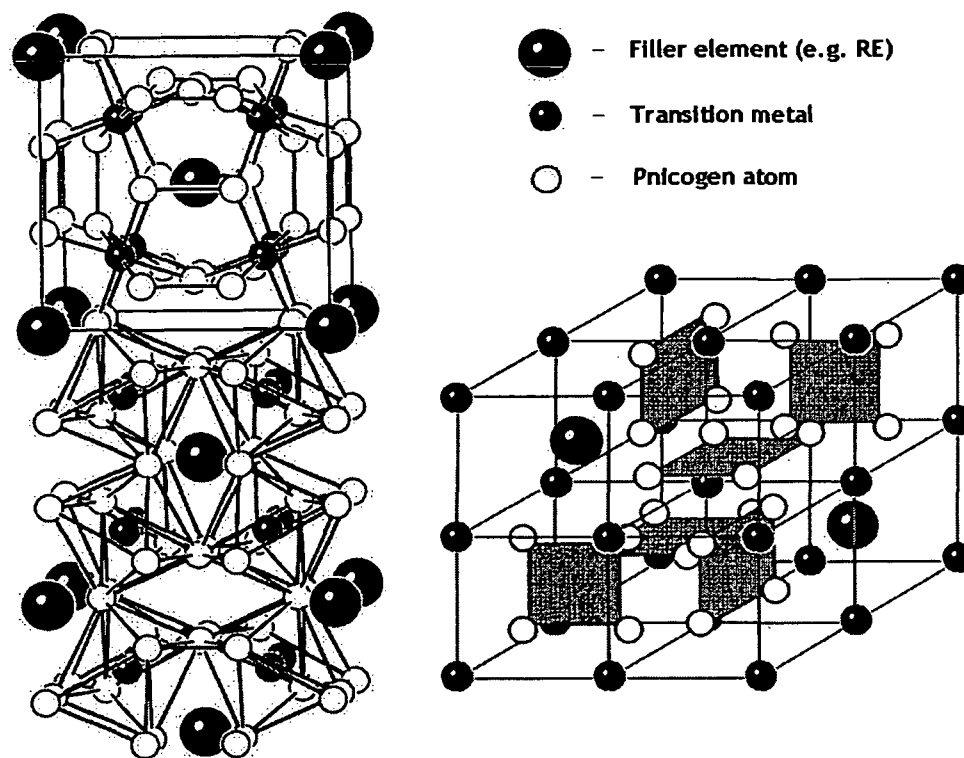
Figure 3.1: Crystal structure of filled skutterudites, $LaFe_4Sb_{12}$ type of structure, space group $Im\bar{3}$, No. 204. Left hand side, top: unit cell, bottom: illustration of the octahedral coordination of pnicogen around transitions atoms (from Danebrock et al. [97]). Right side: Representation, where transition atoms build the cubic lattice with planar rectangular rings of pnicogen atoms (from Fleurial et al. [98]).

pnicogen atoms X are located at the g sites. In other words, the structure consists of an infinite three-dimensional array of trigonally distorted and tilted TX_6 octahedrons sharing corners with six neighboring octahedra, the metal T lying in the center of each octahedron. Due to the significant T-T distances, no transition metal atom has an other atom T as nearest neighbor. In a different representation of the structure the metal atoms build up a simple cubic sublattice, while the pnicogen atoms are arranged as planar rectangular four-membered rings forming linear arrays along the three principal crystallographic directions (100), (010) and (001). The structure according to this representation is depicted in Fig. 3.1 together with the octahedral view of the arrangement. Two positional parameters y and z are sufficient to allow for specification of the exact position of the X atoms as well as determination of interatomic distances, y and z together with the lattice constant a thus

completely characterize the skutterudite structure [99, 100]:

$$d(T - X) = a[(1/4)^2 + (y - 1/4)^2 + (z - 1/4)^2]^{1/2}, \qquad (3.1)$$

$$d_1(X - X) = 2az, \qquad (3.2)$$

$$d_2(X - X) = a(1 - 2y). \qquad (3.3)$$

In his work Oftedal [95] assumed a square planar arrangement of the pnicogen rings ($d_1 = d_2$), which lead to the so-called Oftedal relation

$$2(y + z) = 1. \qquad (3.4)$$

If simultaneously a regular octahedral configuration of the transition metal atoms T applies, then y and z are equal to $1/4$, which would imply a structural change from the skutterudite structure to the more symmetric ReO_3 type of structure. In fact, violation of both the Oftedal relation as well as of the perfect octahedral arrangement of the transition atoms maintains correct bonding conditions and is most favorable to the skutterudite structure. This is obvious from the actual slight trigonal antiprismatic distortion of the octahedral TX_6 blocks and the rectangular rather than square coordination of the pnicogen rings [99, 100]. Confirmation of latter assumptions was established for all binary skutterudites [101, 102, 103, 104, 105, 106, 107].

The skutterudite structure is primarily stabilized by the mainly covalent X-X and T-X bonds, since the transition metal atoms are too far apart from each other as to be of significance. Following considerations are important to understand formation and possible substitutions within the skutterudite system. Keeping in mind that all 9 binary skutterudites are diamagnetic semiconductors, no unpaired spins are present. The rectangular configuration of the pentavalent pnicogen atoms implies the contribution of two valence electrons, one each for bonding with the nearest neighbor X atoms, whereas the 3 remaining electrons can be attributed to bonding with the two nearest metal atoms. Considering the TX_6 octahedral complex around one T atom, $(5 - 2) \cdot \frac{1}{2} \cdot 6 = 9$ electrons are provided by the pnicogen atoms towards TX_6. Their engagement with 9 electrons provided by T satisfies the 18-electron rare-gas configuration resulting in diamagnetism and semiconducting behavior. From the metal atoms' perspective, each T atom contributes $6 \cdot \frac{1}{2} = 3$ electrons for bonding with the 6 neighboring X atoms, it is thus in a trivalent, $3d^6$ low-spin state. This is considered the reason, why it has been impossible to synthesize skutterudites containing other transition metals than those of group 9. One exception is NiP_3, the only binary pure Ni skutterudite. The assumption of the additional electron provided by Ni not participating in any bonds and thus of its promotion into the conduction band giving rise to paramagnetism and metallic behavior was already earlier approved experimentally [108]. Apart from pure binary skutterudites with transition

metals other than those of the Co group, solid solutions are indeed possible, if the elemental impurity is able to form the same bonds as the component it has to replace and if the covalent radii are not differing from each other to a greater extent. The valence of e.g. Fe or Ni thus has to be such as to closely match the covalent radius of Co. Fe^{3+} and Ni^{4+} states as well as paramagnetism and metallic behavior can be expected due to the presence of an unpaired electron in a non-bonding d-orbital in former and an additional electron promoted into the conduction band in latter case. Further details including solid solution limits are referred to in [109, 110].

A structural feature of skutterudites was recognized by Jeitschko et al. in 1977 [111]. The tilt of the TX_6 octahedrons provides large icosahedral voids, that the authors managed to fill with electropositive elements, the first of which having been La resulting in $LaFe_4P_{12}$. The rare earth therein occupies the body-centered cubic a site of the structure (compare Fig. 3.1). The formula corresponding to filled skutterudites is RET_4X_{12}, where in contrast to binary skutterudites T is not restricted to group 9 transition metals, since the electropositive element RE supplies the missing electron of group 8 metals with respect to e.g. Co. Indeed, truly ternary skutterudites just exist with T=Fe, Ru or Os, elements of group 8. In recent years a large variety of filler elements were managed to be accommodated in the large voids of the structure, that in general may be alkaline earth, lanthanoide or actinoide atoms. A compilation of the already synthesized filled skutterudite compounds is available in [96, 111, 112, 113, 114, 115, 116]. Due to the rather rigid skutterudite structure the application of common preparation techniques was not successful in incorporating rare earths heavier (smaller) than Eu with the exception of Yb in the case of Sb based compounds, which may exhibit a divalent oxidation state and thus a suitable ionic radius [117]. Nevertheless, employing high pressure methods even Gd, Tb, Dy, Ho, Er, Tm, Lu and Y could be inserted into the voids of the skutterudite structure [118].

As far as bonding conditions in filled skutterudites are concerned one first has to consider the electronically saturated polyanionic complex $[T_4X_{12}]^{4-} \sim [TX_3]^{1-}$ resembling the TX_3 blocks of the binary skutterudite structure. The bonds between framework and filler elements can thus be assumed to be of ionic type. From the general formula describing ternary skutterudites, RET_4X_{12}, a complete filling of the icosahedral voids is expected, however, the possible degree of filling is strongly dependent on the particular filler element and on the transition metal most plausibly due to differences in valence and thus in radius between various filler elements as well as due to saturation effects of the bonds stabilizing framework and RE atoms. Pr-filled skutterudites are no exception as will be discussed in more detail in a forthcoming section. Depending on the valence of the particular filler element, a filled skutterudite compound is expected to be isoelectronic to binary

skutterudites and thus diamagnetic and semiconducting (R^{4+}) or should give
rise to paramagnetic and metallic behavior if the valence is differing. Ex-
perimental evidence for former predictions was obtained by means of Ce, Th
and U, elements commonly found in a tetravalent state: both $CeFe_4P_{12}$ and
UFe_4P_{12} exhibit electrical resistivities characteristic of semiconducting mate-
rials. Nevertheless, magnetic susceptibility data clearly indicate temperature
dependent paramagnetism with an effective magnetic moment of $\mu_{eff} = 1.07$
μ_B associated with mixed or intermediate valence for the former compound,
while ferromagnetic order below 3.15 K sets on for the latter, which was at-
tributed to ordering of localized 5f electrons [119]. It is interesting to note
that Ce tends to be close to the 4+ state in $CeFe_4As_{12}$ too, whereas the larger
cell dimensions in $CeFe_4Sb_{12}$ favor a 3+ state. A cell contraction is generally
observed when proceeding from Sb over As to P based skutterudites [120]
affecting both insertability of a particular element and its valence. Litera-
ture data concerning above discussed characteristics of skutterudites such as
valence of the filler element, possible filling fraction etc. will be mentioned
when comparison with the presented data of the investigated samples within
this thesis is absorbing.

3.1.2   Transport properties and thermoelectric applica-
bility

Several attempts were made to alter transport properties of binary skutteru-
dites favorable to increasing their thermoelectric potential. Since this thesis
deals with Sb based skutterudites exclusively, details about As and P based
compounds will be neglected in the following.

   One of the first extensive studies focused on binary $CoSb_3$ and the effect
of replacement of Co by several metals, Cu, Zr, Al, Ti, Fe and Ni and of
Sb by Ge, Sn, Pb, Bi, Se and Te [121, 122, 109]. $CoSb_3$ is characterized by
an activation type of transport behavior with an energy gap of 0.5 eV, an
electrical resistivity of about 33-100 mΩcm and thermopower values of up to
-200 μV/K at 300 K. Such properties, however, are only distinctly affected
in the case of Fe and Ni substitution on the Co site and Sn and Te replacing
Sb. Small amounts of Fe as well as Ni ($\leq$ 1at%) lead to an improvement
of both electrical conductivity and Seebeck coefficients. While thermopower
changes sign in former case due to electron deficiency of Fe compared to Co,
the small fraction of Ni even enhances $S(T)$ to values around -300 μV/K at
600 K. Substitutions on the pnicogen site with Sn and Te also led to dramatic
effects on the electronic transport properties, since Sn and Te act as electron
acceptor and electron donor, respectively [123]. The positive effect of Fe and
Ni substitution on the electronic transport properties has since then been
starting point for detailed investigations also on filled skutterudites, where the

electropositive filler element may significantly influence electrical resistivity and thermopower because of the introduction of additional electrons into the structure. On the basis of e.g. $RE(Fe,Ni)_{4-x}Co_xSb_{12}$ with RE=La, Ce, Nd, Sm, Eu and Yb, several authors explored the viable way of enhancing electronic transport and Seebeck coefficients by substitutions on the transition metal T site [124, 125, 126, 127, 128]. A similar starting point was chosen within this thesis in order to improve the thermoelectric potential of the parent compound $PrFe_4Sb_{12}$ as will be discussed in detail below.

Binary skutterudites on the one hand possess outstanding, - from a thermoelectric point of view - desirable electronic properties, on the other hand relatively high thermal conductivities have usually compensated for their decent electronic conduction and extraordinary high Seebeck coefficients as far as an elevated figure of merit is concerned. Again considering $CoSb_3$, the assumption of the validity of the Wiedemann-Franz law (equ. 1.60) reveals, that the electronic part, in the worst case, just makes up about 20% of the total thermal conductivity. Depending on density of the particular skutterudite material and on crystal quality, pure $CoSb_3$ exhibits thermal conductivities in the range between 60 and 110 mW/cmK at room temperature. The values for less dense compounds as well as polycrystalline material lie near the lower border constrained by pronounced phonon scattering on grain boundaries. This grain size dependent effect was indeed elucidated experimentally [129].

Several possibilities are conceivable, that would increase phonon scattering, thus lower the lattice thermal conductivity λ_{ph} and make this class of materials competitive to state-of-the-art thermoelectric materials such as Bi_2Te_3 based alloys exhibiting thermal conductivities lower by a factor of about 10 in comparison to binary skutterudites. Doping generally results in a reduction of λ_{ph} due to the impurities acting as point defects, additionally, electron-phonon interactions may further be responsible for a decrease of the lattice thermal conductivity as revealed for Ni-doped $CoSb_3$. Strong point defect scattering can be generally only expected, if a considerable difference in mass and binding energy exists between host and impurity atom, it is strongly frequency dependent and cuts out high-frequency phonons. Since both requirements are not fulfilled in latter material, the impact on λ_{ph} was proposed to be a direct consequence of the relatively large effective masses found in Ni-doped $CoSb_3$ [130], that were predicted by band structure calculations [131]. An other way to reduce lattice thermal conductivity is the formation of solid solutions between binary and ternary skutterudites. Thereby advantage is taken of enhanced phonon scattering caused by both mass and strain fluctuations, examples of which are the alloys $RhSb_3$-$IrSb_3$ [132], $CoAs_3$-$CoSb_3$ [133] or $Fe_{0.5}Ni_{0.5}Sb_3$-$Ru_{0.5}Pd_{0.5}Sb_3$ [134].

By far the greatest reduction of the lattice thermal conductivity was achieved by filling the large voids of the structure with electropositive ele-

ments mentioned in the preceding section. The key to understand the link between void filling and lattice thermal conductivity is the so-called thermal or atomic displacement parameter ADP of a particular lattice site. It is a measure for the mean-square displacement of an atom about its equilibrium position, directly connected with the magnitude of the vibrations of the atom and experimentally accessible via x-ray or neutron diffraction data. The filler atoms exhibit exceptionally large ADPs in the filled skutterudite structure, that theoretically can be accounted for in terms of localized harmonic oscillators (Einstein oscillators) resembling localized vibrational modes interacting with the normal modes of the structure and thus reducing the lattice thermal conductivity. Due to the weak coupling among filler atoms and framework, to a first estimate, electronic properties are thereby only influenced to a small extent leaving electrical conductivity or thermopower more or less unaffected.

These features would comply well with the phonon-glass electron-crystal (PGEC) concept proposed by Slack in 1995 [5], which defines the ideal thermoelectric material as a material with decoupled electronic and vibrational degrees of freedom. It should look like a good crystalline solid with high electrical conductivity and charge carrier mobility and on the other hand should vibrationally resemble a glassy or amorphous solid with low thermal conductivity. Compounds suitable to realize this concept may be materials characterized by open crystal structures containing large cavities or voids. In fact, filled skutterudites to a great extent seem to fulfill these premises.

It is remarkable, that already a very small fraction of electropositive filler elements is sufficient to strongly influence heat transfer. E.g. Uher et al. have compared $Ce_yCo_4Sb_{12}$ samples with different values of y and shown, that greater filler fractions than 5% do not cause significant changes in thermal conductivity any more [135]. Similar results were obtained for other rare earth element containing skutterudites [136]. From a thermal transport point of view complete filling is not necessary to achieve the maximum reduction of λ_{ph} anyway, since maintaining randomness in the occupancy of the cavities gives rise to an enhanced phonon scattering rate compared to a perfectly ordered crystal.

3.1.3   Pr filled skutterudites

Beyond their prospective thermoelectric properties filled skutterudites also exhibit extraordinary ground state features predominantly due to their respective filler elements, emphasis will be drawn to Pr filled skutterudites primarily within this section. In most cases the semiconducting behavior of binary skutterudites is altered by the additional electrons introduced into the structure by the multi-valent filler element, exceptions are above discussed $CeFe_4X_{12}$ with X=P and As or UFe_4P_{12}, where Ce and U are (at least close to) tetravalent. Nevertheless, long range magnetic order occurs in the lat-

ter and paramagnetism is observed in the two former compounds [119]. A large number of filled skutterudites are metals, e.g. $LaFe_4X_{12}$ (X=P, As, Sb) [120], $CeFe_4Sb_{12}$ (Ce in 3+ state) [137] or $EuFe_4Sb_{12}$ [97]. Superconducting phase transitions were identified in the La containing compounds $LaFe_4Sb_{12}$, $LaFe_4P_{12}$, $LaRu_4P_{12}$ and $LaOs_4P_{12}$ [138, 139, 140], in $EuFe_4Sb_{12}$, $NdFe_4Sb_{12}$, $SmFe_4Sb_{12}$ [97], $EuFe_4P_{12}$ [141] or high-pressure synthesized $GdRu_4P_{12}$ and $TbRu_4P_{12}$ [142] long range ferro-, ferri- or antiferromagnetic order occurs. It is worth noting that superconductivity in Fe containing compounds is very rarely observed [143]. In the partially filled Yb compounds $Yb_{0.1}Rh_4Sb_{12}$ and $Yb_{0.02}Ir_4Sb_{12}$ a variable range hopping type of electrical conductivity was discovered [117], whereas $CeOs_4sb_{12}$ exhibits features reminiscent of Kondo insulators [144]. In $CeRu_4Sb_{12}$ evidence was found of non-Fermi-liquid behavior [145, 146, 147, 148].

Pr filled skutterudites have attracted even more attention during the past 2 years, not because of their outstanding thermoelectric performance, but rather due to exciting physical phenomena observed as shortly outlined below. While $PrRu_4As_{12}$ and $PrRu_4Sb_{12}$ are superconductors below 2.4 and 1 K, respectively [149, 150], $PrRu_4P_{12}$ reveals a metal to insulator (MI) transition at 60 K, the origin of which having been subject of a series of investigations. No distinct anomalies in the magnetic susceptibility around T_{MI} and no hysteresis in the electric resistivity suggest a crystal electric field determined non-magnetic ground state Γ_1 or Γ_3 and the transition to be of second order. Latter assumption is corroborated by no evidence of structural changes in x-ray diffraction patterns above and below the MI transition [151]. A temperature independent Pr^{3+} state was further confirmed from x-ray absorption edge data ruling out origin of the transition due to a change from Pr^{3+} at high to Pr^{4+} at low temperatures (charge ordering) [152]. However, electron diffraction measurements performed by Lee at al. [153] revealed superlattice spots in the diffraction patterns indicating the transition to be accompanied by a slight lattice distortion, which may arise from the opening of a band gap due to a nesting of the Fermi surface. The origin of the MI transition was thus attributed to antiferro-quadrupolar ordering or to a charge density wave phenomenon. Although specific heat data favor latter origin [154], theoretical considerations accounting for coupling of the phonon modes (arising from the lattice distortion) with the Γ_3 non-magnetic doublet are able to explain the unique symmetry-lowering structural phase transition accompanied by anti-quadrupolar ordering [155].

Similar arguments allow the explanation of a phase transition around $T_{trans} = 6.4$ K in $PrFe_4P_{12}$, which was first ascribed to onset of long range antiferromagnetic order [143]. Furthermore, highly enhanced effective electron masses were confirmed by de Haas-van Alphen measurements [156] consistent with a large Sommerfeld coefficient to the specific heat [157], a negative

logarithmic temperature dependence of the electrical resistivity below 130 K
as well as giant values of the thermopower attaining -50 μV/K just around
the supposedly antiferromagnetic phase transition [158]. However, neutron
diffraction studies revealed no additional magnetic reflections below T_{trans}
[159] giving rise to the assumption of a non-magnetic ground state. Confir-
mation of the latter was established via measurements of the elastic constants
in $PrFe_4P_{12}$, that revealed the doublet Γ_3 as ground state [160]. Superlattice
reflections evidenced by x-ray diffraction data below 6.4 K due to a displace-
ment of the Fe ions again favor antiferro-quadrupolar ordering [161]. The
origin of the heavy electron state above T_{trans} in high magnetic fields and the
significantly suppressed heavy fermion behavior in the order state up to now
remain less than clear. Especially since Kondo type of interactions are rather
uncommon in Pr compounds because of their relatively stable 4f electronic
configuration (compare below). An explanation could be the large coordi-
nation number of Pr in the filled skutterudite structure causing enhanced
hybridization effects [162]. $PrFe_4P_{12}$ is most probably characterized by coex-
istence of anti-quadrupolar ordering and quadrupolar Kondo coupling arising
from the quadrupolar fluctuations of the Pr ions [3, 4].

$PrOs_4Sb_{12}$ shows a superconducting phase transition at $T_c = 1.85$ K and
heavy quasi particles as evident from specific heat measurements [1, 2, 3].
Besides the unusual finding of heavy fermion behavior due to hybridization
of the 4f state of Pr, which has only been found in $PrInAg_2$ [163] and above
discussed filled skutterudite $PrFe_4P_{12}$ so far, the interplay of superconduc-
tivity and highly correlated electrons is very exceptional. A very limited
number of compounds is known based on Ce and U exhibiting heavy fermion
superconductivity, such as $CeCu_2Si_2$ [164], UBe_{13} [165] or most recently dis-
covered $CePt_3Si$ [166]. Again the non-magnetic Γ_3 doublet arising from the
cubic crystal electric field caused lifting of the 9-fold degenerate $J = 4$ total
angular momentum of Pr^{3+} was proposed as ground state from both mag-
netic susceptibility and inelastic neutron scattering investigations. This also
indicates the heavy quasi particles, mediating the superconducting state, to
originate from interactions between conduction electron system and the Pr
ions' quadrupolar degrees of freedom.

The following chapters describe physical ground state properties as well
as thermoelectric features of the system $Pr_yFe_{4-x}(Co,Ni)_xSb_{12}$ in detail, since
interesting results, considering the already discovered phenomena in related
Pr filled skutterudites, can be expected. Special emphasis is drawn to crystal
electric field influences and magnetic ground state properties, that may de-
viate distinctly from those of other Pr compounds. Whenever it is possible,
results are compared with data of isomorphous compounds already available
in literature.

Parameter	$Pr_{0.73}Fe_4Sb_{12}$	$Pr_{0.21}Fe_{2.5}Ni_{1.5}Sb_{12}$	$Fe_2Ni_2Sb_{12}$
a [nm]	0.91369(2)	0.90964(1)	0.90785(1)
Data collection	Image Plate	Image Plate	Image Plate
Radiation	$CuK\alpha$	$CuK\alpha$	$CuK\alpha$
Reflections measured	84	81	81
Θ range	$8\leq 2\Theta \leq 100$	$8\leq 2\Theta \leq 100$	$8\leq 2\Theta \leq 100$
Number of variables	24	19	19
$R_F = \sum |F_0 - F_c|/\sum F_0$	0.04	0.059	0.054
$R_I = \sum |I_{oB} - I_{cB}|/\sum I_{oB}$	0.039	0.043	0.042
$R_{wP} = \left[\sum w_i|y_{oi} - y_{ci}|^2/\sum w_i|y_{oi}|^2\right]^{1/2}$	0.064	0.054	0.128
$R_P = \sum |y_{oi} - y_{ci}|/\sum |y_{oi}|$	0.044	0.04	0.088
$R_e = \left[(N - P + C)/\sum w_i y_{0i}^2)\right]^{1/2}$	0.066	0.027	0.036
$\chi^2 = (R_{wP}/R_e)^2$	0.9	4.1	12.9
Atom parameters			
Pr in 2a (0,0,0)			
B_{iso} $[10^2$ nm$^2]$	1.28(1)	1.96(1)	-
Occupancy	0.73(2)	0.21(5)	-
T in 8c $(\frac{1}{4},\frac{1}{4},\frac{1}{4})$	8Fe	5Fe+3Ni	4Fe+4Ni
B_{iso} $[10^2$ nm$^2]$	0.90(4)	0.58(5)	1.25(5)
Occupancy	1	1	1
Sb in 24g (0,y,z)			
y	0.15978(1)	0.15800(4)	0.15730(8)
z	0.33480(1)	0.33500(4)	0.33488(8)
B_{iso} $[10^2$ nm$^2]$	1.63(2)	0.88(4)	1.59(2)
Occupancy	1	1	1
Interatomic distances [nm]; standard deviations generally < 0.0005 nm			
Pr-12Sb	0.3390	0.3369	0.3359
Pr-8T	0.3956	0.3939	0.3931
T-6Sb	0.2549	0.2544	0.2540
T-2Pr	0.3956	0.3939	0.3931
Sb-2T	0.2549	0.2544	0.2540
Sb-1Pr	0.3390	0.3369	0.3359

Table 3.1: Structural data of selected compounds of the series $Pr_yFe_{4-x}(Co,Ni)_xSb_{12}$, space group $Im\bar{3}$, No. 204.

3.2 Crystal structure

The obtained x-ray powder diffraction patterns of the series $Pr_yFe_{4-x}(Co,Ni)_xSb_{12}$ and of $Pr_{0.5}Co_4Sb_{10}Sn_2$ were indexed on the basis of a body-centered cubic structure corresponding to space group $Im\bar{3}$ (No. 204). Isotypism was confirmed with the filled skutterudite $(LaFe_4P_{12})$ type of structure as derived by Jeitschko et al. [111]. Rietveld refinements of the x-ray intensities converged satisfactorily for a fully ordered atom arrangement with respect to the atom site distribution among Pr, Fe/(Co,Ni) and Sb atoms. Since Fe, Co and Ni are known to cause difficulties in discrimination due to their similar electronic configurations leading to almost identical x-ray scattering powers and close chemical alloying behavior, Fe and Co/Ni atoms were assumed to be randomly distributed at the transition metal c sites. Refinement of the occupation factors revealed a full occupancy of the Fe/(Co,Ni) sublattice, whereas considerable defects in the Pr sites strongly dependent on the particular Co and Ni concentration were observed. A

summary of refinement data of selected compounds can be found in table 3.1. Note, that due to the usually strong correlation with isotropic temperature factors B_{iso}, occupancies were kept constant in the final Rietveld runs in order to refine B_{iso}. As evident from table 3.1, the thermal parameters of the rare earth tend to be rather small when compared to the prediction of their large displacement. This has to be attributed to strong influence of occupation, peak shape and absorption etc. on the thermal parameters, which in powder refinements, in contrast to single crystal or neutron diffraction data, leads to values of B_{iso}, that should not be overinterpreted.

In the case of the Co/Ni containing samples the final Pr content was evaluated from a combined Rietveld refinement and EPMA investigation, where the latter also served to determine the final Fe/(Co,Ni) content. Since materials crystallizing in the filled skutterudite structure do not form directly from the melt, only long time annealing may guarantee and result in single-phase samples. It is therefore essential to have a proper compositional starting ratio of the elements and to compensate for Sb losses due to vaporization during the arc-melting process. Only minor shifts with respect to the nominal starting composition were detected after annealing, additional peaks in the x-ray diffraction patterns could be identified as free Sb and minor amounts of $FeSb_2$ [167]. Results of selected simultaneous refinements of filled skutterudite phase with impurity phases are shown in figures 3.2 and 3.3. Note, that $Pr_{0.57}Fe_{3.5}Ni_{0.5}Sb_{12}$ was revealed to possess the largest amount of impurities (<5%). For the refinement the arrangement of free Sb atoms was assumed to be accounted for by the structure of free Sb metal, trigonal space group $R\bar{3}m$ (No. 166). The calculated Bragg positions corresponding to the latter are given in the second line on the bottom of Figs. 3.2 and 3.3, whereas the third line represents the Bragg positions of $FeSb_2$ (space group $Pnnm$, No. 58). It is interesting to point out, that there is a strong correlation between the intensities of the reflections at $2\Theta \simeq 19°$ and $24°$ associated with (h,k,l) values of (0,0,2) and (1,1,2) and Pr filling fraction. The smaller the occupation of the 2a sites, the more pronounced Bragg peaks are observed.

Lattice paramaters a of $Pr_yFe_{4-x}(Co,Ni)_xSb_{12}$ as function of the respective T=(Co,Ni) content x as derived from x-ray as well as EPMA data are depicted in Fig. 3.4. Cell dimensions of the unfilled ternary compound $Fe_2Ni_2Sb_{12}$ and $CoSb_3$ were also added, since comparison with filled counterpart allows for direct evaluation of the influence of the rare earth element occupying the large cavities of the structure. $Fe_{4-x}Ni_xSb_{12}$ only exists for $x = 2$, since any greater deviation from stoichiometry changes the valence electron count and formation is impeded. This is understood from simple arguments based on binary $CoSb_3$, which can be described by the ionic formula $Co^{3+} Sb_3^{1-}$. Assuming Fe to be in a 2+ state and Ni to be tetravalent in $Fe_2Ni_2Sb_{12}$, the total valence electron count remains constant the latter compound electronically resem-
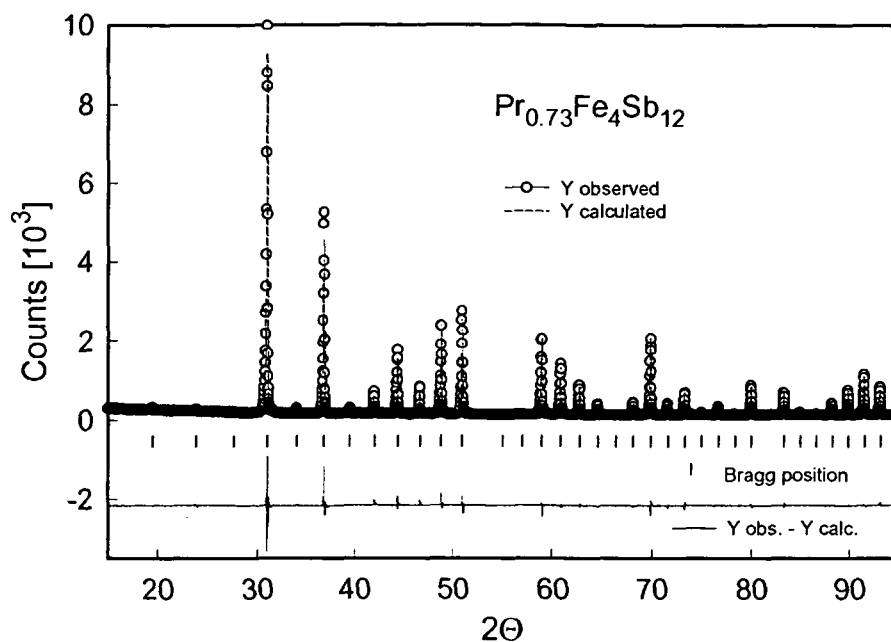
Figure 3.2: X-ray diffraction pattern of $Pr_{0.73}Fe_4Sb_{12}$.
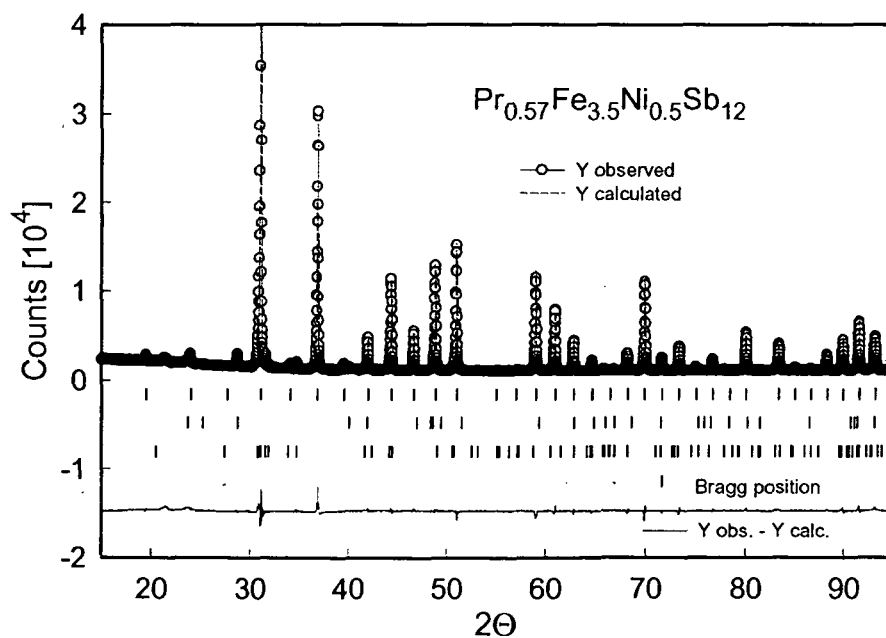
Figure 3.3: X-ray diffraction pattern of $Pr_{0.57}Fe_{3.5}Ni_{0.5}Sb_{12}$. The vertical marks index the atomic Bragg peaks for filled skutterudite structure (first line), free Sb (second line) and $FeSb_2$ (third line), see text.
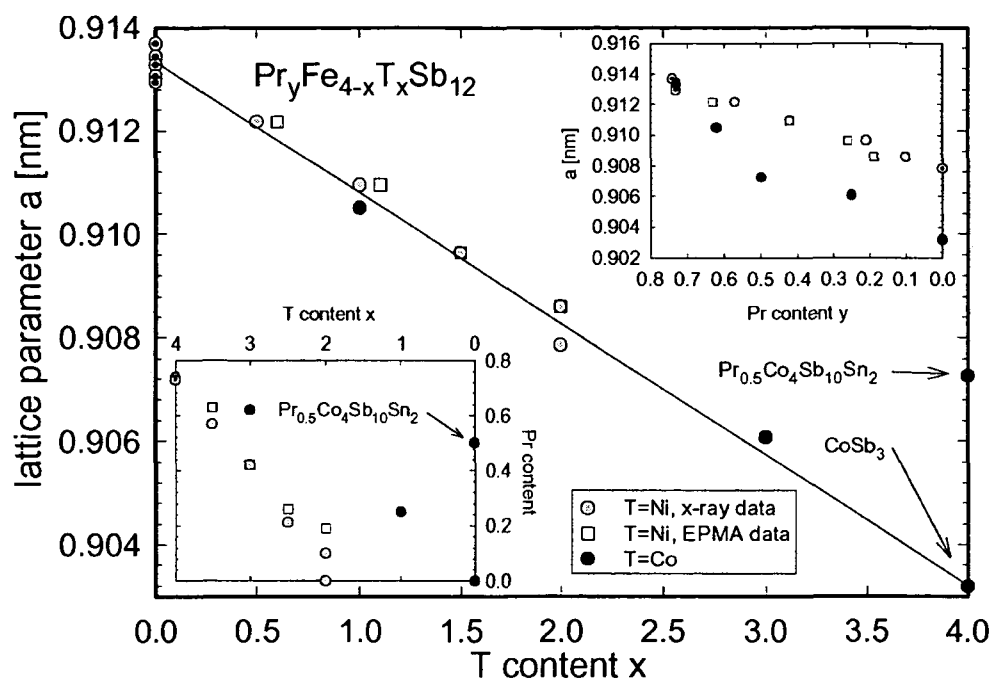
Figure 3.4: Dependencies between lattice parameter a, Fe content $4 - x$ and Pr filling fraction y of $Pr_y Fe_{4-x}(Co,Ni)_x Sb_{12}$.

bling binary skutterudites. Formation is therefore only expected for $x = 2$, which has been verified experimentally, compare e.g. [168]. True ternary skutterudites such as $Fe_2 Ni_2 Sb_{12}$ should not be confused with doped binary skutterudites such as the systems $Co_{1-x} Ni_x Sb_3$ and $Co_{1-x} Fe_x Sb_3$, where only small concentrations of Fe and Ni ($x < 0.1$) have significant impacts on electrical and thermal properties [169, 130, 170].

A linear decrease of the lattice dimensions is observed when proceeding from parent $Pr_{0.73} Fe_4 Sb_{12}$ with $a = 0.91369$ nm to $Fe_2 Ni_2 Sb_{12}$ with $a = 0.90785$ nm, both values agree well with those stated by Braun et al. [113] and Chapon et al. [171]. In the case of Fe/Co substitution the lattice constant reduces to 0.90607 nm for $Pr_{0.25} FeCo_3 Sb_{12}$ and 0.90319 for binary $CoSb_3$. With respect to the related filled skutterudite system $Eu_y Fe_{4-x} Co_x Sb_{12}$ [127], the substantial reason for the change of the lattice constant from $a = 0.9160$ nm ($x = 0$) to $a = 0.90319$ nm ($x = 4$) was attributed to both the Fe/Co substitution and the amount of Eu within the structure. The rare earth was proposed to somewhat blow up the lattice, since in the pure Co compounds $Eu_y Co_4 Sb_{12}$ the lattice constant increases from $a = 0.90319$ nm for pure $CoSb_{12}$ to $a = 0.90608$ nm for $y = 0.2$, $a = 0.90924$ nm for $y = 0.44$ [128] and $a = 0.90941$ for $y = 0.55$ [172]. This indicates a cell volume change of about

2%. A similar, but smaller effect was deduced for $Yb_yCo_4Sb_{12}$ [128]. This finding is surprising when comparing the dimensions of the void with the free ion volume of the rare earth occupying it. It was mentioned before that one of the reasons, why filled skutterudites exhibit strongly reduced lattice thermal conductivities, are their exceptionally large atomic displacement parameters arising from their loose bonding and rattling in the oversized cages. One would thus assume the filler element to have only minor influence on the lattice parameter. In fact, the volume increase in $Eu_yCo_4Sb_{12}$ could be to some extent related to a valence change of the Eu ions. X-ray absorption edge measurements evidenced an increase of the valence of Eu from close to magnetic Eu^{2+} in $Eu_{0.83}Fe_4Sb_{12}$ to a valence of approximately 2.6 in $Eu_{0.2}Co_4Sb_{12}$ and 2.35 in $Eu_{0.44}Co_4Sb_{12}$ [127]. The Eu valence thus seems to sensitively depend on the amount of incorporated Eu. Considering the lanthanoid contraction leading to a decrease in volume with increasing valence, the larger lattice constants in $Eu_yCo_4Sb_{12}$ with higher Eu content can be conceived. As for $Fe_2Ni_2Sb_{12}$ with $a = 0.90785$ nm and its filled variant $Pr_{0.1}Fe_2Ni_2Sb_{12}$ with $a = 0.9086$, only a minor change occurs corroborating the assumption that substitution on the transition metal site primarily determines cell dimensions, whereas filler concentration may only be of importance in the case of intermediate or mixed valence systems. On the other hand, the significantly larger lattice dimensions of $Pr_{0.5}Co_4Sb_{10}Sn_2$ compared to those of unfilled $CoSb_3$ would imply a relatively strong impact of the filler element on the cell dimensions, since substitution of Sb by Sn should not contribute to such an extent due to Sb and Sn atoms possessing similar size. However, in the case of homologous Fe/(Co,Ni) substituted and Ce filled skutterudites [125, 171] and also for the System $(Sn,Eu,Yb)_yNi_4Sb_{12-x}Sn_x$ the cell volume was revealed to remain rather independent of the type of filler element as well as of filling fraction, too [173].

The insets of Fig. 3.4 provide plots of lattice constants and Co/Ni content vs. Pr occupation. As mentioned above considerable defects in the Pr sites were observed both from x-ray as well as EPMA data. A maximum filling fraction of 73% was reached in the parent compound, which is strongly reduced as Fe is substituted by Ni reaching 10% according to x-ray, a less dramatic effect applies with respect to the Co containing samples. An amount of 50% Pr could be achieved in the Sn substituted compound $Pr_{0.5}Co_4Sb_{10}Sn_2$, which arises from the fact, that the electron deficiency of Sn compared to Sb can be compensated by additional electropositive Pr. $Eu_{0.56}Co_4Sb_{11}Sn$ and $Eu_{0.83}Co_4Sb_{10}Sn_2$ are examples of homologous compounds, where the same arguments apply [128]. Although only recently closely inspected and explicitly mentioned in literature, incomplete occupation of the 2a sites by rare earth elements are common to a large number of already synthesized ternary filled skutterudites. While complete filling could be achieved in the case of

e.g. $EuFe_4P_{12}$ or $NdOs_4Sb_{12}$, only 94% of U could be accommodated in an Fe-P lattice or 83% of Nd in an Fe-Sb lattice [174, 175]. As mentioned above, the amount of Ni or Co further limits the possible amount of insertable Pr, Ni substitution results in a more rapid reduction of the possible filler fraction. Generally, forcing more rare earth atoms into the structure just results in the formation of secondary impurity phases. Higher amounts of rare earth elements than in polycrystalline materials seem to be accomplished in single crystals, see e.g. [74]. A reasonable approach to the understanding of the reduction of the maximum Pr content in the series $Pr_yFe_{4-x}Ni_xSb_{12}$ will be presented in chapter 3.7 on the basis of low lattice thermal conductivity arising from solid solution formation between a filled $PrFe_4Sb_{12}$ sublattice and an empty sublattice $\Box Fe_2Ni_2Sb_{12}$, where $\Box$ denotes the unoccupied cavities of the structure.

3.3 Magnetic properties

Fig. 3.5 depicts inverse magnetic susceptibilities of $Pr_yFe_{4-x}(Co,Ni)_xSb_{12}$ and $Pr_{0.5}Co_4Sb_{10}Sn_2$ as functions of temperature at an externally applied magnetic field of 1 T. Above about 50 K and below 250 K $1/\chi$ of all samples shown apart from $Pr_{0.21}Fe_{2.5}Ni_{1.5}Sb_{12}$ and $Pr_{0.25}FeCo_3Sb_{12}$ follows a modified Curie-Weiss type of temperature dependence. The smooth upturn at higher temperatures most probably originates from systematic measurement insufficiency and is therefore neglected in the following. The significant deviation of the susceptibility of $Pr_{0.21}Fe_{2.5}Ni_{1.5}Sb_{12}$ and $Pr_{0.25}FeCo_3Sb_{12}$ from a simple Curie-Weiss behavior evident from the steadily increasing slope of $1/\chi$ already at temperatures above 150 K, on the other hand, may arise from an enhanced, more than underlying diamagnetic signal. The large inverse magnetic susceptibilities exhibited by $Pr_{0.25}FeCo_3Sb_{12}$ and $Pr_{0.21}Fe_{2.5}Ni_{1.5}Sb_{12}$ reaching 800 and 1000 mol/emu at room temperature, respectively, correspond to small χ values of $1.2663 \cdot 10^{-3}$ and $0.9458 \cdot 10^{-3}$ emu/mol, that are generally considered to be additively composed of paramagnetic and diamagnetic signal:

$$\chi_{meas} = \chi_{para} + \chi_{dia}. \tag{3.5}$$

In an attempt to roughly estimate the magnitude of the expected diamagnetic contribution, simply the tabulated diamagnetic susceptibilities of the constituent elements of a certain compound were summed up and gave values of about $0.230 \cdot 10^{-3}$ emu/mol in both cases. χ_{dia} of a large number of elements are found e.g. in [176]. These results would account for about 20 to 25% of the experimentally deduced total susceptibilities at room temperature, are thus already of distinct importance for overall χ_{meas}. Furthermore, free Sb segregated at grain boundaries of the polycrystalline material - the presence of which was confirmed by refinement of the observed x-ray data - may
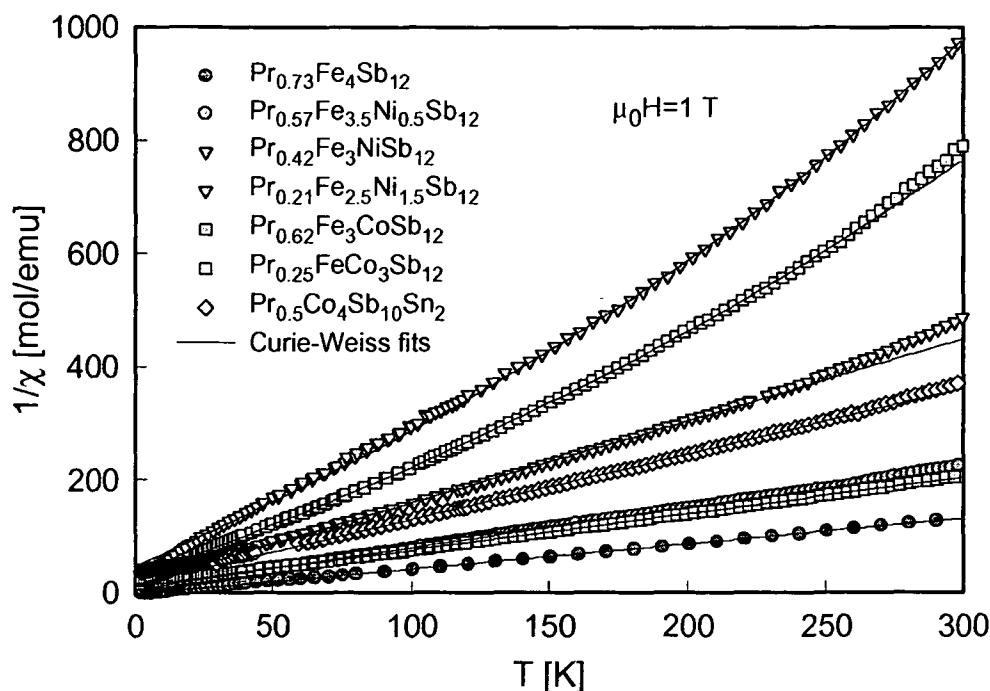
Figure 3.5: Temperature dependent inverse magnetic susceptibility $1/\chi(T)$ of $Pr_yFe_{4-x}(Co,Ni)_xSb_{12}$ and $Pr_{0.5}Co_4Sb_{10}Sn_2$. The solid lines represent least-squares fits according to a modified Curie-Weiss law (for details see text).

most probably be responsible for an additional enhancement of the already significant diamagnetic signal. Corroborating this assumption, an excess of free Sb was already noticed to be of importance also for the magnitude of the magnetoresistance in the case of $Eu_{0.83}Fe_4Sb_{12}$, where the reported giant magnetoresistance observed, could later be attributed to free Sb, which itself exhibits an enormous response of the resistivity in an applied magnetic field [177, 178]. The small susceptibilities of $Pr_{0.21}Fe_{2.5}Ni_{1.5}Sb_{12}$ and $Pr_{0.25}FeCo_3Sb_{12}$ in combination with enhanced diamagnetism could therefore be the reason for the appreciable deviation of $1/\chi$ from typical Curie-Weiss behavior.

In order to derive effective magnetic moments and paramagnetic Curie temperatures of the compounds under investigation least-squares fits to the susceptibility data in terms of a modified Curie-Weiss law according to equation 1.76 were performed at temperatures above 60 K (solid lines in Fig. 3.5). Generally, the temperature independent term χ_0 is added taking into account additional electron-electron interactions (Pauli susceptibility). In the case of $Pr_{0.21}Fe_{2.5}Ni_{1.5}Sb_{12}$ and $Pr_{0.25}FeCo_3Sb_{12}$ χ_0 was accepted to adopt negative values during evaluation procedure. The deduced values of $-0.492 \cdot 10^{-3}$

	μ_{eff}^{meas} [μ_B]	θ_p [K]	$\mu_{eff}^{Pr^{3+}}$	μ_{eff}^{sub} [μ_B]	χ_0	χ_{300K}^{meas} [10^{-3} emu/mol]	χ_{dia}^{theor}
$Pr_{0.73}Fe_4Sb_{12}$	4.15	5.45	3.06	2.81	0	-	
$Pr_{0.57}Fe_{3.5}Ni_{0.5}Sb_{12}$	3.26	-8.13	2.70	1.82	0.273	-	
$Pr_{0.42}Fe_3NiSb_{12}$	2.35	-10.40	2.32	0 (0.37)	0	-	
$Pr_{0.21}Fe_{2.5}Ni_{1.5}Sb_{12}$	1.98	-22.77	1.64	1.11	-0.492	0.9458	~ -0.230
$Pr_{0.62}Fe_3CoSb_{12}$	3.52	-17.6	2.82	2.11	0.0008	-	
$Pr_{0.25}FeCo_3Sb_{12}$	2.16	-15.84	1.79	1.21	-0.537	1.2663	~ -0.230
$Pr_{0.5}Co_4Sb_{10}Sn_2$	2.63	-12.46	2.53	0 (0.71)	0	-	

Table 3.2: Measured effective magnetic moments μ_{eff}^{meas}, paramagnetic Curie temperatures θ_p and temperature independent susceptibilities χ_o of $Pr_yFe_{4-x}Ni_xSb_{12}$ and $Pr_{0.5}Co_4Sb_{10}Sn_2$ deduced employing least-squares fits to the experimental data. $\mu_{eff}^{Pr^{3+}}$ and μ_{eff}^{sub} are Pr and Fe/Sb sublattice related calculated effective magnetic moments, χ_{dia}^{theor} represents theoretical diamagnetic susceptibilities, see text.

$-0.537 \cdot 10^{-3}$ emu/mol are of reasonable magnitude, if one considers, that χ_0 is negligible in all other compounds of the series. However, the fact, that χ_0 just represents a fitting parameter, has to be kept in mind when interpreting the derived values. Results of the least-squares fits are listed in table 3.2 together with room temperature values of the total measured susceptibility as well as the calculated theoretical diamagnetic contribution discussed above.

The effective magnetic moment μ_{eff} is reduced from 4.15 μ_B to 1.58 μ_B as Fe is substituted by Ni and the Pr content lowers, a slightly larger value was reported by Danebrock et al. for $PrFe_4Sb_{12}$, where a magnetic susceptibility study revealed an effective magnetic moment of 4.6 μ_B [97]. With increasing Co concentration μ_{eff} approaches a value of 2.16 μ_B in $Pr_{0.25}FeCo_3Sb_{12}$, while the higher effective magnetic moment evaluated for $Pr_{0.5}Co_4Sb_{10}Sn_2$ seems to be a direct consequence of 50% of the voids being occupied by the rare earth. The paramagnetic Curie temperature θ_p amounts to 5.45 K in $Pr_{0.73}Fe_4Sb_{12}$ and continuously decreases when proceeding through the series. Since Pr should exhibit a 3+ electronic configuration, μ_{eff} of $Pr_{0.73}Fe_4Sb_{12}$, 4.15 μ_B, has to be compared with the magnetic moment associated with that of free Pr^{3+}, 3.58 μ_B. The measured quantity exceeds the theoretical Pr moment considerably, a significant magnetic contribution of the $[Fe_4Sb_{12}]$ sublattice is thus required in order to match the observed magnetic moment. Assuming both rare earth as well as $[Fe_4Sb_{12}]$ contribution to be simply additive,

equation 3.6 yields an effective magnetic moment of 2.81 μ_B arising from the [Fe_4Sb_{12}] sublattice.

$$\mu_{eff}^{meas} = \sqrt{y(\mu_{eff}^{Pr^{3+}})^2 + (\mu_{eff}^{[Fe_{4-x}T_xSb_{12}]})^2} \qquad (3.6)$$

The same calculation was performed for all other samples, the evaluated magnetic moments are summarized in table 3.2 evidencing even for $Pr_{0.1}Fe_2Ni_2Sb_{12}$ a non-vanishing contribution of the [$Fe_2Ni_2Sb_{12}$] sublattice. $Pr_{0.5}Co_4Sb_{10}Sn_2$, on the other hand, seems to be characterized by the absence of a magnetic moment carrying sublattice, since experimentally derived μ_{eff} is very close to the theoretically predicted value (the quantity given in the brackets of table 3.2 represents the result according to expression 3.6). The same applies for $Pr_{0.42}Fe_3NiSb_{12}$, nevertheless, a contribution of [Fe_3NiSb_{12}] would be expected when closely inspecting the Ni dependence of μ_{eff}. The deviation of this compound from the overall trend may be attributed to the worse reproduction of the magnetic susceptibility by the Curie-Weiss fit compared to the other compounds of the series or also plausibly to impurity effects.

Magnetic properties of Fe-Sb sublattices in filled skutterudite systems have been subject of extensive discussion, while hardly any evidence for a paramagnetic contribution arising from the sublattice has yet been found in phosphide systems. For $PrFe_4P_{12}$, e.g., several studies revealed an effective magnetic moment very close to that of the free filler element [143, 179, 180], the non-magnetic rare earth filled skutterudite $LaFe_4P_{12}$, in contrast, was reported to exhibit a magnetic moment of 1.46 μ_B [120]. The weak temperature dependence of the magnetic susceptibility may point to some kind of strong Pauli paramagnetism, whereas Mößbauer measurements clearly deny the Fe atoms to behave magnetically [181].

The proposed magnetic contribution of the polyanionic sublattices in the series $Pr_yFe_{4-x}(Co,Ni)_xSb_{12}$ is backed by conclusions drawn for isomorphous skutterudite systems. Even the non-magnetic alkaline earth filler elements Ca, Sr and Ba give rise to effective magnetic moments between 3.7 and 4 μ_B/f.u. in Fe-Sb based filled skutterudites, in $LaFe_4Sb_{12}$ $\mu_{eff} = 3.0$ μ_B was observed clarifying directly the paramagnetic character of [Fe_4Sb_{12}] in these compounds [97]. The higher values in the former cases can be attributed to the transfer of two alkaline electrons per formula unit into the polyanionic sublattice leading to two out of four Fe atoms carrying uncompensated spins, while trivalent La donates three electrons. The one spin-uncompensated Fe atom per formula unit should therefore have a magnetic low-spin d^5 electronic configuration. This assumption is corroborated by the development of a paramagnetic moment in the system $Co_{1-x}Fe_xSb_{12}$ when starting from pure diamagnetic $CoSb_3$, where μ_{eff} asymptotes to about 1.7 μ_B/Fe atom as a function of the Fe concentration x. According to the formula $\mu_{eff} = 2[s(s+1)]^{1/2}\mu_B$ for

spin-only Fe^{3+} in a d^5 system, the theoretical value of 1.73 μ_B is in line with the experimental data [169]. An even more controversial case is $CeFe_4Sb_{12}$. Up to now several attempts have failed to explain the magnetic moment of $\mu_{eff} = 3.0$ μ_B in $CeFe_4Sb_{12}$, although intermediate valence between 3+ and 4+ state as well as strong hybridization of the Ce 4f level with the conduction band in combination with crystal electric field effects lowering the ground state degeneracy were considered [97, 124, 182]. However, with increasing Co content the observed moment lowers in $Ce_yFe_{4-x}Co_xSb_{12}$, similar to the results derived above for the homologous Pr series. A detailed study on $Eu_yFe_{4-x}(Co,Ni)_xSb_{12}$ also in this case evidenced a significant contribution of the polyanion complex to the total effective magnetic moment. Even the pure Co compounds $Eu_{0.44}Co_4Sb_{12}$ and $Eu_{0.2}Co_4Sb_{12}$ were derived to exhibit effective magnetic moments, that, in order to explain their magnitude, have to originate from both rare earth as well as Co-Sb polyanion although in clear contradiction to the diamagnetism of binary $CoSb_3$ [127]. Surprisingly, μ_{eff} of Sn substituted variants of latter compounds almost perfectly matches the free Eu moment pointing to the absence of a moment bearing Co-Sb-Sn sublattice [128]. This fact agrees nicely with the zero moment of $[Co_4Sb_{10}Sn_2]$ in $Pr_{0.5}Co_4Sb_{10}Sn_2$ as revealed from the presented magnetic susceptibility data. The observed effective magnetic moments of the polyanionic complex in Sb based filled skutterudites, as well as that of the pure Co compounds, can be related to certain features of the density of states and to a significant deviation of the band structure of binary skutterudites in comparison to their filled counterparts. The rare earth filler elements, independent of their magnetic state, enhance magnetism of the particular Sb sublattice [183]. In particular, band structure calculations for $LaFe_4P_{12}$ [184] and $LaFe_4Sb_{12}$ [185] evidenced much narrower valence and conduction bands for the latter due to the larger lattice constant. Additionally, a double-peak structure of the Fe d partial density of states (DOS) below the Fermi energy in $LaFe_4Sb_{12}$ backs the assumption of Fe carrying a magnetic moment as proposed from magnetic susceptibility. Spin-polarized calculations also support a magnetic solution [185]. These calculations generally showed similar features within a certain family of filled skutterudites apart from the 4f contribution of a particular rare earth filler element. From these theoretical considerations, assuming pronounced similarities of the DOS between $LaFe_4Sb_{12}$ and that of skutterudites filled with other rare earth elements, the magnetic moments of the polyanion found in the Fe-Sb filled skutterudite systems follow from a distinct feature of the Fe 3d partial density of states around the Fermi energy.

The low temperature part of the inverse magnetic susceptibility of $Pr_{0.73}Fe_4Sb_{12}$ is depicted in the inset of Fig. 3.6b. The distinct curvature below about 6 K is reminiscent of the onset of long range magnetic order. A.c. susceptibility measurements - the results are found in the same Fig. -
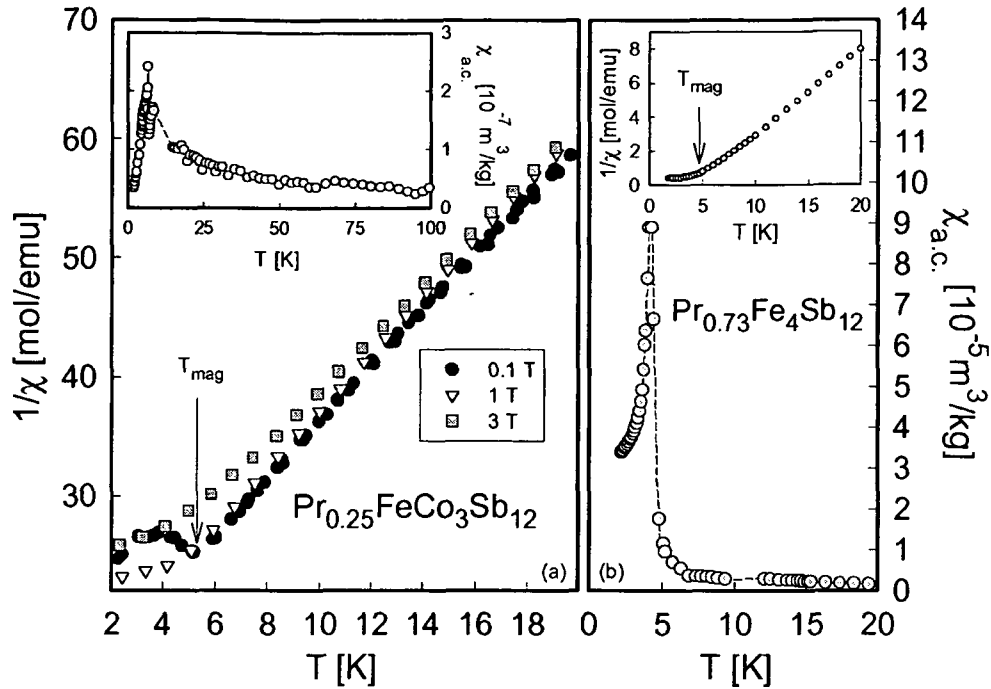
Figure 3.6: (a) Temperature dependent inverse magnetic susceptibility $1/\chi(T)$ of $Pr_{0.25}FeCo_3Sb_{12}$ in externally applied magnetic fields of 0.1, 1 and 3 T. Inset: a.c. magnetic susceptibility $\chi_{a.c.}$ of $Pr_{0.25}FeCo_3Sb_{12}$ vs. temperature. (b) A.c. magnetic susceptibility $\chi_{a.c.}$ of $Pr_{0.73}Fe_4Sb_{12}$ plotted as a function of temperature. Inset: Low temperature $1/\chi(T)$ of $Pr_{0.73}Fe_4Sb_{12}$.

additionally served to shed light onto this observation. Both low temperature $1/\chi(T)$ as well as $\chi_{a.c.}(T)$ data do neither unambiguously favor ferro- nor antiferromagnetic order, however, the height of the jump in the a.c. susceptibility evidences bulk long range magnetic order. The transition was evaluated to occur at about $T_{mag} = 4.5$ K, which is slightly below the transition temperature of $T = 5$ K proposed by Danebrock et al. [97]. Already at a Ni content of $x = 0.5$ and a Co concentration of $x = 1$ the respective low temperature susceptibility curves of $Pr_yFe_{4-x}(Co,Ni)_xSb_{12}$ (not shown) lack any sign of magnetic order as will be verified by low temperature resistivity measurements presented in a following section. It has to be mentioned, that long range magnetic order seems to emerge again in the compound $Pr_{0.25}FeCo_3Sb_{12}$, Fig. 3.6a displays $1/\chi(T)$ of latter sample as a function of temperature at various externally applied magnetic fields. The small upturn evident from the 0.1 T curve is characteristic of a magnetic transition, however, it vanishes already in a field of 1 T. Although the transition is also seen in $\rho(T)$ (compare section 3.5), the magnitude of the anomaly observed in $\chi_{a.c.}(T)$, shown in the

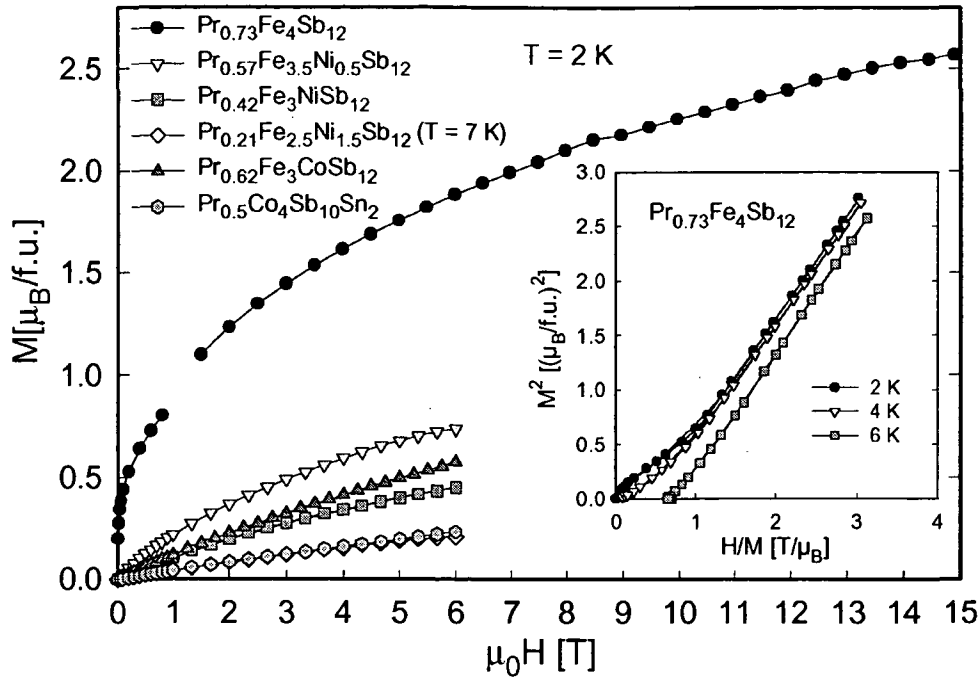Figure 3.7: Isothermal magnetization M at 2 K as a function of the magnetic field $\mu_0 H$ of $Pr_y Fe_{4-x}(Co,Ni)_x Sb_{12}$ and $Pr_{0.5}Co_4 Sb_{10}Sn_2$. Inset: Arrott plots of $Pr_{0.73}Fe_4 Sb_{12}$ at 2, 4 and 6 K.

inset of Fig. 3.6a, clearly denies it to be of bulk nature and thus to be due to an impurity phase present. The unlikely re-appearance of magnetic order in combination with only 25% of Pr and low Fe content corroborates this conclusion.

Results of isothermal magnetization measurements taken at 2 K are displayed in Fig. 3.7. From both $M(H)$ data and Arrott plots given in the inset of the figure, ferromagnetism in $Pr_{0.73}Fe_4 Sb_{12}$ cannot be validated, although at small fields, the $M(H)$ curve exhibits signs of spontaneous magnetization. In contrast to ferromagnetism, concluded by Danebrock et al. [97] exclusively from magnetic susceptibility measurements, the overall picture presented here rather points to some type of complicated antiferromagnetic spin arrangement, which, even on the basis of elastic neutron diffraction data collected below T_{mag}, could not be satisfactorily resolved due to a rather weak intensity pattern.

Closely inspecting the magnetization curve of the parent compound $Pr_{0.73}Fe_4 Sb_{12}$, the complete absence of saturation and the significantly lower M values of about 1.9 μ_B/f.u. at a magnetic field of 6 T corresponding to roughly 2.6 μ_B/Pr ion compared to the theoretical saturation magnetization

of $M_{sat} = gJ$, 3.2 μ_B, point to crystal electric field (CEF) effects lifting the ground state degeneracy of the $J = 4$ total angular momentum of Pr^{3+}. Nevertheless, it has to be mentioned, that magnetization at 15 T reaches $2.6\mu_B$/f.u. (3.6 μ_B/Pr ion), which would exceed the theoretical value of 3.2 μ_B by far. The origin of this experimental matter cannot be totally ascribed to the magnetization contribution due to the $[Fe_4Sb_{12}]$ sublattice (see below), further studies would be needed in order to clarify the obtained magnitude of M at higher fields. The crystal symmetry of a compound essentially determines the ground state degeneracy and the energies of the resulting respective CEF levels of the rare earth ion. Neglecting any influence of vacancies and slight lattice distortions in the Pr sublattice, cubic symmetry of the 2a site of the filled skutterudite structure splits the rare earth $J = 4$ total angular momentum into a singlet Γ_1, a doublet Γ_3 and in the triplets Γ_4 and Γ_5 (or Γ_4^1 and Γ_4^2, see below). Due to the even total angular momentum (non-Kramers ion) also non-magnetic ground states can be the consequence, which accounts for the ground state properties of isomorphous skutterudites $PrRu_4P_{12}$, $PrFe_4P_{12}$ and $PrOs_4Sb_{12}$, outlined in section 3.1.3, where the doublet Γ_3 was revealed as CEF ground state and magnetic order was explained in terms of quadrupolar ordering [155, 1, 3, 4]. With increasing Ni and Co content the magnetization obtained at 6 T drops rapidly, while M of $Pr_{0.57}Fe_3NiSb_{12}$ amounts to 0.74 μ_B/f.u., most surprisingly, $Pr_{0.5}Co_4Sb_{10}Sn_2$ exhibits just a value of 0.21 μ_B/f.u. at 6 T, although about 50% of cavities of the structure are occupied by the filler element. If insignificant changes in the CEF level scheme were assumed for all compounds, magnetization at 6 T would be expected to be higher for the substituted samples, in particular for the Sn containing pure Co compound. As illustrated with respect to the system $YbCu_{5-x}Al_x$, substitution may indeed strongly affect CEF splitting, although crystal structure as well as Yb position in latter series remain unchanged [186]. Besides, rather strong irregularities in the CEF splittings can also be expected to be caused by the consecutive lowering of the rare earth content, which is most probably accompanied by deviations of the local field around the filler elements from cubic symmetry due to e.g. lattice distortions giving rise to changes in the charge distribution within the structure.

In order to estimate the CEF scheme for parent $Pr_{0.73}Fe_4Sb_{12}$ a first attempt was made by analyzing magnetic susceptibility data. An inelastic neutron diffraction investigation then served to verify the thereby obtained results, which indeed evidenced close agreement with the susceptibility derived CEF level scheme. The application of the Van Vleck formula (equation 1.78, section 1.6.2) to the susceptibility due to crystal electric fields χ_{CEF} requires the isolation of the susceptibility contribution originating solely from Pr. With λ denoting the molecular field parameter arising from exchange interactions between Pr ions, the relation $1/\chi_{CEF} = 1/\chi^{Pr} + \lambda$ was assumed.
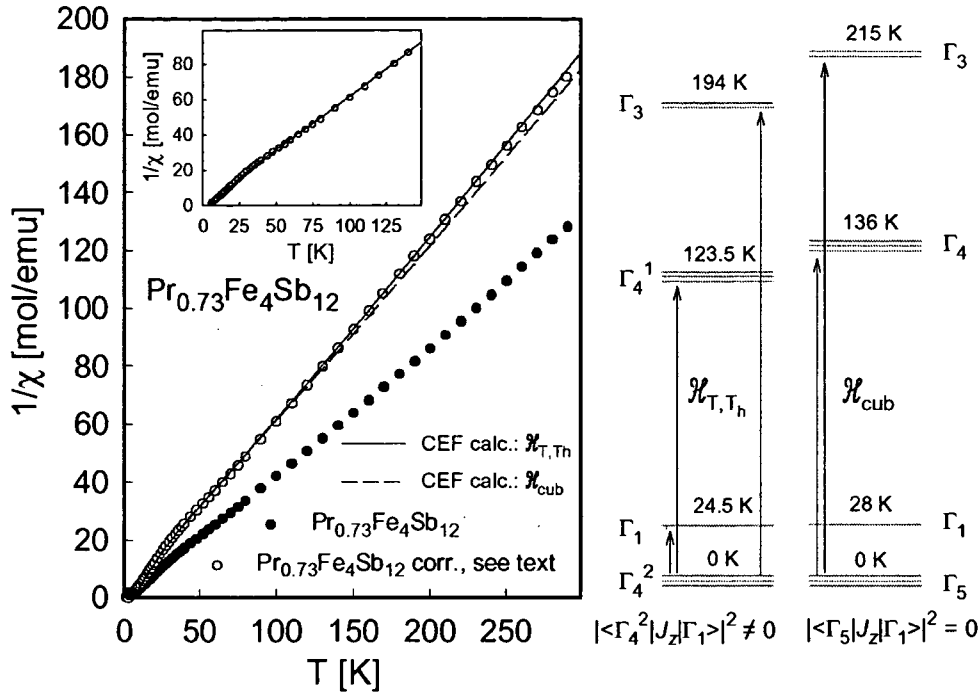
Figure 3.8: Left: $1/\chi(T)$ of $Pr_{0.73}Fe_4Sb_{12}$ as well as $1/\chi(T)$ solely associated with Pr. Solid and dashed lines are results of CEF calculations, see text. Right: Calculated CEF level scheme based on Hamiltonians given in expressions 3.7 and 3.8.

Although representing just a rough approximation, the contribution of Pr and that of the $[Fe_4Sb_{12}]$ sublattice were considered to be simply additive, i.e. $\chi = \chi^{Pr} + \chi^{[Fe_4Sb_{12}]}$, as well as $\chi^{[Fe_4Sb_{12}]}$ was supposed to be adequately accounted for by a simple Curie type of temperature dependence C/T with C re-calculated from the above obtained effective magnetic moment of the sublattice, $\mu_{eff}^{[Fe_4Sb_{12}]} = 2.81 \ \mu_B$. Subtraction from the total susceptibility and extrapolation to a Pr content of 100% by multiplication with $1/0.73$ resulted in χ^{Pr}, which is plotted in Fig. 3.8 as $1/\chi(T)$ and denoted by $Pr_{0.73}Fe_4Sb_{12}$ corr.

According to section 1.6.1, the general Hamiltonian for cubic symmetry is

$$H_{cub} = B_4^0(O_4^0 + 5O_4^4) + B_6^0(O_6^0 - 21O_6^4), \tag{3.7}$$

which has to be upgraded for point groups T and T_h resulting in

$$H_{T,T_h} = B_4^0(O_4^0 + 5O_4^4) + B_6^0(O_6^0 - 21O_6^4) + B_6^2(O_6^2 - O_6^6). \tag{3.8}$$

In contrast to long time belief, the Hamiltonian 3.7 cannot accurately account for crystal electric fields in the cubic point groups T and T_h, since the latter

do not contain two types of symmetry operations found for other cubic point groups: rotations through $\pi/2$ about the fourfold axis (sym. operation C_4) and Umklappung, rotations through π perpendicular to the principle rotation axis (sym. operation C_2') [59]. With respect to Hamiltonian 3.7, the additional term $B_6^2(O_6^2 - O_6^6)$ in Hamiltonian 3.8 leaves the degeneracy of each CEF sublevel unchanged, however, with increasing parameter B_6^2, eigenvalues and eigenfunctions are altered. In the case of Pr^{3+} ($J = 4$), the eigenfunctions of singlet Γ_1 and doublet Γ_3 remain the same, whereas the states Γ_4 and Γ_5 are mixed resulting in new eigenfunctions deviating from those derived for $B_6^2 = 0$. Note, that in the following Γ_4^1 and Γ_4^2 will be used as notation for the new mixed states, that approach Γ_4 and Γ_5 upon decreasing B_6^2. The mixing of states has one further consequence especially of importance for the interpretation of inelastic neutron patterns. Whereas a vanishing parameter B_6^2 gives rise to a zero matrix element between triplet Γ_5 and singlet Γ_1, the mixing of Γ_4 and Γ_5 states yields a non-vanishing transition probability $|\langle \Gamma_4^2 | J_z | \Gamma_1 \rangle|^2$, consequently neutron induced transitions between these multiplets can be observed.

To be able to directly compare the influence of the additional term on the CEF level scheme, the corrected inverse susceptibility of $Pr_{0.73}Fe_4Sb_{12}$ was modeled according to the Van Vleck relation (equ. 1.78) employing both Hamiltonians. Since polycrystalline material was used for magnetic investigations, susceptibility contributions perpendicular and parallel to the applied magnetic field were calculated first and then summed up in terms of $\chi_{CEF} = \frac{1}{3}(2\chi_\perp + \chi_\parallel)$. Reasonable results were obtained for the parameters $B_4^0 = 0.036$ K, $B_6^0 = 0.00122$ K and $B_6^2 = 0.001$ K in the case of Hamiltonian 3.8 and for $B_4^0 = 0.04$ K and $B_6^0 = 0.00133$ K in the case of a vanishing parameter B_6^2, for the molecular field constant λ a value of 5 mol/emu was revealed. The corresponding inverse magnetic susceptibilities are added in Fig. 3.8 as solid and dashed lines. Including the term $B_6^2(O_6^2 - O_6^6)$ yields more precise results especially in the elevated temperature range above about 150 K, while convincing agreement with the experimental data can be confirmed for both Hamiltonians at lower temperatures, where the calculated susceptibilities merge. The thus derived CEF level splittings are also found in Fig. 3.8 evidencing the magnetic triplet Γ_4^2 (Γ_5) as ground state followed by the singlet Γ_1 at 24.5 and 28 K and the triplet Γ_4^1 (Γ_4) at 123.5 and 136 K. The uppermost level in both cases is the doublet Γ_3 situated at energies of 194 and 215 K, respectively. Both Hamiltonians revealed the expectedly same level scheme, the energies of the particular levels are slightly modified to lower values by the additional term in expression 3.8. However, one has to keep in mind, that the adjustment of the CEF parameters was done by trial and error, better results are of course conceivable, which could alter the separation of the levels, but should, on the other hand, not affect the relative
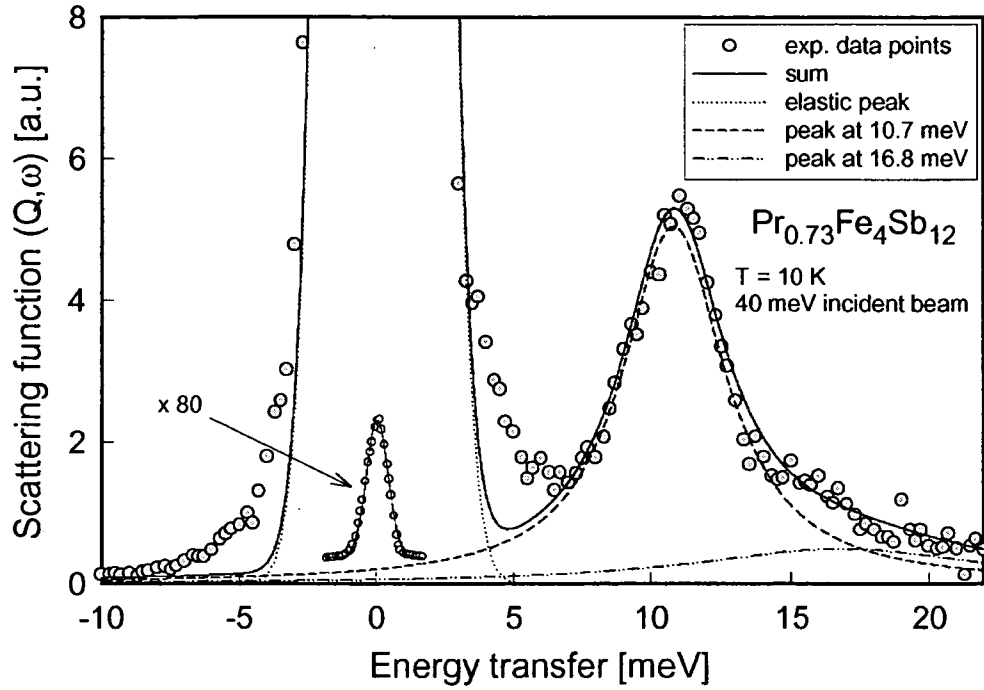
Figure 3.9: Inelastic neutron scattering pattern obtained at 10 K upon 40 meV incident neutron beam: scattering function $S(Q,\omega)$ vs. energy transfer.

positions among the multiplets. The observation of long range magnetic order in $Pr_{0.73}Fe_4Sb_{12}$ is also compatible with a Γ_4^2 ground state, since the latter is associated with a magnetic moment of $\mu = 1.98 \ \mu_B$ further explaining the magnitude of experimental magnetization obtained at 2 K and fields below 6 T. The approximation made in order to obtain the contribution originating from Pr may be the greatest possible source of error.

Inelastic neutron scattering was performed in order to verify the picture drawn for CEF splitting in $Pr_{0.73}Fe_4Sb_{12}$. Incident neutron beams of energies of 40 and 11 meV resulted in the two spectra depicted in figures 3.9 and 3.10. A first view at the data corresponding to the 40meV spectrum, reveals the elastic peak centered at 0 meV as well as an inelastic peak with a maximum situated roughly around 10 meV. Qualitative modeling of the pattern was achieved in terms of one Gaussian contribution accounting for the elastic peak (dotted line in Fig. 3.9) and one simple Lorentzian function (dashed line) for the inelastic excitation. Gaussian and Lorentzian distributions are given in expressions 3.9 and 3.10, where A denotes a constant, ω_0 the center and Γ the width of the distributions.

$$S(\omega) \propto A \exp -\frac{1}{2}\left(\frac{\hbar w - \hbar w_0}{\Gamma}\right)^2 \tag{3.9}$$
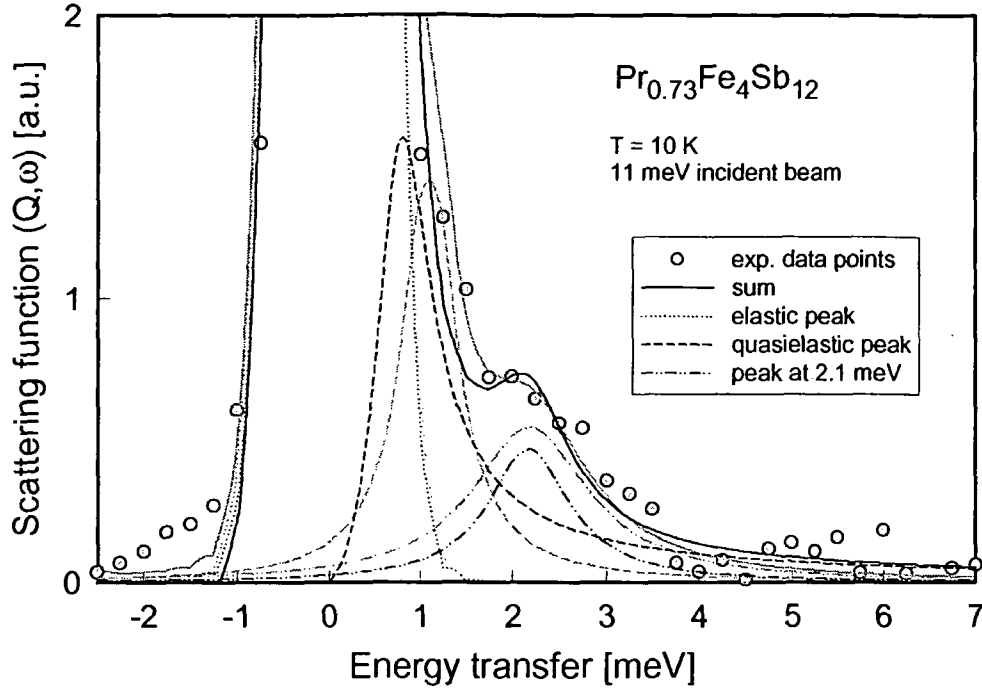
Figure 3.10: Inelastic neutron scattering spectrum obtained at 10 K upon 11 meV incident neutron beam: scattering function $S(Q, \omega)$ vs. energy transfer.

$$S(\omega) \propto \frac{A\omega}{(\hbar\omega - \hbar\omega_0)^2 + \Gamma^2} \tag{3.10}$$

Least-squares fits to the data revealed the latter to center at 10.7 meV, in perfect agreement with the CEF triplet Γ_4^1 according to above calculations. Whereas the position of this peak is evident right away, neutron induced population of the uppermost doublet Γ_3 situated roughly around 200 K is less than obvious. However, in order to match the experimentally obtained structure, a second Lorentzian with rather low intensity was employed centered at 16.8 meV yielding convincing results.

The spectrum derived upon the 11meV incident neutron beam was analyzed employing a Gaussian and two Lorentzians, where one accounts for the quasielastic signal (dashed line in Fig. 3.10) and the other for the inelastic peak (dashed-dotted line) associated with the singlet Γ_1 at 2.11 meV (24.5 K). Grey and black colored lines in the figure simply represent two different approximations, where slight modifications of the quasielastic Lorentzian were applied. Note, that according to Hamiltonian 3.7 transitions from ground state Γ_5 (Γ_4^2) to this level would be forbidden due to the vanishing matrix element. Again, summing up the contributions of all peaks evidences overall agreement with the experimental data. Especially the slight s-type of struc-
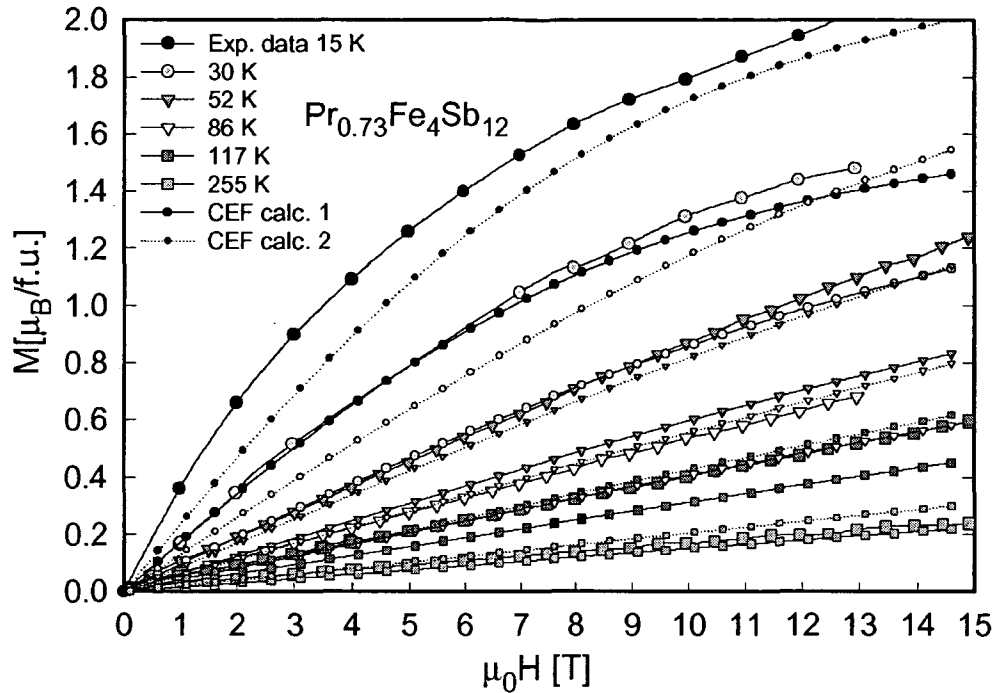
Figure 3.11: Comparison between experimentally deduced and calculated magnetization of $Pr_{0.73}Fe_4Sb_{12}$ in the paramagnetic temperature range. Large symbols correspond to experimental data, whereas smaller symbols denote calculated quantities, compare text.

ture around 2 meV is well reproduced by the Lorentzian associated with the non-magnetic singlet state backing the CEF conclusions drawn as well as probing the revised Hamiltonian for cubic point groups T and T_h. It has to be noted that there is still uncertainty, since intensities for the various transitions calculated from the CEF scheme should be compared with the available neutron data. The latter was not possible due to insufficient background evaluation, inelastic scattering on isomorphous non-magnetic $La_{0.83}Fe_4Sb_{12}$ could not yet be performed.

Fig. 3.11 illustrates experimental and calculated isothermal magnetizations in the paramagnetic temperature range. The latter was obtained simply by taking into account above derived CEF parameters without any other free adjustable variable, in this case H_{T,T_h} was employed only. CEF calc. 1 and CEF calc. 2 denote results of basically the same calculations, in the first case, however, the data was multiplied by a factor of 0.73 in order to match the experimental magnetization given in μ_B/f.u. instead of μ_B/Pr ion. As evident from the figure, convincing agreement between experiment and model calculation cannot be confirmed. If the factor 0.73 is neglected (CEF calc. 2), results

are improving, but can thus be considered only a crude approximation. This general discrepancy between measured magnetization and calculation may be attributed to the assumptions necessary in determining the contribution of Pr to the magnetic susceptibility, since elucidation of magnetism in the [Fe$_4$Sb$_{12}$] sublattice has not been possible yet in Sb based filled skutterudite compounds. High field Mössbauer results for Pr$_{0.73}$Fe$_4$Sb$_{12}$, which are currently being carried out, up to now are in contrast to the magnitude of the susceptibility-derived magnetic moment, since the internal magnetic field arising from core and valence contribution of Pr is by far too small. Besides the inadequate separation of Pr and sublattice contribution to $\chi(T)$, an important Fe contribution to the magnetization could be considered at a first glance due to the large effective moment of the sublattice. On the other hand, such a feature is rather unlikely, because of the fact, that itinerant moments are generally known to account for a relatively small magnetization even if a significant effective moment is observed [187]. Inelastic neutron diffraction data may obviously also be interpreted differently especially as far as low and high energy peaks are concerned associated with first excited state and uppermost doublet level, however, agreeing on the positions chosen reflects the observed pattern quite well. In order to undoubtedly determine CEF related quantities, single crystal material seems to be of high importance, which unfortunately was not available for further investigations.

3.4 Specific heat

Temperature dependent heat capacity data of Pr$_y$Fe$_{4-x}$(Co,Ni)$_x$Sb$_{12}$ up to 30 K are depicted in Fig. 3.12 as C_p/T vs. T. Additionally, external magnetic fields of up to 9 T were applied in the case of Pr$_{0.73}$Fe$_4$Sb$_{12}$ and Pr$_{0.25}$FeCo$_3$Sb$_{12}$, results are given in Fig. 3.13, left hand scale. The pronounced anomaly with a maximum slightly below 5 K marks the onset of long range magnetic order in parent Pr$_{0.73}$Fe$_4$Sb$_{12}$ in perfect agreement with magnetic investigations. With increasing magnetic field, the observed peak in the specific heat becomes washed out and essentially vanishes at fields higher than 3 T, which is commonly referred to in terms of anisotropy of the phase boundary in the H vs. T plane. Considering Pr$_{0.25}$FeCo$_3$Sb$_{12}$, a small peak in C_p/T appears roughly around 5 K, which is identified as indication for magnetic order. The magnitude of the anomaly is rather small corroborating it to originate from an impurity phase, which was proposed analyzing magnetic susceptibility data (compare previous section). A magnetic field of 1 T is sufficient to suppress this impurity based magnetic transition.

CEF splitting of the 9-fold degenerated ground state of Pr^{3+} in cubic environment should give rise to pronounced Schottky anomalies at low temperatures, which can indeed be verified from experimental findings at least
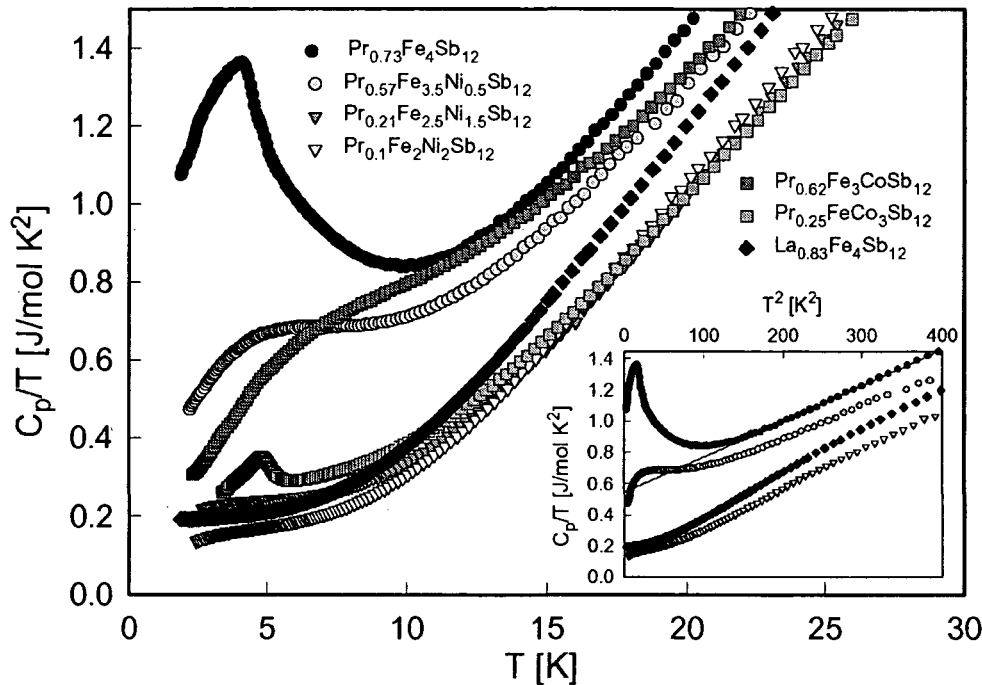
Figure 3.12: Temperature dependent specific heat C_p of $Pr_yFe_{4-x}(Co,Ni)_xSb_{12}$ as well as of $La_{0.83}Fe_4Sb_{12}$ plotted as C_p/T vs. T. Inset: Low temperature C_p/T of selected samples as a function of T^2.

in the case of $Pr_{0.57}Fe_{3.5}Ni_{0.5}Sb_{12}$ and $Pr_{0.57}Fe_{2.5}Ni_{1.5}Sb_{12}$ below about 10 K, where C_p/T evidences broad humps in the curvature. Similar observations are expected for $Pr_{0.73}Fe_4Sb_{12}$, however, the impact of the onset of long range magnetic order on the heat capacity superposes a present Schottky contribution. In accordance with significantly lower Pr contents, such Schottky anomalies are absent in all compounds with y below 0.21, in fact, specific heat data of these compounds resemble those of $La_{0.83}Fe_4Sb_{12}$, which is added in Fig. 3.12 for comparison. The influence of the rare earth filler element on the thermodynamic properties diminishes appreciably upon lowering Pr fraction. Specific heat further allows for direct evaluation of the entropy associated with magnetic order and CEF level scheme via relation 1.87, section 1.6.4. Since magnetic entropy can be directly calculated for a particular CEF scheme in terms of equ. 1.89, it is also able to sensitively probe the latter. In order to isolate the magnetic contribution of the specific heat of $Pr_{0.73}Fe_4Sb_{12}$, heat capacity data of the non-magnetic reference compound $La_{0.83}Fe_4Sb_{12}$ was subtracted neglecting any inaccuracies, that may originate from different rare earth filling contents. Employing expression 1.87, the thereby derived magnetic entropy S_{mag} of $Pr_{0.73}Fe_4Sb_{12}$ is added in Fig. 3.13, right hand

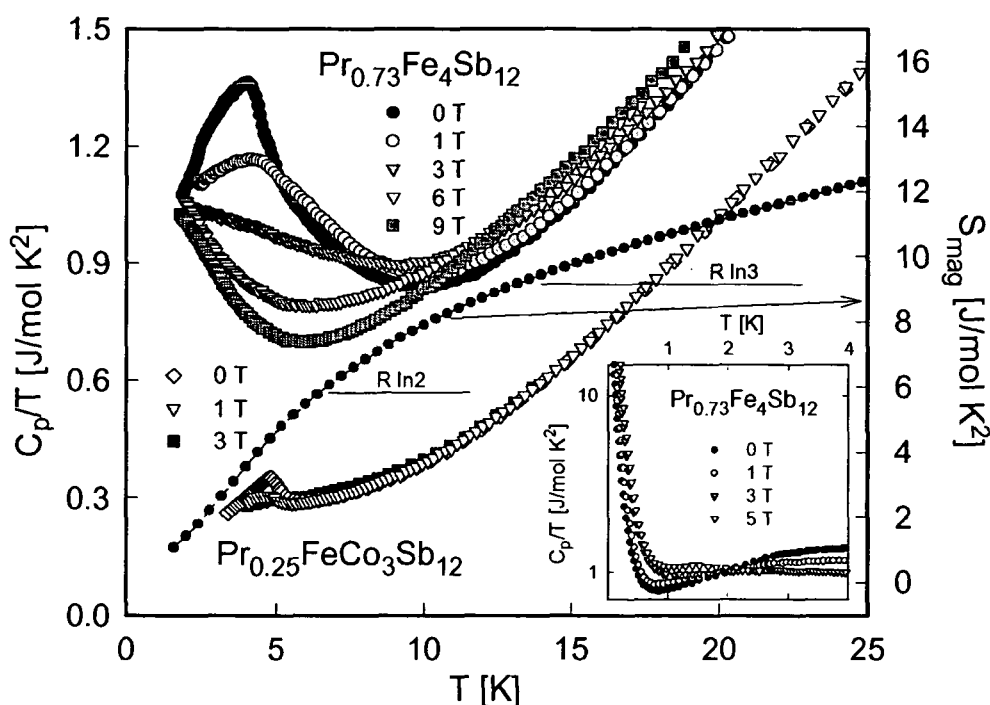Figure 3.13: Right hand scale: Temperature dependent specific heat C_p of $Pr_{0.73}Fe_4Sb_{12}$ and $Pr_{0.25}FeCo_3Sb_{12}$ plotted as C_p/T vs. T in various externally applied magnetic fields. Left hand scale: Magnetic entropy $S_{mag}(T)$ of $Pr_{0.73}Fe_4Sb_{12}$. Inset: Low temperature magnetic field dependent specific heat of $Pr_{0.73}Fe_4Sb_{12}$.

scale. The entropy release amounts to roughly $R\ln2$ at 7 K and $R\ln3$ near 13 K. Invoking the CEF splitting adopted based on magnetic susceptibility and inelastic neutron scattering, the calculated magnetic entropy yields about $S_{mag} = 10$ J/molK^2 at 15 K, which is almost in perfect agreement with the experiment independently supporting the proposed CEF model.

The electronic contribution to the specific heat is found to be remarkably high in $Pr_{0.73}Fe_4Sb_{12}$ showing only little dependence on the applied magnetic field. The inset of Fig. 3.12 allows for a close look at the low temperature electronic heat capacity of selected compounds, since according to expression 1.85, section 1.6.4, electronic and lattice contribution may be thereby deduced. In the temperature range between 11 and 20 K, where the heat capacity is nearly unaffected by the magnetic transition, the value of γ, associated with the electronic contribution $C_e = \gamma T$ was evaluated to amount to 540 mJ/molK^2 applying a least-squares fit to the data. Such strongly enhanced values are well known in heavy fermion compounds based on Ce, Yb or U, but were also revealed for Pr containing materials such as $PrInAg_2$

[163], in particular also for related filled skutterudite compounds $PrFe_4P_{12}$ and $PrOs_4Sb_{12}$ [157, 1]. With decreasing rare earth content the electronic contribution lowers indicating it to be essentially due to Pr, however, even $La_{0.83}Fe_4Sb_{12}$ exhibits a large γ of about 200 mJ/molK^2, in convincing agreement with γ evaluated from band structure calculations and mainly referred to the Fe 3d contribution [185].

The inset of Fig. 3.13 displays the very-low temperature specific heat of $Pr_{0.73}Fe_4Sb_{12}$, which is characterized by a significant rise due to the nuclear contribution primarily associated with the $I = 5/2$ core total angular momentum of Pr being subject to strong intrasite hyperfine interactions with the surrounding 4f electrons. To quantitatively account for such a nuclear Schottky contribution to the heat capacity derived from Fe^{57}, Sb^{121}, Sb^{123} and Pr^{141}, an average magnetic field and Zeeman splitting was assumed. The best fit of the low temperature upturn was established in a local field of approximately 87 T, but includes only 7.3% of all nuclei leading to the conclusion, that the hyperfine term arises only due to one kind of nuclei. The assumption of a local field of 73 T at the Pr sites as well as of a slightly enhanced average magnetic field in comparison to the external field on all the other nuclei sites, yielded the best fitting results. The strong internal field obtained presumably refers to Pr vacancies (about 27%) in the skutterudite structure. At temperatures above the pronounced nuclear connected upturn, $C_p(T)$ increases as the external magnetic field rises. Such a feature is generally understood in terms of fluctuations of the order parameter prior to a field induced phase transition or to destruction of the ordered state by the magnetic field. Similar observations were reported with respect to $PrFe_4P_{12}$ [188].

3.5   Electrical resistivity

Another possibility to probe susceptibility- and inelastic neutron scattering derived CEF level splitting is the measurement of the electrical resistivity. There, conduction electrons are subject to CEF dependent spin disorder scattering. On the other hand, from a thermoelectric point of view, the magnitude of the electrical resistivity $\rho(T)$ represents a critical parameter for the thermoelectric figure of merit, since carrier concentration and thus resistivity and thermopower are strongly related quantities. At a first glance, high electrical conductivity would be favorable to a high ZT, but on the other hand such conditions are usually accompanied by relatively low Seebeck coefficients entering the calculation of the figure of merit quadratically. Efficient thermoelectric materials are thus commonly semiconductors or materials close to this state. In order to improve the thermoelectric performance, starting with parent $Pr_{0.73}Fe_4Sb_{12}$, the carrier concentration may be altered due to additional

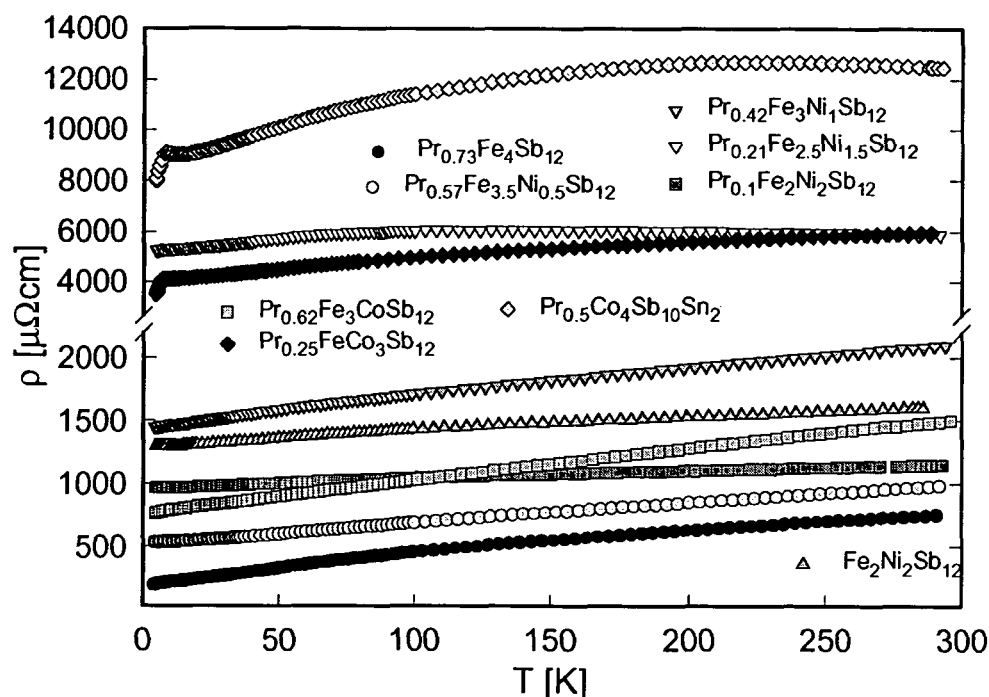Figure 3.14: Temperature dependent absolute electrical resistivity $\rho(T)$ of $Pr_yFe_{4-x}(Co,Ni)_xSb_{12}$ and $Pr_{0.5}Co_4Sb_{10}Sn_2$.

electrons provided by Co or Ni and consequently the thermopower changes as well. The evolution of $\rho(T)$ of $Pr_yFe_{4-x}(Co,Ni)_xSb_{12}$ with increasing Co/Ni content as well as CEF effects influencing resistivity will be outlined in the following.

Temperature dependent absolute electrical resistivities $\rho(T)$ of $Pr_yFe_{4-x}(Co,Ni)_xSb_{12}$ and $Pr_{0.5}Co_4Sb_{10}Sn_2$ are plotted in Fig. 3.14. A general trend is observable when proceeding through the series of compounds towards decreasing Fe concentration. Whereas $Pr_{0.73}Fe_4Sb_{12}$ possesses well developed metallic electrical conductivity with values of ρ between about 200 and 700 $\mu\Omega cm$ at low temperature and 300 K, respectively, the overall absolute resistivity values within the whole temperature range significantly augment reaching almost 6000 $\mu\Omega cm$ for $Pr_{0.21}Fe_{2.5}Ni_{1.5}Sb_{12}$ at room temperature followed by a strong decrease down to about 1000 $\mu\Omega cm$ for $Pr_{0.1}Fe_2Ni_2Sb_{12}$. A similar enhancement of $\rho(T)$ is observed in the case of Co substitution. It has to be mentioned that the magnitude of $\rho(T)$ is considerably influenced by the mechanical quality of a particular sample. The resulting data might thus deviate from the actual 'intrinsic' resistivity in some cases due to porosity, cracks, wholes etc. To some extent the large resistivity range covered by this series is also a consequence of

crystallographic disorder at the a sites of the unit cell due to incomplete Pr filling as well as of disorder at the Fe/(Co,Ni) sites. The overall observed trend, however, seems not to be affected evident from following considerations. The carrier concentration of diamagnetic and semiconducting $CoSb_3$ is altered by completely substituting Co with Fe, since Fe possesses one electron less than Co leading to the introduction of four holes per formula unit (Fe_4Sb_{12}). Unfortunately, pure Fe_4Sb_{12} does not exist due to electron deficiency making void filling with electropositive elements necessary in order to enable synthetization. As Fe is re-substituted for by Co or Ni in $Pr_yFe_{4-x}(Co,Ni)_xSb_{12}$, the hole concentration is diminished, a process further promoted by the additional electrons donated by trivalent Pr. As a consequence the electrical resistivity rises. According to this simple carrier count model exact charge compensation, in order to resemble the charge state of binary $CoSb_3$, should be yielded if the relations $3y = 4 - x$ and $3y = 4 - 2x$ are fulfilled in the case of Co and Ni substitution, respectively. The factor 2 in latter equations accounts for the additional electron of Ni compared to Co, y denotes the rare earth filling fraction and x the Co/Ni content. Employing these relations, charge compensation is expected in between a Ni concentration of $x = 2.5$ and $x = 2$ in fine agreement with the experimental findings. Upon further Fe decrease, $\rho(T)$ is reduced in accordance with the assumption of a surplus of electrons giving rise to n-type, electron dominated transport also indicated by the thermopower changing sign (compare following section). A comparison of $Pr_{0.1}Fe_2Ni_2Sb_{12}$ and unfilled $Fe_2Ni_2Sb_{12}$ illustrates the influence of the additional electrons provided by the filler element, since $\rho(T)$ of the latter exceeds that of the former. Too, in the case of the Co containing samples, $Pr_{0.25}FeCo_3Sb_{12}$, exhibiting the highest absolute resistivity values, is close to an electronically compensated configuration. The substitution of Sb by Sn has an even more significant impact on $\rho(T)$ in $Pr_{0.5}Co_4Sb_{10}Sn_2$, since the electron deficiency (2 electrons per formula unit) of the polyanion $[Co_4Sb_{10}Sn_2]$ caused by Sn is almost completely compensated by 50% void filling with Pr donating roughly 1.5 electrons per formula unit. The applicability of the simple carrier count model is also corroborated by thermopower data outlined in the following section and its overall validity has already been demonstrated for isomorphous filled skutterudite systems $Ce_yFe_{4-x}(Co,Ni)_xSb_{12}$ [189, 171] and $Eu_yFe_{4-x}(Co,Ni)_xSb_{12}$ [127, 128]. Nevertheless, this model allows just for a crude estimation of the carrier concentration, since characteristics of the generally complex band structures of filled skutterudites are not at all entering the considerations. Besides, with respect to the system $Co_{1-x}Fe_xCo_3$, it was shown from Hall measurements, that, up to $x \leq 1$ at.% Fe, the hole concentration increases as 0.28 holes/Fe atom, while larger Fe ratios only lead to an increase at a rate of 0.03 holes/Fe. Fe thus seems

to have less impact on the carrier concentration than assumed performing a simple carrier count. On the other hand, transport properties of filled skutterudites may follow different rules due to significant differences in band structure compared to their unfilled variants, the simple carrier count model obviously satisfactorily applies for $Pr_yFe_{4-x}(Co,Ni)_xSb_{12}$.

All compounds with the exception of $Pr_{0.21}Fe_{2.5}Ni_{1.5}Sb_{12}$ and $Pr_{0.5}Co_4Sb_{10}Sn_2$ exhibit metallic behavior within the whole temperature range, however, strongly deviating from $\rho(T)$ of simple metals, which usually can be accounted for in terms of a Bloch-Grüneisen type of temperature dependence. Even in the case of the reference compound $La_{0.83}Fe_4Sb_{12}$ ($\rho(T)$ is added in Fig. 3.15c), where the rare earth does not carry a magnetic moment, appropriate results cannot be achieved. Since the polyanion complex $[Fe_4Sb_{12}]$ was shown to be the origin of an effective magnetic moment, magnetic interactions between conduction electron system and paramagnetic sublattice seem to cause this significant deviation from a simple metallic temperature dependence. In combination with crystalline electric field effects in the Pr containing samples, latter considerations most probably prevent the application of a Bloch-Grüneisen law.

The weak anomaly at a temperature around 5 K in parent $Pr_{0.73}Fe_4Sb_{12}$ points to an onset of long range magnetic order, which is in line with the magnetic susceptibility and specific heat derived transition. $\rho(T)$ of latter compound is depicted again in Fig. 3.15c for closer inspection. Too consistent with susceptibility data, long range magnetic order vanishes with decreasing Fe concentration, no features characteristic of a magnetic phase transition appear for $Pr_{0.62}Fe_3CoSb_{12}$ nor for $Pr_{0.57}Fe_{3.5}Ni_{0.5}Sb_{12}$. Nevertheless, $Pr_{0.25}FeCo_3Sb_{12}$ and $Pr_{0.5}Co_4Sb_{10}Sn_2$ seem to undergo magnetic phase transitions evident from the kinks in the electrical resistivities at about 7 K. Already proposed for the former with respect to a slight anomaly in a field of 0.1 T in $1/\chi(T)$ as the effect of a magnetic impurity, which could not be detected during refinement, magnetic ordering in latter sample has to be attributed to the influence of an impurity as well. No signs of a transition near 7 K were obtained from magnetic measurements. Although this second magnetic phase could not be identified, the observed effect may originate from small traces of $PrSb_2$, which shows an antiferromagnetic transition at 5.1 K [190]. The almost identical transition temperatures of both samples point to the influence of the same impurity phase. Besides, recovery of magnetic order at low Fe content is very unlikely, especially at temperatures above the transition observed for the parent compound. In the case of the pure Co sample, although a filling fraction of 50% was achieved, the large absolute resistivity values in the range of $m\Omega cm$ are expected to inhibit RKKY interactions mediated by the conduction electron system and thus long range magnetic order, if not, however, originating from impurity effects. The enhanced $\rho(T)$
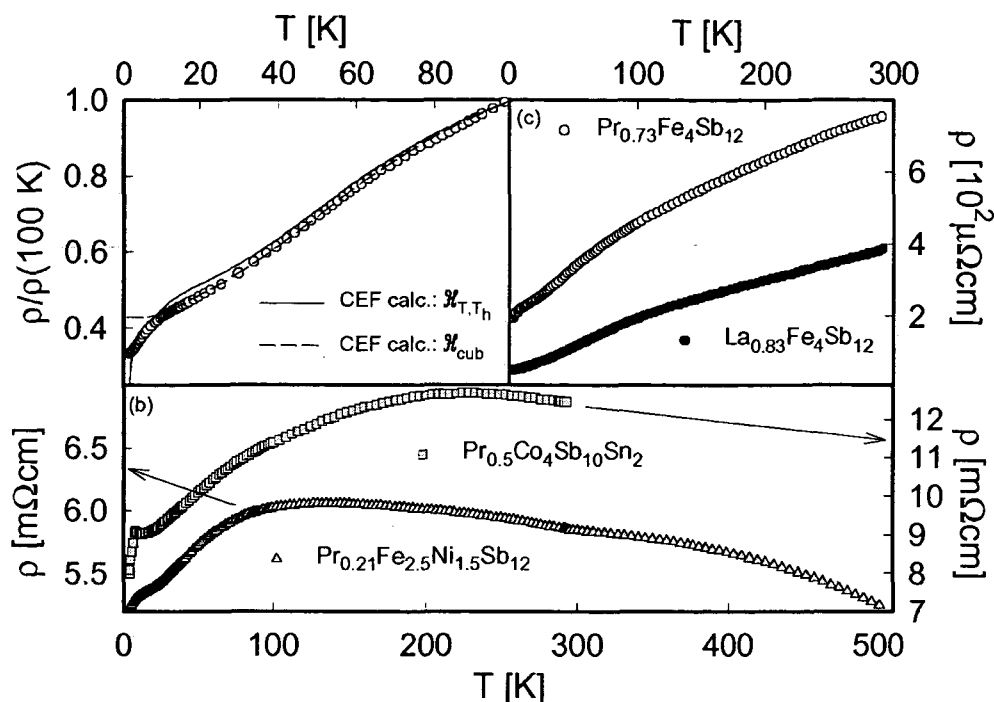
Figure 3.15: (a) $\rho(T)$ of $Pr_{0.73}Fe_4Sb_{12}$ normalized to 100 K, solid and dashed lines are model curves based on Hamiltonians 3.7 and 3.8, see text. (b) Temperature dependent absolute electrical resistivity $\rho(T)$ of $Pr_{0.21}Fe_{2.5}Ni_{1.5}Sb_{12}$, left scale, and of $Pr_{0.5}Co_4Sb_{10}Sn_2$, right scale. (c) $\rho(T)$ of $Pr_{0.73}Fe_4Sb_{12}$ and $La_{0.83}Fe_4Sb_{12}$.

values also explain the strong effect of a small amount of a magnetic phase on the temperature dependence below the transition.

The almost complete charge compensation observed for $Pr_{0.21}Fe_{2.5}Ni_{1.5}Sb_{12}$ and $Pr_{0.5}Co_4Sb_{10}Sn_2$ as predicted by the carrier count model has interesting consequences on the overall curvature of $\rho(T)$, too. Fig. 3.15b displays electrical resistivities of $Pr_{0.21}Fe_{2.5}Ni_{1.5}Sb_{12}$ and $Pr_{0.5}Co_4Sb_{10}Sn_2$. The temperature dependencies at lower temperatures resemble those of metals with a positive slope as the temperature increases, whereas a broad maximum in $\rho(T)$ is followed by a decrease evidencing semiconductor-like behavior at elevated temperatures. Similar features were observed in related skutterudite $Eu_{0.65}Fe_{2.6}Ni_{1.4}Sb_{12}$, which itself is close to a charge compensated state and possesses the highest absolute resistivity values within the series $Eu_yFe_{4-x}Ni_xSb_{12}$. On the basis of $Sn_{0.21}Ni_4Sb_{7.1}Sn_{4.9}$, $Eu_{0.8}Ni_4Sb_{5.8}Sn_{6.2}$ and $Yb_{0.6}Ni_4Sb_{6.7}Sn_{5.3}$, also revealing such temperature dependencies, a model was proposed and quantitatively applied in terms of a small gap in the density of states close to the Fermi energy causing this

activation type of behavior at higher temperatures [128]. As the temperature rises all states below this gap are becoming occupied, $\rho(T)$ exhibits a metallic temperature dependence. If thermal activation energy is sufficient to promote charge carriers into states located beyond the energy gap in the density of states, resistivity changes slope and decreases towards elevated temperatures. The occurrence of such a temperature dependence is most probably related to these compounds being close to total charge compensation, close to semiconducting behavior, since the gap widths deduced range between 0.07 to 0.2 eV, similar to the magnitude of the width known for binary $CoSb_3$ $(E_g \approx 0.5$ eV) [191]. In the case of $Pr_{0.21}Fe_{2.5}Ni_{1.5}Sb_{12}$ and $Pr_{0.5}Co_4Sb_{10}Sn_2$, quantitative application of above model was not successful due to the peculiar structure of $\rho(T)$ at low temperatures, nevertheless, the model illustrates the observed temperature dependencies at least qualitatively.

In order to probe the CEF level splitting obtained in terms of magnetic susceptibility and inelastic neutron diffraction investigations, $\rho(T)$ of $Pr_{0.73}Fe_4Sb_{12}$ is plotted in Fig. 3.15a normalized to a temperature of 100 K. Calculations were performed based on expression 1.50, section 1.5.1, which represents the spin-disorder resistivity contribution in the presence of CEF effects. Thereby both the commonly used Hamiltonian for cubic point groups and the corrected Hamiltonian for cubic point groups T and T_h were employed. Besides the CEF parameters B_4^0, B_6^0 and B_6^2 no further free parameter entered the calculations, the results of which are depicted in Fig. 3.15a as solid and dashed lines. Surprisingly, the peculiar structure of $\rho(T)$ down to low temperatures, where long range magnetic order sets on, is already well reproduced by the spin-disorder calculation, although electron-phonon interactions were neglected completely. At a first glance the resulting model curve based on H_{cub} matches the experimental resistivity to a greater extent. Nevertheless, apart from the stronger overall discrepancy between $\rho(T)$ and the latter, for H_{T,T_h}, even at temperatures below 20 K, decent qualitative agreement can be validated. This overall picture indicates the proposed CEF scheme to be plausible and not contradictory to electrical resistivity data. However, for a precise treatment the herein omitted phonon contribution to $\rho(T)$ would definitely have to be considered.

3.5.1 Pressure and magnetic field dependent electrical resistivity

Temperature and pressure dependent electrical resistivities of $Pr_{0.73}Fe_4Sb_{12}$, $La_{0.73}Fe_4Sb_{12}$ and unfilled $Fe_2Ni_2Sb_{12}$ are plotted in figures 3.16 and 3.17. Within the limit of resolution the magnetic transition temperature of the former seems to be unaffected by externally applied pressure up to 16.5 kbar. Usually, in terms of a local moment picture, an increase of T_{mag} with in-
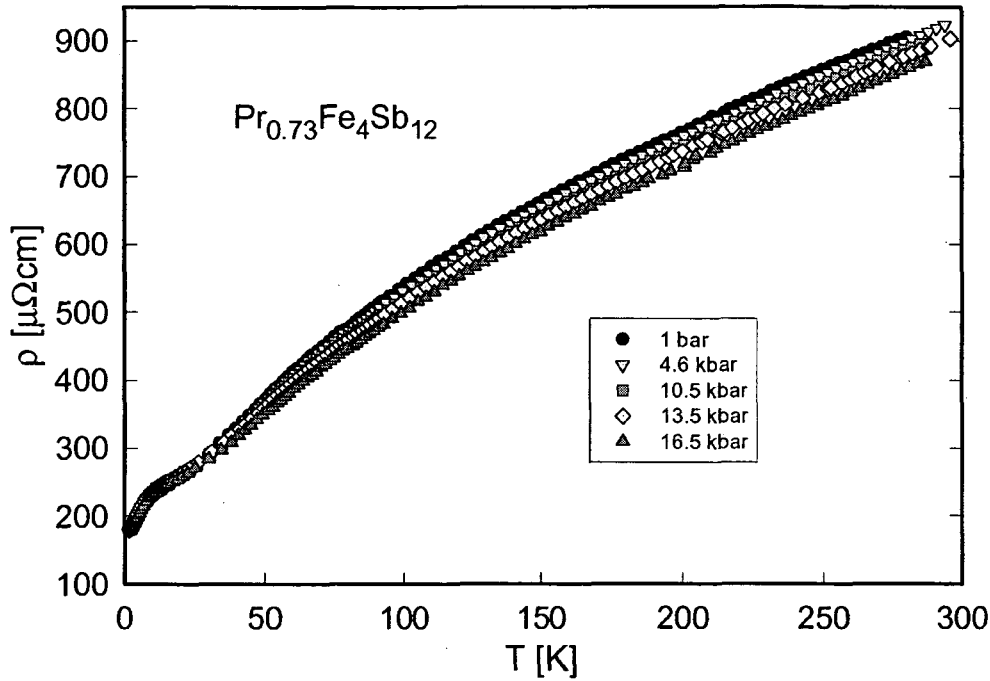
Figure 3.16: Temperature and pressure dependent absolute electrical resistivity $\rho(T)$ of $Pr_{0.73}Fe_4Sb_{12}$.

creasing pressure can be expected due to the magnetic ions being forced closer to each other resulting in an enhancement of the RKKY interaction strength [192]. On the other hand, a consecutive reduction of absolute $\rho(T)$ is observed up to 16.5 kbar, comparable to the pressure response obtained for $La_{0.73}Fe_4Sb_{12}$ but in contrast to that of unfilled $Fe_2Ni_2Sb_{12}$ exhibiting an increase upon pressure. This feature fits well into a picture proposed for rare earth filled skutterudites on the basis of a pressure-charge carrier correlation [193]: according to the simple charge carrier count and the positive Seebeck coefficients discussed in the next section for both Pr and La filled samples hole dominated transport is revealed. In contrast, $Fe_2Ni_2Sb_{12}$ is somewhat electron rich. In fact, the type of charge carrier seems to determine the pressure response of a particular compound. While the influence of pressure on skutterudites exhibiting holes as primary charge carriers gives rise to increasing resistivities in the whole temperature range, the reduction of $\rho(T)$, e.g. observed for $Fe_2Ni_2Sb_{12}$, reflects its electron dominated charge carrier concentration. The assumption of a correlation between charge carrier concentration and pressure response seems to hold for almost all, at least Fe(Co,Ni)-Sb based filled skutterudites independent of the particular ground-state as evident from combined pressure and transport investigations [128].
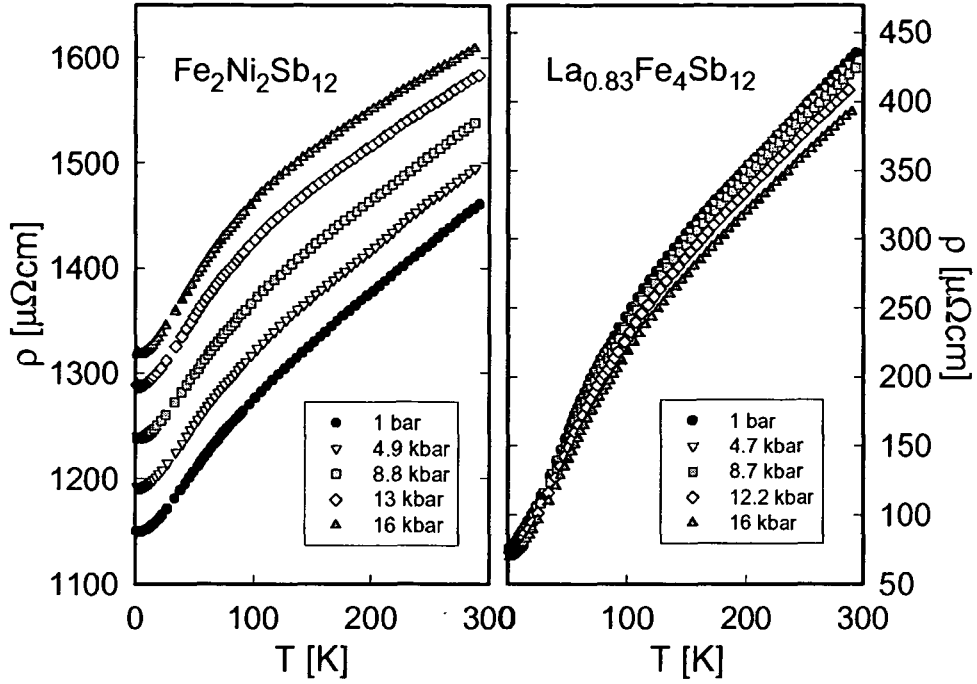
Figure 3.17: Temperature- and pressure dependent absolute electrical resistivity $\rho(T)$ of $La_{0.83}Fe_4Sb_{12}$ (a) and $Fe_2Ni_2Sb_{12}$ (b).

However, in the case of $CeFe_4Sb_{12}$, supposedly also hole dominated such as most $REFe_4Sb_{12}$ compounds, an increase upon pressure is observed, which may be resulting from pronounced Kondo type of interactions [194].

At temperatures below T_{mag} $Pr_{0.73}Fe_4Sb_{12}$ is characterized by an increase of the absolute values of $\rho(T)$ upon increasing magnetic fields as depicted in the inset of Fig. 3.18a, whereas externally applied magnetic fields give rise to reduced values at elevated temperatures. In order to analyze the low temperature magnetically ordered regime least-squares fits were applied to the experimental data in terms of electron scattering on spin waves:

$$\rho(T) = \rho_0 + AT^n \exp(-\Delta/k_B T). \tag{3.11}$$

A is a constant and ρ_0 denotes the temperature independent residual resistivity contribution, while Δ represents a gap in the spin wave energy spectrum, the finite energy of Δ being at least required to excite a spin wave. The lower inset of Fig. 3.18a visualizes the decrease of the parameter n with increasing field from $n = 1.57$ at 0 to $n = 0.65$ at 5 T. The parameter A decreases upon rising magnetic field, while Δ amounts to 0.289, 0.472 and 1.718 K for 0, 1 and 5 T, respectively. These results do not favor a ferromagnetic spin arrangement, which is usually accompanied by a T^2 dependence of the elec-
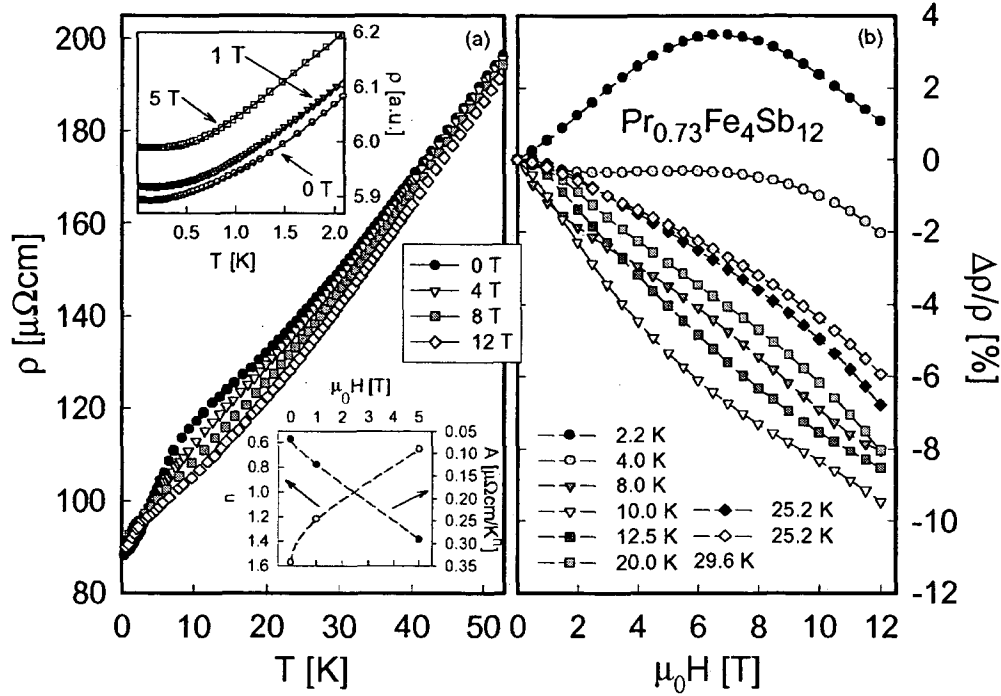
Figure 3.18: (a) Temperature dependent electrical resistivity $\rho(T)$ of $Pr_{0.73}Fe_4Sb_{12}$ in various externally applied magnetic fields. Lower inset: parameters n and A vs. $\mu_0 H$ obtained in terms of least-squares fits according to equ. 3.11, results are shown in upper inset as solid lines. (b) Isothermal magnetoresistance $\Delta\rho/\rho$ of $Pr_{0.73}Fe_4Sb_{12}$ vs. magnetic field.

trical resistivity at low temperatures [32, 33], instead, they rather support the assumption of antiferromagnetic order in $Pr_{0.73}Fe_4Sb_{12}$. In fact, isothermal magnetoresistance measurements carried out both below and above the magnetic phase transition at $T_{mag} = 4.5$ K support an antiferromagnetic solution. Magnetoresistance $\Delta\rho/\rho$ is positive at a temperature of 2.2 K evidencing a maximum at about 7 T and decreasing at higher fields. In terms of an antiferromagnetic structure increase and subsequent decrease of $\Delta\rho/\rho$ may indicate a spin re-orientation, a magnetic field induced cross-over into the ferromagnetic state. The decrease of the magnetoresistance at high fields is then associated with quenching of spin fluctuations common to ferromagnetic materials, whereas rounding and broadening of the maximum at 7 T can be understood from domain wall motion and polycrystalline effects [37]. However, no field induced feature at 7 T and 2 K was revealed with respect to magnetization, see Fig. 3.7, possibly arising from different preferred orientations of the various pieces of the polycrystalline sample, since strong anisotropy between the $\langle 100 \rangle$ and $\langle 111 \rangle$ directions has already been reported
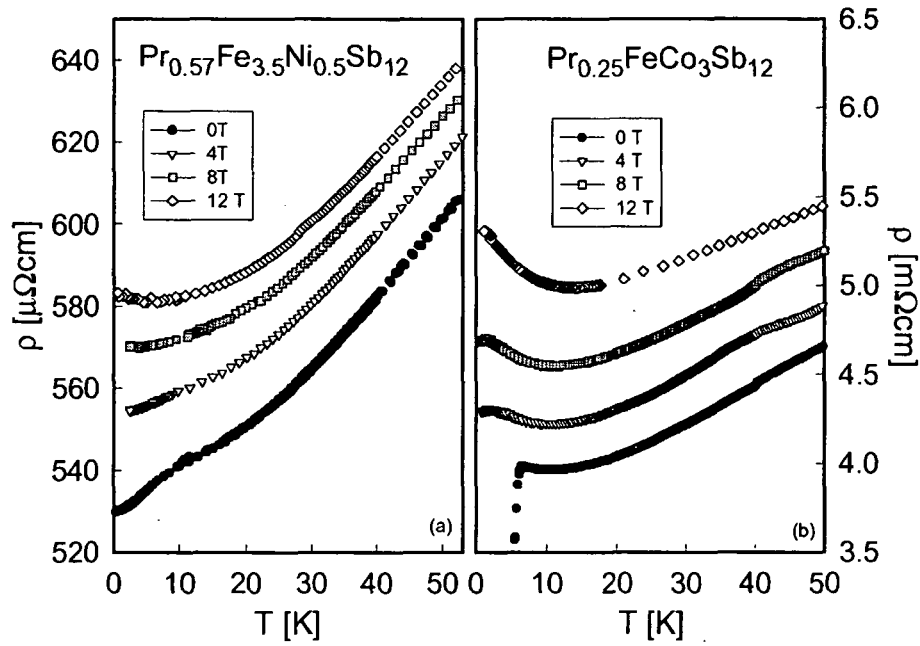
Figure 3.19: Temperature dependent electrical resistivity $\rho(T)$ of $Pr_{0.57}Fe_{3.5}Ni_{0.5}Sb_{12}$ (a) and $Pr_{0.25}FeCo_3Sb_{12}$ (b) in external magnetic fields of up to 12 T.
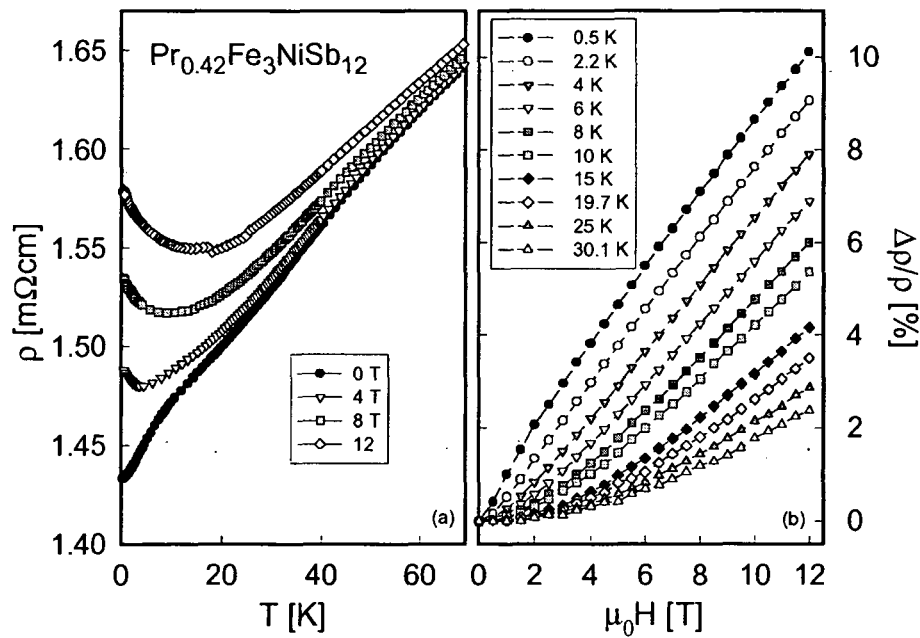

Figure 3.20: Temperature dependent electrical resistivity $\rho(T)$ of $Pr_{0.42}Fe_3Ni_1Sb_{12}$ in various external magnetic fields (a). Isothermal magnetoresistance $\Delta\rho/\rho$ of $Pr_{0.42}Fe_3Ni_1Sb_{12}$ (b).
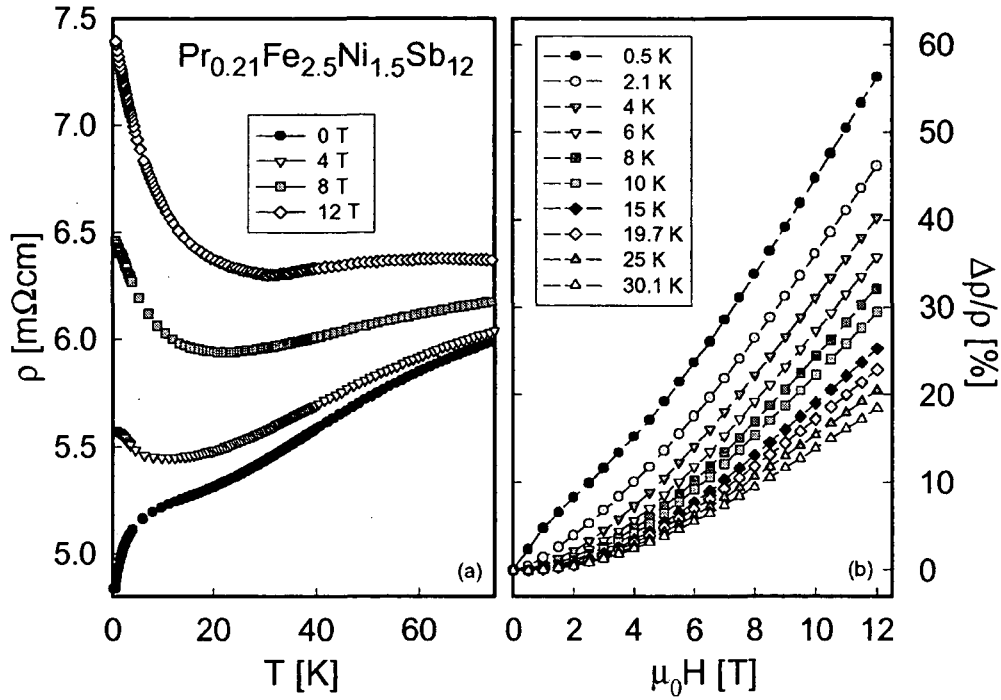
Figure 3.21: (a) Temperature dependent electrical resistivity $\rho(T)$ of $Pr_{0.21}Fe_{2.5}Ni_{1.5}Sb_{12}$ in various externally applied magnetic fields. (b) Isothermal magnetoresistance $\Delta\rho/\rho$ of $Pr_{0.21}Fe_{2.5}Ni_{1.5}Sb_{12}$.

for isomorphous single crystal $PrFe_4P_{12}$ [188]. At 4 K isothermal magnetoresistance crosses over to negative values and remains negative towards higher temperatures in the paramagnetic regime, the largest value is reached at 10 K with $\Delta\rho/\rho \approx -10\%$.

Figures 3.19, 3.20 and 3.21 depict electrical resistivities of Pr filled skutterudite compounds with Ni contents of $x = 0.5$, 1 and 1.5 as well as of $Pr_{0.25}FeCo_3Sb_{12}$ under the influence of magnetic fields. Common to these compounds is an increase of the absolute resistivity in the whole temperature range. In the case of the Co containing compound, the magnetic transition of the impurity phase is clearly suppressed in a field of 4 T, moreover, below about 20 K, externally applied magnetic fields induce an increase of $\rho(T)$ towards lower temperatures, a feature characteristic of semiconducting materials. The high absolute resistivity in the range of mΩcm classifies this sample as significantly charge carrier depleted. Since electronic transport is essentially understood in terms of a distribution function for the charge carriers just in the vicinity of the Fermi energy, the magnetic field seems to strongly affect the shape of the density of states at the Fermi energy, which in combination with classical magnetoresistance effects results in the

observed temperature dependence below 20 K. This lower-temperature up-turn of the electrical resistivity is found to be significantly enhanced in the case of $Pr_{0.21}Fe_{2.5}Ni_{1.5}Sb_{12}$, where in a field of 12 T $\rho(T)$ increases by one mΩcm below 30 K, which explains the large values of $\Delta\rho/\rho$ of close to 60% at 0.5 K, see Fig. 3.21b. Even at 30 K, this compound still exhibits a magnetoresistance of about 20%, which may be partly associated with the influence of free Sb segregated at grain boundaries of the structure. $\Delta\rho/\rho$ of $Pr_{0.42}Fe_3NiSb_{12}$, in contrast, amounts to only 2% at the same temperature, which is in line with the evanescent Sb impurity content. The considerable impact of free Sb on the magnetoresistance has been revealed with respect to $Eu_{0.83}Fe_4Sb_{12}$, where the large effect of above 100% at 10 K could be later attributed to be almost entirely due to free Sb [177].

3.6 Thermopower

Figure 3.22 displays the temperature dependent thermopower $S(T)$ of several rare earth filled Fe-Sb based skutterudites for the sake of comparison with $Pr_{0.73}Fe_4Sb_{12}$. Common to all compounds, in particular independent of the groundstate, with the exception of the Yb containing skutterudite is a minimum in $S(T)$ below about 50 K followed by an increase and a crossover to positive Seebeck coefficients. The kink evident for $Eu_{0.83}Fe_4Sb_{12}$ around 90 K marks the onset of long range magnetic order [127], whereas the broad maximum in $Yb_{0.8}Fe_4Sb_{12}$ possibly originates from strongly correlated electron phenomena giving rise to this Kondo coherence peak in the thermopower [195]. A similar curvature was observed for Yb-Ce filled variants with respect to the system $Ce_{1-p}Yb_pFe_4Sb_{12}$ [196]. The magnitude of the minimum in $S(T)$ of $Pr_{0.73}Fe_4Sb_{12}$ exceeds that of the others, a fact, that is in line with the significantly enhanced electronic specific heat contribution to C_p/T amounting to several hundred mJ/molK^2 and pointing to heavy fermion behavior. Indeed, the overall temperature dependence of the thermopower of $Pr_{0.73}Fe_4Sb_{12}$ shows features also found in Kondo systems - the pronounced extremum in combination with a sign change of $S(T)$ at elevated temperatures, if the particular compound undergoes a magnetic phase transition. These universal indications, however, can be modified by CEF effects [197, 198]. Unfortunately, to our knowledge, thermoelectric power data with respect to isomorphous P or As based skutterudites are not available so far in order to be able to unambiguously relate these features to heavy electrons. Neither are Seebeck coefficients of $PrInAg_2$, besides $PrFe4P_{12}$ and $PrOs_4Sb_{12}$ the only Pr based heavy fermion compound. The thermoelectric power of all samples lies within a range between 50 and 90 $\mu V/K$ at room temperature, the highest value is indeed obtained for $Pr_{0.73}Fe_4Sb_{12}$, which may be further enhanced via transition metal substitution illustrated in the following.

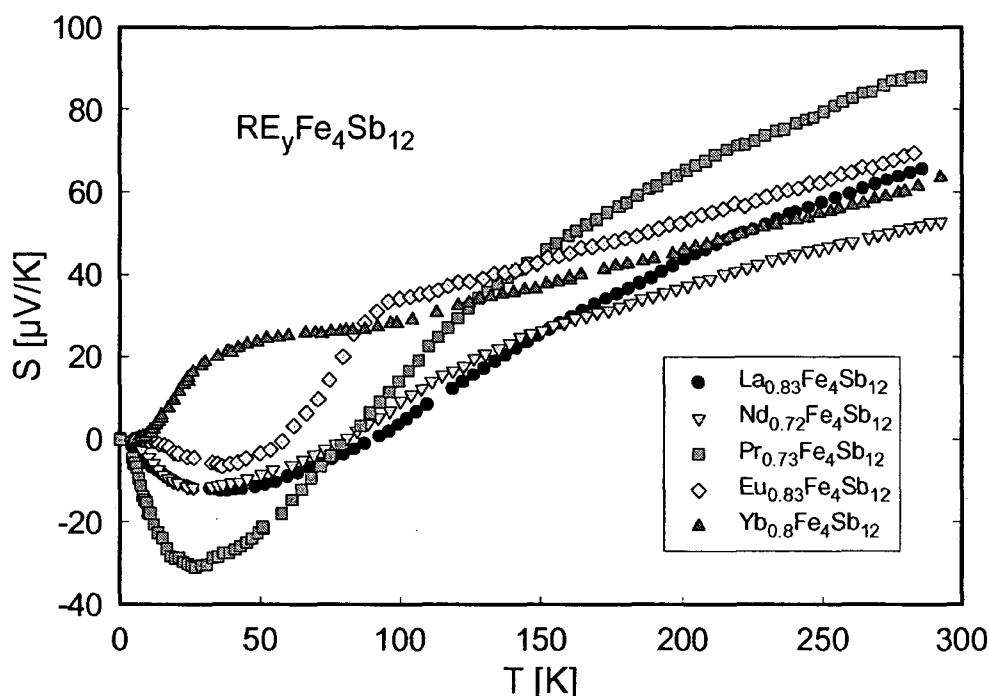Figure 3.22:   Temperature dependent thermoelectric power $S(T)$ of $RE_yFe_4Sb_{12}$.

Seebeck coefficients of $Pr_yFe_{4-x}(Co,Ni)_xSb_{12}$ and $Pr_{0.5}Co_4Sb_{10}Sn_2$ as a function of temperature are compiled in Fig. 3.23. The minimum observed for the parent compound vanishes immediately upon reduction of the Fe concentration. At temperatures above 200 K all samples under investigation exhibit a somewhat linear rise of the thermopower, which saturates for $Pr_{0.21}Fe_{2.5}Ni_{1.5}Sb_{12}$, $Pr_{0.42}Fe_4NiSb_{12}$ and $Pr_{0.1}Fe_2Ni_2Sb_{12}$ evident from broad maxima around 450, 580 and 600 K, respectively. The evolution of the thermopower proceeding through the series follows the same principles as deduced from electrical resistivity measurements: a strong increase of the absolute thermopower upon Fe/Ni exchange occurs reaching values of about 225 $\mu V/K$ for $Pr_{0.21}Fe_{2.5}Ni_{1.5}Sb_{12}$ roughly around 400 K. According to the one-band model, the Seebeck coefficients essentially depend on the charge carrier concentration [199] - in agreement with the rise of $\rho(T)$, $S(T)$ at first enhances since additional electrons provided by Ni reduce the hole concentration until charge compensation is achieved, $Pr_{0.21}Fe_{2.5}Ni_{1.5}Sb_{12}$ is somewhat charge carrier depleted. Beyond this critical Ni content of $x = 2.5$, the surplus of electrons due to further reduction of Fe consequently initiates n-type behavior, thus electron dominated transport causing the thermopower to change sign, which explains the overall negative values of $Pr_{0.1}Fe_2Ni_2Sb_{12}$. Fe/Co

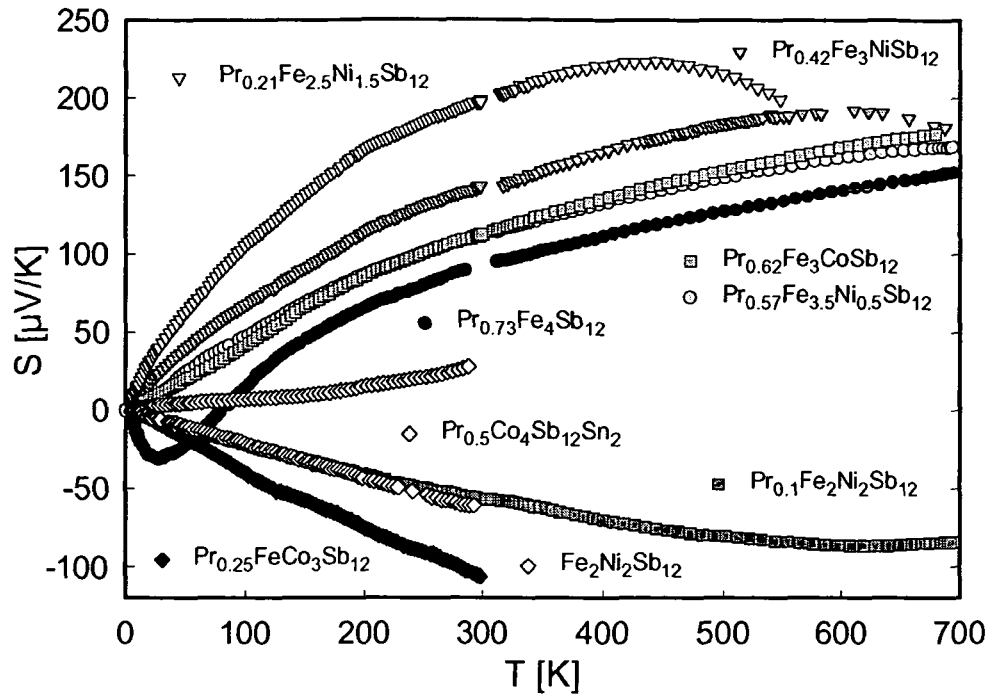Figure 3.23: Temperature dependent Seebeck coefficients $S(T)$ of $Pr_y Fe_{4-x}(Co,Ni)_x Sb_{12}$ and $Pr_{0.5}Co_4 Sb_{10}Sn_2$.

substitution has a similar effect on $S(T)$ with crossover to electrons as primary charge carriers at a Co concentration between $x = 1$ and $x = 3$.

These observations corroborate the simple carrier count model presented in section 3.5, whereupon charge compensation should be yielded according to $3y = 4 - x$ and $3y = 4 - 2x$ for Co and Ni substitution, respectively, giving rise to electronic states close to those of semiconductors with strongly enhanced thermopower and relatively bad electrical conductivity just as observed. On the other hand, relating $Pr_{0.73}Fe_4 Sb_{12}$ and its well developed electrical conductivity originating from an enhanced charge carrier density to the simplified picture of the thermopower mainly depending on the charge carrier concentration drawn above, the magnitude of $S(T)$ observed would not be expected, since simple metals just exhibit values generally no greater than a few $\mu V/K$. In fact, it was shown from band structure calculations, that large electron and hole effective masses are responsible for such findings [200]. This is underscored by Hall measurements on $Ce_y Co_4 Sb_{12}$ evidencing the expected increase in carrier density upon Ce filling, which allowed for calculation of the electron effective masses ($\sim 5m_e$) from room temperature thermopower data assuming a single parabolic band [201]. The magnitude of $S(T)$ of $Pr_y Fe_{4-x}(Co,Ni)_x Sb_{12}$ is thus governed by a subtle interplay between

band effects and doping level, nevertheless, the simple carrier count model sufficiently reproduces the observed evolution as the Fe content is reduced.

Comparison with available literature data on thermopower of related filled skutterudite compounds reveals the series $Pr_yFe_{4-x}(Co,Ni)_xSb_{12}$ to be ranked on top. Binary skutterudites were reported to possess Seebeck coefficients in the range of several hundred $\mu V/K$, compare e.g. undoped n-type $CoSb_3$ with -300 $\mu V/K$ [109], lightly doped p-type $CoSb_3$ with 225 $\mu V/K$ at room temperature [202] or $IrSb_3$ containing 0.15 at% Pt with nearly -500 $\mu V/K$ above 400 K [203]. Although such magnitudes until now have not been achieved in filled skutterudites, their lower electrical resistivities as well as strongly reduced thermal conductivities presented in the next section favor the filled variants in terms of a decent figure of merit. The highest thermopower in filled skutterudite systems have so far been observed in $CeFe_{4-x}Co_xSb_{12}$. Values close to 200 $\mu V/K$ above room temperature were derived [98] even surpassed by $Pr_{0.21}Fe_{2.5}Ni_{1.5}Sb_{12}$ and $Pr_{0.42}Fe_3NiSb_{12}$ as discussed above. Although the minor amount of impurities may alter 'real' $S(T)$ slightly, it has to be mentioned, that single phase samples in general seem to be very difficult to produce. X-ray refinement of the supposedly most suitable series for thermoelectric application $CeFe_{4-x}Co_xSb_{12}$, too, resulted in up to 5% impurities according to Fleurial et al [98].

3.7   Thermal conductivity and figure of merit

A first glance at the thermal conductivity data of $Pr_yFe_{4-x}Ni_xSb_{12}$, $Pr_yFe_{4-x}Co_xSb_{12}$ and $Pr_{0.5}Co_4Sb_{10}Sn_2$ given in figures 3.24 and 3.25 illustrates the reduction of the overall values compared to unfilled $Fe_2Ni_2Sb_{12}$ exhibiting a $\lambda(T)$ in the 40 to 50 mW/cmK range in good agreement with data deduced by Fleurial et al. [168]. Compared to polycrystalline $CoSb_3$, where 50 mW/cmK already represents the absolute lower limit achieved at room temperature, grain boundary scattering is responsible for a nearly 50% decrease of the thermal conductivity with respect to single crystal $CoSb_3$ ($\lambda(300K) \sim$ 100-120 mW/cmK) [96]. Further reduction was reported upon doping, however, thermal conductivities below 30 mW/cmK were not observed, compare e.g. Fe, Ni, Pd or Pt doped $CoSb_3$ [204, 130].

$\lambda(T)$ of all Pr filled samples under investigation is found below 30 mW/cmK at least up to temperatures of 150 K, where heat losses due to radiation gain importance causing the unphysical rise of the thermal conductivities. In order to theoretically account for this systematic measurement error, the total thermal conductivity was separated into electronic λ_e and lattice contribution λ_{ph} in terms of the Wiedemann-Franz law given in equation 1.60. Although derived in the scope of the free electron model, the Wiedemann-Franz law is commonly used to estimate electronic and lattice
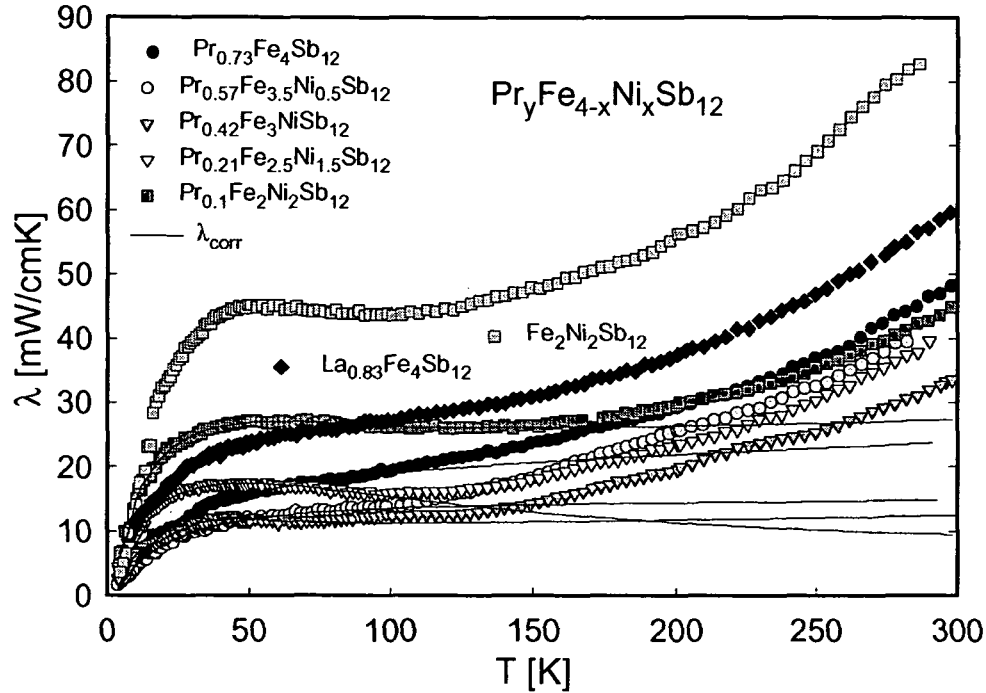
Figure 3.24: Thermal conductivity λ of $Pr_yFe_{4-x}Ni_xSb_{12}$ plotted as a function of temperature. Solid lines denote theoretical thermal conductivity data accounting for heat losses due to radiation, see text.

thermal conductivities. However, it has to be mentioned, that the Lorenz number entering the calculation, $2.45 \times 10^{-8}W\Omega K^{-2}$, is usually only valid in the case of simple metals. Employing a Debye-based model for the lattice thermal conductivity proposed by Callaway et al. [48, 49] (for details compare section 1.5.3) in the temperature range of 4 to about 150 K depending on the particular sample, the total thermal conductivity was then re-calculated by summing of theoretical lattice contribution extrapolated to room temperature and electronic contribution obtained via Wiedemann-Franz relation. The solid lines in Figs. 3.24 and 3.25 denote the theoretically corrected total thermal conductivities. If the deviation of the experimentally obtained thermal conductivity data from those calculated indeed originates from radiation losses, is generally revisable via the temperature dependence of $\lambda_{meas} - \lambda_{corr}$. In a first order approximation the Stefan Boltzmann law describes the heat emitted by a particular material via radiation as

$$Q_{rad} = \sigma\epsilon A(T^4_{sample} - T^4_{surrounding}) \qquad (3.12)$$

with the radiating surface A; σ and ϵ denote the Boltzmann constant and
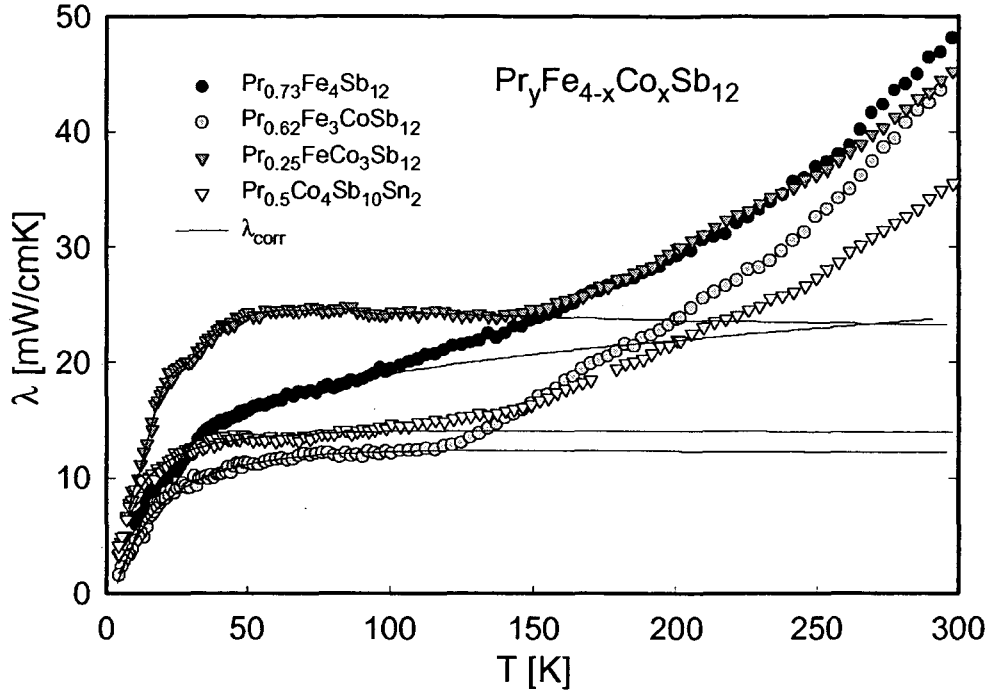
Figure 3.25:   Thermal   conductivity λ of $Pr_yFe_{4-x}Co_xSb_{12}$ and $Pr_{0.5}Co_4Sb_{10}Sn_2$ plotted as a function of temperature.   Solid lines denote theoretical thermal conductivity data accounting for heat losses due to radiation, see text.

relative emissivity of sample and surroundings. Consequently,

$$Q_{rad} = 2\sigma\epsilon AT^3\Delta T, \qquad (3.13)$$

where ΔT is the thermal gradient along the sample. For this reason, radiation effects manifest themselves in a cubic-in-T dependence of the thermal conductivity at elevated temperatures. Thus, adherence of a T^3 dependence can be expected with respect to $\lambda_{meas} - \lambda_{corr}$ [205, 206]. This is illustrated for parent $Pr_{0.73}Fe_4Sb_{12}$ in Fig. 3.26. The data deduced by application of a least-squares fit to the experimental lattice thermal conductivity according to Callaway's model below about 120 K in combination with extrapolation to room temperature, subtracted from the total measured effect, yields reasonably a T^3 dependence.

In some cases, the observed temperature dependence of λ_{ph} was only insufficiently modeled, therefore approximations were made such as to satisfy the T^3 condition. The lattice contribution of $Fe_2Ni_2Sb_{12}$ is added in Fig. 3.26a in order to demonstrate this procedure. $Fe_2Ni_2Sb_{12}$ is chosen here for two reasons: firstly, because of its $\lambda_{ph}(T)$ exceeding that of the other sam-

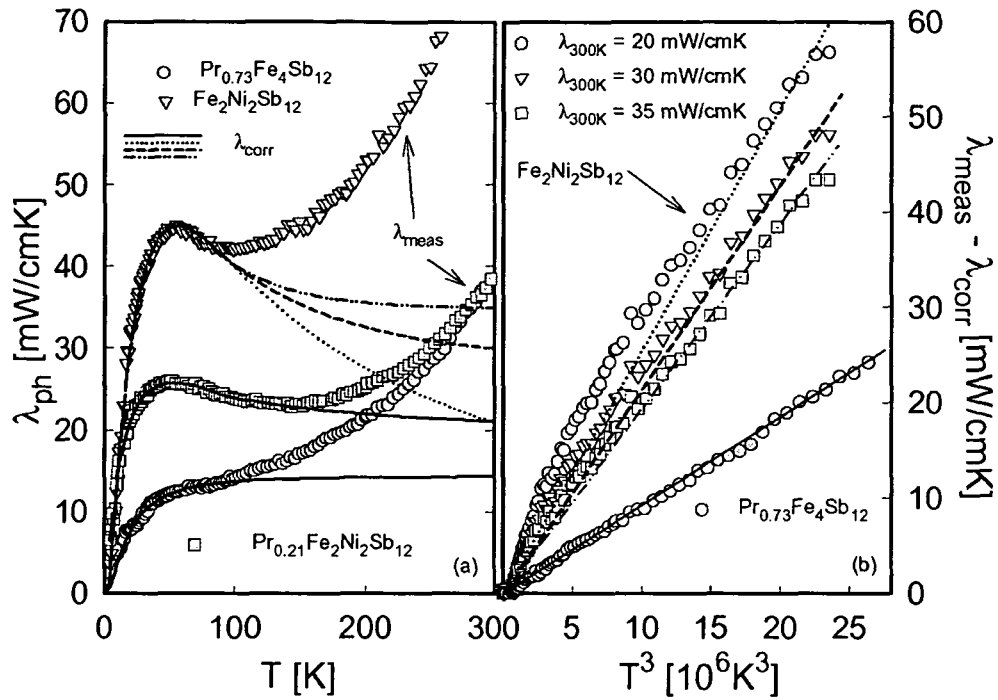Figure 3.26: (a) Lattice thermal conductivity $\lambda_{ph}(T)$ of $Pr_{0.73}Fe_4Sb_{12}$, $Pr_{0.1}Fe_2Ni_2Sb_{12}$ and $Fe_2Ni_2Sb_{12}$. Dashed and dotted lines: model calculation correcting for heat losses due to radition, in the case of $Fe_2Ni_2Sb_{12}$, with default room temperature values of 20, 30 and 35 mW/cmK. (b) $\lambda_{meas} - \lambda_{corr}$ of $Pr_{0.73}Fe_4Sb_{12}$ and $Fe_2Ni_2Sb_{12}$ vs. T^3.

ples and secondly because of the fact, that $Pr_{0.1}Fe_2Ni_2Sb_{12}$ provides a lower limit to the room temperature lattice thermal conductivity of $Fe_2Ni_2Sb_{12}$, since filling of the voids in former expectedly results in overall reduced values compared to those of latter compound. The left panel of Fig. 3.26 shows the lattice component of $Fe_2Ni_2Sb_{12}$. While the curvature below 100 K is well reproduced by the fit, the further temperature dependence can only be estimated. Extrapolation to room temperature was performed indicated by the dashed and dotted lines, whereby values of 20, 30 and 35 mW/cmK were assumed at 300 K. The thus derived curves are plotted in the right panel as a function of T^3 evidencing rough linearity in the case of the estimated room temperature value of 35 mW/cmK also meeting the condition that the lattice thermal conductivity of filled $Pr_{0.1}Fe_2Ni_2Sb_{12}$ stays well below that of unfilled $Fe_2Ni_2Sb_{12}$.

Figures 3.27 and 3.28 display lattice and electronic thermal conductivities of $Pr_yFe_{4-x}(Co,Ni)_xSb_{12}$ and $Pr_{0.5}Co_4Sb_{10}Sn_2$ obtained employing the Wiedemann-Franz law. Note, that in the following the radiation-corrected

Figure 3.27: Temperature dependent lattice and electronic thermal conductivity, (a) $\lambda_{ph}(T)$ and (b) $\lambda_e(T)$, of $Pr_yFe_{4-x}Ni_xSb_{12}$.

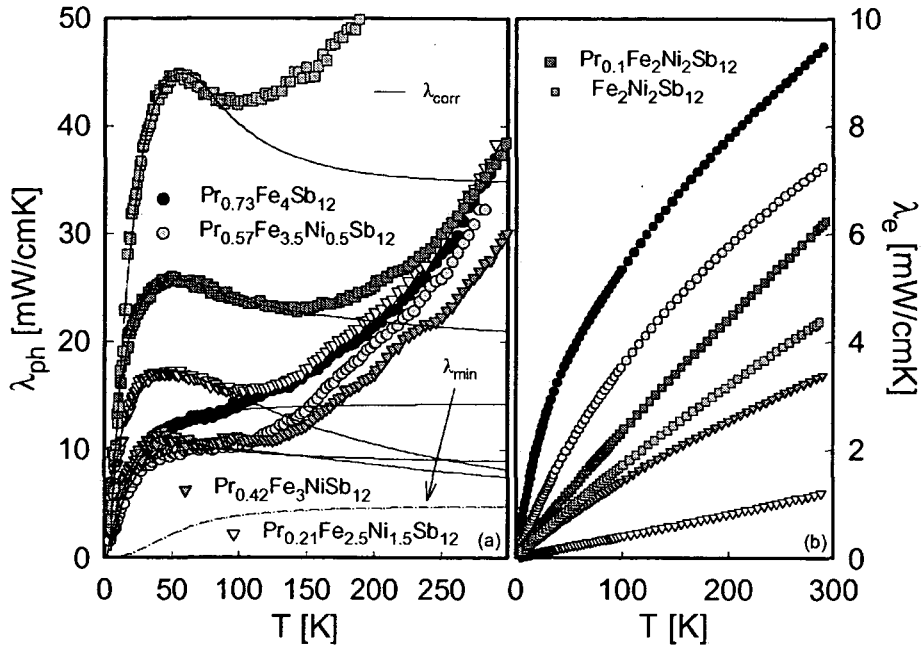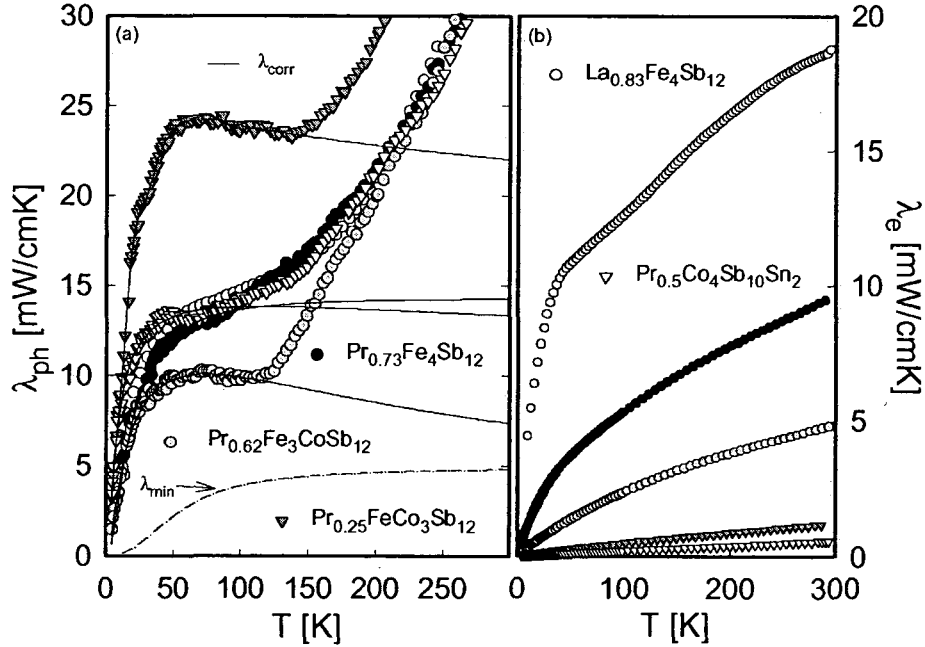

Figure 3.28: Temperature dependent lattice and electronic thermal conductivity, (a) $\lambda_{ph}(T)$ and (b) $\lambda_e(T)$, of $Pr_yFe_{4-x}Co_xSb_{12}$ and $Pr_{0.5}Co_4Sb_{10}Sn_2$.

lattice thermal conductivities are used for interpretation. With increasing electronic performance of a particular sample, λ_e gains importance as evident from parent $Pr_{0.73}Fe_4Sb_{12}$. The electronic contribution nearly amounts to 10 mW/cmK at 300 K, close to the value obtained for λ_{ph}. On the other hand, due to poor electrical conductivities, λ_e may also stay below about 10% of the overall quantity, compare e.g. $Pr_{0.25}FeCo_3Sb_{12}$ or $Pr_{0.21}Fe_{2.5}Ni_{1.5}Sb_{12}$. It is interesting to point out that the lattice contributions of $La_{0.83}Fe_4Sb_{12}$ (data are added in Fig. 3.28) and the isomorphous Pr filled compound are of about the same size, while the electronic parts differ significantly due to additional scattering processes in the latter associated with interactions between conduction electrons and the Pr magnetic moments resulting in an increased thermal resistivity.

The composition dependence of the lattice thermal conductivity of $Pr_yFe_{4-x}(Co,Ni)_xSb_{12}$ follows a characteristic trend, which is found to be in overall good agreement with that of homologous series of Ce and Eu filled skutterudites. The already strongly reduced phonon contribution of $Pr_{0.73}Fe_4Sb_{12}$ ($\lambda_{ph,300K} \sim 14$ mW/cmK) decreases further upon both Co and Ni substitution, reaches a minimum near 7 mW/cmK for a filling fraction of 0.6 corresponding to Fe:Co and Fe:Ni ratios of 3:1 and 3.5:0.5, respectively, and increases again with higher Co/Ni and lower Pr content. Generally, a strong reduction of the lattice thermal conductivity is observed upon filling of the skutterudite structure with electropositive elements, which due to their loose bonding exhibit large thermal displacement parameters and are subject to anharmonic localized vibrations effectively interfering with the normal modes of the structure as outlined in section 3.1.2. Since already a small amount of filler element satisfactorily affects heat transport [135], it is conceivable, that a filling fraction of close to 100% does not favor a reduced lattice contribution λ_{ph}. An enhanced phonon scattering rate is indeed the result, if disorder is maintained within the structure corroborated by the experimental results presented herein, where the samples with 57 and 62 % void filling reveal the lowest λ_{ph} values. Besides the impact of the filler element, the substitution on the transition metal site seems to contribute to the reduction of the lattice thermal conductivity as well. However, since the negligible mass differences between Fe and Co or Ni are not expected to be of significant impact on mass and strain fluctuations determining the scattering rate, a concept was adopted proposed by Meisner et al. [125] for $Ce_yFe_{4-x}Co_xSb_{12}$ based on solid solution formation between a completely filled $CeFe_4Sb_{12}$ sublattice and an empty sublattice $\square Co_4Sb_{12}$ with $\square$ representing the unfilled cavities of the structure. It can be shown, performing a model calculation with an assumed solid solution series $(REFe_4Sb_{12})_\alpha(\square Co_4Sb_{12})_{1-\alpha}$ in terms of a theory for point defect scattering [49], that the observed composition dependence of the thermal conductivity follows from mass fluctuation scat-

nominal composition	hypothetical solid solution	calculated Pr content
$Fe_2Ni_2Sb_{12}$	$\square Fe_2Ni_2Sb_{12}$	-
$Pr_{0.21}Fe_{2.5}Ni_{1.5}Sb_{12}$	$(Pr_{0.73}Fe_4Sb_{12})_{0.25}(\square Fe_2Ni_2Sb_{12})_{0.75}$	0.19
$Pr_{0.42}Fe_3NiSb_{12}$	$(Pr_{0.73}Fe_4Sb_{12})_{0.50}(\square Fe_2Ni_2Sb_{12})_{0.50}$	0.37
$Pr_{0.57}Fe_{3.5}Ni_{0.5}Sb_{12}$	$(Pr_{0.73}Fe_4Sb_{12})_{0.75}(\square Fe_2Ni_2Sb_{12})_{0.25}$	0.55
$Pr_{0.73}Fe_4Sb_{12}$	$Pr_{0.73}Fe_4Sb_{12}$	0.73

Table 3.3: Calculated maximum Pr content if the series $Pr_yFe_{4-x}Ni_xSb_{12}$ is thought of as solid solution $(Pr_{0.73}Fe_4Sb_{12})_\alpha(\square Fe_2Ni_2Sb_{12})_{1-\alpha}$.

tering mainly between the rare earth and the cavity $\square$. In the case of Fe/Ni substitution the similar composition dependence of λ_{ph} is understood considering a hypothetical solid solution $(REFe_4Sb_{12})_\alpha(\square Fe_2Ni_2Sb_{12})_{1-\alpha}$. The fact that the lowest lattice thermal conductivity values are not obtained in filled skutterudite samples with fully occupied a sites is thus a direct consequence of the necessary rare earth-$\square$ disorder of the structure guaranteeing enhanced phonon scattering.

Furthermore, this concept may be considered an approach to the understanding of the reduction of the maximum rare earth content starting from pure Fe compounds. In table 3.3, the results on the hypothetical solid solution $(Pr_{0.73}Fe_4Sb_{12})_\alpha(\square Fe_2Ni_2Sb_{12})_{1-\alpha}$ are presented revealing calculated filling fractions close those experimentally obtained. From a study of the available literature data it seems that the solubility range of the filler element increases upon decreasing Fe content, that it just arises from the Co_4Sb_{12} or $Fe_2Ni_2Sb_{12}$ sublattice. 50% void filling in $Pr_{0.5}Co_4Sb_{10}Sn_2$ represents the upper limit, but on the other hand, the rare earth content may be lowered significantly, compare e.g. $Ce_yCo_4Sb_{12}$ [135] or $Eu_yCo_4Sb_{12}$ [172, 127], where solubility of Ce in Co_4Sb_{12} in the range of $y = 0$ to $y = 0.1$, whereas from $y = 0$ to a filling fraction of as much as 55% in the latter were reported. Although insertion of the highest possible amount of rare earth has been the principal intention throughout the studies available on filled skutterudites and staying well below the maximum content achievable was actually never really attempted, it can be concluded that the solubility range in pure Fe skutterudites is very narrow, since pure Fe_4Sb_{12} does not exist and the additional electrons provided by the introduced element are needed to electronically stabilize the compound.

According to the PGEC approach formulated by Slack [5], a suitable thermoelectric material manifests itself in a decoupling of electronic and vibrational degrees of freedom. Especially low lattice thermal conductivities are of significant importance, thermal transport should reveal characteristics found in glass-like materials, where the phonon mean free path is of the order of the phonon wavelength. λ_{min}, which is added in figures 3.27 and 3.28 allows for comparison of experimentally obtained lattice thermal conductivities and the-
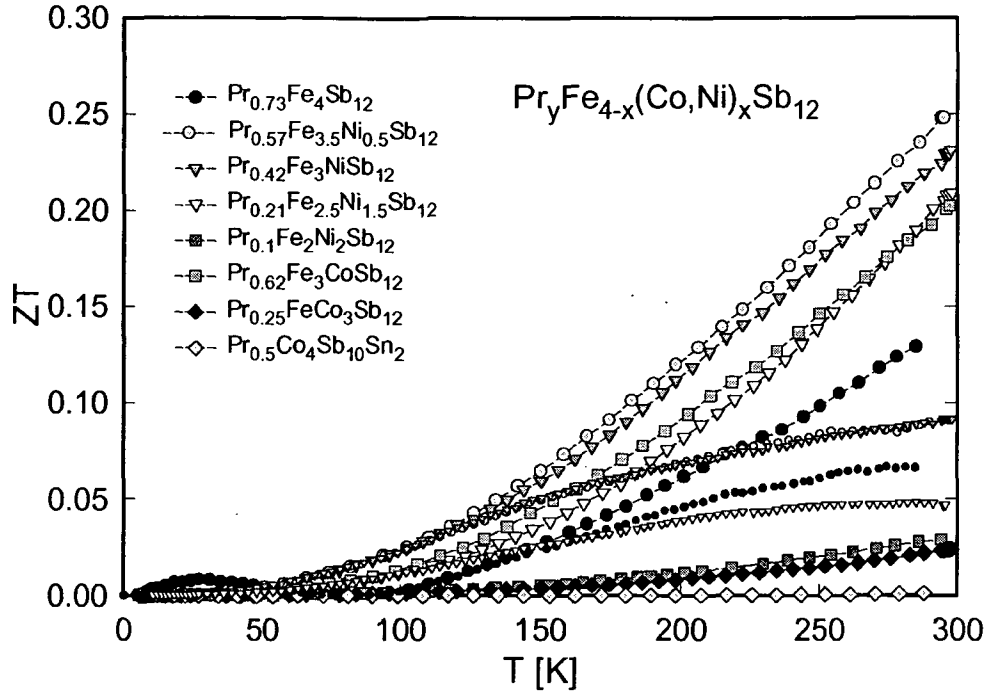
Figure 3.29: Figure of merit ZT vs. T of $Pr_y Fe_{4-x}(Co,Ni)_x Sb_{12}$ and $Pr_{0.5}Co_4 Sb_{10} Sn_2$. The small symbols correspond to ZT of selected samples neglecting radiation losses.

oretically possible lowest values. Based on the Einstein model an expression for the minimum lattice thermal conductivity λ_{min},

$$\lambda_{min} = (\frac{3n}{4\pi})^{1/3}\frac{k_B^2 T^2}{\hbar\Theta_D}\int_0^{\Theta_D/T}\frac{x^3 e^x}{(e^x - 1)^2}dx, \qquad (3.14)$$

was originally proposed by Slack [207] and later modified by Cahill and Pohl [208]. With an average number of electrons per unit volume of $n = 44.57 \times 10^{28}/m^3$, hereby the 34 atoms per unit cell in combination with the lattice constant of $Pr_{0.73}Fe_4 Sb_{12}$ were considered, and a Debye temperature of 200 K, which is in the range of the usually argued quantity, λ_{min} was calculated. Obvious from Figs. 3.27 and 3.28, λ_{min} of about 5 mW/cmK is not reached, however, λ_{ph} of $Pr_{0.57}Fe_{3.5}Ni_{0.5}Sb_{12}$, $Pr_{0.42}Fe_3 NiSb_{12}$ and also of $Pr_{0.62}Fe_3 CoSb_{12}$ is of the same order of magnitude illustrating the successful approach to minimizing thermal conductivity in the series of filled skutterudites $Pr_y Fe_{4-x}(Co,Ni)_x Sb_{12}$.

Fig. 3.29 depicts the thermoelectric figure of merit ZT of $Pr_y Fe_{4-x}(Co,Ni)_x Sb_{12}$ and $Pr_{0.5}Co_4 Sb_{10} Sn_2$. For the evaluation the radiation corrected thermal conductivities were taken, the derived values are there-

fore afflicted with error. For comparison, ZT calculated without radiation correction are added in the figure for selected samples (small symbols). At room temperature, the highest value is accomplished in $Pr_{0.57}Fe_{3.5}Ni_{0.5}Sb_{12}$ with 0.25. This sample is characterized by very low thermal conductivity in the range of 10 mW/cmK and a thermopower of about 140 $\mu V/K$ at 300 K. In combination with relatively well developed metallic conductivity of comparable magnitude to that of parent $Pr_{0.73}Fe_4Sb_{12}$, the crucial interplay between the three transport quantities entering the thermoelectric figure of merit is clearly demonstrated. It is thus important to guarantee strongly reduced thermal conductivities and on the other hand to maintain a favorable balance among electrical resistivity and Seebeck coefficients. Note, that not the compound with the highest overall thermopower, $Pr_{0.21}Fe_{2.5}Ni_{1.5}Sb_{12}$, also exhibits the highest figure of merit, since electrical resistivity of several mΩcm automatically limits ZT. ZT exceeding unity above 600 K has so far been reported for several Ce, Yb and also Ba filled skutterudites [98, 209, 210, 211, 212, 213], the room temperature values of which resembling those of the series $Pr_yFe_{4-x}(Co,Ni)_xSb_{12}$. A further enhancement of the figure of merit can be also expected here at higher temperatures than experimentally available.

Chapter 4

$RE_2Zn_6Ge_3$ with RE=La, Ce, Pr, Nd, Sm and Gd: crystal structure and physical properties

Only a few compounds belonging to the ternary Zn germanides containing rare earth elements have been successfully prepared and characterized so far presumably arising from the rather crucial synthetization processes necessary due to the low melting and boiling point of Zn leading to inapplicability of standard high-frequency and arc-melting techniques (compare section 2.1.2). Little information is thus available on crystal chemistry and physical properties. A short review of the available data is given in the following paragraph.

$YbZn_2Si_2$ and $YbZn_2Ge_2$ have been both observed to crystallize in the body centered tetragonal $BaAl_4$ type of structure (space group $I4/mmm$), the former further corresponding to the ordered $BaAl_4$ variant $ThCr_2Si_2$ type of structure. Both ternary Zn compounds exhibit non-magnetic ground states and temperature independent Pauli-like magnetic susceptibilities attributed to Yb in 2+ ionic state [6]. As for Eu containing ternary Zn compounds, EuZnGe [214] and $EuZn_2Ge_2$ were recently reported on, the latter to supposedly (see next section) crystallize in the $CaBe_2Ge_2$ structure (space group $P4/nmm$), another ternary derivative of $BaAl_4$. It was further pointed out to order antiferromagnetically at low temperatures in combination with a metamagnetic-like transition at an external magnetic field of about 0.5 T. Grytsiv et al. proposed a Néel temperature of 7.5 K [69], Kranenberg et al. long range magnetic order below $T_N = 10$ K [7]. Besides reports on $RE_4Zn_5Ge_6$ (RE=Gd, Tm and Lu) [215] and $NdZn_{1.5}Ge_{0.5}$ (AlB_2 type of structure, space group $hP3$) [216], literature data exist concerning phase equilibria for the ternary systems {Ce, Nd, Gd }-Zn-Ge within isothermal sections at 600 °C ({Gd,Ce}-Zn-Ge [217, 218]) and 870 °C (Nd-Zn-Ge [219]).

Parameter	$Nd_2Zn_6Ge_3$	$Sm_2Zn_6Ge_3$	$Gd_2Zn_6Ge_3$
a [nm]	0.76378(2)	0.76119(2)	0.75939(3)
c [nm]	0.40817(3)	0.40519(1)	0.40295(3)
Data collection	Image Plate	Image Plate	Image Plate
Radiation	$CuK\alpha$	$CuK\alpha$	$CuK\alpha$
Reflections measured	63	61	60
Θ range	$12.5 \leq 2\Theta \leq 100$	$12.5 \leq 2\Theta \leq 100$	$12.5 \leq 2\Theta \leq 100$
Number of variables	26	26	26
$R_F = \sum |F_0 - F_c| / \sum F_0$	0.030	0.050	0.056
$R_I = \sum |I_{oB} - I_{cB}| / \sum I_{oB}$	0.036	0.050	0.054
$R_{wP} = \left[\sum w_i |y_{oi} - y_{ci}|^2 / \sum w_i |y_{oi}|^2 \right]^{1/2}$	0.042	0.032	0.023
$R_P = \sum |y_{oi} - y_{ci}| / \sum |y_{oi}|$	0.029	0.023	0.017
$R_e = \left[(N - P + C) / \sum w_i y_{0i}^2 \right]^{1/2}$	0.008	0.019	0.016
$\chi^2 = (R_{wP}/R_e)^2$	22.7	2.84	1.98
Atom parameters			
RE in 2c (1/3,2/3,0)	Nd	Sm	Gd
B_{iso} [10^2 nm^2]	0.62(2)	0.63(1)	1.06(2)
Zn1 in 3f (x,0,0)	x=0.1897(1)	x=0.1909(1)	x=0.1916(1)
B_{iso} [10^2 nm^2]	0.89(3)	0.73(3)	0.57(3)
Zn2 in 3g (x,0,1/2)	x=0.7112(1)	x=0.7132(1)	x=0.7128(1)
B_{iso} [10^2 nm^2]	0.75(3)	0.55(3)	0.55(3)
Ge in 3g (x,0,1/2)	x=0.3827(1)	x=0.3860(1)	x=0.3871(1)
B_{iso} [10^2 nm^2]	0.67(2)	0.53(2)	0.70(2)
Interatomic distances [nm]; standard deviations generally < 0.0005 nm			
RE-6Ge	0.31351	0.31122	0.30983
RE-3Zn1	0.32370	0.32193	0.32078
RE-6Zn2	0.34100	0.34009	0.33876
Zn1-2Zn1	0.25095	0.25168	0.25201
Zn1-2Zn2	0.28167	0.27945	0.27856
Zn1-Ge	0.25175	0.25119	0.25026
Zn2-Ge	0.25090	0.24906	0.24733

Table 4.1: Structural data of $RE_2Zn_6Ge_3$ (RE=Nd, Sm, Gd), space group $P\bar{6}2m$, No. 189, standardized using the program Structure Tidy [223].

Beyond the interest in their crystal structures and basic physical ground state properties, $RE_2Zn_6Ge_3$ compounds may be suitable for thermoelectric applications since silicides and germanides are generally considered promising thermoelectric materials: compare e.g. (SiGe) alloys, that have been successfully used starting in the 1970's for space power applications, since ZT values close to unity are reached at temperatures higher than 1000 K [220], $Mg_2(Si,Sn)$ solid solutions with ZT of 0.8 [221] or $Mg_2Si_{0.6}Ge_{0.4}$ exceeding the figure of merit's unity with 1.68 [222].

4.1   Crystal Structure

Determination of the atom arrangement in $RE_2Zn_6Ge_3$ was carried out on the basis of the successfully grown single crystals of $Ce_2Zn_6Ge_3$. The absence of systematic extinctions led to compatibility with several hexagonal and trigonal space groups. Employing direct methods, the low-symmetry space group $P\bar{3}$ was found to satisfactorily account for the observed x-ray patterns, search

Parameter	$La_2Zn_6Ge_3$	$Ce_2Zn_6Ge_3$	$Pr_2Zn_6Ge_3$
a [nm]	0.77088(2)	0.76769(2)	0.76543(2)
c [nm]	0.41496(3)	0.41159(2)	0.40984(3)
Data collection	Image Plate	Nonius Kappa CCD	Image Plate
Radiation	$CuK\alpha$	$MoK\alpha$	$CuK\alpha$
Reflections measured	63	$678 > 4\sigma(F_0)$ of 698	63
Θ range	$12.5 \leq 2\Theta \leq 100$	$2.04 \leq 2\Theta \leq 90.58$	$12.5 \leq 2\Theta \leq 100$
Number of variables	26	16	26
$R_F = \sum |F_0 - F_c| / \sum F_0$	0.050	$R_{F2}(678) = 0.033$	0.057
$R_I = \sum |I_{oB} - I_{cB}| / \sum I_{oB}$	0.051	$R_{F2}(698) = 0.034$	0.050
$R_{wP} = [\sum w_i |y_{oi} - y_{ci}|^2 / \sum w_i |y_{oi}|^2]^{1/2}$	0.072	$wR2 = 0.08; R_{int} = 0.541$	0.069
$R_P = \sum |y_{oi} - y_{ci}| / \sum |y_{oi}|$	0.049	mosaicity $= 0.565(3)$	0.048
$R_e = [(N - P + C)/ \sum w_i y_{0i}^2)]^{1/2}$	0.025	extinction $= 0.130(7)$	0.021
$\chi^2 = (R_{wP}/R_e)^2$	8.3	GOF $=1.074$	11.0

Atom parameters			
RE in 2c (1/3,2/3,0)	La	Ce	Pr
B_{iso} [10^2 nm^2]	0.38(2)	$U_{equ.} = 0.0069(1)^a$	0.46(2)
Zn1 in 3f (x,0,0)	x=0.1880(2)	x=0.1896(1)	x=0.1888(2)
B_{iso} [10^2 nm^2]	0.67(4)	$U_{equ.} = 0.0107(2)^a$	0.86(5)
Zn2 in 3g (x,0,1/2)	x=0.7089(2)	x=0.7107(1)	x=0.7096(2)
B_{iso} [10^2 nm^2]	0.71(4)	$U_{equ.} = 0.0127(2)^a$	0.75(4)
Ge in 3g (x,0,1/2)	x=0.3775(2)	x=0.3808(1)	x=0.3810(2)
B_{iso} [10^2 nm^2]	0.57(4)	$U_{equ.} = 0.0075(1)^a$	0.62(4)

Interatomic distances [nm]; standard deviations generally < 0.0005 nm			
RE-6Ge	0.31856	0.31597	0.31482
RE-3Zn1	0.32766	0.32541	0.32490
RE-6Zn2	0.34423	0.34297	0.34139
Zn1-2Zn1	0.25101	0.25210	0.25030
Zn1-2Zn2	0.28615	0.28378	0.28313
Zn1-Ge	0.25374	0.25277	0.25226
Zn2-Ge	0.26408	0.25326	0.25152

^{a} Anisotropic atomic displacement parameters (10^2 nm^2): Ce: $U_{11} = U_{22} = 0.006(1)$, $U_{33} = 0.0074(1)$, $U_{12} = 0.00330(6)$; Zn1: $U_{11} = 0.0091(2)$; $U_{22} = 0.0142(4)$, $U_{33} = 0.0105(3)$, $U_{12} = 0.0071(2)$; Zn2: $U_{11} = 0.0095(3)$, $U_{22} = 0.0086(4)$, $U_{33} = 0.0197(4)$, $U_{12} = 0.0127(2)$; Ge: $U_{11} = 0.0070(2)$; $U_{22} = 0.0079(3)$, $U_{33} = 0.0080(2)$, $U_{12} = 0.0039(1)$.

Table 4.2: Structural data of $RE_2Zn_6Ge_3$ (RE=La, Ce, Pr), space group $P\bar{6}2m$, No. 189, standardized using the program Structure Tidy [223].

for higher symmetry revealed correct resembling of the given atom arrangement by the space group $P\bar{6}2m$. Since distinguishing between Zn and Ge atoms, that are nearly isoelectronic and thus possess similar x-ray scattering powers, is difficult employing x-ray diffraction analyses, the Ge atoms were identified to be located at the 3g site (0.3808, 0, 1/2) by comparison of balanced displacement factors and interatomic distances with the sum of the atomic radii. Similar problems arose in identifying a compatible space group of higher symmetry for above mentioned $EuZn_2Ge_2$. Kranenberg et al. [7] discussed the $CaBe_2Ge_2$ structure proposed by Grytsiv et al. [69], however, stated isotypism with the ordered $BaAl_4$ variant $ThCr_2Si_2$ type of structure, since the lattice-ordering scheme is mainly determined by the site distribution of nearly isoelectronic Zn and Ge, which were also found to be hardly extractable from x-ray diffraction data. However, elastic neutron scattering measurements performed on the two compounds $Pr_2Zn_6Ge_3$ and $Nd_2Zn_6Ge_3$
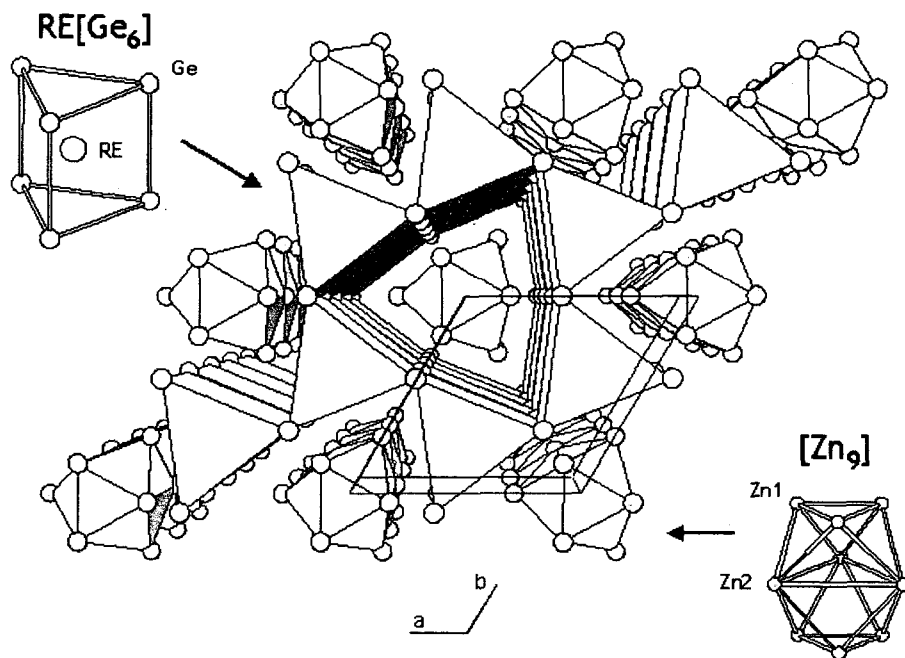
Figure 4.1: Crystal structure of RE$_2$Zn$_6$Ge$_3$ in a three-dimensional view along the c-axis (space group $P\bar{6}2m$, No. 189). The trigonal prisms of Ge atoms around the RE elements RE[Ge$_6$] and the Zinc clusters [ZN$_9$] represent the basic components of the structure, the solid lines denote the standardized unit cell.

corroborated the structural assumptions adopted from x-ray refinements of the Ce$_2$Zn$_6$Ge$_3$ single crystals, because the difference in neutron scattering length of Zn compared to Ge permits distinct determination of the atom site distribution. The formula Ce$_2$Zn$_6$Ge$_3$ was thus derived to account for a fully ordered atom arrangement, too in good agreement with compositions controlled by EPMA and with the additionally prepared fairly single phase bulk samples. The latter were also used to rule out any contamination or solubility of In flux in the single crystals by comparison of the lattice parameters. Refinement of the occupancies of all crystallographic sites and in the final run of the anisotropic displacement factors, on the one hand, did not reveal any significant deviations from stoichiometry and on the other resulted in an R-value of as low as 0.03 confirming the proposed structural model. X-ray diffraction patterns of all other compounds (RE$_2$Zn$_6$Ge$_3$ with RE=La, Pr, Nd, Sm and Gd) could also be indexed on the basis of a hexagonal unit cell, a close inspection of the x-ray intensities, the size of the unit cell as well as absence of systematic extinctions implied isotypism with the derived Ce$_2$Zn$_6$Ge$_3$ structure type in agreement with above mentioned neutron diffraction analy-
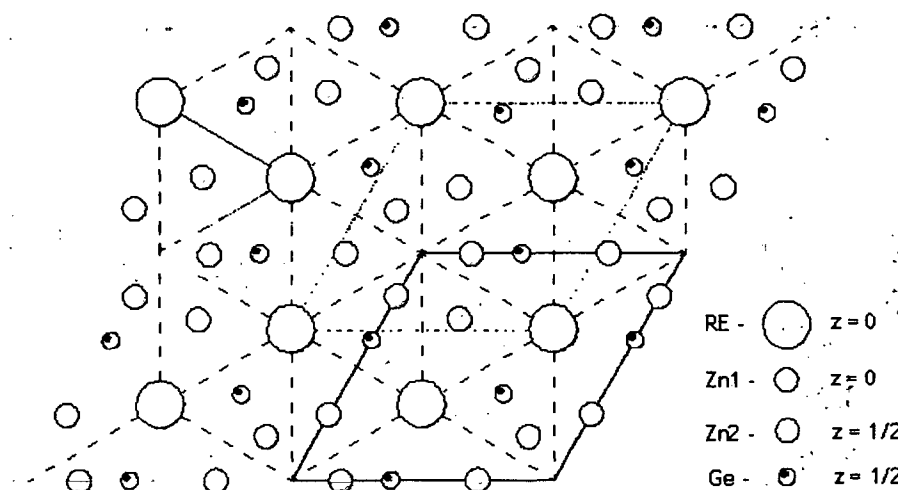
RE - ◯ z = 0

Zn1 - ◯ z = 0

Zn2 - ◯ z = 1/2

Ge - ◑ z = 1/2

Figure 4.2: Projection of the crystal structure of $RE_2Zn_6Ge_3$ onto the xy-plane with the solid line defining the standardized unit cell and the dashed line indicating the magnetic unit cell.

sis. Details concerning Rietveld refinements and structural characteristics of Ce single crystals as well as of all bulk samples are compiled in tables 4.1 and 4.2.

Along with the crystal structure of $RE_2Zn_6Ge_3$ in a three-dimensional representation along the [001]-axis corresponding to space group $P\bar{6}2m$, figure 4.1 depicts the two basic components the structure consists of. These trigonal prisms, spanned by six Ge atoms and incorporating the particular rare earth element, and the clusters of Zn atoms denoted by $[Zn_9]$ are arranged in the way, that the Zn clusters, face connected to each other, build infinite columns parallel to the c-axis surrounded by six edge-connected trigonal Ge prisms forming channels around each $[Zn_9]$ column. The rhomboid denoted by the solid line corresponds to the standardized unit cell of the structure. It is also added in Fig. 4.2 displaying the projection of the $RE_2Zn_6Ge_3$ structure onto the xy-plane. This view permits the direct identification of the atom distribution among the different lattice sites listed in the middle sections of tables 4.2 and 4.1. Unoccupied site 1a (0,0,0) is encircled by three Zn1 atoms at the 3f positions at (0.1896,0,0), while the rare earth is situated in 2c at (1/3,2/3,0) surrounded by slightly distorted hexagonal prisms of Ge and Zn2, both located in the 3g sites at (0.7089,0,1/2) and (0.3808,0,1/2), respectively (the absolute x-values of the particular sites' coordinates stated here represent those of single crystal $Ce_2Zn_6Ge_3$).

Lattice constants and unit cell volumes as functions of the particular rare earth element in $RE_2Zn_6Ge_3$ are found in Fig. 4.3. A gradual decrease of the
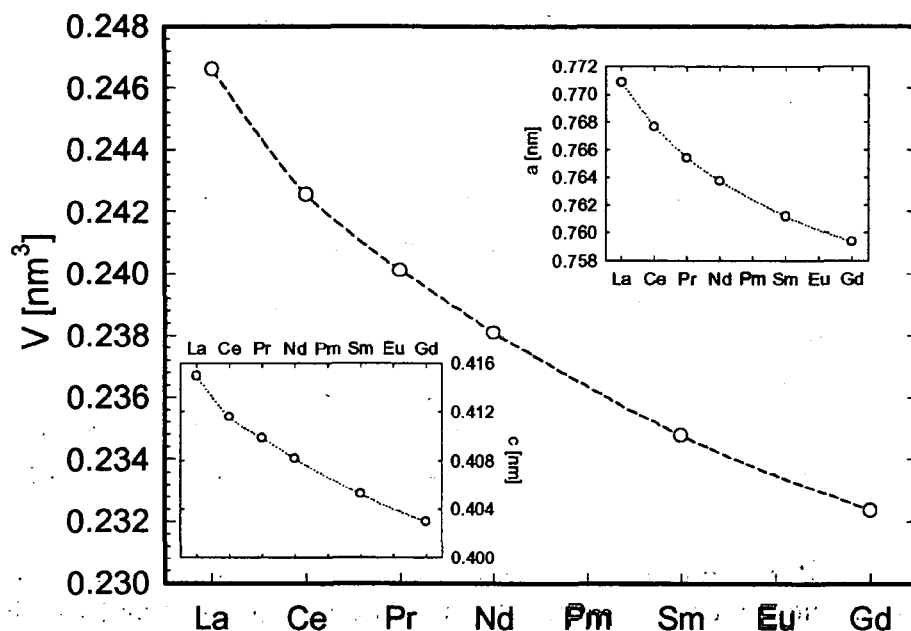
Figure 4.3: Lattice constants and unit cell volume of RE$_2$Zn$_6$Ge$_3$ vs. rare earth element.

lattice parameters is observed when starting with La and proceeding through the lanthanoid series apparently caused by the lanthanoid contraction. Considering the generally obeyed oxidation rule of the rare earth elements leading to a prevalence of the 3+ oxidation state, figure 4.3 clearly indicates a 3+ state of RE for all compounds under investigation, since the decreasing trend of the lattice parameters is not violated in any case and La as well as Gd are expected to fulfill the oxidation rule. Thus for Ce and also Sm, possibly existing in 4+ and 2+ state, respectively, too, a trivalent ground state applies. Magnetic measurements presented within the next sections will underline this assumption.

4.2 Magnetic properties

Inverse magnetic susceptibilities of RE$_2$Zn$_6$Ge$_3$ as function of temperature at an externally applied field of 0.1 T are given in figure 4.4, magnetic measurements of the La containing compound were not performed due to the absence of localized magnetic moments. Note, that the absolute values of the susceptibilities of Pr$_2$Zn$_6$Ge$_3$ and Sm$_2$Zn$_6$Ge$_3$ were respectively multiplied by factors of 1.2 and 1/4 in order to enable direct comparison among all compounds
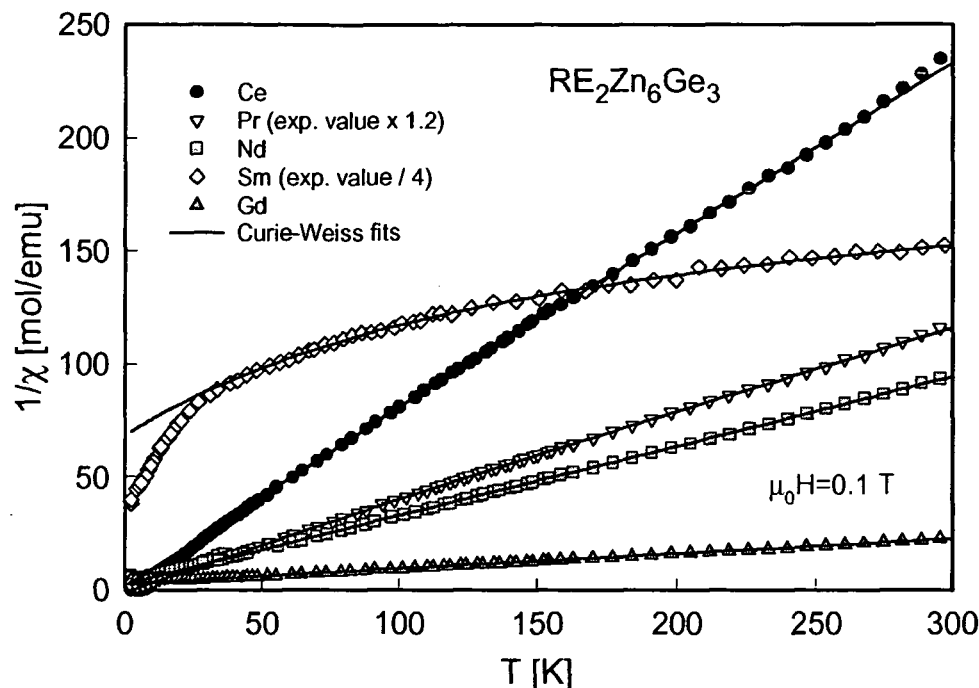
Figure 4.4: Inverse magnetic susceptibility $1/\chi(T)$ of $RE_2Zn_6Ge_3$. In order to visualize all curves in the depicted temperature range, experimental data of $Pr_2Zn_6Ge_3$ and $Sm_2Zn_6Ge_3$ were multiplied by 1.2 in the case of Pr and divided by a factor of 4 for Sm, respectively. The solid lines represent least-squares fits according to a modified Curie-Weiss law (for details see text).

under investigation. Above about 50 K, $1/\chi$ of all samples follows a modified Curie-Weiss type of behavior, the smooth upturn of the experimental data clearly visible in $Ce_2Zn_6Ge_3$ above about 270 K causing the deviation from the expected Curie-Weiss law, yet, has no physical origin, it rather stems from systematic measurement errors.

The temperature dependence of $1/\chi$ of $Sm_2Zn_6Ge_3$, distinctly differing from that of the other compounds, is characteristic of Sm intermetallics for two reasons. It arises from the rather small g-value $\left(\frac{2}{7}\right)$ of Sm^{3+} as well as from groundstate $\left(^6H_{5/2}\right)$ and first excited multiplet $\left(^6H_{7/2}\right)$ being only separated by about 1500 K. In order to fully account for the experimentally observed temperature dependencies of Sm containing compounds, the first excited multiplet in combination with crystal electric field effects within both multiplets has to be considered. Additionally spin-orbit splitting among the different CEF levels and exchange interactions induced by CEF split levels may contribute as well, compare e.g. [224, 225]. A review of the magnetic properties of binary Sm compounds can be found in [226].

$RE_2Zn_6Ge_3$	Ce	Pr	Nd	Sm	Gd
ordering temperature [K]	7.2	7.1	4.5	7.4	28.8
type of long range magnetic order: ↑↑ - ferromagn., ↑↓ - antiferromagn.	↑↑	↑↓	↑↓	↑↓	↑↓
free RE^{3+} moment [μ_B] according to $g\sqrt{J(J+1)}$	2.54	3.58	3.62	0.84	7.94
effective magnetic moment μ_{eff} [μ_B]	2.18	3.35	3.62	0.73	7.52
paramagn. Curie temperature θ_p [K]	1.07	2.83	-8.56	-58	-38.7
Magnetization at 2K and 6T [μ_B/f.u.]					

Table 4.3: Summary of the magnetic properties of $RE_2Zn_6Ge_3$ as deduced from experimental data, as well as hypothetical magnetic moments corresponding to the 3+ electronic configuration of the particular free rare earth ion.

The solid lines in figure 4.4 correspond to least-squares fits to the experimental data in terms of a modified Curie-Weiss law according to equation 1.76, where the temperature independent susceptibility contribution χ_0 was added referring to the influence of the conduction electron system on the overall magnetic response. The thus deduced paramagnetic Curie temperatures and effective magnetic moments are summarized in table 4.3. Close agreement with the theoretical free RE^{3+} magnetic moments, also given in table 4.3, is observed in all cases. Even $Sm_2Zn_6Ge_3$, neglecting any peculiar influence of CEF effects and the low-lying first excited multiplet, fairly well matches its hypothetical free ion moment of 0.84 μ_B with $\mu_{eff} = 0.73\mu_B$. The deviation of the experimentally derived effective Gd moment from the theoretically expected one possibly originates from the somewhat insufficient approximation of the measurement data, since CEF effects are absent due to the purely spherical S state of Gd^{3+} implying compliance with the full free ion moment. $Ce_2Zn_6Ge_3$ exhibits a slightly reduced effective magnetic moment, an observation frequently attributed to hybridization effects of the $4f^1$ state with the conduction band giving rise to deviations from a pure 3+ state. However, other experimentally derived properties of $Ce_2Zn_6Ge_3$, discussed in the following sections, do not at all indicate any presence of hybridization effects. Thus CEF splitting of the Ce $J = \frac{5}{2}$ total angular momentum

may be of significant importance in comprehending the magnetic behavior of $Ce_2Zn_6Ge_3$.

The paramagnetic Curie temperatures θ_p of $RE_2Zn_6Ge_3$ with RE = Sm, Nd and Gd derived employing Curie-Weiss fits reveal negative Curie temperatures indicative of antiferromagnetic interactions. The strongly enhanced value of θ_p = -38.7 in the case of Gd is thus the result of the free Gd^{3+} ion's large g-factor of 2 incorporated into the de Gennes factor $(g-1)^2 J(J+1)$ = 15.75 in combination with significant exchange interaction strength between localized Gd moments and conduction electrons, see equation 1.84. The high ordering temperature of $Gd_2Zn_6Ge_3$, closely inspected below, fits well into this picture. Discussed in section 1.6.2, in terms of the molecular field theory, paramagnetic and (anti-)ferromagnetic (Neel) Curie temperatures coincide, experimentally derived paramagnetic Curie and magnetic transition temperatures, however, mostly differ due to the insufficiency of the molecular field theory in combining these magnetic regimes. Still, experimentally observed high (low) paramagnetic Curie temperatures are considered related to respective higher or lower magnetic transition temperatures. A θ_p of - 58 in $Sm_2Zn_6Ge_3$ possibly originates from an unrealistic reproduction of the magnetic susceptibility by the simple Curie-Weiss law employed as already outlined in a previous paragraph. Nevertheless, strong exchange interactions may be present giving rise to the large paramagnetic Curie temperature, although a de Gennes factor of 4.46 and long range magnetic order just below 7.4 K (see below) would disagree with this result.

The positive paramagnetic Curie temperatures θ_p = 1.07 and 2.83 K of $Ce_2Zn_6Ge_3$ and $Pr_2Zn_6Ge_3$ can be related to ferromagnetic interactions. Figure 4.5 displays the isothermal magnetization M as a function of externally applied field $\mu_0 H$ of $RE_2Zn_6Ge_3$ at 2 K (decent data for Sm are only available up to $\mu_0 H$ =1 and were multiplied by a factor of 10). In line with its positive θ_p, $Ce_2Zn_6Ge_3$ exhibits spontaneous magnetization at 2 K rapidly saturating at fields above $\mu_0 H$ =1 T and reaching 1.6 μ_B at 6 T. the saturation magnetization of 0.8 μ_B/Ce atom stays well below the theoretical value of gJ=2.14 μ_B for free Ce^{3+}. This further backs the assumption of CEF effects being of importance in understanding the magnetic properties of $Ce_2Zn_6Ge_3$, both reduced effective magnetic moments due to the first excited CEF level lying substantially above the ground state as well as the observed value of M at 6 T, can be associated with lifting of the $2(J+1)$-fold degeneracy of the Ce 3+ ground state $(J = \frac{5}{2})$. $Pr_2Zn_6Ge_3$ is characterized by a more complicated variation of $M(H)$ at 2 K. A rapid increase of the magnetization at small fields indicative of spontaneous magnetization is followed by a tendency of saturation, while at a field of $\mu_0 H$ =1 T a metamagnetic-like change of slope is observed possibly due to spin-flip processes aligning additional magnetic moments parallel to the applied magnetic field. The magnetization reaches

about 1 μ_B/f.u. roughly below the magnetic field driven metamagnetic transition at 1 T, thus around 0.5 μ_B/Pr atom. Too Nd$_2$Zn$_6$Ge$_3$ undergoes a metamagnetic transition at a field of about 2-3 T.

In order to clarify the perceptions extracted from $M(H)$ data, low temperature magnetic susceptibilities of RE$_2$Zn$_6$Ge$_3$ are plotted in Fig. 4.6a. The anomalies in $1/\chi(T)$, reflected by a change of slope and designated by arrows in the figure, suggest onset of long range magnetic order. Magnetic transitions into antiferromagnetic order can be clearly identified for Nd$_2$Zn$_6$Ge$_3$, which is consistent with the magnetic field induced metamagnetic transition observed, and Gd$_2$Zn$_6$Ge$_3$, for both samples, $1/\chi(T)$ towards lower temperatures is characterized by an increase below the respective Neel temperatures $T_N = 4.5$ and 28.8 K. The Sm as well as Pr and Ce containing compounds exhibit slight kinks at about 7.4, 7.1 and 7.2 K, from the results of the presented isothermal magnetization measurements at 2 K, antiferromagnetic order can be assigned to the two former and long range ferromagnetic order to the latter. Additionally performed a.c. magnetic susceptibility data shown in Fig. 4.6b further serve to determine magnetic transition temperatures for Pr and Nd compounds, the findings of which agreeing well with the other experimental results.

The small-field net-magnetization and the spin-flip processes around a magnetic field of 1 T exhibited by Pr$_2$Zn$_6$Ge$_3$ are signs for a peculiar antiferromagnetic spin arrangement, a similar observation applies to Nd$_2$Zn$_6$Ge$_3$. Elastic neutron diffraction patterns obtained at 1.5 and 9 K (Nd: 7 K) are depicted in Fig. 4.7. The spectrum taken above the magnetic ordering temperature reflects the atomic structure of the compounds, note, that due to worse statistics in the case of Nd, some atomic peaks have not developed to such an extent as compared to the Pr compound. Additional reflections at 1.5 K clearly evidence antiferromagnetic order, the vertical marks on the bottom of Fig. 4.7 index calculated Bragg peak positions, the first line corresponding to atomic Bragg peaks, whereas the second line indicates both atomic and magnetic peaks. Refinement of the experimentally derived data based on the hexagonal parent structure gave rise to adoption of the antiferromagnetic spin structures illustrated in Fig. 4.8. Both Nd$_2$Zn$_6$Ge$_3$ and Pr$_2$Zn$_6$Ge$_3$ possess magnetic unit cells with an a parameter identical to that of the atomic arrangement (the standardized magnetic unit cell is denoted by the dashed rhomboid in Fig. 4.2) but with differing c parameters, $c_{mag} = 2c_{nuc}$ in the former and $c_{mag} = 3c_{nuc}$ in the latter compound. While the magnetic structure of Nd$_2$Zn$_6$Ge$_3$ is characterized by antiferromagnetic (a, b)-planes, that are stacked together antiferromagnetically along the c-axis, ferromagnetic (a, b)-planes of Pr ions are combined in the way along c, that two spin-up planes are followed by one spin-down plane ($++-++-++-...$) in Pr$_2$Zn$_6$Ge$_3$.
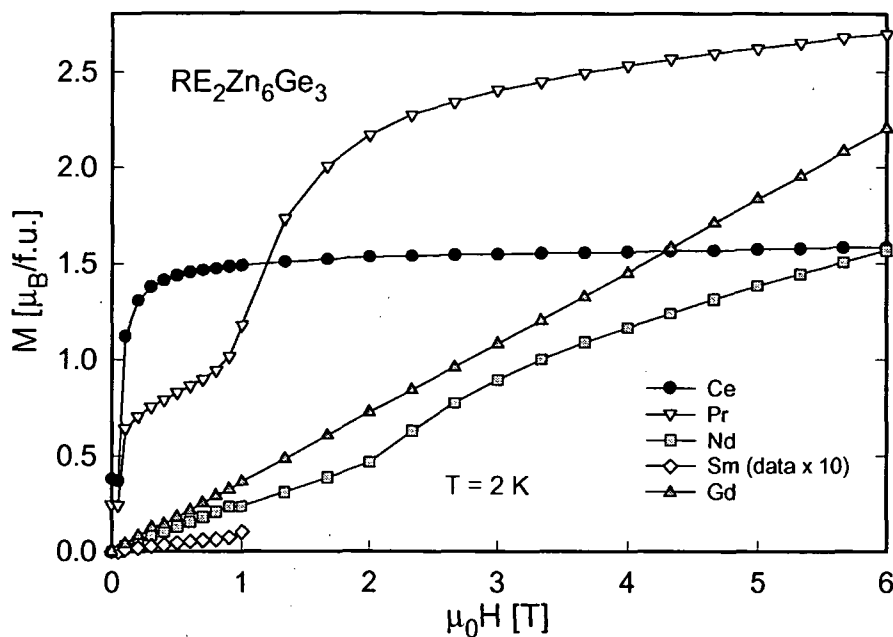
Figure 4.5: Isothermal magnetization M vs. magnetic field $\mu_0 H$ at 2 K of $RE_2Zn_6Ge_3$, data of Sm were multiplied by a factor of 10.
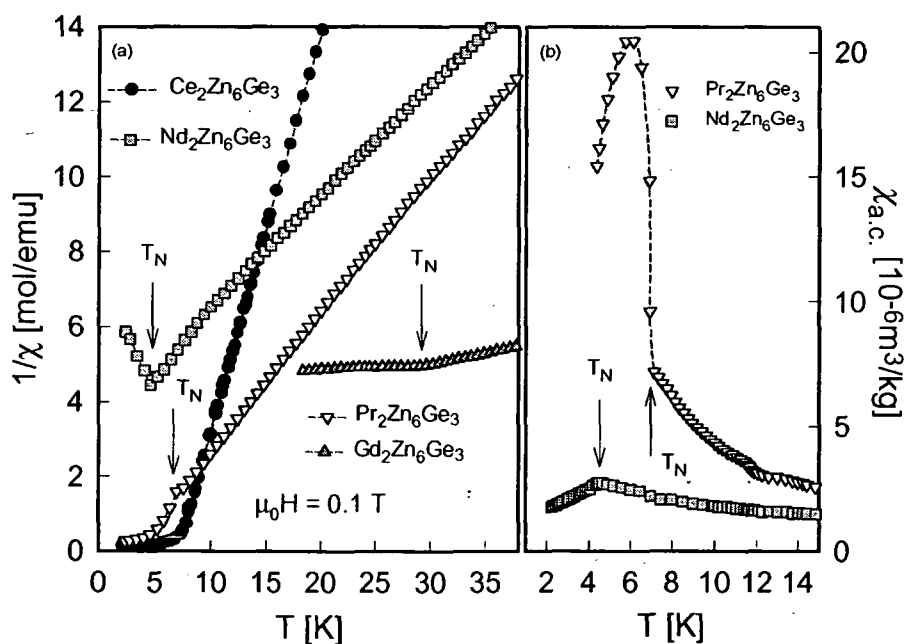
Figure 4.6: (a) Low temperature magnetic susceptibility of $RE_2Zn_6Ge_3$ plotted as $1/\chi$ as a function of temperature,(b) a.c. magnetic susceptibility $\chi_{a.c.}(T)$ of $Nd_2Zn_6Ge_3$ and $Pr_2Zn_6Ge_3$.
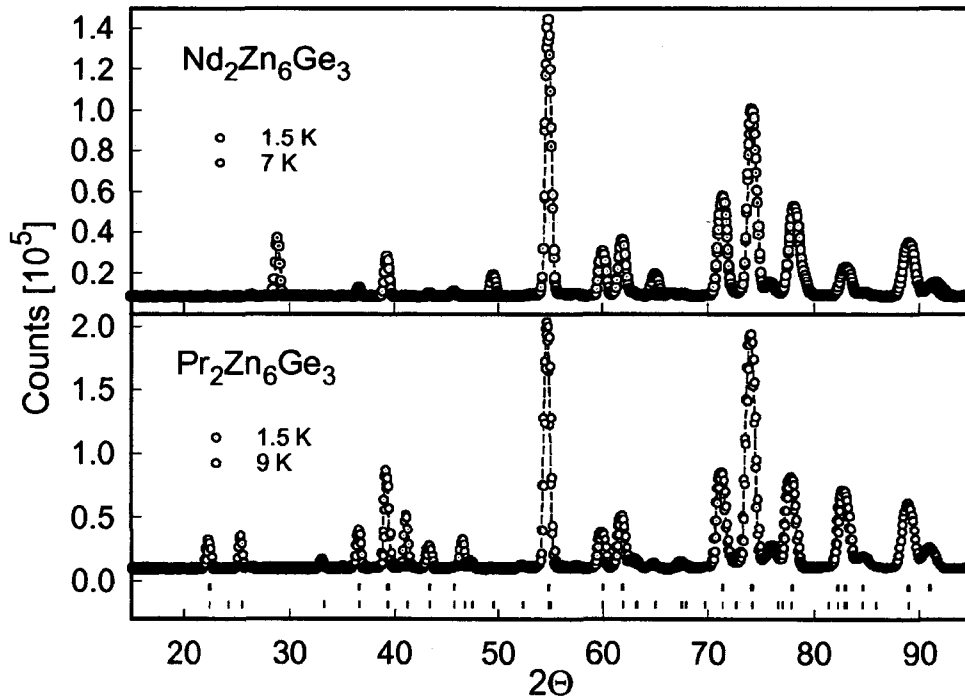
Figure 4.7: Elastic neutron diffraction patterns of Pr$_2$Zn$_6$Ge$_3$ and Nd$_2$Zn$_6$Ge$_3$ taken above and below the magnetic transition temperatures. The vertical marks for Pr$_2$Zn$_6$Ge$_3$ index atomic (first line) and atomic+magnetic Bragg peaks (second line).
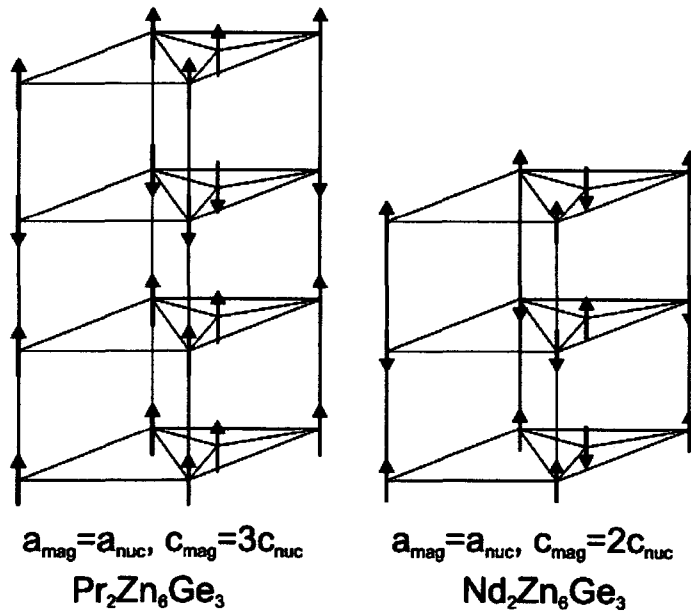
Figure 4.8: Magnetic structures of Nd$_2$Zn$_6$Ge$_3$ and Pr$_2$Zn$_6$Ge$_3$.

According to the neutron data, magnetic moments associated with the particular rare earth ions amount to 2.20(4) μ_B for the Nd and 2.97(7) μ_B for Pr, which in the latter case can be approximatively related to the value obtained from isothermal magnetization data. Since an external magnetic field of about 1 T causes a spin re-orientation, the saturation magnetization at 6 T cannot be used for comparison with the moments deduced from neutron diffraction, however, this value of 2.7 μ_B would still stay well below the full one of 5.94 μ_B/f.u. expected from neutron data. 5.94 μ_B per magnetic unit cell correspond to 1.98 μ_B per crystallographic unit cell. If one considers polycrystalline material, where in general only a fraction of one third of the total magnetic response is measured as bulk effect due to uniaxial spin alignment [227], the magnetic moment per Pr atom yields 0.66 μ_B. Considering the magnetization of $Pr_2Zn_6Ge_3$ at 2 K and below the critical field of 1 T, 0.5 μ_B/Pr atom, rough agreement is confirmed with the value of 0.7 μ_B deduced from neutron diffraction.

4.3 Specific heat

Specific heat measurements were performed for $La_2Zn_6Ge_3$, $Ce_2Zn_6Ge_3$ and $Pr_2Zn_6Ge_3$ in the temperature range from 2 to about 70 K, results of which are given in Fig. 4.9, where C_p is plotted as C_p/T vs. T. Apart from non-magnetic $La_2Zn_6Ge_3$ temperature dependent specific heat curves are characterized by anomalies around 7 K reminiscent of magnetic phase transitions. The height of the jump in C_p at the ordering temperature clearly excludes impurities from being source of magnetic contributions to the total heat capacity, rather evidencing bulk nature of the transition.

The solid line in inset (b) of Fig. 4.9 denotes the results of a least-squares fit to the experimental data of the La containing sample below 8 K in terms of the expression $C_p/T = \gamma + \beta T^2$. In order to extract the electronic contribution γ as well as the lattice part β, the representation C_p/T vs. T^2 was chosen permitting direct evaluation of latter coefficients. The electronic contribution amounts to an expectedly low value of roughly 2.5 mJ/molK consistent with pure metallic behavior, β yields 0.001028 J/molK^4. According to section 1.6.4, β is directly proportional to the Debye temperature Θ_D resulting in Θ_D =124 K. A common procedure to approximate the overall heat capacity of metallic compounds usually assumes a Debye spectrum given by expression 1.86 for the lattice contribution to C_p. In this case however, the simple Debye model did not yield convincing agreement with the experimental data, whereas adding of three Einstein functions lead to accurate fitting results in the overall temperature range (compare inset (a) of Fig. 4.9). Thereby the following expression was employed, after the electronic contribution to C_p
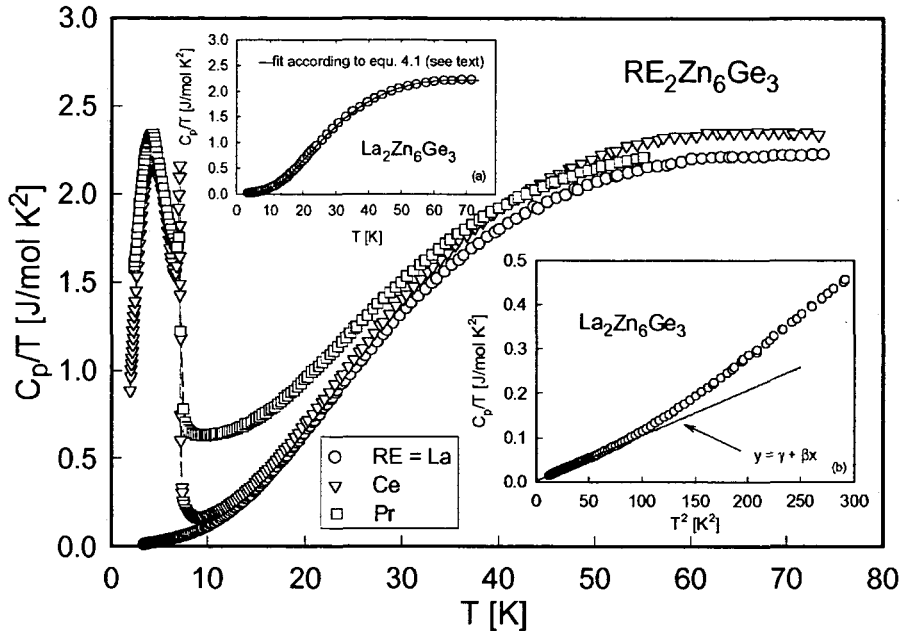
Figure 4.9: Temperature dependent specific heat C_p of $RE_2Zn_6Ge_3$ with RE=La, Ce and Pr plotted as C_p/T vs. T. Inset a: Least-squares fit to C_p/T of $La_2Zn_6Ge_3$ in terms of equation 4.1. Inset b: Low temperature specific heat of $La_2Zn_6Ge_3$ plotted as C_p/T vs. T^2, the solid line represents a fit according to the expression $y = \gamma + \beta x$ (see text).

obtained from the low temperature fit had been subtracted:

$$C_{ph}(T) = \frac{9R}{\omega_D^3} \int_0^{\omega_D} \frac{\omega^2 \left(\frac{\omega}{2T}\right)^2}{\sinh^2 \left(\frac{\omega}{2T}\right)} d\omega + \sum_{i=1,2,3} c_i R \frac{\left(\frac{\omega_{Ei}}{2T}\right)^2}{\sinh^2 \left(\frac{\omega_{Ei}}{2T}\right)}. \qquad (4.1)$$

The notation ω_D instead of Θ_D serves to distinguish between low temperature derived and 'overall' Debye temperature, since in general ω_D and Θ_D may differ due to the fact, that ω_D should be only determined by acoustic phonon modes in contrast to Θ_D being an average value over acoustic as well as optical branches of the phonon dispersion relation. Considering 11 atoms per formula unit, the phonon dispersion relation of $RE_2Zn_6Ge_3$ consists of 3 acoustic and 30 optical branches. The parameters c_i are then evaluated in the way, that they weight the respective fractions of La, Zn and Ge to one formula unit. Thus $\sum c_i = 30$, since the 3 acoustic modes are assumed to be accounted for by the Debye contribution, $c_1 = 16.4$, $c_2 = 8.19$ and $c_3 = 5.45$ was agreed on to be a reasonable parametrization in accordance with the compositional ratio among La, Zn and Ge. Surprisingly $\omega_D = 121K$ and $\Theta_D = 124K$ are quite close to each other, the three Einstein temperatures amount to $\omega_{E1} = 236K$,
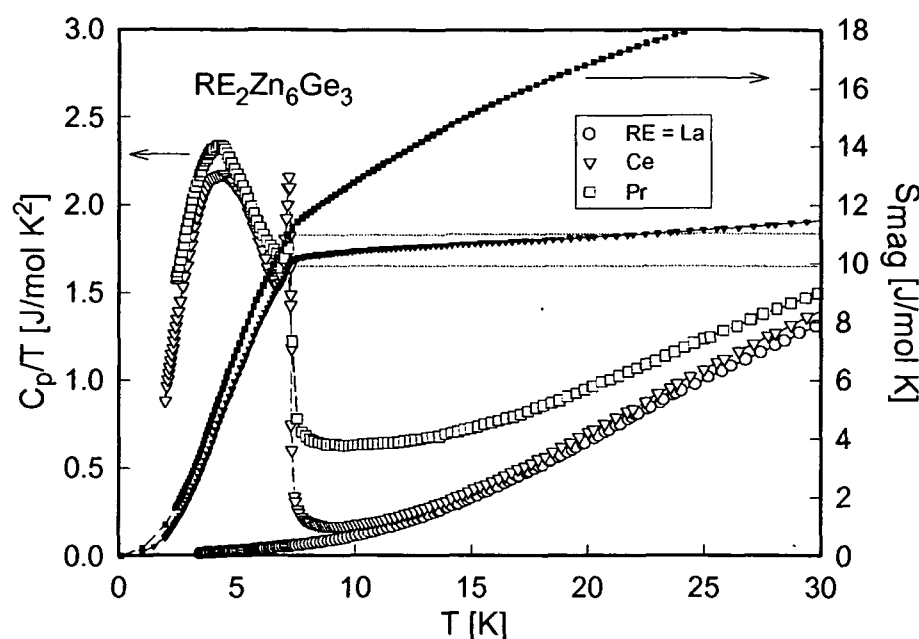
Figure 4.10: Left hand scale: temperature dependent specific heat C_p of $RE_2Zn_6Ge_3$ with RE=La, Ce and Gd plotted as C_p/T vs. T. Right hand scale: temperature dependent magnetic entropy S_{mag} of $Ce_2Zn_6Ge_3$ and $Pr_2Zn_6Ge_3$.

$\omega_{E2} = 129K$ and $\omega_{E3} = 121K$, which, due to the magnetic transitions in all other compounds investigated, have to be accepted as is without further possibilities of comparison or interpretation.

Subtraction of $C_p(T)$ of La $_2Zn_6Ge_3$ from the total heat capacity of $Ce_2Zn_6Ge_3$ and $Pr_2Zn_6Ge_3$, thus eliminating electronic and lattice parts, resulted in the magnetic contributions, that via integration according to equation 1.87 allowed the calculation of the magnetic entropies released at T_{ord}. Note, that differences in volume, mass and melting point between La and Ce and Pr, properties usually regarded to scale specific heat data of compounds differing in their constituent elements, were neglected during subtraction due to only minor errors of about 1% caused thereby. In Fig. 4.10 $S_{mag}(T)$ of Ce and Pr sample are plotted as filled, small symbols on the right hand scale. S_{mag} reaches about 10.3 and 11.2 J/molK per formula unit at T_{ord}, a value close to twice $R\ln 2$ (5.7 J/molK) and usually attained at T_{ord} of two magnetic ions per formula unit in a doublet ground state. The significant deviations from the predictable values considering a total angular momentum of $J = 5/2$ for Ce on the one hand and $J = 4$ for Pr on the other hand, twice $R\ln 6$ and twice $R\ln 9$, therefore have to be attributed to the influence of the crystal electric field. In the paramagnetic temperature range, above the onset of long
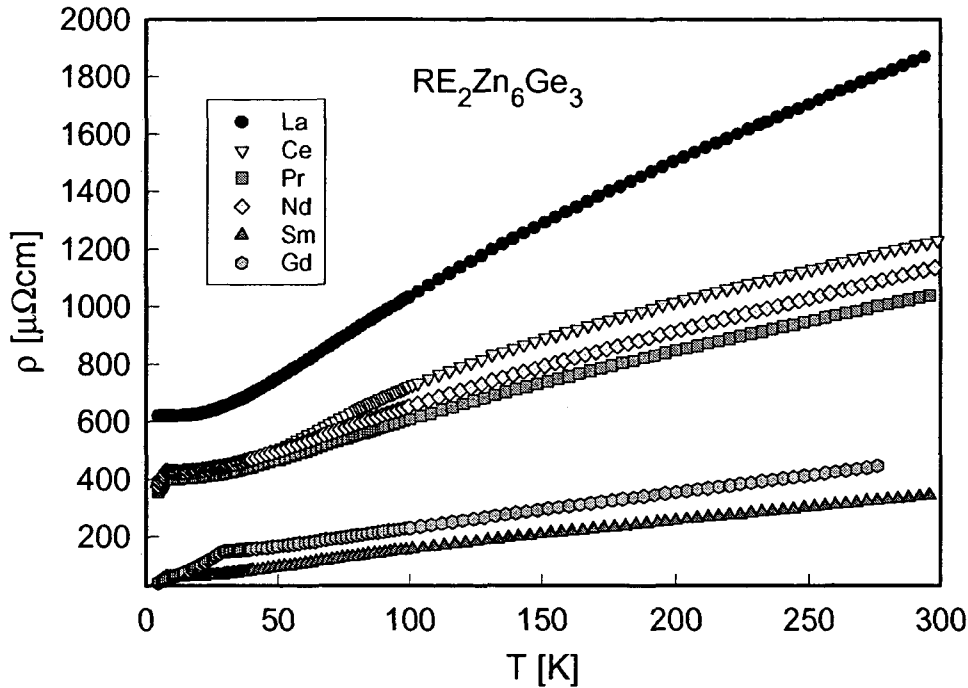
Figure 4.11: Temperature dependent electrical resistivity $\rho(T)$ of RE$_2$Zn$_6$Ge$_3$.

range magnetic order, quite dissimilar slopes in S_{mag} are observed. While the entropy of Ce$_2$Zn$_6$Ge$_3$ exhibits just a slight increase, a steep rise is found for Pr$_2$Zn$_6$Ge$_3$ reaching roughly $2R\ln 4$ at 60 K. The former observation would be in line with a substantial separation of ground state and first exited multiplet, while the latter points to a first excited level quite close to the ground state.

4.4 Electrical resistivity

Electrical resistivities $\rho(T)$ of RE$_2$Zn$_6$Ge$_3$ are displayed in figure 4.11. All compounds are characterized by temperature dependencies implying metallic behavior throughout the whole temperature range. It is worth noting, that Ce$_2$Zn$_6$Ge$_3$ too exhibits purely metallic behavior from 0.5 to 300 K. Commonly a logarithmic contribution to the electrical resistivity indicating Kondo type of interactions can be deduced for Ce compounds, such hybridization effects, however, seem to be absent or of only diminished importance in Ce$_2$Zn$_6$Ge$_3$ (compare specific heat and magnetoresistance). Apart from La$_2$Zn$_6$Ge$_3$, where La does not carry magnetic moments, distinct kinks below 30 K mark the onset of long range magnetic order asserted by magnetic susceptibility measurements. No systematic trend can be observed as far
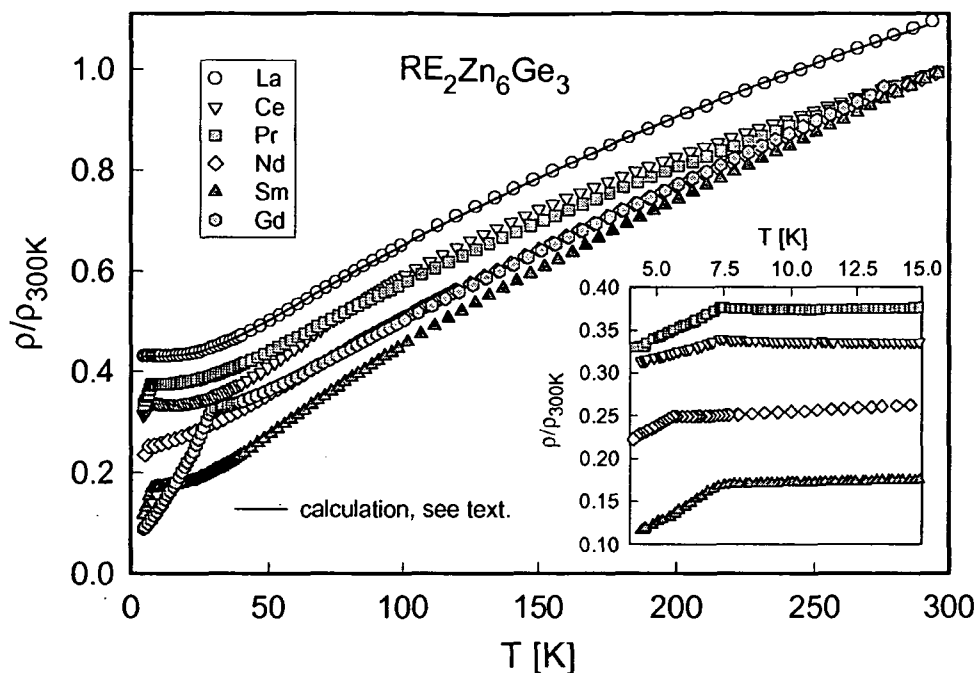
Figure 4.12: Temperature dependent electrical resistivity of $RE_2Zn_6Ge_3$ plotted in a normalized representation ρ/ρ_{300K}. For the sake of visibility the curve of $La_2Zn_6Ge_3$ was shifted by a factor of 0.1

as absolute values are concerned when proceeding through the lanthanoid series, possibly due to the samples' availability only in sintered form and the therefore pronounced grain boundary effects disguising physical actualities that would be anticipated: $^8S_{7/2}$ represents the ground state multiplet of Gd^{3+}, thus a greatly increased absolute resistivity would be expected for $Gd_2Zn_6Ge_3$ when compared to $\rho(T)$ of the La containing compound, since above the magnetic transition temperature spin disorder scattering of conduction electrons by magnetic moments is constant in the absence of CEF effects (pure S-state of Gd^{3+}), mainly determined by the de Gennes factor and generally contributes remarkably to the total electrical resistivity (compare equation 1.49 in section 1.5.1). However, the opposite is observed leading to the above conclusions, since resistivity as well as thermal conductivity, outlined in a forthcoming section, are certainly highly dependent on mechanical quality and features of the investigated sample. Overall, the absolute values except those of $La_2Zn_6Ge_3$ lie below about 1200 $\mu\Omega cm$, which would, from a thermoelectric point of view, be already favorable to an increased figure of merit.

In order to be able to relate the magnetic transition temperatures ex-

tracted from magnetic measurement data to the position of the kinks in $\rho(T)$ and to more closely inspect the peculiar curvatures of the electrical resistivity of some of the samples, $\rho(T)$ is depicted in Fig. 4.12 in a normalized representation both in the low temperature and in the overall temperature range. Note, that ρ/ρ_{300K} of La$_2$Zn$_6$Ge$_3$ was shifted by a factor of 0.1 for the sake of visibility. Neglecting a slight shift of T_N towards higher temperatures in the case of Nd$_2$Zn$_6$Ge$_3$ presumably due to minor inaccuracy in temperature determination during measurement, there is convincing agreement among susceptibility- and resistivity-derived transition temperatures.

Since CEF splitting of the total angular momentum is absent in Gd$_2$Zn$_6$Ge$_3$, the linear increase of $\rho(T)$ complies with its expected temperature dependence. All other compounds behave differently with electrical resistivities deviating from linearity, a fact, which - apart from La$_2$Zn$_6$Ge$_3$ carrying no magnetic moments - is attributed to the influence of the crystal electric field. $\rho(T)$ of the latter is well accounted for in terms of a temperature independent residual resistivity ρ_0 and a Bloch-Grüneisen term (compare expression 1.47) in combination with a Mott-Jones contribution BT^3 allowing for reproduction of the strong curvature of $\rho(T)$. It is usually ascribed to enhanced s-f scattering of the conduction electrons and determined by the density of f-states at the Fermi energy [28, 29]. Note, that an additional Mott-Jones contribution sufficiently reproducing $\rho(T)$ generally conceals the parameters derived resulting in hardly interpretable results since its impact on the least-squares fit is of great significance and its physical applicability in a certain material less than obvious. The solid line in Fig. 4.12 represents the least-squares fit to the data of La$_2$Zn$_6$Ge$_3$ revealing a Debye temperature Θ_D of 175 K. The deviation from the value of roughly 125 K deduced from specific heat data arises from the different definitions of latter physical quantity in the context of specific heat and electrical resistivity and possibly mainly from the required addition of the Mott-Jones T^3 term in order to obtain convincing fitting results.

4.4.1   Magnetoresistance

Figures 4.13-4.16 show temperature dependent electrical resistivities measured in various externally applied magnetic fields of up to 12 T (a) as well as reduced resistivities $\rho(B)/\rho(0)$ as functions of the magnetic field μ_0H (b). Common to the samples under investigation, namely RE$_2$Zn$_6$Ge$_3$ with RE=Ce, Pr, Nd and Sm, an overall increase of the absolute electrical resistivities is observed as the external magnetic field is raised from 0 to 12 T. In general such a trend is expected and referred to as classical magnetoresistance (compare section 1.5.1).

Whereas the pronounced anomaly indicating the onset of long range magnetic order is already greatly smeared at a field of 4 T in the case of the Ce

Figure 4.13: Temperature dependent electrical resistivities in various externally applied magnetic fields (a) and reduced isothermal resistivities $\rho(B)/\rho(0)$ of $Nd_2Zn_6Ge_3$.

Figure 4.14: Temperature dependent electrical resistivities in various externally applied magnetic fields (a) and reduced isothermal resistivities $\rho(B)/\rho(0)$ of $Sm_2Zn_6Ge_3$.

and Pr containing compounds, it remains apparent up to at least 8 and 10 T in Nd$_2$Zn$_6$Ge$_3$ and Sm$_2$Zn$_6$Ge$_3$, respectively. This observation would be in accordance with the elevated paramagnetic Curie temperatures deduced for the latter samples, since the paramagnetic Curie temperature θ_p is considered a measure for the magnetic interaction strength between localized magnetic moments. Neglecting the influence of CEF effects in the determination of θ_p, high values correspond to greater interaction strength, stronger fields are therefore necessary to influence long range magnetic order. Especially in the case of Sm ($\theta_p = -58$ K), this assumption may explain the non-vanishing magnetic phase transition even in a field of 10 T and the only minor shift of T_N towards lower temperatures with increasing fields. In contrast, a distinct decrease of T_N in combination with smearing above 6 T is observed for Nd with $\theta_p = -8.56$ K. The disappearing sign of onset of long range magnetic order in $\rho(T)$ at lower fields in Ce$_2$Zn$_6$Ge$_3$ and Pr$_2$Zn$_6$Ge$_3$ may also, to some extent, be attributed to the polycrystalline character of these materials.

An other interesting feature evident from the selected representation of the zero-field resistivity curves of Ce and Pr samples in figures 4.15a and 4.16a, is the minimum in $\rho(T)$ just above the respective magnetic ordering temperature. Such observations are common to both ferromagnetic and antiferromagnetic materials. In the former case, applying for Ce$_2$Zn$_6$Ge$_3$, the minimum originates from critical magnetic fluctuations in a range just above T_C, that tend to maintain limited order among spins in small areas of the lattice containing comparatively few spins. These processes are of dynamic nature in a way, that in this temperature range assemblies of ordered spins continuously form and dissolve in different parts of the lattice. The characteristic curvature above T_N of antiferromagnetic materials, on the other hand, is understood in terms of superzone boundary effects describing the introduction of new periodicities into the lattice due to the antiferromagnetic alignment of the spins producing an additional magnetic Brioullin zone differing from that of the lattice. Especially in the case of Pr$_2$Zn$_6$Ge$_3$, where two spin-up planes and one spin-down plane alternate, the appearance of a magnetic Brioullin zone is most plausible.

Isothermal magnetization measurements led to the assumption of ferromagnetic order in Ce$_2$Zn$_6$Ge$_3$. Least-squares fits to the electrical resistivity data given in Fig. 4.15 were applied below T_C, since in general $\rho(T)$ should then follow a T^2 dependence [32, 33]. The results listed in table 4.4 support a ferromagnetic solution considering a zero-field exponent of 1.95, which is close to the theoretically expected value of 2. However, with increasing magnetic field the parameter n augments rapidly reaching 2.91 at 6 T, a fact rather pointing to some type of canted or non-collinear type of magnetic order. Interpreting these findings, one should also keep in mind the limited temperature range covered by the fitting procedure due to the magnetic phase transition
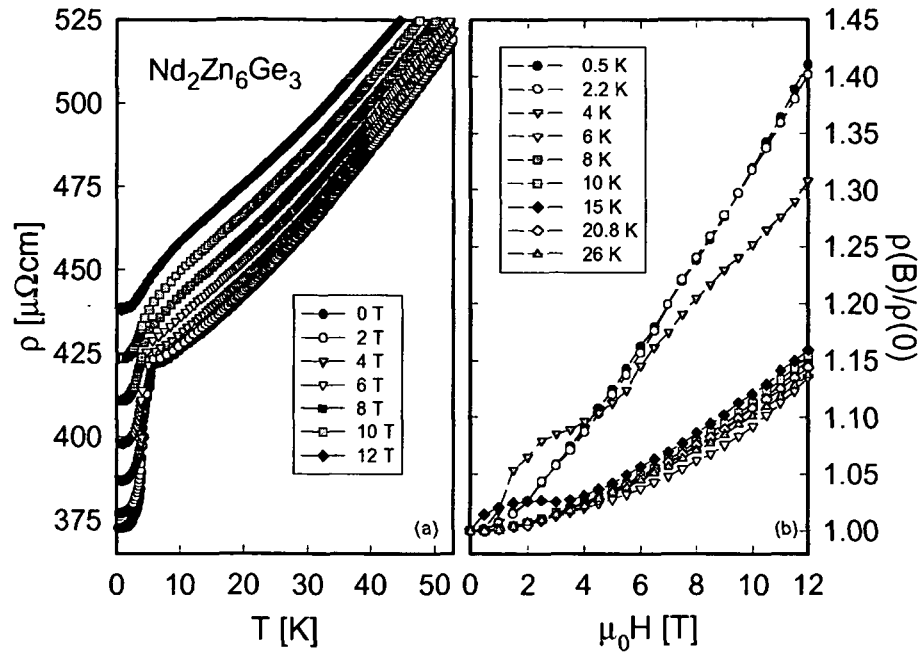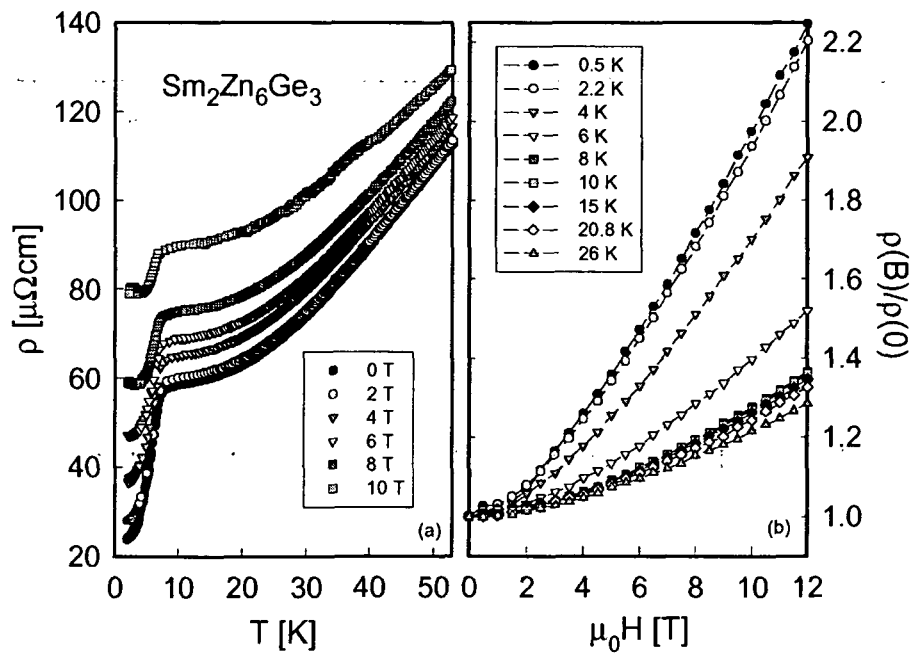
Figure 4.15: Temperature dependent electrical resistivities in various externally applied magnetic fields (a) and reduced isothermal resistivities $\rho(B)/\rho(0)$ of $Ce_2Zn_6Ge_3$.
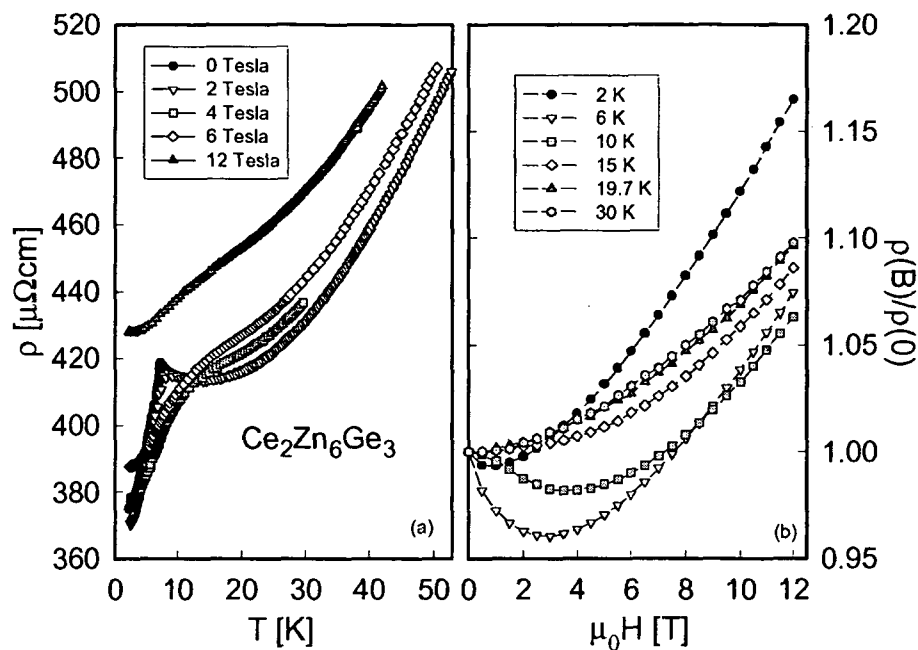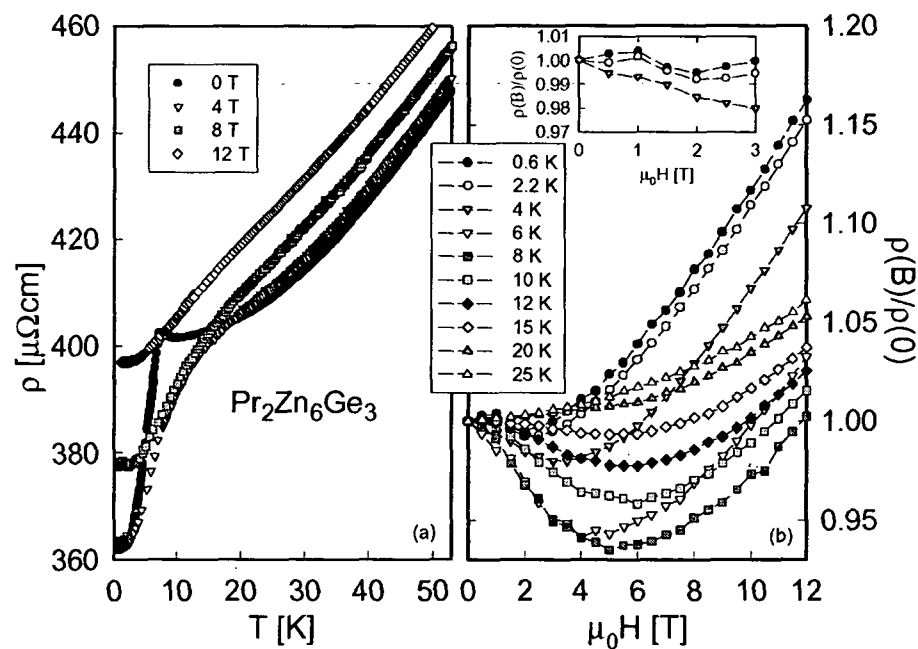

Figure 4.16: Temperature dependent electrical resistivities in various externally applied magnetic fields (a) and reduced isothermal resistivities $\rho(B)/\rho(0)$ of $Pr_2Zn_6Ge_3$.

μ_0H [T]	A [$\mu\Omega$cm/K^n]	n
0	0.9953	1.95
2	0.7132	2.16
4	0.1196	2.63
6	0.0499	2.91

Table 4.4: Parameters A and n deduced employing least-squares fits to the electrical resistivity curves of Ce$_2$Zn$_6$Ge$_3$ below 6 K in various external magnetic fields according to the expression $\rho(T) = \rho_0 + AT^n$.

at a temperature of as low as about 7 K.

Reduced isothermal resistivity curves $\rho(B)/\rho(0)$ of Nd$_2$Zn$_6$Ge$_3$ and Sm$_2$Zn$_6$Ge$_3$, depicted in figures 4.13b and 4.14b, with values above unity clearly resemble those typical of antiferromagnetic materials as outlined in section 1.5.1. For both compounds the strong, almost linear rise with increasing fields at temperatures below the onset of magnetic order is significantly flattened at temperatures above 8 K, further increasing the temperature, no dramatic change in slope and absolute values is observed. The distinctly differing devolution of $\rho(B)/\rho(0)$ taken at 4 K of the Nd sample most probably is of non-physical origin, since the curves at 0.5 and 2.2 K lack any similar signs of field-induced spin re-orientations, although isothermal magnetization data discussed above propose spin-flip processes at an external magnetic field of roughly 2-3 T.

As for Ce$_2$Zn$_6$Ge$_3$, the magnitude of $\rho(B)/\rho(0)$ rules out any hybridization effects between Ce ions and conduction band or generally Kondo type of interactions, since such mechanisms are known to cause large negative values of the magnetoresistance, which, in the representation chosen within this thesis, would correspond to values substantially below unity [228]. The overall field response of Ce$_2$Zn$_6$Ge$_3$ is of complicated nature. Magnetoresistance is essentially positive ($\rho(B)/\rho(0) > 1$) at 2 K, whereas $\rho(B)/\rho(0)$ stays below 1 at 6 to 10 K and fields below 8 T, which can be understood, if quenching of already mentioned spin fluctuations around T_C is considered. Above 10 K positive magnetoresistance is found for all fields applied. Since reduced resistivity values greater than 1 in the magnetically ordered temperature regime usually point to antiferromagnetism, isothermal magnetization taken at 2 K however reveals a ferromagnetic type of behavior with rapid saturation already in a field of 1 T, the observed field dependence of $\rho(B)/\rho(0)$ of Ce$_2$Zn$_6$Ge$_3$ can only be conceived assuming a complicated, possibly non-collinear ferromagnetic structure. The deviation of the low temperature resistivity from a T^2-behavior illustrated in a previous paragraph corroborates this conclusion.

The fully ferromagnetic state would then be achieved at higher fields than available (μ_0H>12 T).

$Pr_2Zn_6Ge_3$ exhibits a similarly complex field dependence of $\rho(B)/\rho(0)$. This is most probably due to the specific antiferromagnetic structure proposed for this compound characterized by repeated stacking of two spin-up and one spin-down planes and also due to the polycrystalline material in contrast to neutron diffraction measurements, where single crystals were used. $\rho(B)/\rho(0)$ is mainly positive for temperatures below 4 K and fields above 6 T. The low field response of $Pr_2Zn_6Ge_3$ (see inset of Fig. 4.16b) shows a slight increase at temperatures up to 2.2 K and a field of 1 T followed by negative magnetoresistance up to 3 T. This change of slope could be attributed to some type of spin re-orientation also evident from isothermal magnetization data. However, $\rho(B)/\rho(0)$ stays below 1 between 6 and 12 K, a fact generally inconsistent with long range antiferromagnetic order at least below T_N. At temperatures above 15 K magnetoresistance is positive in the whole field range.

4.5 Thermopower

The most important but nevertheless least predictable and governable property of thermoelectric materials is the thermopower since entering the figure of merit quadratically. In contrast to electrical resistivity and thermal conductivity, transport phenomena, that are highly sensitive to mechanical characteristics of a certain sample, thermopower is determined mostly by intrinsic properties regardless of mechanical quality or shape of the material. The experimentally obtained Seebeck coefficients thus represent 'final' values only modified by improving sample quality etc. to a small extent, while resistivity and thermal conductivity may still be moderately adjustable.

Fig. 4.17 displays the absolute Seebeck coefficients $S(T)$ of $RE_2Zn_6Ge_3$ as a function of temperature. Apart from $Gd_2Zn_6Ge_3$, where the s-type change of slope in $S(T)$ around 30 K reflects the onset of long range magnetic order, all other samples show little structure up to room temperature independent of the magnetic state of the particular rare-earth element incorporated. Negative values between -14 and -22 μV/K, indicative of electrons mainly governing electronic transport, are reached at room temperature staying well below those of state of the art thermoelectric materials or other promising candidates for future thermoelectric applications, where at least an absolute thermopower of 100 μV/K can be confirmed.

$S(T)$ of $Ce_2Zn_6Ge_3$ does not show any unique features expected for Ce compounds, where physical ground state properties are dominated by Kondo type of interactions. Large Seebeck coefficients in a temperature range comparable to the characteristic temperature of the system are usually observed
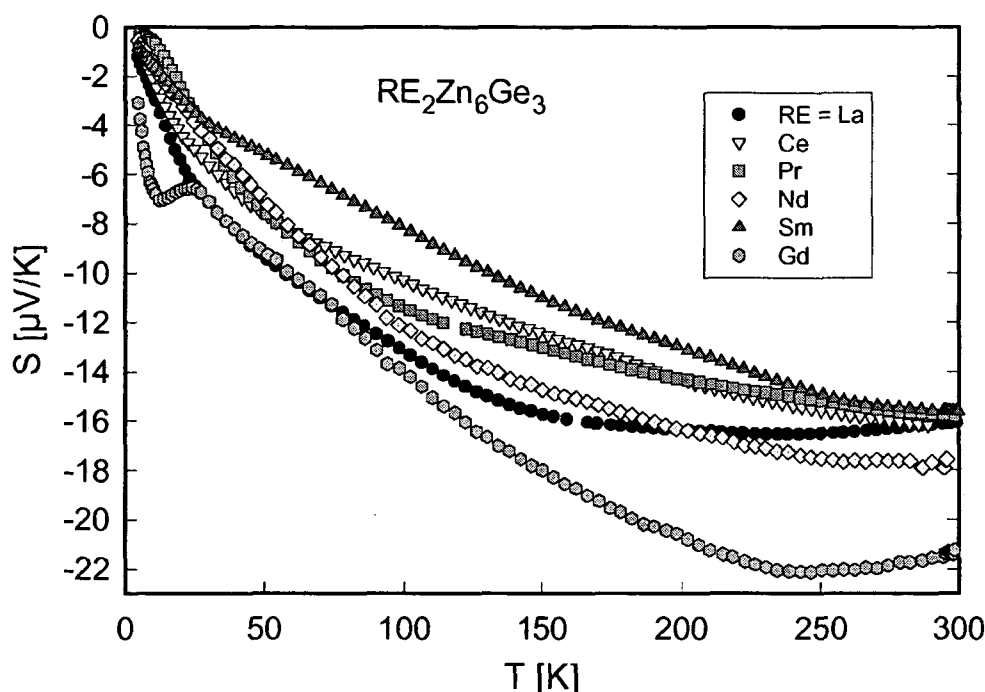
Figure 4.17: Temperature dependent thermopower $S(T)$ of RE$_2$Zn$_6$Ge$_3$.

[197] in addition to sign changes and distinct minima of the thermopower, if the particular material undergoes a magnetic phase transition [198]. The two Kondo compounds CePtSn and CePdSn e.g., both exhibiting long range antiferromagnetic order below 7 K similar to Ce$_2$Zn$_6$Ge$_3$, perfectly match above theoretical predictions with maxima in $S(T)$ around their Kondo temperatures in combination with sign changes and minima at temperatures well above the onset of magnetic order [229].

4.6   Thermal conductivity and figure of merit

The thermal conductivity of all samples was measured in the temperature range between 4 and 300 K, Fig. 4.18 displays $\lambda(T)$ as a function of temperature. The solid lines indicate results of a correction procedure accounting for heat losses due to radiation at temperatures above about 150 K previously employed for the filled skutterudite series Pr$_y$Fe$_{4-x}$(Co,Ni)$_x$Sb$_{12}$ (compare section 3.7). Again, the expected T^3 dependence of the difference between measured and corrected thermal conductivity is obeyed. It is demonstrated with respect to Pr$_2$Zn$_6$Ge$_3$ in the inset to Fig. 4.18. The overall values of $\lambda(T)$ are very low, typically in the range of 10 to 50 mW/cmK at room temperature, which would be comparable to filled skutterudites. However, thermal conduc-
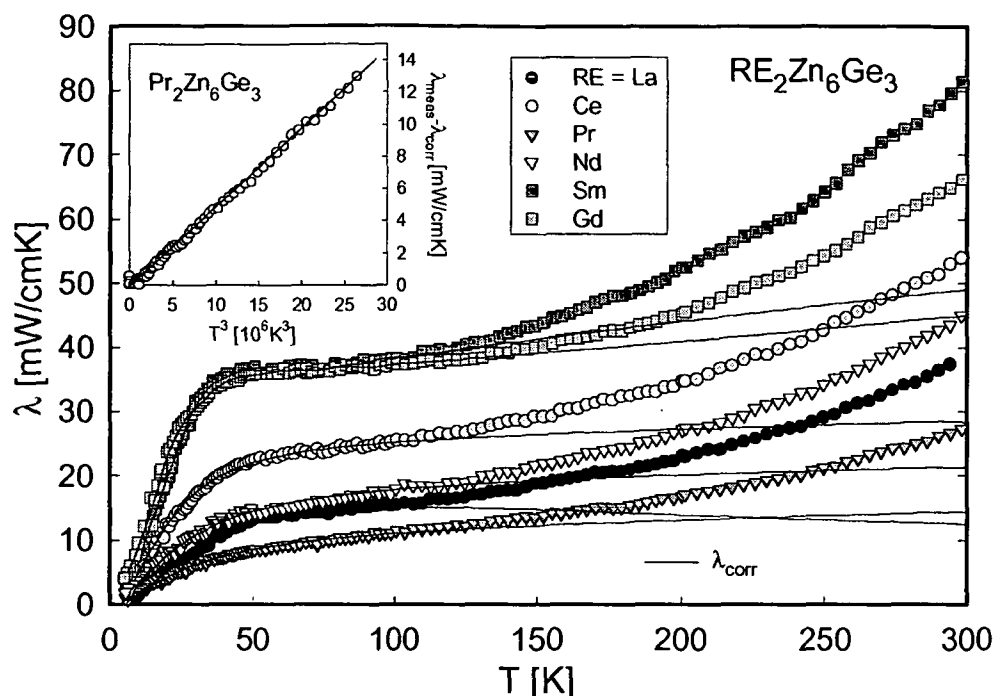
Figure 4.18: Temperature dependent thermal conductivity $\lambda(T)$ of $RE_2Zn_6Ge_3$. The solid lines indicate data corrected for heat losses due to radiation at elevated temperatures, see text. Inset: $\lambda_{meas} - \lambda_{corr}$ of $Pr_2Zn_6Ge_3$ vs. T^3.

tivity data are presumably severely influenced by pronounced grain boundary effects of the porous sintered pellets. As a consequence, irregularities arise out of line with the expected sequence inferred from an increasing magnetic scattering effect when proceeding from La to Gd. The same observations were already made analyzing electrical resistivity data, separation of lattice and electronic contribution to the total thermal conductivity by applying the Wiedemann-Franz relation did thus not yield meaningful outcome.

Nevertheless, calculation of the figure of merit ZT of $RE_2Zn_6Ge_3$ allows for an estimation of the thermoelectric performance, because overall magnitudes of both electrical resistivity and thermal conductivity are at least well defined by the available data. Due to the small Seebeck coefficient the figure of merit does not even come close to values known for e.g. skutterudites or also clathrates, ZT stays below 0.01 in the whole temperature range clearly disqualifying the series $RE_2Zn_6Ge_3$ for consideration as candidate for future thermoelectric applications.

Chapter 5

Clathrate I Si and Ge phases

5.1 The clathrate material system

'Clathrate' derives from Latin 'clathratus', 'furnished by a lattice'. Wells et
al. [230] defined clathrate materials as inclusion complexes, in which particles
of one substance are completely enclosed in cavities formed by the crystal lat-
tice or present in large molecules of another substance, i.e., the crystal takes
in foreign molecules during growth, that cannot escape until the crystal is
decomposed. Davy [231] first mentioned the formation of clathrates on the
basis of crystalline water complexes with inclusion molecules such as Cl_2 -
so-called gas hydrates or ice clathrates, since gas molecules are entrapped in
crystalline H_2O. Ice clathrates are thus characterized by a hydrogen-bonded
framework similar to that of normal ice, but with a more open structure con-
taining different types of cavities enclosing atoms or molecules. The crystal
structure was determined by von Stackelberg [232], Clausen [233] and Pauling
and Marsh [234], the formation of two types of clathrates was reported, type I
and type II. Now, 9 different clathrate structures are known, type I-IX, which
were attempted to be classified by Jeffrey [235], yet, types IV, V, VIII and
IX lack any representatives among hydrate based clathrates, see below.

In 1965 Kaspar et al. [236] and later Gallmeier et al. [237] and Cros et al.
[238] succeeded in synthesizing clathrate compounds on the basis of Si and
Ge. The latter occupy the H_2O positions known from ice clathrates forming
extended three-dimensional frameworks with huge voids, that may be filled
by alkaline atoms - type I clathrates according to the formula $M_8^I X_{46}^{IV}$ and
type II clathrates $M_{24}^I X_{136}^{IV}$ with M=Na, K, Rb and X=Si, Ge, Sn. Ternary
derivatives of clathrate I, $M_8^{II} B_{16}^{III} X_{30}^{IV}$ (M^{II}=Sr, Ba; B^{III}=Al, Ga, In and
X^{IX}=Si, Ge), were discovered by Schuster and Westerhaus et al. [239, 240]
with respect to X-atom/group-III element substitution. Whereas $Ba_8 M_8 Ge_{38}$
with M=Zn, Cd and In also adopts type I structure, $Ba_8 Ga_{16} Sn_{30}$ was found
to crystallize in the new clathrate framework structure type VIII [241, 242].

Type I clathrates generally show metallic behavior, whereas the semiconducting properties of Si or Ge are maintained in type II clathrates, however, highly dependent on the filling fraction of the voids [238]. It is thus more appropriate to label clathrate II by the formula $M_x^I X_{136}^{IV}$. Little alkaline metal element concentrations are sufficient to drive those materials from semiconducting into metallic state. Substitution, on the other hand, is able to compensate for the additional electrons donated by the filler element [243]. Charge compensation in substituted clathrate compounds may be also obtained by vacancy formation in the X-atom (Si, Ge, Sn) sublattice, since donor-acceptor interactions between alkaline and substituted atoms in the case of full charge compensation might lead to a semiconducting state approaching the band structure of pure Ge. Simple stoichiometric rules were proposed for the defect phases [244]: $Ba_8Cd(Zn)_xGe_{42-1/2x}\square_{4-1/2x}$, where $4 < x < 8$, and $Ba_8In_xGe_{42-3/4x}\square_{4-1/4x}$ with $4 < x < 16$. $\square$ denotes a void in the Ge framework.

Furthermore, transition element substitution such as in $Ba_8T_yS_{6-y}(Si,Ge)_{40}$ with T=Ni, Pd, Pt, Cu, Ag and Au [245] gives rise to superconductivity, compare e.g. $Ba_8T_xSi_{46-x}$ (T=Cu, Ag, Au), $(Na,Ba)_8Si_{46}$ and $Ba_8Ga_{16}Ge_{30}$ [246, 247, 248]. A ferromagnetic ground state with a transition temperature of 10 K was revealed for $Ba_8Mn_2Ge_{44}$ [249]. $Eu_8Ga_{16}Ge_{30}$ also exhibits long range ferromagnetic order, divalent Eu fills the guest sites in the latter [250, 251, 252, 253]. $Eu_8Ga_{16}Ge_{30}$ is particularly interesting because of the fact, that it forms both in clathrate I and clathrate VIII structure. It undergoes a phase transformation from low-temperature α-$Eu_8Ga_{16}Ge_{30}$ to high temperature β-$Eu_8Ga_{16}Ge_{30}$ at about 696°C, long range magnetic order sets on at 10.5 and 36 K in former and latter case, respectively [254]. Synthesized via transport reactions, semiconducting $X_8A_8Ge_{38}$ with X=Cl, Br, I and A=P, As, Sb was pointed out to crystallize in the clathrate I structure as well [72]. Just recently Ba_6Ge_{25-x} and isotopic Ba_6Ge_{23} and $Ba_6In_3Ge_{22}$ were discovered adopting a crystal structure derived from type I [255, 256, 257], the chiral clathrate structure IX, which was first mentioned for $Ba_6In_4Ge_{21}$ [258], while Shatruk et al. [259] reported on superstructure formation to clathrate type I in defect $Sn_{14}In_{10}P_{21.8}I_8$. Compounds crystallizing in the type III structure are $A_{30}Na_{1.33x-10}Sn_{172-x}$ (A=Cs, Rb), three clathrates could be obtained according to this formula, namely $Cs_{30}Na_{2.5}Sn_{162.6}$, $Cs_{30}Na_{2.9}Sn_{162.3}$ and $Cs_{13.8}Rb_{16.2}Na_{2.8}Sn_{162.4}$ [260] - the apparently very narrow stoichiometry range provoked the authors to assume the chemical formula $Cs_{30}Na_3Sn_{162}$. Summarizing, intermetallic clathrates only adopting clathrate I, II, III and VIII and IX type of structures have been successfully synthesized and characterized so far, whereas hydrates seem to lack members of the IV, V, VIII and IX types. Overall more than 110 intermetallic compounds have been reported on, the majority of which belonging to the clathrate structure of type I.

From a chemical point of view, hydrate and intermetallic clathrates behave quite differently. Week van der Waals bonds between hydrogen and oxygen atoms are responsible for rather unstable ice clathrates, slight heating or low pressure is sufficient to initiate decomposition. On the other hand, the stability of intermetallic clathrates against chemical reagents can be attributed to the covalent bonds among Si/Ge framework atoms. For both ice clathrates and their intermetallic derivatives, the guest atoms within the large cavities form bonds to the whole cage avoiding direct bonding to certain atoms of the framework [261, 262].

Due to this 'shared interaction' mechanism, formation is mainly possible with alkaline and alkaline earth atoms as inclusion atoms. Eu represents an exception arising from its very stable 4f configuration, other filler atoms with p, d or f outer electrons, able to establish direct bonding, inhibit formation of the clathrate structure.

Already as early as in 1981 several authors mentioned smaller magnitudes and anomalous temperature dependencies of the thermal conductivities of ice clathrates incorporating molecules or atoms within their cavities compared to pure ice [263, 264], the same applies for intermetallic clathrates [265, 266, 267, 268, 269]. Similar temperature dependencies are generally considered typical for amorphous or glass-like solids. The filler atom in clathrates supposedly performs strongly localized vibrations distinctly detached from the host framework and therefore interfering with the normal modes of the lattice and thus reducing the overall lattice thermal conductivity. The impact of the atom or molecule residing in the cavities of the structure is comparable to that of the filler element in skutterudite compounds, which lead to an increasing effort in material research in order to improve the thermoelectric performance and to elucidate the issue of viability of the PGEC concept in clathrate intermetallics (PGEC ... phonon-glass electron-crystal, proposed by Slack [5], compare section 3.1.2). In fact, Blake et al. [270], who approached the PGEC concept with respect to clathrate $Sr_8Ga_{16}Ge_{30}$ in terms of density functional calculations providing calculated transport coefficients, showed, that Slack's concept works surprisingly well for latter compound. Furthermore, the calculated physical quantities were found to be in good agreement with the experimentally deduced ones. The Sr atoms can indeed be considered loosely bound rattling atoms in their large cages, the authors found evidence for only a little charge transfer between Sr and framework atoms, to a first approximation, the former can be assumed electronically neutral. Electrical conductivity and Seebeck coefficients arise from bands, that originate from electron densities located around the framework atoms. Although a number of Sr based bands lie near the Fermi energy, the contribution of which to conductivity as well as thermopower is negligible. From these findings Blake et al. concluded Sr to be able to scatter phonons without affecting the electronic

properties of $Sr_8Ga_{16}Ge_{30}$, a proof for the viability of the PGEC concept in clathrate intermetallics. The main part of investigations performed on clathrate compounds focused on their prospective thermoelectric properties, above mentioned $Sr_8Ga_{16}Ge_{30}$ e.g., exhibits Seebeck coefficients approaching $-320\mu V/K$ at 300 K [243], the figure of merit amounts to $ZT = 1.05$ above 700 K, values of comparable magnitude were obtained for $Ba_8Ga_{16}X_{30}$ (X=Si, Ge, Sn) [271].

The following sections are devoted to the crystal structure of clathrate intermetallics as well as to a systematic ordering scheme proposed for all known clathrate structures on the basis of a clathrate structure tree rooting at a simple Ge or Si sublattice. Physical properties and thermoelectric features of the prepared samples, framework-deficient solid solutions $Ba_8Al_xSi_{42-3/4x}\square_{4-1/4x}$ and $Ba_8Ga_xSi_{42-3/4x}\square_{4-1/4x}$ with $x = 8, 12, 16$ as well as $Ba_8Cu_4Si_{42-x}Ga_x$ ($x = 0$, 4, 6, 8), $Ba_8In_{16}Ge_{30}$ and rare earth substituted clathrates $Eu_{2-x}(Sr,Ba)_{6-x}M_ySi_{46-y}$ with M=Cu, Al and Ga, are presented subsequently.

5.2 Crystal structure and clathrate ordering scheme

Focusing on intermetallic clathrates, the main structural unit of clathrate I, II, III, VIII and also IX type of structures is a pentagonal Ge_{20} dodecahedron (5^{12}). Note, that framework atoms are referred to as Ge only in the following. The pentagonal Ge_{20} dodecahedron is depicted in Fig. 5.1 together with the other basic structural building blocks, which, arranged differently or distorted, result in the 5 different types of intermetallic clathrates all belonging to the cubic system. The unit cell of type I, standardized $Ba_8Al_{16}Ge_{30}$ type of structure, space group $Pm\bar{3}n$, No. 223 [223], comprises 2 pentagondodecahedra, each creating a void with $\bar{3}m$ symmetry, that are isolated and mutually connected through 6 face-sharing Ge_{24} tetrakaidecahedra ($5^{12}6^2$). The latter are formed by 12 pentagonal and 2 hexagonal faces building voids with $\bar{4}m2$ symmetry. Since the samples prepared within this thesis all belong to clathrate I structure, the latter is displayed in figs. 5.2 and 5.3 on the basis of two different representations chosen in order to illustrate the position of the two main structural units - isolated Ge_{20} dodecahedra face-connected to channels of Ge_{24} tetrakaidecahedra (the respective polyhedra are shaded in the figures). In contrast, the 16 Ge_{20} dodecahedra per unit cell are in direct contact in clathrate type II, space group $Fd\bar{3}m$, No. 227, where layers of pentagonal dodecahedra are packed along the threefold cubic axis with 8 larger Ge_{28} hexakaidecahedra ($5^{12}6^4$, center with $4\bar{3}m$ symmetry) situated between those layers [238]. As pointed out above, type II compounds may be

pentagondodecahedron   tetrakaidecahedron
        5^{12} $5^{12}6^2$

clathrate VIII polyhedra
with 3 additional atoms ($\sim 3^4 4^3 5^3$)

pentakaidecahedron   hexakaidecahedron
        $5^{12}6^3$ $5^{12}6^4$
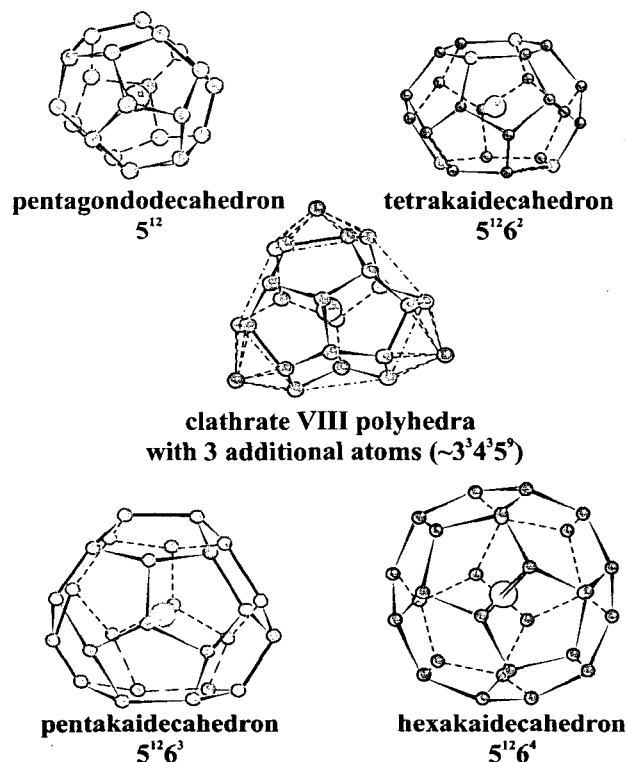
Figure 5.1: Main structural building blocks of intermetallic clathrate compounds.

synthesized non-stoichiometrically, i.e. not all the cavities according to the chemical formula have to be filled with inclusion atoms. While type III, space group $P4_2/mnm$, No. 136, is a combination of 5^{12} and $5^{12}6^2$ polyhedra as well as pentakaidecahedra ($5^{12}6^3$) [260], see Fig. 5.1, clathrate VIII primarily consists of Ge_{20} polyhedra, which are deformed and 'split' into triangles and trapezoids, the structure is accounted for in terms of space group $I\bar{4}3m$, No. 217 [241]. Pentagonal dodecahedra sharing 3 pentagonal faces with each other, arranged in a complex three-dimensional network, make up type IX (e.g. Ba_6Ge_{25}, space group P_132, No 213). Since all spaces cannot be filled therewith, two interstices exist: a Ge_{20} open cage with six pentagonal faces and 2 open square windows and a pseudo-cubic space surrounded by 8 Ge atoms [256].

Framework-deficient solid solutions $Ba_8Al_xSi_{42-3/4x}\square_{4-1/4x}$ and $Ba_8Ga_xSi_{42-3/4x}\square_{4-1/4x}$ with x=8, 12, 16 as well as $Ba_8Cu_4Si_{42-x}Ga_x$ (x=0, 4, 6, 8), $Ba_8In_{16}Ge_{30}$ and rare earth substituted clathrates $Eu_{2-x}(Sr,Ba)_{6-x}M_ySi_{46-y}$ with M=Cu, Al and Ga were prepared, x-ray intensity patterns of which were all indexed on the basis of the standardized clathrate I-$Ba_8Al_{16}Ge_{30}$ type of structure according to space group $Pm\bar{3}n$,

Figure 5.2: Clathrate I type of structure, space group $Pm\bar{3}n$, No. 223, isolated Ge_{20} pentagonal dodecahedra are shaded.

Figure 5.3: Clathrate I type of structure, space group $Pm\bar{3}n$, No. 223, channels of Ge_{24} tetrakaidecahedra are shaded.

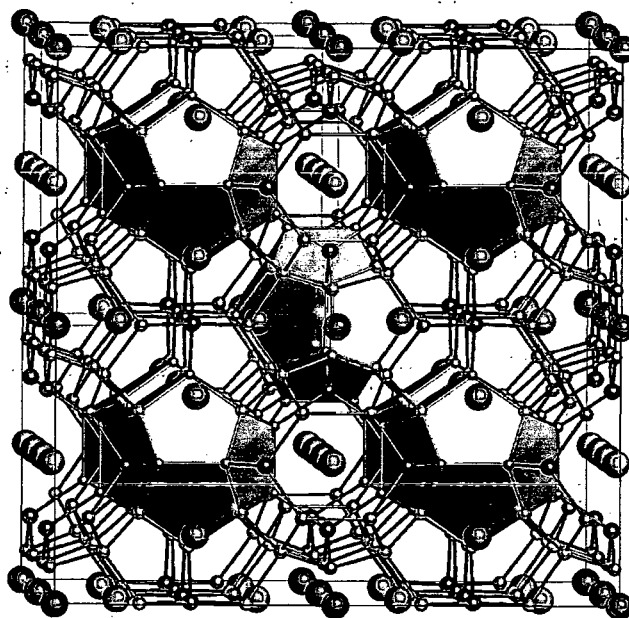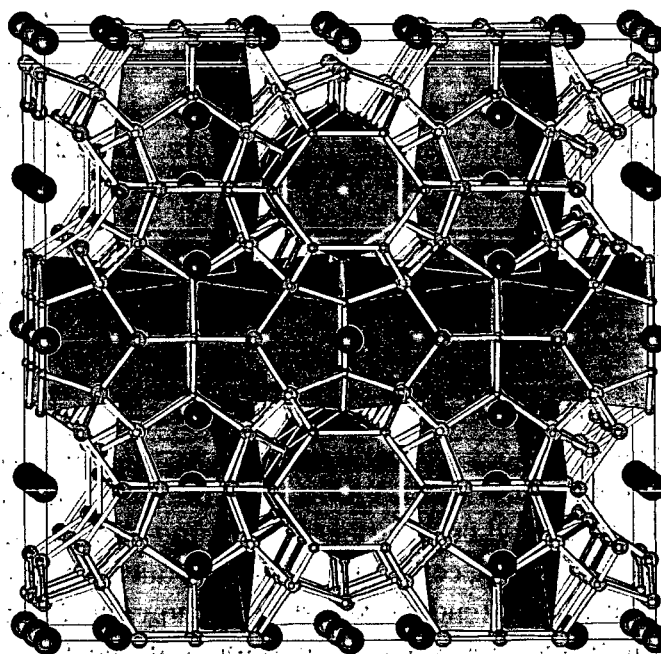| Parameter	$Ba_8In_{16}Ge_{30}$	$Ba_8Ga_{12}Si_{33}$
a [nm]	1.12177(1)	1.04861(2)
V [nm^3]	1.411	1.1530
ρ_x [Mg m^{-3}]	6.056	4.118
Reflections measured	148	125
Θ range	$15\leq 2\Theta \leq 100$	$15\leq 2\Theta \leq 100$
Number of variables	26	28
$R_F = \sum |F_0 - F_c| / \sum F_0$	0.085	0.058
$R_I = \sum |I_{0B} - I_{cB}| / \sum I_{0B}$	0.099	0.101
$R_{wP} = [\sum w_i |y_{oi} - y_{ci}|^2 / \sum w_i |y_{oi}|^2]^{1/2}$	0.107	0.091
$R_P = \sum |y_{0i} - y_{ci}| / \sum |y_{0i}|$	0.076	0.065
$R_e = [(N - P + C) / \sum w_i y_{0i}^2)]^{1/2}$	0.039	0.031
$\chi^2 = (R_{wP}/R_e)^2$	7.67	8.78
Calculated composition	$Ba_8In_{16.87}Ge_{29.13}$	$Ba_8Ga_{11.5}Si_{33.2}$

Atom parameters		
Ba1 in 2a (0,0,0)		
B_{iso} [10^2 nm^2]	0.98(5)	1.71(3)
Occupancy	1	1
Ba2 in 6d ($\frac{1}{4},\frac{1}{2}$,0)		
B_{iso} [10^2 nm^2]	3.8(1)	3.00(3)
Occupancy	1	1
M1 in 6c ($\frac{1}{4}$,0,$\frac{1}{2}$)		
B_{iso} [10^2 nm^2]	2.20(5)	1.75(5)
Occupancy	0.75In + 0.25Ge	0.8Ga + 0.2Si
M2 in 16i (x,x,x)		
x	0.18506(7)	0.1838(1)
B_{iso} [10^2 nm^2]	1.85(3)	1.65(5)
Occupancy	0.20In + 0.80Ge	0.97Si + 0.03Ga
M3 in 24k (0,y,z)		
y	0.11639(7)	0.1195(1)
z	0.30571(7)	0.3064(1)
B_{iso} [10^2 nm^2]	1.91(3)	1.50(3)
Occupancy	0.38In + 0.62Ge	0.73Si + 0.27Ga

Table 5.1: X-ray powder refinement data of $Ba_8In_{16}Ge_{30}$ and $Ba_8Ga_{12}Si_{33}$, $Ba_8Al_{16}Ge_{30}$ type of structure, space group $Pm\bar{3}n$, No. 223.

No. 223. Observations of significant deviations from centrosymmetry claimed e.g. for $Na_8(Ga,Ge)_{46}$ with space group $P\bar{4}3n$ [240] were not revealed, neither from Rietveld refinement, nor from single crystal investigations. Rietveld refinement data and results from single crystal studies of selected clathrate compounds are compiled in tables 5.1, 5.3 and 5.2.

As evident from table 5.3, substitution of Ba by the rare earth Eu seems to have a stabilizing effect on the clathrate structure. While in clathrates solely containing Ba, both 2a and 6d positions are occupied by Ba, single crystal x-ray data of the Eu containing compounds evidence full atomic order among Eu and Ba atoms. The former tend to exclusively occupy the 2a sites, the smaller voids in the Si/Ge framework, whereas Ba is found in the 6d position. Similar observations apply for $EuSr_7Al_{10}Si_{36}$. Partial (Sr,Ba)/Eu substitution thus leads to the formation of new quaternary ordered versions of the $Ba_8Al_{16}Ge_{30}$ structure type. The tendency of the rare earth to occupy the smaller voids of the structures, to reside within the Ge_{20} pentagonal dodecahedra, may be
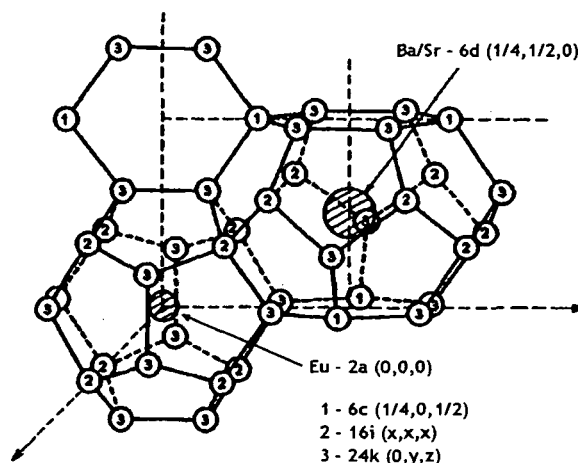
Figure 5.4: Pentagonal dodecahedra and tetrakaidecahedra in clathrate type I, the numbers indicate 6c, 16i and 24k sites of the structure occupied by the compound-dependent framework atoms.

understood considering the smaller ionic radius of Eu^{2+} (magnetic investigations revealed divalent Eu, see below), 0.204 nm, compared to that of Ba or Sr (0.224 nm and 0.215 nm). From x-ray data of $Eu_2Ba_6Cu_4Si_{42}$ the dimensions of the polyhedra were deduced to amount to $R = 0.338$ nm in the case of the roughly spherical 5^{12} polyhedra and $r_1 = 0.357$ nm and $r_2 = 0.393$ nm for the $5^{12}6^2$ tetrakaidecahedra entrapping Ba or Sr.

Fig. 5.4 depicts an isolated unit of one dodecahedron and one tetrakaidecahedron in order to illustrate positions of the different lattice sites occupied by framework atoms and filler elements. Distinguishing between Al and Si atoms in $Eu_2Ba_6Al_8Si_{36}$ was not possible during x-ray refinement due to only a difference of one electron giving rise to similar scattering power. However, Al may be identified to be situated in the 6c sites by the significantly longer interatomic distances. Even single-crystal data practically revealed full occupancy for all framework sites. Locating stoichiometric defects was not possible, although $Eu_2Ba_6Al_8Si_{36}$ is obviously stabilized by framework defects, most probably randomly distributed over the whole group IV framework, since a correct stoichiometric compound '$Eu_2Ba_6Al_8Si_{38}$' could not be obtained as single phase sample. It would thus be correct to address latter sample as $Eu_2Ba_6Al_8Si_{36}\square_2$.

The compositions of the framework-deficient solid solutions $Ba_8Al_xSi_{42-3/4x}\square_{4-1/4x}$ and $Ba_8Ga_xSi_{42-3/4x}\square_{4-1/4x}$ with $x=8$, 12, 16 and $\square$ representing lattice defects, are similar to the series $Ba_8In_xGe_{42-3/4x}\square_{4-1/4x}$ reported in [244]. In contrast to $Ba_8Cu_4Si_{42-x}Ga_x$ ($x=0$, 4, 6, 8), lattice

	Eu$_2$Ba$_6$Cu$_4$Si$_{42}$		Eu$_2$Ba$_6$Al$_8$Si$_{36}$		I$_8$Sb$_8$Ge$_{38}$	
Central atom	Ligand	Distance [nm]	Ligand	Distance [nm]	Ligand	Distance [nm]
Eu/I1	- 8Si1	3.284(2)	- 8M	3.353(2)	-8M2	3.4599(5)
	-12Si2	3.412(1)	-12Si	3.404(1)	-12M3	3.5943(8)
Ba/I2	-8Si2	3.4690(8)	-8Si	3.5551(9)	-8M3	3.6538(6)
	-4Cu	3.644(1)	-4Al	3.7106(9)	-4M1	3.8463(3)
Cu/Al/M1	-4Si2	2.387(1)	-4Si	2.503(1)	-4M3	2.5313(7)
	-4Ba	3.644(1)	-4Ba	3.7106(9)	-4I2	3.8463(3)
Si1/M/M2	-1Si1	2.357(3)	-1M	2.382(3)	-1M2	2.502(2)
	- 3Si2	2.3866(9)	-3Si	2.411(1)	-3M3	2.5233(5)
	-1Eu	3.284(1)	-1Eu	3.353(2)	-1I1	3.4599(5)
Si2/M3	-2Si1	2.3866(9)	-2M	2.411(2)	-2M2	2.5233(5)
	-1Cu	2.387(1)	-1Si	2.420(3)	-1M1	2.5313(7)
	-1Si2	2.459(3)	-1Al	2.503(1)	-1M3	2.552(1)
	-1Eu	3.412(1)	-1Eu	3.404(1)	-1I1	3.5943(8)
	-2Ba	3.4690(8)	-2Ba	3.5519(9)	-2I2	3.6538(6)

Table 5.2: Interatomic distances of Eu$_2$Ba$_6$Cu$_4$Si$_{42}$, Eu$_2$Ba$_6$Al$_8$Si$_{36}$ and I$_8$Sb$_8$Ge$_{38}$.

defects are required for charge compensation. All of these compounds may be divided into two groups, one comprising samples of the formula Ba$_8$M$_x$Ge(Si)$_{46-x}$, where transition metals of the Ni and Cu subgroups replace the framework atoms located at the 6c sites, so-called 'Cordier' phases [245] (in our case M=Cu), and the other one containing compounds with framework deficiencies subject to above mentioned stoichiometric rules. An attempt to combine these two groups of clathrates resulted in two compounds of intermediate position between group 1 and group 2, Ba$_8$Ni$_4$Ga$_{14}$Ge$_{28}$ and Ba$_8$Cu$_4$Si$_{36}$Ga$_6$. Probably, the formation conditions of the members of both groups are similar - in 'Cordier' phases the electroneutrality point is approached by substitution of group IV elements such as the Si/Ga replacement in Ba$_8$Ga$_8$Si$_{36}\square_2$, but the cavities are occupied by transition metal atoms.

Considering the distinctly reduced interatomic distances of the framework composed of Ge, Si or substituted atoms given in table 5.2 compared to the sum of the atomic radii, the expectedly mainly covalent bonds among the framework atoms are clearly revealed. On the other hand, the distances between framework and filler atoms situated in the voids provided by the polyhedra of the structure are significantly longer indicating weak interactions among host and guest atoms. The latter is in line with observations on isomorphous compounds already outlined in literature [261, 262]. This weak interaction among guest and host atoms is the origin of the large atomic displacement parameters in clathrate intermetallics and in turn gives rise to the strongly reduced thermal conductivities observed [250, 252]. Similar characteristics account for the unique transport properties of filled skutterudites, compare section 3.1.2.The lattice parameters of all compounds prepared, given in table 5.4, reveal the blow-up of the lattice upon replacement

Parameter	$Eu_2Ba_6Cu_4Si_{42}$	$Eu_2Ba_6Al_8Si_{36}$	$I_8Sb_8Ge_{38}$
Crystal size	50x28x56 μm^3	70x42x56 μm^3	28x30x90 μm^3
a [nm]	1.03068(2)	1.04951(2)	1.08790(3)
ρ_x [Mg cm^{-3}]	3.885	3.383	6.123
μ_{abs} [mm^{-1}]	11.18	8.80	30.70
Θ range	2$\leq$ 2Θ $\leq$74; 120 s/frame	2$\leq$ 2Θ $\leq$70; 60 s/frame	2$\leq$ 2Θ $\leq$72.6; 40 s/frame
Total number of frames	205	205	201
Reflections measured	390$\leq$ 4σ(F$_0$) of 528	398$\leq$ 4σ(F$_0$) of 487	531$\leq$ 4σ(F$_0$) of 592
Mosaicity	< 0.52	< 0.56	< 0.44
Number of variables	16	18	22
$R_F^2 = \sum |F_0^2 - F_c^2| / \sum F_0^2$	0.034	0.034	0.0375
R_{int}	0.068	0.069	0.068
$wR2$	0.112	0.086	0.102
GOF	1.137	1.135	1.155
Extinction (Zachariasen)	0.00299(6)	0.00124(3)	0.0023(2)

Atom parameters			
X1 in 2a (0,0,0)	2Eu	2Eu	2I1
Occupancy	1.00(1)	1.00(1)	1.00(1)
$U_{11}=U_{22}=U_{33}$	0.0166(2)	0.0166(2)	0.0138(3)
X2 in 6d ($\frac{1}{4},\frac{1}{2}$,0)	6Ba	6Ba	6I2
Occupancy	1.00(1)	1.00(1)	1.00(1)
$U_{11}=U_{22}$	0.0331(3)	0.0242(2)	0.0199(3)
U_{33}	0.0200(3)	0.0163(3)	0.0109(4)
M1 in 6c ($\frac{1}{4}$,0,$\frac{1}{2}$)	4Cu+2Si	6Al1	5.2Ge1+0.8Sb1
Occupancy	1.00(1)	1.00(1)	1.00(1)
$U_{11}=U_{22}$	0.0136(6)	0.0083(11)	0.0178(7)
U_{33}	0.0120(4)	0.0102(7)	0.0126(5)
M2 in 16i (x,x,x)	20Si1	14Si1+2Al2	12.5Ge2+3.5Sb2
x	0.18398(9)	x=0.18448(9)	0.18362(4)
Occupancy	1.00(1)	1.00(1)	1.00(1)
$U_{11}=U_{22}=U_{33}$	0.0110(3)	0.0127(5)	0.0116(2)
M3 in 24k (0,y,z)	20Si2	24Si2	20.36Ge3+3.64Sb3
y	0.1193(1)	0.1158(1)	0.11732(7)
z	0.3088(1)	0.3029(1)	0.30886(7)
Occupancy	1.00(1)	1.00(1)	1.00(1)
U_{11}	0.0127(5)	0.0134(6)	0.0135(3)
U_{22}	0.0125(5)	0.0116(6)	0.0143(3)
U_{33}	0.0108(5)	0.0134(6)	0.0142(3)
Residual density; min, max	1.61, -4.49	1.34, -3.25	1.67, -3.62
Principal mean	Eu 0.0166 0.0166 0.0166	Eu 0.0166 0.0166 0.0166	I1 0.0138 0.0138 0.0138
square atomic	Ba 0.0330 0.0330 0.0200	Ba 0.0243 0.0243 0.0162	I2 0.0199 0.0199 0.0109
displacements U	Cu 0.0136 0.0120 0.0120	Al1 0.0102 0.0102 0.0083	M1 0.0178 0.0126 0.0126
	Si1 0.0117 0.0117 0.0096	M 0.0135 0.0135 0.0112	M2 0.0117 0.0117 0.0114
	Si2 0.0129 0.0123 0.0108	Si2 0.0139 0.0134 0.0111	M3 0.0155 0.0142 0.0123

Table 5.3: X-ray single-crystal data of $Eu_2Ba_6Cu_4Si_{42}$, $Eu_2Ba_6Al_8Si_{36}$ and $I_8Sb_8Ge_{38}$, $Ba_8Al_{16}Ge_{30}$ type of structure, space group $Pm\bar{3}n$, No. 223, origin at center.

Tetrahedral four-coordinated framework formation of pentagondodecahedra $MGe_{20}(5^{12})$

+ Ge_{24} cage $(5^{12}6^2)$

+ Ge_{28} cage $(5^{12}6^4)$

+ $5^{12}6^2$, $5^{12}6^3$ polyhedra

clathrate I
K_8Ge_{46-x}
Pm3n

clathrate II
Na_xSi_{136}
Fd3m

subtraction of Ge from Ge_{24}

clathrate III
$Cs_{30}Na_{1.33x-10}Sn_{172-x}$
$P4_2/mnm$

clathrate IX
Ba_6Ge_{25}
$P4_132$

deformation of pentagondodecahedra

partial substitution of Ge by third element

clathrate IX
$Ba_6Ge_{21}In_4$
$P4_132$

clathrate VIII
$Ba_8Ga_{16}Sn_{30}$
I43m

6d site substitution only
(by transition metals: Mn, Ni, Pd, Cu, Ag, Au, Cd, Zn)

random substitution
(Al, Ga, In, Bi, Tl, Sb, As)

Clathrate-like phases
$Ba_8P_{16}Cu_{30}$

"Cordier" phases
$Ba_8Ni_6Ge_{40}$
Pm3n

8:16:30, 8:12:33, 8:8:36 phases
i.e. $Ba_8Ga_{12}Si_{33}$, $K_8Ga_8Sn_{38}$, $Ba_8Al_{16}Ge_{30}$ Pm3n

"mixed" phases, including Eu-substituted phases

Structure distortions, defect ordering ⟶ **Superstructures and distorted clathrate phases**
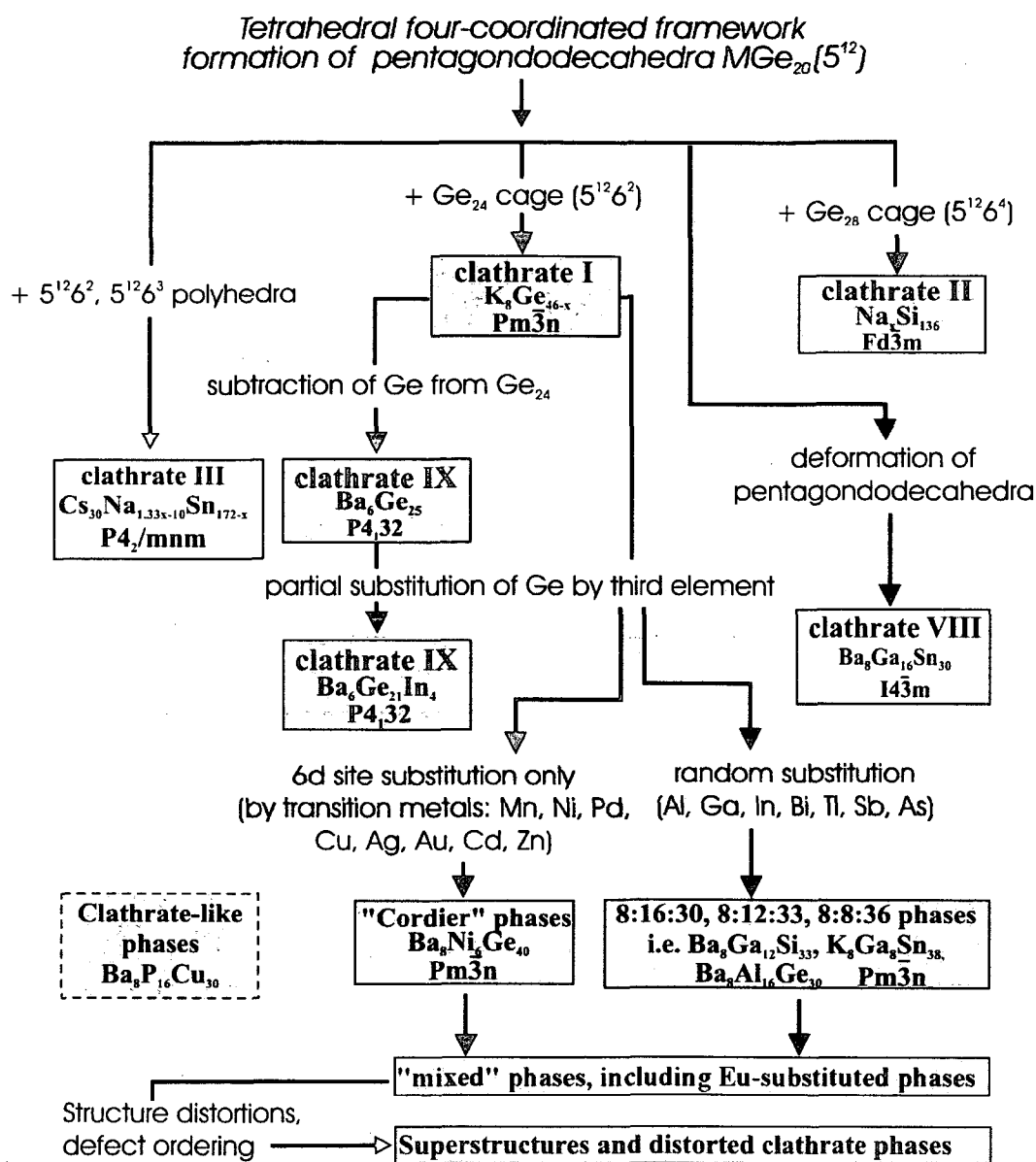
Figure 5.5: Intermetallic clathrate structure family tree. Superstructures to Sn-containing clathrates I such as observed for $Sn_{14}In_{10}P_{21.8}I_8$ [259] are not listed.

Compound	Lattice parameter [nm]	Compound	Lattice parameter [nm]
$Ba_8Cu_6Si_{40}$	$1.03278(2)^a$	$Eu_2Ba_6Cu_4Si_{42}$	$1.03053(2)$
$Ba_8Cu_4Si_{42}$	$1.03266(4)$	$Eu_2Ba_6Cu_4Si_{38}Ga4$	$1.03641(5)$
$Ba_8Cu_4Si_{38}Ga_4$	$1.03823(1)$	$Eu_2Ba_6Al_8Si_{36}$	$1.04951(2)$
$Ba_8Cu_4Si_{36}Ga_6$	$1.04038(5)$	$EuSr_7Al_{10}Si_{36}$	$1.0454(2)$
$Ba_8Cu_4Si_{34}Ga_8$	$1.04279(4)$		
		$Ba_8Al_{16}Ge_{30}$	$1.08518(1)^a$
$Ba_8Ga_8Si_{36}$	$1.04350(1)$	$Ba_8In_{16}Ge_{30}$	$1.12177(1)^a$
$Ba_8Ga_{12}Si_{33}$	$1.04705(2)$		
		$Ba_8Cu_4Ga_{20}Si_{22}$	$1.05089(6)$
$Ba_8Al_8Si_{36}$	$1.04890(1)$	$Ba_8Ni_4Ga_{14}Ge_{28}$	$1.07798(2)$
$Ba_8Al_{12}Si_{33}$	$1.05654(1)$		
$Ba_8Al_{16}Si_{30}$	$1.06285(1)^a$		

Table 5.4: Lattice parameters of all samples prepared. ^{a}Compounds already known in literature, our lattice parameters are presented.

of Si by larger group III elements such as Ga.

Since basic structural units and conventional framework packing mode are common to all intermetallic clathrate structure types, a novel systematic ordering scheme can therefore be proposed rooting at a tetrahedal four-coordinated Si or Ge framework based on formation of Si_{20} or Ge_{20} pentagonal dodecahedra, see Fig. 5.5. Whereas clathrate I requires additional $5^{12}6^2$ tetrakaidecahedra, clathrate II comprises the 5^{12} dodecahedra and $5^{12}6^4$ hexakaidecahedra. Deformation of the 5^{12} polyhedra leads to formation of clathrate VIII, while 5^{12}, $5^{12}6^2$ and $5^{12}6^3$ polyhedra are found in clathrate III. Clathrate IV is simply derived from clathrate I by subtraction of one framework atom from the $5^{12}6^2$ tetrakaidecahedra. Partial substitution of Ge or Si in type I by a third element results in the 'Cordier'- as well as defect phases and also in the rare earth substituted clathrate I type of compounds.

5.3 Magnetism in Eu substituted type I clathrates

Fig. 5.6 depicts temperature dependent inverse magnetic susceptibilities of $Eu_2Ba_6Cu_4Si_{42}$, $Eu_2Ba_6Cu_4Si_{38}Ga_4$ as well as of defect $Eu_2Ba_6Al_8Si_{36}$ and $Eu_2Ba_6Ga_8Si_{36}$ in a magnetic field of 0.1 T. Note, that in order to avoid overlap of the curves, the inverse magnetic susceptibilities $1/\chi(T)$ of the two former were shifted by additive factors of 5 and 2 mol/emu, respectively. Magnetic investigations with respect to $EuSr_7Al_{10}Si_{36}$ were not performed, since electrical resistivity data illustrated below evidence no signs of long range magnetic order at least down to 1.5 K, which also represents the lower limit of the experimentally accessible temperature range as far as magnetic measurements are concerned.
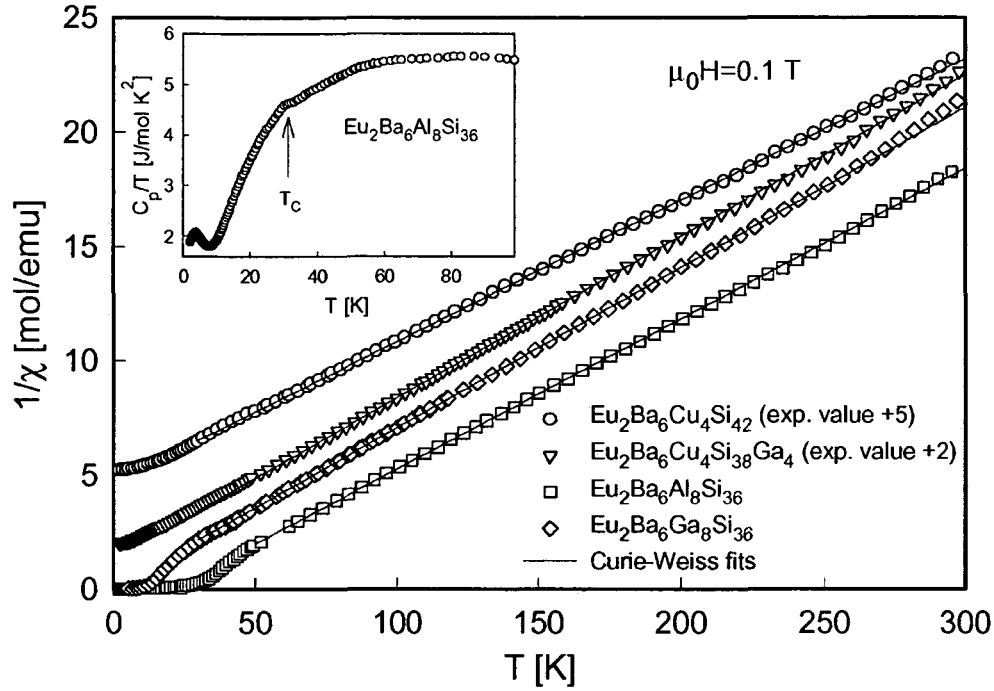
Figure 5.6: Inverse magnetic susceptibility $1/\chi$ of Eu substituted type I clathrates as a function of temperature in an externally applied magnetic field of 0.1 T. Solid lines: least-squares fits according to a modified Curie-Weiss law. Inset: Specific heat C_p of $Eu_2Ba_6Al_8Si_{36}$ plotted as C_p/T vs. T.

Above about 50 K all samples follow a simple Curie-Weiss type of behavior, which was accounted for in terms of least-squares fits according to equ. 1.76, results are denoted by the solid lines in the figure. Table 5.5 summarizes thereby deduced effective paramagnetic moments μ_{eff}, paramagnetic Curie temperatures θ_p and values of the temperature independent susceptibility contribution χ_0. Rather low paramagnetic Curie temperatures of 5.3, 9.3 K and 19.5 K indicate moderate ferromagnetic type of interactions among magnetic moments with the exception of $Eu_2Ba_6Ga_8Si_{36}$, for which a small negative Curie temperature of -1 K was derived. The calculated effective magnetic moments amount to respective values of 8.05, 7.52, 7.81 and 7.56 μ_B, which are, at least in the case of $Eu_2Ba_6Cu_4Si_{42}$ and $Eu_2Ba_6Al_8Si_{36}$, close to $\mu_{eff} = g\sqrt{J(J+1)}$ of 7.94 μ_B corresponding to the effective moment associated with free Eu^{2+} ($J = 7/2$). The significantly lower moments derived for $Eu_2Ba_6Cu_4Si_{38}Ga_4$ as well as for $Eu_2Ba_6Ga_8Si_{36}$ may be attributed to either defects in the Eu 2a sites or to the Eu ionic state differing from pure divalency.

	μ_{eff} $[\mu_B]$	θ_p [K]	χ_0 $[10^{-4}$ emu/mol]	T_C [K]
$Eu_2Ba_6Cu_4Si_{42}$	8.05	5.25	0.0008	5
$Eu_2Ba_6Cu_4Si_{38}Ga_4$	7.53	9.31	0.2058	6
$Eu_2Ba_6Al_8Si_{36}$	7.81	19.54	0.0068	32
$Eu_2Ba_6Ga_8Si_{36}$	7.56	-1	0.5471	12

Table 5.5: Effective magnetic moments μ_{eff}, paramagnetic Curie temperatures θ_p and temperature independent susceptibilities χ_0, deduced employing least-squares fits to the experimental data, as well as magnetic ordering temperatures T_C of Eu containing clathrates.

In order to undoubtedly determine the valence state of the rare earth, L_{III} absorption edge measurements were carried out for $Eu_2Ba_6Cu_4Si_{42}$ at 10 as well as 300 K and for $Eu_2Ba_6Cu_4Si_{38}Ga_4$ and $Eu_2Ba_6Al_8Si_{36}$ at room temperature. Fig. 5.7a displays the obtained spectra vs. energy of the incident x-ray beam. The spectra are essentially characterized by a single, enhanced peak centered at an energy of slightly above 6970 eV, which is in perfect agreement with the position of the absorption edge of magnetic Eu^{2+} situated at 6973 eV. If a trivalent Eu state or some type of intermediate or mixed valence applied, the emergence of a second peak centered at 6982 eV would be expected, compare e.g. Eu filled skutterudite system $Eu_yFe_{4-x}Co_xSb_{12}$ [127] or $YbPd_{1-x}Ag_xGa_2$ [90], where x-ray absorption spectroscopy revealed double peak structures, the two peaks corresponding to di- and trivalent Eu or Yb in the latter case. This proof of divalency favors defects in the Eu sites to be origin of the reduced effective magnetic moment obtained for $Eu_2Ba_6Cu_4Si_{38}Ga_4$, since polycrystalline material was used for investigations of physical properties. Furthermore, as mentioned in the last section, even based on single-crystal material, refinement of x-ray diffraction data tended to state full occupancy for all framework sites, although stoichiometric defects were present and meant such as e.g. in $Eu_2Ba_6Al_8Si_{36}$. To a similar extent, refinement may have been insufficient in locating defects in the 2a rare earth sites. Although no L_{III} data are available, similar conclusions can be drawn for $Eu_2Ba_6Ga_8Si_{36}$, any deviations from divalency of the rare earth seem very unlikely.

Anomalies in the $1/\chi(T)$ curves of all compounds at temperatures below 50 K correspond to the onset of long range magnetic order. A.c. magnetic
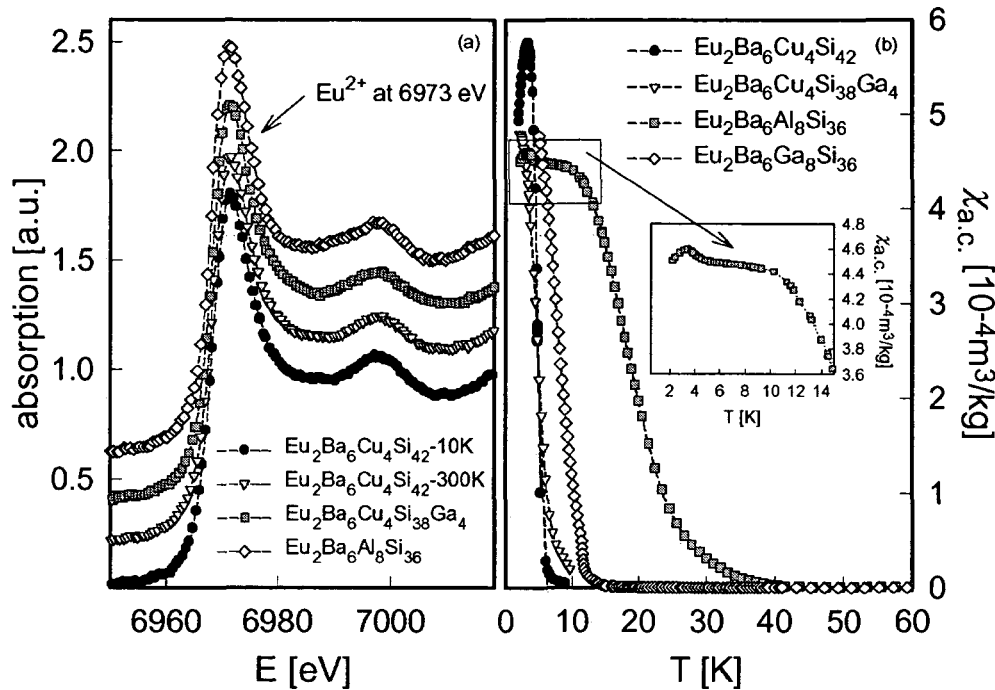
Figure 5.7: (a) Eu-L$_{III}$ absorption edge spectra of Eu$_2$Ba$_6$Cu$_4$Si$_{38}$Ga$_4$ and Eu$_2$Ba$_6$Al$_8$Si$_{36}$ taken at room temperature as well as of Eu$_2$Ba$_6$Cu$_4$Si$_{42}$ obtained at 10 and 300 K vs. energy. Data were respectively shifted towards higher absorptions for better visibility. (b) Temperature dependent a.c. magnetic susceptibility $\chi_{a.c.}(T)$ of Eu$_2$Ba$_6$Al$_8$Si$_{36}$, Eu$_2$Ba$_6$Cu$_4$Si$_{42}$, Eu$_2$Ba$_6$Cu$_4$Si$_{38}$Ga$_4$ and Eu$_2$Ba$_6$Ga$_8$Si$_{36}$. Data of the two latter compounds were respectively divided by factors of 2 and 5.

susceptibility data shown in Fig. 5.7b clearly corroborate the assumed magnetic transitions, analyses in a standard manner in combination with Arrott plots given in Fig. 5.8 reveal ordering temperatures of about 5 to 6 in the case of Eu$_2$Ba$_6$Cu$_4$Si$_{42}$ and Eu$_2$Ba$_6$Cu$_4$Si$_{38}$Ga$_4$ and 32 K and about 12 K for Eu$_2$Ba$_6$Al$_8$Si$_{36}$ and Eu$_2$Ba$_6$Ga$_8$Si$_{36}$, respectively. The low but positive Curie temperatures of the three former are in good agreement with the deduced transition temperatures, whereas θ_p of latter compound obviously does not follow this trend with a Curie temperature of close to zero. One should keep in mind, that the Curie-Weiss law cannot be accepted as irrevocable, since it is based on model assumptions in the scope of the molecular field approximation, however, as will be discussed in section 5.4, also electrical resistivity of Eu$_2$Ba$_6$Ga$_8$Si$_{36}$ is inconsistent with magnetic data, which most probably is a hint for significant sample inhomogeneities. It is interesting to more closely inspect low temperature a.c. susceptibility data of Eu$_2$Ba$_6$Al$_8$Si$_{36}$, the

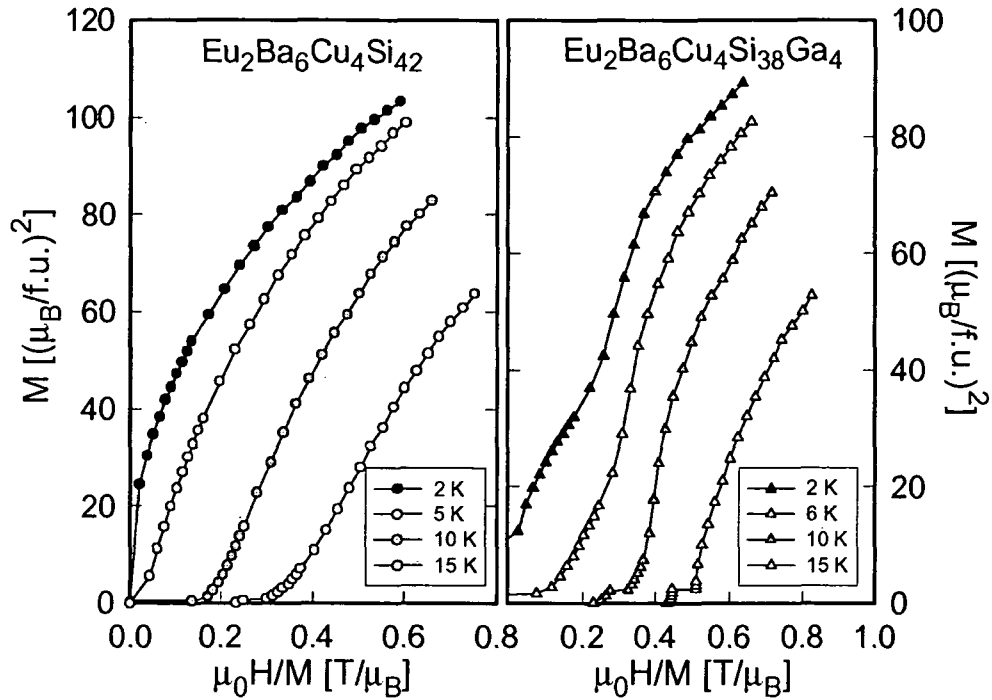Figure 5.8: Arrott plots of $Eu_2Ba_6Cu_4Si_{42}$ and $Eu_2Ba_6Cu_4Si_{38}Ga_4$.

inset of 5.7b evidences a small hump in $\chi_{a.c.}(T)$ at about 3 K superposed to the large signal originating from the magnetic transition at 32 K. This slight anomaly seems to be due to magnetic ordering of an Eu containing impurity phase. In order to validate this assumption, the inset of Fig. 5.6 presents the specific heat of $Eu_2Ba_6Al_8Si_{36}$ plotted as C_p/T vs. temperature, where the arrow in the figure indicates the magnetic transition at a temperature of roughly 32 K. At $T < 10$ K a pronounced peak with a maximum at about 3 K emerges, the position of which resembling that of the small hump observed in $\chi_{a.c.}(T)$. Taking into account specific heat exclusively and thus neglecting a.c. susceptibility results, the appearance of the anomaly at low temperatures may arise for two different reasons: an impurity phase not detected via x-ray investigations is present magnetically ordering around 3 K or the small maximum in C_p/T is referred to as a Schottky anomaly due to long range magnetic order among the Eu moments setting on at higher temperatures. The specific heat of ferromagnetic materials (no magnetization data for $Eu_2Ba_6Al_8Si_{36}$ are available, nevertheless a ferromagnetic spin arrangement is assumed by analogy to the other Eu containing clathrates, see below) can be calculated in terms of the molecular field approximation - besides the characteristic feature marking the onset of magnetic order (32 K in $Eu_2Ba_6Al_8Si_{36}$), an additional change of the curvature of the specific heat

is usually induced below the magnetic ordering temperature originating from lifting of the ground state degeneracy caused by the immense internal magnetic field (molecular field driven Zeeman effect). The change in curvature becomes stronger with the number of energy levels existent, thus for increasing total angular momentum J [272]. In the representation chosen, C_p/T, this characteristic feature may seem even more pronounced. However, assuming the internal Zeeman effect to be responsible for the anomaly at about 3 K would in turn imply a significant jump in the specific heat at T_C, since also the height of the jump is related to the magnitude of J. The high J value of Eu^{2+} ($J = 7/2$) is apparently insufficient to produce a significant jump in C_p at T_C, furthermore, the structure of the feature at 3 K is distinctly peaked, such a magnetic field induced effect is therefore rather unplausible. It has to be attributed to impurity effects instead, which also explains the slight hump in $\chi_{a.c.}(T)$ at the same temperature of about 3 K.

Neglecting $Eu_2Ba_6Ga_8Si_{36}$ in following considerations for the reason of inconsistent magnetic and electrical resistivity results mentioned above, the large difference between the ordering temperatures of the Cu containing compounds and that of $Eu_2Ba_6Al_8Si_{36}$ is somewhat surprising, since, based on computational calculations of band structure and electronic configurations with respect to $Sr_8Ga_{16}Ge_{30}$ illustrated in section 5.1, filler element and framework are only loosely bound and electronically to some extent independent from each other. Taking into account the localized character of the 4f configuration of Eu^{2+} and the significant interatomic distances among Eu ions (> 1 nm), the RKKY mechanism is responsible for indirect interactions between Eu moments via conduction electron system and consequently for the alignment of spins and onset of long range magnetic order. Neglecting any compositional influence of the framework atoms on the band structure, the 2% smaller unit cell of $Eu_2Ba_6Cu_4Si_{42}$ compared to that of $Eu_2Ba_6Al_8Si_{36}$ would be expected to give rise to magnetic ordering already at higher temperatures than observed due to stronger indirect interaction. The distinctly larger absolute resistivity values of the latter presented in the next section would be in line with this assumption, although one has to keep in mind the often poor sample quality strongly affecting electrical resistivity and thus complicating possible interpretations. However, the opposite is observed; magnetic order sets on at about 32 K in $Eu_2Ba_6Al_8Si_{36}$ and only at 5 to 6 K in $Eu_2Ba_6Cu_4Si_{42}$ hinting to either a pronounced impact of $(Al,\square)/Cu$ substitution on the band structure or to inhomogeneities of the prepared samples. In view of this significant composition dependence of the transition into long range magnetic order, the former is more likely.

Isothermal magnetization data of $Eu_2Ba_6Cu_4Si_{42}$ and $Eu_2Ba_6Cu_4Si_{38}Ga_4$ evidence spontaneous magnetization below the respective magnetic ordering temperatures reflecting ferromagnetic type of order for both compounds. Nei-
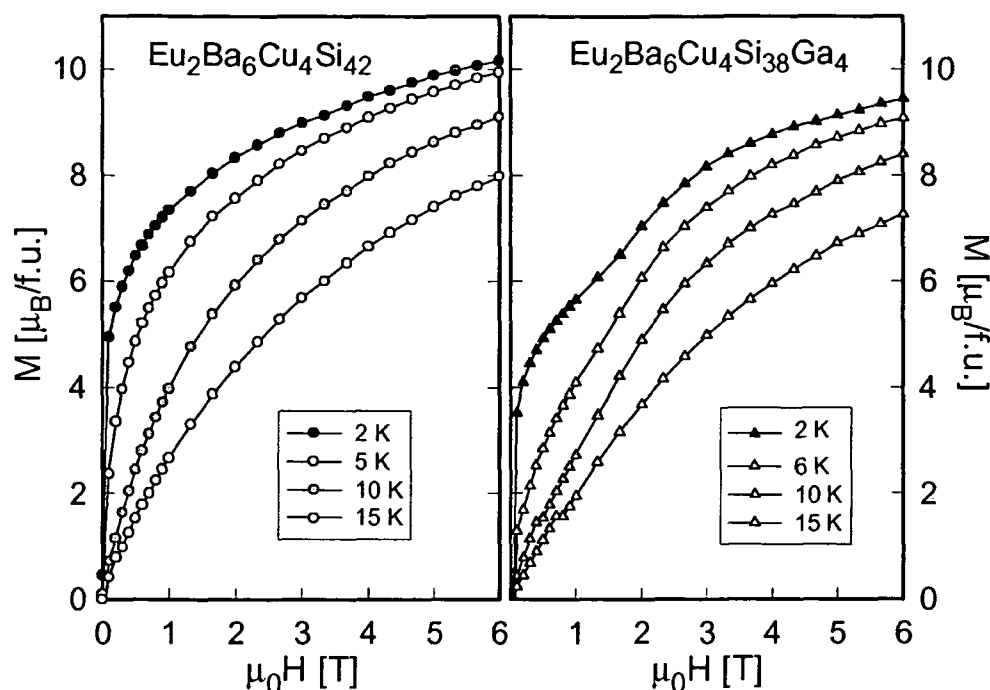
Figure 5.9:   Isothermal magnetization $M(H)$ of $Eu_2Ba_6Cu_4Si_{42}$ and $Eu_2Ba_6Cu_4Si_{38}Ga_4$ at various temperatures below and above the respective magnetic transition.

ther sample reaches full saturation at the maximum field of 6 T and the lowest available temperature of 2 K. While magnetization of $Eu_2Ba_6Cu_4Si_{42}$ amounts to about 10.2 μ_B/f.u. at 6 T, M of $Eu_2Ba_6Cu_4Si_{38}Ga_4$ yields a slightly lower value of 9.4 μ_B/f.u. In both cases, the experimentally deduced quantities, 5.1 and 4.7 μ_B per Eu ion are far below the theoretical saturation magnetization of 7 μ_B arising from divalent Eu. Since Eu^{2+} resembles the electronic configuration of Gd^{3+} with $J = S = 7/2$ and thus possesses no angular degrees of freedom possibly interacting with the surrounding field caused by neighboring ions and charge carriers, crystal electric field effects are absent. The distinctly reduced non-saturating magnetization observed therefore has to be attributed to a peculiar ferromagnetic spin arrangement more complicated than that of a collinear ferromagnet. It rather points to some kind of canted spin alignment or ferrimagnetic order. In contrast, $Eu_8Ga_{16}Ge_{30}$ shows full saturation and a magnetization of 7 μ_B/Eu atom already at a magnetic field of 2 T indicating collinear ferromagnetic type of order [253]. Neglecting again the different framework composition, this could be due to the smaller distances among Eu ions in the latter, where the fraction of Eu amounts to 15 at.%, while Eu accounts for only about 4 at.% in $Eu_2Ba_6Cu_4Si_{42}$ and $Eu_2Ba_6Cu_4Si_{38}Ga_4$
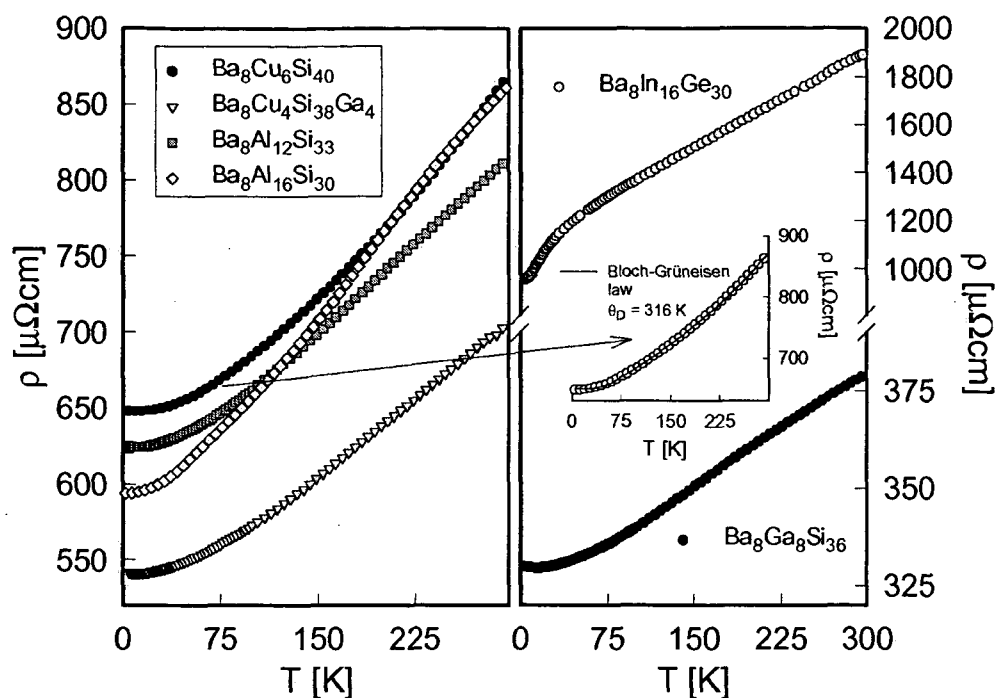
Figure 5.10: Temperature dependent electrical resistivity $\rho(T)$ of various Ba filled clathrates.

leading to significantly longer distances in the Eu sublattice.

Closely inspecting $M(H)$ of $Eu_2Ba_6Cu_4Si_{38}Ga_4$ taken at 2 K, the assumption of canted ferromagnetic order is corroborated by the slight hump at a field of about 1.5 T indicative of a metamagnetic-like spin re-orientation. However, even above this supposed spin re-orientation at 1.5 T, the magnetic field seems to be not sufficient to align all spins, the saturation magnetization thus staying well below 7 μ_B/Eu atom. $M(H)$ at 6 K still exhibits signs of this metamagnetic transition. It is worth noting that this observation does not necessarily contradict the result obtained by constructing the corresponding Arrott plot (Fig. 5.8), where, at a first glance, magnetic order seems to be absent already at 6 K - the obvious deviation from pure ferromagnetic order in $Eu_2Ba_6Cu_4Si_{38}Ga_4$ prevents the magnetization from being accepted as primary order parameter, thus inhibiting the usually adopted interpretation of Arrott plots.

5.4   Electrical resistivity

Figures 5.10, 5.11 and 5.12 display temperature dependent electrical resistivities $\rho(T)$ of a number of clathrate type I compounds prepared. Due to

brittleness of certain samples, preparation for physical characterization was not possible in all cases, the results presented in the following nevertheless provide an overview of the transport properties of type I clathrates. All samples under investigation show typically metallic behavior in the whole temperature range, which is in agreement with general observations made with respect to Si or Ge based type I clathrates. In contrast to type II compounds, where the semiconducting properties of the unfilled framework can be maintained via incomplete filling of 2a and 6d sites [238], additional charge donated by divalent earth alkaline elements such as Sr or Ba and also by Eu leads to predominantly metallic configurations in clathrates of type I. In this case framework substitution is the only possibility to achieve semiconductor-like properties, compare e.g. $Sr_8Ga_{16+x}Ge_{30-x}$, where semiconducting behavior at low Ga content is observed. Upon increasing values of x, the system is driven towards metallic conductivity [243]. It is interesting, that, on the other hand, the majority of Sn based type I clathrates known so far are semiconductors [273].

Apart from rare earth substituted compounds, where spin-disorder contributions have to be considered in the paramagnetic temperature range, and from $Ba_8In_{16}Ge_{30}$, all other samples exhibit a $\rho(T)$ at least qualitatively obeying a Bloch-Grüneisen law arising from electron-phonon interactions. However, quantitative analyses of the electrical resistivities only yielded convincing results in the case of $Ba_8Cu_6Si_{40}$ (inset of Fig. 5.10), applying least-squares fits to the experimental data in all other cases revealed residuals not arriving at adequately low values especially due to deviations of $\rho(T)$ from simple Bloch-Grüneisen dependence at temperatures below 150 K. Nevertheless, reasonable estimates of the Debye temperature could be deduced, θ_D was found to range inbetween 300 and 340 K. The enhanced values of latter quantity arise from the mainly covalent bonds among group III and IV elements setting up the rigid framework of the structure. In comparison, significantly lower values (100-200 K) were reported for filled skutterudites pointing to a softened $CoAs_3$-type of framework. However, if the pnicogen atom, compare chapter 3 on filled skutterudites, is replaced or partially substituted by Ge, again a higher degree of covalent bonding is introduced. $Ni_4As_{9.1}Ge_{2.9}$ exhibiting a Debye temperature of $\theta_D = 260$ K represents an example, θ_D was found to be at least 50 K higher than θ_D of Sb or Sn based variants [173].

The electrical resistivity of $Ba_8In_{16}Ge_{30}$ behaves differently. It evidences strong deviation from the curvature expected for simple metallic conduction, although no magnetic moments are present and thus a zero spin-disorder contribution to $\rho(T)$ applies. The temperature dependence is rather comparable to that frequently found in strongly correlated electron systems: an almost linear decrease towards lower temperatures is followed by a strong change of slope such as observed near 50 K. However, Kondo interactions or heavy
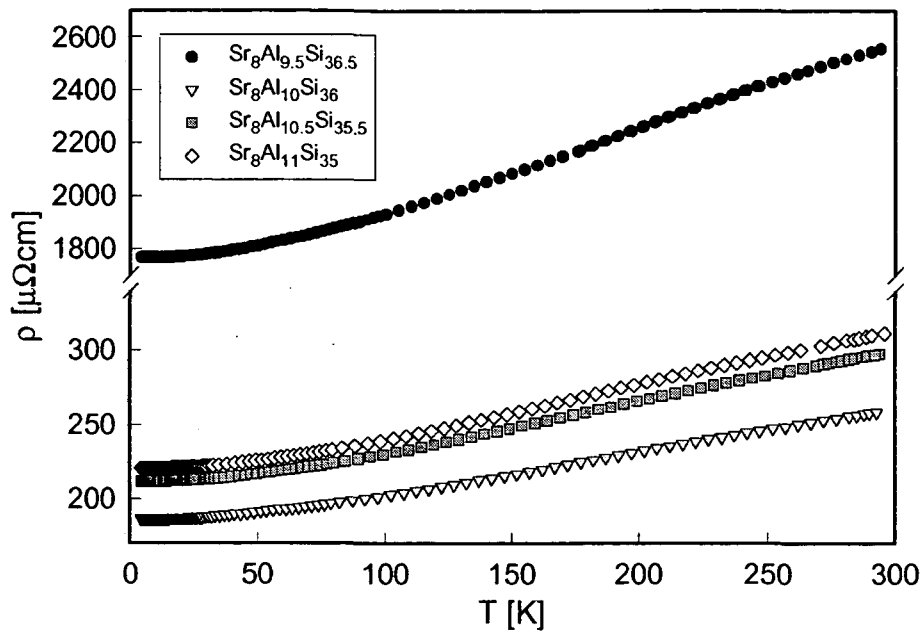
Figure 5.11: Temperature dependent electrical resistivity $\rho(T)$ of $Sr_8Al_{9+x}Si_{37-x}$.
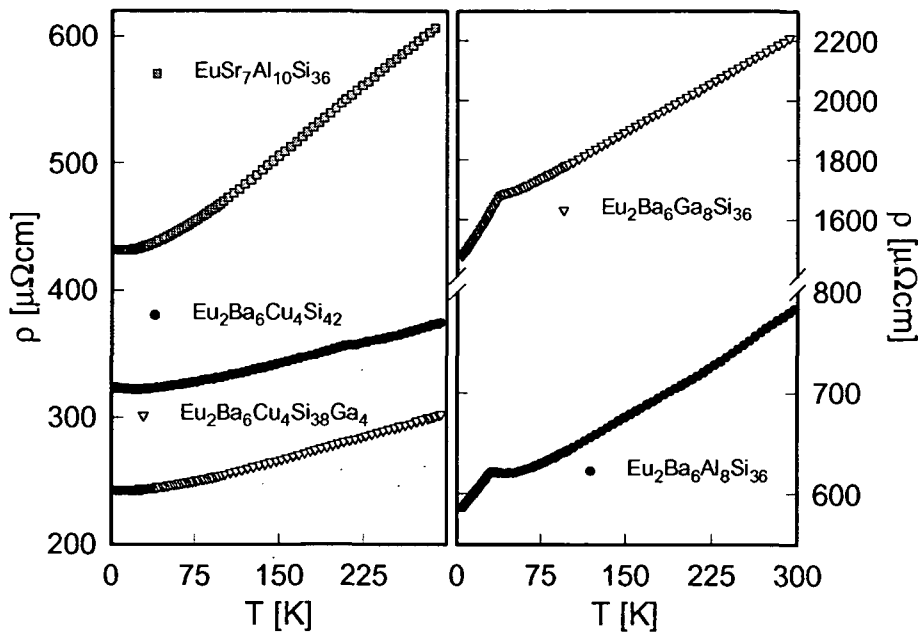

Figure 5.12: Temperature dependent electrical resistivity $\rho(T)$ of Eu substituted clathrates.

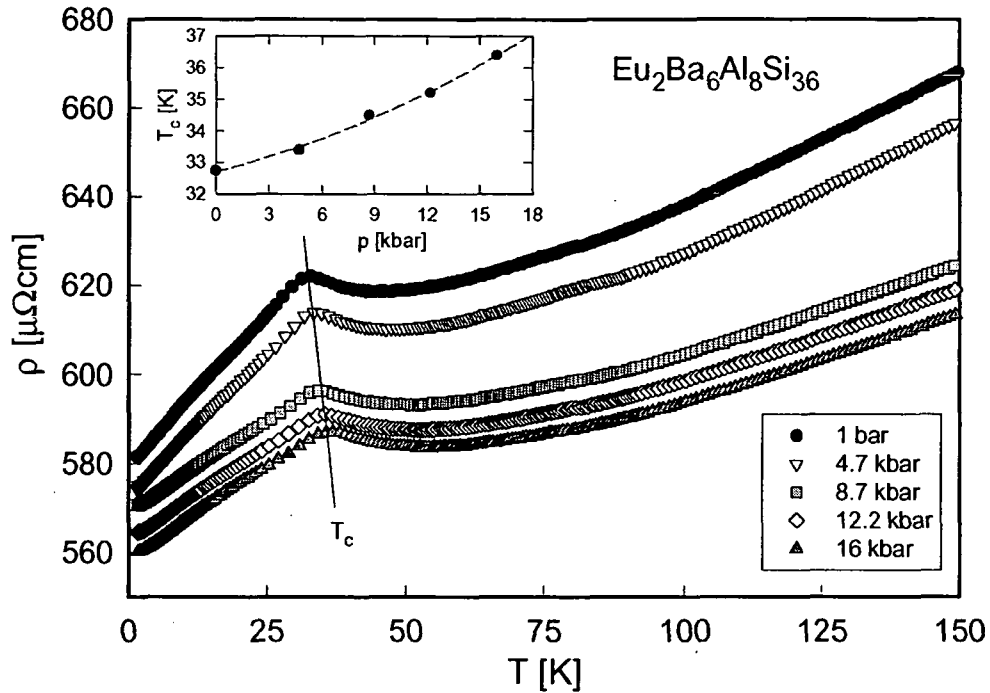Figure 5.13: Temperature dependent electrical resistivity of $Eu_2Ba_6Al_8Si_{36}$ for pressures of up to 16 kbar.

fermion behavior can be ruled out as origin of the distinct curvature in the electrical resistivity.

$\rho(T)$ of $Eu_2Ba_6Ga_8Si_{36}$ and $Eu_2Ba_6Al_8Si_{36}$ reflect the onset of long range magnetic order at temperatures of about 38 and 32 K. Pronounced kinks mark the abrupt ceasing of scattering of charge carriers by the - above the transition - disordered rare earth magnetic moments. This is in latter case in accordance with magnetic data deduced employing d.c. and a.c. susceptibility measurements. For $Eu_2Ba_6Ga_8Si_{36}$, however, magnetic investigations revealed a magnetic transition temperature of about 12 K. The large discrepancy between electrical resistivity and magnetic susceptibility derived T_C most probably stems from sample inhomogeneities. Due to the large absolute values of $\rho(T)$ small traces of an impurity phase may significantly influence the overall curvature, yet, no indication of a subsequent transition around 12 K observed in both d.c. and a.c. susceptibility data could be confirmed.

The shallow minimum in the electrical resistivity of $Eu_2Ba_6Al_8Si_{36}$ slightly above the ordering temperature can be attributed to magnetic fluctuations maintaining limited order among few spins in small areas of the lattice. Similar observations are commonly made in materials subject to ferromagnetic transitions as already outlined with respect to $Ce_2Zn_6Ge_3$ in chap-

ter 4, section 4.4.1. Since resistivity measurements of $Eu_2Ba_6Cu_4Si_{42}$ and $Eu_2Ba_6Cu_4Si_{38}Ga_4$ covered a temperature range down to liquid helium temperature, the magnetic transitions expected from a.c. susceptibility obviously occur below 4.2 K. It was practically impossible to assign a correct T_C to a particular sample due to the relatively broad transitions evident from $\chi_{a.c.}(T)$ data, therefore, the proposed transition temperatures of 5 K for both compounds have to be revised at least to values close to or below 4.2 K.

Additionally, electrical resistivity measurements were performed for $Eu_2Ba_6Al_8Si_{36}$ under pressure in steps of about 4 kbar up to 16 kbar, results are depicted in Fig. 5.13. A significant decrease of the absolute resistivity with increasing pressure is observed, which may, if assumed to be mainly due to the spin-disorder contribution of $\rho(T)$ given in equation 1.49, be caused either by reduction of the exchange coupling constant Γ or of the effective carrier mass $m^\star$ upon the mutual approach of the magnetic moments. Some irregularities in the change of $\rho(T, p)$ possibly originate from poor sample quality. Decreasing overall resistivity is accompanied by an increase of the magnetic ordering temperature, the initial rate of this change was deduced to yield about 0.22 K kbar^{-1} and leads to a T_C of 36.5 K at 16 kbar. A positive $\partial T_C / \partial p$ generally points to well localized magnetic magnetic moments and RKKY interactions mediated via conduction electron system giving rise to long range magnetic order. This is in line with the large interatomic distances between Eu ions situated at the 2a lattice sites within the clathrate structure. Application of pressure decreases the interatomic distances, thus RKKY interaction enhances and initiates long range magnetic order earlier than at ambient pressure conditions. Itinerant systems are expected to exhibit the opposite pressure dependence - a decrease of the transition temperature upon increasing pressure [192].

5.5 Thermopower

Highly efficient thermoelectric materials require elevated thermopower values at least in the temperature range of their designated application. This transport quantity represents the key to an enhanced figure of merit. Temperature dependent absolute Seebeck coefficients of samples, for which quality as well as size permitted experimental studies, are found in Fig. 5.14. With the exception of $Eu_2Ba_6Cu_4Si_{38}Ga_4$, all samples are n-type giving rise to a negative $S(T)$ at temperatures above 150 K. Since, in a first approximation, the sign of the thermoelectric power depends on the type of charge carriers mainly governing transport, negative values point to electrons as primary charge carriers in accordance with the fact, that divalent filler elements (Ba, Sr, Eu) residing within the polyhedra of the lattice act as heavy dopants initiating metallic behavior.
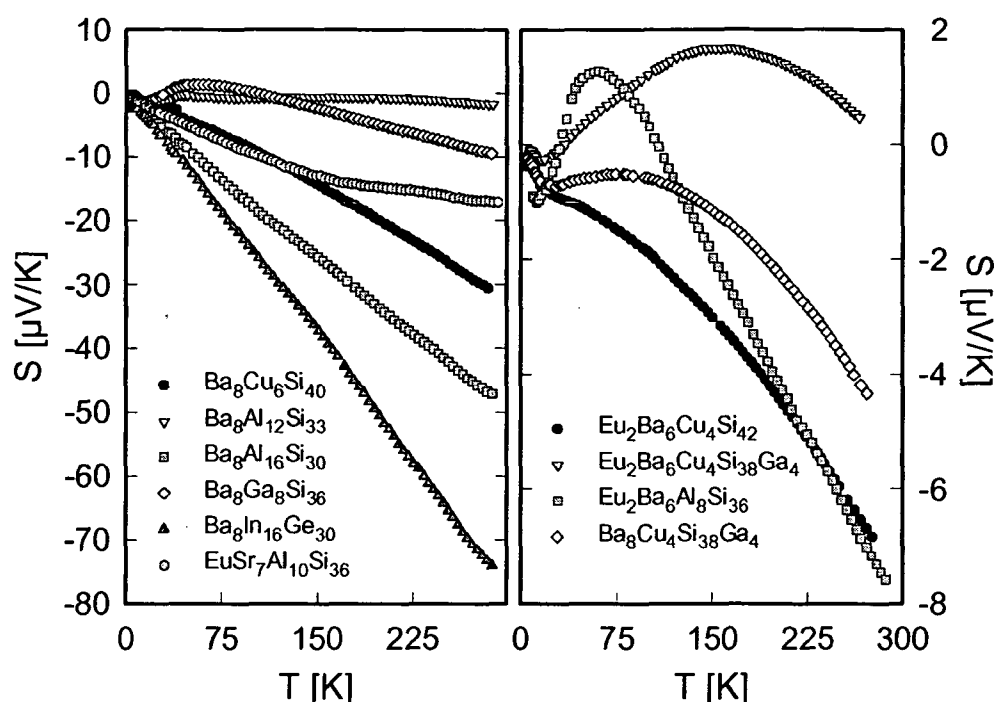
Figure 5.14: Temperature dependent Seebeck coefficients $S(T)$ of type I clathrate compounds.

Common to all Ba filled compounds is apparently the almost linear decrease of the thermoelectric power at elevated temperatures and generally no pronounced structure excluding strong electron interactions. Several Eu substituted variants behave differently: whereas $Eu_2Ba_6Cu_4Su_{42}$ shows a linear decrease as the temperature rises, $Eu_2Ba_6Al_8Si_{36}$ exhibits a positive maximum around about 60 K, consequently thermopower changes sign and decreases to small negative values of about -8 $\mu V/K$ at room temperature. $Eu_2Ba_6Cu_4Si_{38}Ga_4$ evidences a broad maximum in the vicinity of 150 K but maintains positive $S(T)$ values throughout the whole temperature range indicating this compound to be a hole dominated system. At least to a first estimate, performing a simple carrier count, the surplus of holes arises from Ga subtracting one electron per formula unit in comparison to Si. However, considering $Ba_8Cu_4Si_{38}Ga_4$, the apparently negative values of the thermoelectric power in the whole temperature range are not sufficiently explained by simple carrier count arguments, since then the sign change of $S(T)$ upon Eu substitution would have to be attributed to a significant change in the number of electrons donated by the particular filler elements. Rather, Eu and Ba are divalent and the amount of electrons donated per formula unit should in both samples yield 16, if any other influences of this partial substi-

tution are neglected. In contrast to the series of filled Pr skutterudites, the more complex clathrate structure seems to inhibit successful establishment of a relation between number of introduced electrons into the semiconducting framework and sign of the thermopower. What still applies to some extent is the fact, that compounds with lower electrical conductivity in general reveal larger Seebeck coefficients and vice versa, the largest thermopower is found for $Ba_8In_{16}Ge_{30}$ exhibiting a value of about -75 $\mu V/K$ at room temperature and, in line with the carrier concentration dependence of the $S(T)$ according to a one band model [199], also the highest absolute resistivity. Nevertheless, the magnitudes and the sign change of the thermopower taking into account $Ba_8Cu_4Si_{38}Ga_4$ and its Eu substituted variant $Eu_2Ba_6Cu_4Si_{38}Ga_4$ cannot be explained in a straight forward way by simply comparing electrical resistivities of the two samples and therefrom drawing a picture comprising charge carrier concentration and thermopower. Although Blake et al. [270] concluded from theoretical calculations the electropositive filler element in clathrate I $Sr_8Ga_{16}Ge_{30}$ to barely affect electronic transport and thermopower of the framework, in order to understand the experimental data obtained for former two compounds, the opposite has to be assumed here. Since the framework in $Ba_8Cu_4Si_{38}Ga_4$ and $Eu_2Ba_6Cu_4Si_{38}Ga_4$ is the same, the partial Ba/Eu substitution has to result in a substantial change of the density of states at the Fermi energy or/and in a change of the charge carrier velocities in bands near the Fermi energy. These arguments seem at least qualitatively reasonable, if one remembers, that the substitution with Eu stabilizes the clathrate structure in the way, that usually equal distribution of Ba among pentagon-dodecahedra and tetrakaidecahedra is limited to the 6d sites upon Ba and Eu exchange, where the latter exclusively occupies the 2a positions. For a rigorous theoretical treatment of the influence of charge carrier velocity and density of states etc. on electronic transport see [261]. Summarizing, too few information exists on band structure and electronic properties of clathrate intermetallics as to be able to fully understand the interplay between framework and filler elements, most of the investigations performed so far have solely focused on exploring thermoelectric properties.

The overall picture available from the experimentally derived data classifies all compounds, for which thermopower measurements were possible, as non-optimized materials with thermopower values clearly below those of other promising candidates for enhanced thermoelectric capability. Apart from $Ba_8In_{16}Ge_{30}$ exhibiting -75 $\mu V/K$ at room temperature, $S(T)$ of all other samples stays well below -50, in most cases even below -20 $\mu V/K$ significantly outperformed by type I clathrates such as $Sr_8Ga_{16}Ge_{30}$ with over -300 $\mu V/K$ at 300 K, $Rb_8Zn_4Sn_{42}$, for which values of -240 $\mu V/K$ were reported, or $Cs_8Zn_4Sn_{34}Ge_8$ with a thermopower of -180 $\mu V/K$ at room temperature [243, 274, 275].
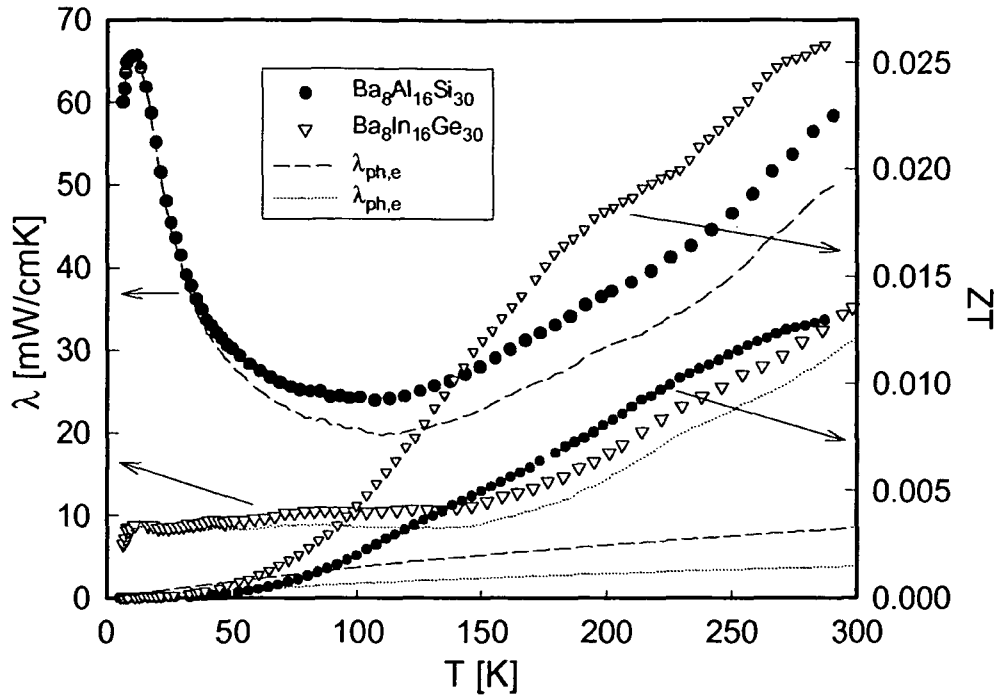
Figure 5.15: Temperature dependent thermal conductivity $\lambda(T)$ (left scale) and figure of merit ZT (right scale) of $Ba_8Al_{16}Si_{30}$ and $Ba_8In_{16}Ge_{30}$. Dashed and dotted lines denote lattice and electronic thermal conductivity contributions of $Ba_8Al_{16}Si_{30}$ and $Ba_8In_{16}Ge_{30}$, respectively.

5.6 Thermal conductivity and figure of merit of $Ba_8Al_{16}Si_{30}$ and $Ba_8In_{16}Ge_{30}$

Due to sample quality and size only two compounds could be undertaken thermal conductivity measurements, $Ba_8Al_{16}Si_{30}$ and $Ba_8In_{16}Ge_{30}$. Fig. 5.15 shows λ as a function of temperature from 4 to 300 K. The overall magnitude is small compared to common intermetallics, neglecting radiation losses above 150 K thermal conductivity remains below 30 mW/cmK for former and near 10 mW/cmK for latter compound. Radiation corrections similar to the procedures described in chapters 3 and 4 for skutterudites and for the series $RE_2Zn_6Ge_3$ were not performed. Yet, the curvature following the experimental curve off about 100 K may be assumed to stay within the range observed at this temperature without any pronounced deviations. Application of the Wiedemann-Franz law (equation 1.60) in both cases reveals only small electronic thermal conductivities, λ_e of $Ba_8In_{16}Ge_{30}$ nevertheless gains importance with increasing temperature due to the very small lattice part, while it amounts to only 14% of the total quantity at room temper-

ature in $Ba_8Al_{16}Si_{30}$. The small thermal conductivity observed especially for $Ba_8In_{16}Ge_{30}$ is attributed to the loosely bound Ba ions within the large polyhedra of the structure giving rise to pronounced interactions with heat-carrying lattice vibrations. Unfortunately, $\lambda(T)$ of Eu substituted clathrates could not be measured, the smaller size of Eu compared to that of Ba in combination with its significantly larger mass could be expected to further enhance phonon scattering and might thus lead to an even lower lattice contribution to the thermal conductivity. The latter has already been reported in literature with respect to e.g. $Eu_4Sr_4Ga_{16}Ge_{30}$ [250], where due to the presence of Eu^{2+}, almost twice as massive as Sr^{2+}, the lowest λ_{ph} values in clathrate compounds were obtained so far. It tracks convincingly the lattice contribution of amorphous SiO_2, a proof for the approximate validity of Slacks PGEC concept. Apart from large differences in size and mass, the distribution of two filler elements over the lattice, although ordered in the way, that rare earth and alkaline element do not share the same lattice sites, can be further considered favorable to reduced lattice thermal conductivity.

The calculated figure of merit of $Ba_8Al_{16}Si_{30}$ and $Ba_8In_{16}Ge_{30}$ is found in Fig. 5.15 denoted by small symbols, right hand scale. ZT stays below 0.03 at room temperature, which is primarily due to thermopower values by far not exceeding -80 $\mu V/K$ at 300 K, clearly not enough for efficient thermoelectric performance. However, it has been demonstrated, that clathrates, if optimized, may indeed represent competitors to state of the art thermoelectric materials. In order to improve ZT of the samples examined within this thesis, further work is necessary focusing on the electronic properties in particular.

Summary

The aim of the present work was the evaluation of ground state properties as well as the exploration of the thermoelectric potential of multinary cage based structures: Pr filled skutterudites, Zn germanides and clathrate I type of structures. In order to rigorously determine their unique characteristics a number of bulk investigations were carried out both on single-crystal and polycrystalline material: x-ray diffraction and EPMA studies to clarify structural aspects, magnetic susceptibility and magnetization measurements, elastic and inelastic neutron scattering, L_{III} absorption edge spectroscopy, specific heat and transport investigations. The latter comprised electrical resistivity, both under pressure and in externally applied magnetic fields, as well as measurements of thermopower and thermal conductivity.

The series of Pr filled skutterudites $Pr_yFe_{4-x}T_xSb_{12}$ with T=Co, Ni were synthesized and the amount of incorporable rare earth was found to decrease as the Fe content is lowered. While for parent $Pr_{0.73}Fe_4Sb_{12}$ long-range magnetic order sets on at 4.5 K, it is suppressed upon transition metal substitution. The $[Fe_{4-x}T_xSb_{12}]$ sublattices seem to contribute substantially to the magnetic behavior of the series of compounds evidencing an additional magnetic moment to that of the rare earth. Based on magnetic susceptibility and inelastic neutron scattering data, the crystal electric field (CEF) splitting was deduced, the latter being subject to a significant alteration when proceeding towards higher Co/Ni concentrations. Specific heat and electrical resistivity were used in order to probe the derived CEF level scheme, the former further revealed heavy electrons from an electronic contribution with a maximum of 540 mJ/molK^2 in the parent sample. From electrical resistivity investigations metallic type of conductivity was validated. A systematic trend is evident from the evolution of the absolute $\rho(T)$ values related with a modification of the carrier concentration upon lowering Pr and Fe contents. This is also reflected by the thermopower, for which a sign change indicates the crossover from hole to electron dominated transport. Seebeck coefficients reaching values of up to 220 μV/K in combination with strongly reduced thermal conductivities in the range of 10 mW/cmK demonstrated the excellent thermoelectric performance of Pr filled skutterudites. The figure of merit was calculated to amount to 0.25 at room temperature for $Pr_{0.57}Fe_{3.5}Ni_{0.5}Sb_{12}$, it

147

may be assumed to attain unity at temperatures above 600 K.

The structure of $RE_2Zn_6Ge_3$ with RE=La, Ce, Pr, Nd, Sm and Gd was determined by means of x-ray diffraction, compositions were controlled employing electron probe micro analyses. The existence of long range antiferromagnetic order was established in terms of magnetic investigations with the exception of the Ce containing compound, which according to isothermal magnetization data exhibits some type of ferrimagnetic order. $Gd_2Zn_6Ge_3$ exhibits the highest transition temperature with $T_N = 28.8$ K. The magnetic structures of $Nd_2Zn_6Ge_3$ and $Pr_2Zn_6Ge_3$ could be resolved from elastic neutron scattering results: $Nd_2Zn_6Ge_3$ is characterized by antiferromagnetic (a, b)-planes, that are stacked together antiferromagnetically along the c-axis, whereas in $Pr_2Zn_6Ge_3$ ferromagnetic (a, b)-planes of Pr ions are combined in the way along c, that two spin-up planes are followed by one spin-down plane. The thermoelectric properties manifested themselves in electrical resistivities characteristic of metallic compounds covering a range between 300 and 1800 $m\Omega cm$ and rather low thermopower (-22 $\mu V/K$ at 300 K in $Gd_2Zn_6Ge_3$). Although thermal conductivity of all samples stays below 50 mW/cmK at room temperature, the figure of merit ZT does not exceed 0.01 for any sample, by far too low for future thermoelectric application.

Novel framework-deficient solid solutions $Ba_8Al_xSi_{42-3/4x}\square_{4-1/4x}$ and $Ba_8Ga_xSi_{42-3/4x}\square_{4-1/4x}$ with x=8, 12, 16 as well as $Ba_8Cu_4Si_{42-x}Ga_x$ (x=0, 4, 6, 8), $Ba_8In_{16}Ge_{30}$ were prepared and isotopism was confirmed with the standardized clathrate I-$Ba_8Al_{16}Ge_{30}$ type of structure. Additonally synthesized rare earth substituted clathrates $Eu_{2-x}(Sr,Ba)_{6-x}M_ySi_{46-y}$ with M=Cu, Al and Ga represent new quartenary ordered variants of the clathrate I structure types. The partial substitution of Ba or Sr by Eu has a stabilizing effect on the clathrate structure, where the alkali earth elements generelly occupy both 2a and 6c sites of the structure. The introduction of Eu leads to a substantial change, since Ba and Sr are then solely found at the 6c position, whereas Eu exclusively occupies the 2a sites. A geometrical analysis of all known intermetallic clathrate crystal structures served to propose a new intermetallic clathrate structure tree. From magnetic investigations the Eu substituted clathrates were shown to order magnetically at low temperatures, in combination with L_{III} absorption edge data a divalent state of Eu could be concluded in the whole temperature range. Measurements of transport properties evidenced metallic behavior for all compounds, the rather small thermoelectric power values generally observed point to the need of further electronic optimization. From thermal conductivity data the impact of the inclusion atoms could be demonstrated, which effectively scatter heat carrying lattice vibrations due to their large anharmonic localized vibrations.

Bibliography

[1] E.D. Bauer, N.A. Frederick, P.-C. Ho, V. S. Zapf, M.B. Maple, Phys. Rev. B **65**, 100506 (2002)

[2] M.B. Maple, P.-C. Ho, V.S. Zapf, N.A. Frederick, E.D. Bauer, W.M. Yuhasz, F.M. Woodward, J.W. Lynn, J. Phys. Soc. Japan **71**, Suppl. 23 (2002)

[3] Y. Aoki, T. Namiki, T.D. Matsuda, H. Sugawara, H. Sato, J. Phys. Chem. Sol. **63**, 1201 (2002)

[4] Y. Aoki, T. Namiki, T.D. Matsuda, H. Sugawara, H. Sato, Physica B **312**, 823 (2002)

[5] G.A. Slack, *CRC Handbook of Thermoelectrics*, edited by D.M. Rowe, CRC Press, Chap. 34, p. 407 (1995)

[6] A. Grytsiv, A. Leithe-Jasper, H. Flandorfer, P. Rogl, K. Hiebl, C. Godart, T. Velikanova, J. Alloys and Comp. **266**, 7 (1998)

[7] C. Kranenberg, D. Johrendt, A. Mewis, R. Pottgen, G. Kotzyba, H. Trill, B. D. Mosel, J. Sol. State Chem. **167**, 107 (2002)

[8] T.J. Seebeck, Abh. K. Akad. Wiss. Berlin, 265 (1822-1823)

[9] J.C. Peltier, Ann. Chim. **56**, 371 (1834)

[10] A.F. Ioffe, *Semiconductor Thermoelements and Thermoelectric Cooling*, Infosearch, London, (1957)

[11] W. Thomson, Proc. Royal Soc. of Edinburgh, 91 (1851)

[12] E. Altenkirch, Phys. Zeitschrift **10**, 560 (1909)

[13] E. Altenkirch, Phys. Zeitschrift **12**, 920 (1911)

[14] A.F. Ioffe, Academy of Sciences of the USSR, Moscow (1949)

[15] H.J. Goldsmid, R.W. Douglas, J. Appl. Phys. **5** (11), 386 (1954)

[16] E. Gratz, H. Nowotny, *Transporttheorie*, lecture notes, TU Vienna (1993)

[17] J.M. Fournier, E. Gratz, *Transport Properties of R and An Intermetallics*, in Handbook on the Physics and Chemistry of Rare Earths, edited by K. A. Gschneidner Jr., L. Eyring, G.H. Lander and G.R. Choppin, Elsevier Science Publishers B.V., Vol **17**, 409 (1993)

[18] F.J. Blatt, P.A. Schroeder, C.L Foiles, *Thermoelectric Power of Metals*, Plenum Press, New York and London (1976)

[19] R.D.Barnard, *Thermoelectricity in Metals and Alloys*, Taylor and Francis LTD, London (1972)

[20] D.D. Pollock, *CRC Handbook of Thermoelectrics*, edited by D.M. Rowe, CRC Press, Chap. 2, p. 8 (1995)

[21] H.J. Goldsmid, *CRC Handbook of Thermoelectrics*, edited by D.M. Rowe, CRC Press, Chap. 3, p. 19 (1995)

[22] G.S. Nolas, J. Sharp, H.J. Goldsmid, *Thermoelectrics - Basic Principles and New Materials Developments*, Springer-Verlag, Berlin Heidelberg (2001)

[23] J. McDougall, E.C. Stoner, Phil. Trans. A **237**, 67 (1938)

[24] P. Rhodes, Proc. Royal Soc. A **204**, 396 (1950)

[25] A.C. Beer, M.N. Chase, P.F. Choquard, Helv. Phys. Acta **28**, 529 (1955)

[26] G. Grimvall, *The Electron-Phonon Interaction in Metals*, in Selected Topics in Solid State Physics, edited by E.P. Wohlfahrt, North Holland, Vol. **16**, 218 (1981)

[27] E. Grüneisen, Ann. Physik **16**, 530 (1933)

[28] N.F. Mott, Proc. Royal Soc. **156**, 368 (1936)

[29] N.F. Mott, H. Jones, *The Theory of the Properties of Metals and Alloys*, Oxford University Press, London (1958)

[30] A.J. Dekker, J. Appl. Phys. **36**, 906 (1965)

[31] V.U.S. Rao, W.E. Wallace, Phys. Rev. B **2**, 4613 (1970)

[32] T. Kasuya, Prog. Theor. Phys. **16**, 227 (1959)

[33] D.L. Mills, P. Lederer, J. Phys. Chem. Sol. **27**, 1805 (1966)

[34] G. T. Meaden, Contemp. Phys. **12**, 313 (1971)

[35] E. Gratz, H. Nowotny, J. Magn. Magn. Mat. **29**, 127 (1982)

[36] A. Hasegawa, A. Yanase, J. Phys. F **10**, 847 (1980)

[37] H. Yamada, S. Takada, Prog. Theor. Phys. B **45**, 1401 (1973)

[38] E. Bauer, E. Gratz, H. Kirchmayer, Z. Phys. B **68**, 63 (1987)

[39] D. Jaccard, M.J. Besnus, J.P. Kappler, J. Magn. Magn. Mat. **63**, 572 (1987)

[40] R. Wawryk, Z. Henkie, T. Cichorek, C. Geibel, F. Steglich, Phys. Stat. Sol. **232**, 4 (2002)

[41] R.P. Huebener, Phys. Rev. A **135**, 1281 (1964)

[42] I.A. Smirnov, V.S. Oskotski, *Thermal conductivity of rare earth compounds*, in Handbook on the Physics and Chemistry of Rare Earths, edited by K. A. Gscheidner, Jr. and L. Eyring, Elsevier Science Publishers B. V., Vol. **16**, 107 (1993)

[43] G. Wiedemann, R. Franz, Ann. Physik **89**, 497 (1853)

[44] M.J. Laubitz, T. Matsumura, Can. J. Phys. **50**, 196 (1972)

[45] M.J. Laubitz, T. Matsumura, P.J. Kelley, Can. J. Phys. **54**, 92 (1976)

[46] E. Bauer, E. Gratz, G. Adam, J. Phys. F **16**, 493 (1986)

[47] A. Rassili, K. Durczewski, M. Ausloos, Phys. Rev. B **58**, 5665 (1998)

[48] J. Callaway, Phys. Rev. **113**, 1046 (1959)

[49] J. Callaway, H. C. von Baeyer, Phys. Rev. **120**, 1149 (1960)

[50] W. Heisenberg, Z. Phys. **49**, 619 (1928)

[51] F. Bloch, Z. Phys. **61**, 206 (1930)

[52] E.C. Stoner, Proc. Royal Soc. London A **165**, 372 (1938)

[53] N.F. Mott, Proc. Phys. Soc. London **47**, 571 (1935)

[54] E.P. Wohlfarth, P. Rhodes, Philos. Mag. **7**, 1817 (1962)

[55] F. Gautier, *Itinerant Magnetism*, in Magnetism of Metals and Alloys, edited by M. Cyrot, Elsevier Science Publishers B. V. (1982)

[56] J. Pierre, *Magnetism of Rare Earth Metals and Intermetallic Compounds*, in Magnetism of Metals and Alloys, edited by M. Cyrot, Elsevier Science Publishers B. V., 245 (1982)

[57] J. Jensen and A.R. Mackintosh, *Rare Earth Magnetism*, Clarendon Press, Oxford (1991)

[58] K.W.H. Stevens, Proc. Phys. Soc. A **65**, 209 (1952)

[59] K. Takegahara, H. Harima, A. Yanase, J. Phys. Soc. Japan, **5**, 1190 (2001)

[60] J.H. Van Vleck, *Theory of Electric and Magnetic Susceptibilities*, Oxford University Press (1932)

[61] M.A. Ruderman and C. Kittel, Phys. Rev. **96**, 99 (1954)

[62] T. Kasuya, Prog. Theor. Phys. **16**, 45 (1956)

[63] K. Yoshida, Phys. Rev. **106**, 893 (1957)

[64] P.G. de Gennes, J. Phys. Radium **23**, 510 (1962)

[65] J.G. Sereni, *Magnetic Systems: Specific Heat*, in Encyclopedia of Materials, Elsevier Science Publishers B. V., 4986 (2001)

[66] L.J. Sundström, *The Low Temperature Heat Capacity*, in Handbook on the Physics and Chemistry of Rare Earths, edited by K. A. Gscheidner, Jr. and L. Eyring, Elsevier Science Publishers B. V., Vol. **1**, 379 (1978)

[67] *Binary Alloy Phase Diagrams 2th edition*, edited by T. D. Massalski, Materials Park, OH: ASM International (1990)

[68] P. Lebeau, J. Figueras, C. R. Acad. Sci. **136**, 1329 (1903)

[69] A. Grytsiv, D. Kaczorowski, A. Leithe-Jasper, P. Rogl, C. Godart, M. Potel, H. Noël, J. Sol. State Chem. **163**, 37 (2002)

[70] B. Andraka, R. Pietri, D. Kaczorowski, A. Leithe-Jasper, P. Rogl, J. Appl. Phys. **87**, 5149 (2000)

[71] R. Pietri, B. Andraka, D. Kaczorowski, A. Leithe-Jasper, P. Rogl, Phys. Rev. B **61**, 12169 (2000)

[72] H. Menke, H.G. von Schnering, Z. Anorg. Allg. Chem. **395**, 223 (1973)

[73] W. Wacha, program STRUKTUR, Diploma thesis, TU Vienna (1989)

[74] A. Jasper-Leithe, D. Kaczorowski, P. Rogl, J. Bogner, M. Reissner, W. Steiner, G. Wiesinger, C. Godart, Sol. State Comm. **109**, 395 (1999)

[75] J. Rodriguez-Carvajal, *FULLPROF: A Program for Rietveld Refinement and Pattern Matching Analysis*, Abstracts of the Satellite Meeting on Powder Diffraction of the XV Congr. Intl. Union of Crystallogr., Talence, France, p. 127 (1990)

[76] Nonius Kappa CCD Program Package COLLECT, DENZO, SCALEPACK, SORTAV, Nonius Delft, the Netherlands (1998)

[77] G.M. Sheldrick SHELX-97, *Program for Crystal Structure Refinement*, (University of Göttingen, Germany); Windows version by McArdle, Natl. Univ. Ireland, Galway (1997)

[78] http://sinq.web.psi.ch/sinq/instr/dmc, *The Double-Axis Multi-Counter Powder Diffractometer at PSI, Villigen, Switzerland.*

[79] http://www.isis.rl.ac.uk/excitations/het, *The HET spectrometer at ISIS, Rutherford Appleton Laboratory, Chilton, United Kingdom.*

[80] St. Berger, Diploma thesis, TU Vienna (1998)

[81] M. Liendl, Diploma thesis, TU Vienna (1995)

[82] A. Eiling, J. Schilling, J. Phys. F **11**, 623 (1981)

[83] W.F. Sherman, A.A. Stadtmuller, *Experimental Techniques in High-Pressure Research*, John Wiley & Sons Ltd. (1987)

[84] M.I. Eremets, *High Pressure Experimental Methods*, Oxford University Press, New York (1996)

[85] R. Hauser, Thesis, TU Vienna (1995)

[86] R. Resel, E. Gratz, A. T. Burkov, T. Nakama, M. Higa, K. Yagasaki, Rev. Sci. Instr. **67**, 1970 (1996)

[87] Ch. Paul, Diploma Thesis, TU Vienna (2001)

[88] T. Holubar, Thesis, TU Vienna (1995)

[89] M. Forsthuber, Thesis, TU Vienna (1993)

[90] Yu. Grin, K. Hiebl, P. Rogl, C. Godart, J. Alloys and Comp. **239**, 127 (1996)

[91] W. Nernst, Sitzungsbericht der K. Preuss. Akad. Wiss. **12**, 261 (1910)

[92] G. Schaudy, Diploma thesis, TU Vienna (1991)

[93] G. Schaudy, Thesis, TU Vienna (1995)

[94] H. Michor, Diploma thesis, TU Vienna (1993)

[95] I. Oftedal, Z. Kristallogr. A **66**, 517 (1928)

[96] C. Uher, *Skutterudites: Prospective Novel Thermoelectrics*, in Semiconductors and Semimetals, Academic Press, edited by T. M. Tritt, Chap. 5, 139 (2001)

[97] M.E. Danebrock, C.B.H. Evers, W. Jeitschko, J. Phys. Chem. Solids **57**, 381 (1996)

[98] J.P. Fleurial, A. Borshchevsky, T. Caillat, D.T. Morelli, G.P. Meisner, 15th International Conference on Thermoelectrics, Conf. Proc., p. 91 (1996)

[99] T. Rosenqvist, Acta Met. **1**, 761 (1953)

[100] S. Rundqvist, N.-O. Ersson, Ark. Kemi **30**, 103 (1968)

[101] U. Ventriglia, Periodico Mineral **26**, 345 (1957)

[102] S. Rundqvist, A. Hede, Acta Chem. Scand. **14**, 893 (1960)

[103] A. Kjekshus, G. Pedersen, Acta Cryst. **14**, 1065 (1961)

[104] N. Mandel, J. Donohue, Acta Cryst. B **27**, 2288 (1971)

[105] A. Kjekshus, D.G. Nicholson, T. Rakke, Acta Chem. Scand. **27**, 1307 (1973)

[106] A. Kjekshus, T. Rakke, Acta Chem. Scand. **A28**, 99 (1974)

[107] Th. Schmidt, G. Kliche, H.D. Lutz, Acta Cryst. C **43**, 1678 (1987)

[108] C.R. Jolibois, Acad. Sci. **150**, 106 (1910)

[109] L.D. Dudkin, N.Kh. Abrikosov, Sov. Phys. Sol. State **1**, 126 (1959)

[110] C.M. Pleass, R.D. Heyding, Canad. J. Chem. **40**, 590 (1962)

[111] W. Jeitschko and D.J. Braun, Acta Crystallogr. B **33**, 3401 (1977)

[112] D.J. Braun, W. Jeitschko, J. Sol. State Chem. **32**, 357 (1980)

[113] D.J. Braun, W. Jeitschko, J. Less-Comm. Met. **72**, 147 (1980)

[114] D.J. Braun, W. Jeitschko, J. Less-Comm. Met. **76**, 33 (1980)

[115] N.R. Dilley, E.J. Freeman, E.D. Bauer, M.B. Maple, Phys. Rev. B **58**, 6287 (1998)

[116] C.B.H. Evers, L. Boonk, W. Jeitschko, Z. Anorg. Allg. Chem. **620**, 1028 (1994)

[117] E. Bauer, A. Galatanu, H. Michor, G. Hilscher, P. Rogl, P. Boulet, H. Noël, Eur. Phys. J. B **14**, 483 (2000)

[118] I. Shirotani, Y. Shimaya, K. Kihou, C. Sekine, J. Sol. State Chem. **174**, 32 (2003)

[119] G.P. Meisner, M.S. Torikachvili, K.N. Yang, M.B. Maple, R.P. Guertin, J. Appl. Phys. **57**, 3073 (1985)

[120] F. Grandjean, A. Gerard, D.J. Braun, W. Jeitschko, J. Phys. Chem. Sol. **45**, 877 (1984)

[121] L.D. Dudkin, N.Kh. Abrikosov, Zh. Neorg. Khim **1**, 2096 (1956)

[122] L.D. Dudkin, N.Kh. Abrikosov, Sov. Phys. Sol. State **2**, 212 (1957)

[123] B.N. Zobrina, L.D. Dudkin, Sov. Phys. Sol. State **1**, 1668 (1960)

[124] B.C. Sales, D. Mandrus, B.C. Chakoumakos, V. Keppens, J.R. Thompson, Phys. Rev. B **56**, 15081 (1997)

[125] G.P. Meisner, D.T. Morelli, S. Hu, J. Yang, C. Uher, Phys. Rev. Lett. **80**, 3551 (1998)

[126] X. Tang, L. Chen, T. Goto, T. Hirai, J. Mater. Res. **16**, 837 (2001)

[127] A. Grytsiv, P. Rogl, St. Berger, Ch. Paul, E. Bauer, C. Godart, B. Ni, M.M. Abd-Elmeguid, A. Saccone, R. Ferro, D. Kaczorowski, Phys. Rev. B **66**, 94411 (2002)

[128] St. Berger, Thesis, TU Vienna (2003)

[129] H. Nakagawa, H. Tanaka, A. Kasama, H. Anno, K. Matsubara, 16th International Conference on Thermoelectrics, Conf. Proc., 351 (1997)

[130] H. Anno, K. Matsubara, Y. Notohara, T. Sakakibara, H. Tashiro, J. Appl. Phys. **86**, 3780 (1999)

[131] J.O. Sofo, G.D. Mahan, Phys. Rev. B **58**, 15620 (1998)

[132] G. Slack, V.G. Tsoukala, J. Appl. Phys. **76**, 1665 (1994)

[133] H.D. Lutz, G. Kliche, J. Sol. State Chem. **40**, 64 (1981)

[134] A. Borshchevsky, T. Caillat, J.P. Fleurial, 15th International Conference on Thermoelectrics, Conf. Proc., 112 (1996)

[135] C. Uher, B. Chen, S. Hu, D.T. Morelli, G.P. Meisner, Mat. Res. Soc. Symp. Proc. **478**, 315 (1997)

[136] G. S. Nolas, J.L. Cohn, G.A. Slack, Phys. Rev. B **58**, 164 (1998)

[137] D. Jung, M. Whangbo, S. Alvarez, J. Inorg. Chem. **29**, 2252 (1990)

[138] G.P. Meisner, Physica B **108**, 763 (1981)

[139] L.E. DeLong, G.P. Meisner, Sol. State Comm. **53**, 119 (1985)

[140] T. Uchiumi, I. Shirotani, C. Sekine, S. Todo, T. Yagi, Y. Nakazawa, K. Kanoda, J. Phys. Chem. Sol. **60**, 689 (1999)

[141] A. Gerard, F. Grandjean, J. Hodges, D. J. Braun, W. Jeitschko, J. Phys. C **16**, 2797 (1983)

[142] C. Sekine, T. Uchiumi, I. Shirotani, K. Matsuhira, T. Sakakibara, T. Goto, T. Yagi, Phys. Rev. B **62**, 11581 (2000)

[143] M.S. Torikachvili, J.W. Chen, Y. Dalichaouch, R.P. Guertin, M. W. McElfresh, C. Rossel, M.B. Maple, G.P. Meisner, Phys. Rev. B **36**, 8660 (1987)

[144] E.D. Bauer, A. Slebarski, C. Sirvent, M.B. Maple, J. Phys.: Cond. Matter **13**, 4495 (2001)

[145] E.D. Bauer, A. Slebarski, R.P. Dickey, E.J. Freeman, C. Sirvent, V.S. Zapf, N.R. Dilley, M.B. Maple, J. Phys.: Cond. Matter **13**, 5183 (2001)

[146] N. Takeda and M. Ishikawa, J.Phys.: Cond. Mater **13**, 5971 (2001)

[147] K. Abe, H. Sato, T.D. Matsuda, T. Namiki, H. Sugawara, Y. Aoki, J. Phys.: Cond. Matter **14**, 11757 (2002)

[148] K. Abe, T.D. Matsuda, H. Sugawara, T. Namiki, Y. Aoki, H. Sato, Physica B **312**, 256 (2002)

[149] I. Shirotani, T. Uchiumi, K. Ohno, C. Sekine, Y. Nakazawa, K. Kanoda, S. Todo, T. Yagi, Phys. Rev. B **56**, 7866 (1997)

[150] N. Takeda and M. Ishikawa, J. Phys. Soc. Japan, **69**, 868 (2000)

[151] C. Sekine, T. Uchiumi, I. Shirotani, T. Yagi, Phys. Rev. Lett. **79**, 3218 (1997)

[152] C.H. Lee, H. Oyanagi, C. Sekine. I. Shirotani, M. Ishii, Phys. Rev. B **60**, 13253 (1999)

[153] C.H. Lee, H. Matsuhata, A. Yamamoto, T. Ohta, H. Takazawa, K. Ueno, C. Sekine, I. Shirotani, T. Hirayama, J. Phys.: Cond. Matter **13**, 45 (2001)

[154] K. Matsuhira, Y. Hinatsu, C. Sekine, I. Shirotani, Physica B **312**, 829 (2002)

[155] S.H. Curnoe, H. Harima, K. Takegahara, K. Ueda, Physica B **312**, 837 (2002)

[156] H. Sugawara, T.D. Matsuda, K. Abe, K. Aoki, H. Sat, S. Nojiri, Y. Inada, R. Settai, Y. Onuki, J. Magn. Magn. Mat. **226**, 48 (2001)

[157] T.D. Matsuda H. Okada, H. Sugawara, Y. Aoki, H. Sato, A.V. Andreev, Y. Shiokawa, V. Sechovsky, T. Honma, E. Yamamoto, Y. Onuki, Physica B **281**, 220 (2000)

[158] H. Sato, Y. Abe, H. Okada, T. Matsuda, H. Sugawara, Y. Aoki, Physica B **281**, 306 (2000)

[159] L. Keller, P. Fischer, T. Hermannsdörfer, A. Dönni, H. Sugawara, T.D. Matsuda, Y. Aoki, H. Sato, J. Alloys and Comp. **323**, 516 (2001)

[160] Y. Nakanishi, T. Simizu, M. Yoshizawa, T. Matsuda, H. Sugawara, H. Sato, Phys. Rev. B **63**, 184429 (2001)

[161] K. Iwasa, Y. Watanabe, K. Kuwahara, M. Kohgi, H. Sugawara, T.D. Matsuda, Y. Aoki, H. Sato, Physica B **312**, 834 (2002)

[162] H. Sugawara, T.D. Matsuda, K. Abe, Y. Aoki, H. Sato, S. Nojiri, Y. Inada, R. Settai, Y. Onuki, Phys. Rev. B **66**, 134411 (2002)

[163] A. Yatskar, W.P. Beyermann, R. Movshovich, P.C. Canfield, Phys. Rev. Lett. **77**, 3637 (1996)

[164] F. Steglich, J. Aarts, C.D. Bredl, W. Lieke, D. Meschede, W. Franz, H. Schäfer, Phys. Rev. Lett **43**, 1892 (1979)

[165] H. R. Ott, H. Rudigier, Z. Fisk, J.L. Smith, Phys. Rev. Lett. **50**, 1595 (1979)

[166] E. Bauer, G. Hilscher, H. Michor, Ch. Paul, E.W. Scheidt, A. Gribanov, Yu. Seropegin, H. Noël, M. Sigrist, P. Rogl, submitted to Phys. Rev. Lett. (2003)

[167] F. Hulliger, Nature **198**, 1081 (1963)

[168] J.P. Fleurial, T. Caillat, A. Borshchevsky, Proc. Symp. Mater. Res. Soc., 175 (1997)

[169] J. Yang, G.P. Meisner, D.T. Morelli, C. Uher, Phys. Rev. B **63**, 144101 (2000)

[170] J. Yang, D.T. Morelli, G.P. Meisner, W. Chen, J.S. Dyck, C. Uher, Phys. Rev. B **65**, 94115 (2002)

[171] L. Chapon, D. Ravot, J. Alloys and Comp. **282**, 58 (1999)

[172] W. Jeitschko, A.J. Foecker, D. Paschke, M. V. Dewalsky, Ch.B.H. Ewers, B. Künnen, A. Lang, G. Kotzyba, U.Ch. Rodewald, M.H. Möller, Z. Anorg. Allg. Chem **626**, 1112 (2000)

[173] A. Grytsiv, P. Rogl, S. Berger, C. Paul, H. Michor, E. Bauer, G. Hilscher, C. Godart, P. Knoll, M. Musso, W. Lottermoser, A. Saccone, R. Ferro, T. Roisnel, H. Noel, J. Phys.: Cond. Matter **14**, 7071 (2002)

[174] C.B.H. Evers, W. Jeitschko, L. Boonk, D.J. Braun, T. Ebel, U.D. Scholz, J. Alloys and Comp. **224**, 184 (1995)

[175] J.W. Kaiser, W. Jeitschko, J. Alloys and Comp. **291**, 66 (1999)

[176] P.W. Selwood, *Magnetochemistry*, Interscience, New York, p. 78 (1956)

[177] E. Bauer, St. Berger, A. Galatanu, M. Galli, H. Michor, G. Hilscher, Ch. Paul, B. Ni, M.M. Abd-Elmeguid, V.H. Tran, A. Grytsiv, P. Rogl, Phys. Rev. B **63**, 224414 (2001)

[178] St. Berger (private communication)

[179] T.D. Matsuda, K. Abe, F. Watanuki, T. Namiki, S.R. Saha, H. Sugawara, Y. Aoki, H. Sato, J. Magn. Magn. Mat. **226-230**, 66 (2001)

[180] T.D. Matsuda, S.R. Saha, K., T. Namiki, H. Sugawara, Y. Aoki, H. Sato, J. Phys. Soc. Jpn. **71**, Suppl. 246 (2002)

[181] G.K. Shenoy, D.P. Noakes, G.P. Meisner, J. Appl. Phys. **53**, 2628 (1982)

[182] D.A. Gajewski, M.R. Dilley, E.D. Bauer, E.J. Freeman, R. Chau, M.B. Maple, D. Mandrus, B.C. Sales, A.H. Lacerda, J. Phys.: Cond. Matter **10**, 6973 (1998)

[183] D.J. Singh, I.I. Mazin, Phys. Rev. B **56**, 1650 (1997)

[184] H. Sugawara, Y. Abe, Y.Aoki, H. Sato, M. Hedo, R. Settai, Y. Onuki, H. Harima, J. Phys. Soc. Japan **69**, 2938 (2000)

[185] K. Takegahara, H. Harima, J. Phys. Soc. Japan. **71**, Suppl. 240 (2002)

[186] E. Bauer (private communication)

[187] E.P. Wohlfarth, Rev. Mod. Phys. **25**, 211 (1953)

[188] Y. Aoki, T. Namiki, T.D. Matsuda, K. Abe, H. Sugawara, H. Sato, Phys. Rev. B **65**, 064446 (2002)

[189] B. Chen, J.H. Xu, C. Uher, D.T. Morelli, G.P. Meissner, J.P. Fleurial, T. Caillat, A. Borshchevsky, Phys. Rev. B **55**, 1476 (1997)

[190] S.L. Bud'ko, P.C. Canfield, C.H. Mielke, A.H. Lacerda, Phys. Rev. B **57**, 13624 (1998)

[191] J. Ackermann, A. Wold, J. Phys. Chem. Sol. **38**, 1013 (1977)

[192] T.F. Smith, J.A. Mydosh, E.P. Wolfarth, Phys. Rev. Lett. **27**, 1732 (1971)

[193] St. Berger, Ch. Paul, M. Della Mea, E. Bauer, A. Grytsiv, P. Rogl, 6th European Workshop of Thermoelectrics, Freiburg, Germany, Conf. Proc. (2001)

[194] E.D. Bauer, R. Chau, N.R. Dilley, M.B. Maple, D. Mandrus, B.C. Sales, J. Phys.: Cond. Matter **12**, 1261 (2000)

[195] V. Zlatic, I. Milat, B. Coqblin, G. Czycholl, Physica B **312**, 171 (2002)

[196] D. Berardan, C. Godart, E. Alleno, St. Berger, E. Bauer, J. Alloys and Comp. **351**, 18 (2003)

[197] S. Maekawa, S. Kashiba, M. Tachiki, J. Phys. Soc. Japan **55**, 3194 (1986)

[198] K.H. Fischer, Zeitschrift f. Phys B: Cond. Matter **76**, 315 (1989)

[199] C.M. Bhandari, D.M. Rowe, *CRC Handbook of Thermoelectrics*, edited by D.M. Rowe, CRC Press, Chap. 5, p. 43 (1995)

[200] D.J. Singh and W.E. Picket, Phys. Rev. B **50**, 11235 (1994)

[201] D.T. Morelli, G.P. Meisner, B. Chen, S. Hu, C. Uher, Phys. Rev. B **56**, 7376 (1997)

[202] D. Mandrus, A. Migliori, T.W. Darling, M.F. Hundley, E.J. Peterson, J.D. Thompson, Phys. Rev. B **52**, 4926 (1995)

[203] T. Caillat, A. Borshchevsky, J.P. Fleurial, 13th International Conference on Thermoelectrics, Conf. Proc., 40 (1995)

[204] S. Katsuyama, Y. Shichijo, M. Ito, K. Majima, H. Hagai, J. Appl. Phys. **84**, 6708 (1998)

[205] K. Gianno, A.V. Sologubenko, M.A. Chernikov, H.R. Ott, I.R. Fisher, P.C. Canfield, Phys. Rev. B **62**, 292 (2000)

[206] T.M. Tritt, V.M. Browning, *Overview of Measurement and Characterization Techniques for Thermoelectric Materials*, in Semiconductors and Semimetals, edited by T.M. Tritt, Academic Press, Chap. 2, p. 25 (2001)

[207] G.A. Slack, in Solid State Physics **34**, edited by F. Seitz and D. Turnbull, Academic Press, p. 57 (1979)

[208] D.G. Cahill, R.O. Pohl, Sol. State Comm. **70**, 927 (1989)

[209] G.S. Nolas, H. Takizawa, T. Endo, H. Sellinschegg, D.C. Johnson, Appl. Phys. Lett. **77**, 52 (2000)

[210] H. Anno, K. Ashida, K. Matsubara, G.S. Nolas, K. Akai, M. Matsura, J. Nagao, Mat. Res. Soc. Symp. Proc. **691**, G2.4.1 (2002)

[211] L. Chen, T. Kawahara, X.F. Tang, T. Goto, T. Hirai, J.S. Dyck, W. Chen, C. Uher, J. Appl. Phys. **90**, 1864 (2001)

[212] L. Chen, Key Eng. Mat. **224-226**, 197 (2002)

[213] J.S. Dyck, W. Chen, C. Uher, L. Chen, X. Tang, T. Hirai, J. Appl. Phys. **91**, 3698 (2002)

[214] F. Merlo, M. Pani, M.L. Fornasini, J. Less-Comm. Met. **171**, 329 (1991)

[215] C. Kranenberg, D. Johrendt, A. Mewis, Z. Anorg. Allg. Chem. **627**, 539 (2001)

[216] D. Rossi, R. Ferro, J. Alloys and Comp. **236**, 212 (1996)

[217] P. Demchenko, O. Bodak, L. Muratova, J. Alloys and Comp. **339**, 100 (2002)

[218] I.M. Opanych, Thesis, Department of Inorganic Chemistry, L'viv State University, L'viv, Ukraine (1996)

[219] P. Salamakha, P. Demchenko, O. Sologub, O. Bodak, J. Alloys and Comp. **278**, 227 (1998)

[220] C.B.Vining, *CRC Handbook of Thermoelectrics*, edited by D.M. Rowe, CRC Press, Chap. 23, p. 277 (1995)

[221] N.D. Marchuck, V.K.Zaitsev, M.I. Fedorov, A.E.Kaliazin, 8th Int. Conf. of Thermoelectric Energy Conversion, Nancy, France, Conf. Proc., 210 (1989)

[222] Y. Noda, H. Kon, Y. Furukawa, N. Otsuka, I.A. Nishida, K. Masumoto, Mat. Trans. JIM **33**, 851 (1992)

[223] E. Parthe, L. Gelato, B. Chabot, M. Penzo, K. Cenzual, R. Gladyshevskii, *Typix Standardized Data and Crystal Chemical Characterization of Inorganic Structure Types*, 8th Edition, Springer-Verlag, Berlin Heidelberg, p. 1568 (1994)

[224] S. Ozeki, Y. Ohe, Y.S. Kwon, Y. Haga, O. Nakamura, T. Suzuki, T. Kasuya, Physica B **171**, 286 (1991)

[225] S. Ozeki, Y.S. Kwon, Y. Haga, G. Kido, T. Suzuki, T. Kasuya, Physica B **169**, 499 (1991)

[226] O. Vogt, K. Mattenberger, *Magn. Meas. on Rare Earth and Actinide Monopnictides and Monochalcogenides*, in Handbook on the Physics and Chemistry of Rare Earths, edited by K. A. Gscheidner, Jr., L. Eyring, G.H. Lander and G.R.Choppin, Elsevier Science Publishers B. V., Vol. **17**, 301 (1993)

[227] K.H. Hellwege, *Einführung in die Festkörperphysik*, 3th Edition, Springer-Verlag, Berlin Heidelberg New York, p. 197 (1988)

[228] E. Bauer, *Kondo Systems and Heavy Fermions: Transport Phenomena*, in Encyclopedia of Materials, Elsevier Science Publishers B. V., 4372, (2001)

[229] J. Sakurai, H. Takagi, S. Taniguchi, T. Kuwai, Y. Isikawa, J.L. Tholence, J. Phys. Soc. Japan **65**, Suppl. B, 49 (1996)

[230] A.F. Wells, in Structural Inorganic Chemistry, 3rd Ed., Oxford Press (1962)

[231] H. Davy, Ann. Chim. **79**, 326 (1811)

[232] M. von Stackelberg, Naturwissenschaften **36**, 27 (1949)

[233] W.F. Claussen, J. Chem. Phys. **19**, 259 (1951)

[234] L. Pauling, R. Marsh, Proc. Nat. Acad. Sci. **38**, 112 (1952)

[235] G. Jeffrey, in *Inclusion Compounds*, edited by J. Atwood et al., Academic Press, p. 135 (1984)

[236] J.S. Kaspar, P. Hagenmuller, R.M. Pouchard, C. Cros, Science **150**, 1713 (1965)

[237] J. Gallmeier, H. Schäfer, A. Weiss, Z. Naturforsch. **24b**, 665 (1969)

[238] C. Cros, M. Pouchard, P. Hagenmuller, J. Sol. State Chem. **2**, 570 (1970)

[239] H.-U. Schuster, W. Westerhaus, Z. Naturforsch. **30b**, 805 (1975)

[240] W. Westerhaus, H.-U. Schuster, Z. Naturforsch. **32b**, 1365 (1977)

[241] B. Eisenmann,H. Schäfer,R. Zagler, J. Less-Comm. Met. **118**, 43 (1986)

[242] A. Czybulka,B. Kuhl, H.-U. Schuster, Z. Anorg. Allg. Chem. **594**, 23 (1991)

[243] G.S. Nolas, J.L. Cohn, G.A. Slack, S.B. Schujman, Appl. Phys. Lett. **73**, 178 (1998)

[244] B. Kuhl, A. Czybulka, H.-U. Schuster, Z. Anorg. Allg. Chem. **621**, 1 (1995)

[245] G. Cordier, P. Woll, J. Less-Comm. Met. **169**, 291 (1991)

[246] R.F.W. Herrmann, K. Tanigaki, S. Kuroshima, H. Suematsu, Chem. Phys. Lett. **283**, 29 (1998)

[247] S. Yamanaka, H.-O. Horie, H. Kawaji, M. Ishikawa, Eur. J. Sol. State Inorg. Chem. **32**, 799 (1995)

[248] J.D. Bryan, V.I. Srdanov, G.D. Stucky, D. Schmidt, Phys. Rev. B **60**, 3064 (1999)

[249] T. Kawaguchi, K. Tanigaki, M. Yasukawa, Appl. Phys. Lett. **77**, 3438 (2000)

[250] J.L. Cohn, G.S. Nolas, V. Fessatidis, T.H. Metcalf, G.A.Slack, Phys. Rev. Lett. **82**, 779 (1999)

[251] V. Pacheco, A. Bentien, W. Carrillo-Cabrera, S. Paschen, F. Steglich, Yu. Grin, ECSSC8 Abstracts (Oslo) P092 (2001)

[252] B.C. Chakoumakos, B.C. Sales, D.G. Mandrus, J. Alloys and Comp. **322**, 127 (2001)

[253] B.C. Sales, B. C. Chakoumakos, R. Jin, J.R. Thompson, D. Mandrus, Phys. Rev. B **63**, 245113 (2001)

[254] S. Paschen, W. Carrillo-Cabrera, A. Bentien, V.H. Tran, M. Baenitz, Yu. Grin, F. Steglich, Phys. Rev. B **64**, 214404 (2001)

[255] S.-J. Kim, S. Hu, C. Uher, T. Hogan, B. Huang, J.D. Corbett, M.G. Kanatzidis, J. Sol. State Chem. **153**, 321 (2000)

[256] H. Fukuoka, K. Iwai, S. Yamanaka, H. Abe, K. Yoza, L. Häming, J. Sol. State Chem. **151**, 117 (2000)

[257] S. Paschen, V.H. Tran, M. Baenitz, W. Carillo-Cabrera, Yu. Grin, F. Steglich, Phys. Rev. B **65**, 134435 (2002)

[258] R. Kröner, R. Nesper, H.G. von Schnering, Z. Kristallogr. **182**, 164 (1988)

[259] M.M. Shatruk, K.A. Kovnir, M. Lindsjö, I.A. Presniakov, L.A. Kloo, A.V. Shevelkov, J. Sol. State Chem. **161**, 233 (2001)

[260] S. Bobev, S.C. Sevov, J. Am. Chem. Soc. **123**, 3389 (2001)

[261] N.P. Blake, S. Latturner, J.D. Bryan, G.D. Stucky, H. Metiu, J. Chem. Phys. **115**, 8060 (2001)

[262] N.P. Blake, D. Bryan, S. Latturner, L. Mollnitz, G.D. Stucky, H. Metiu, J. Chem. Phys. **114**, 10063 (2001)

[263] R.G. Ross, P. Anderson, G. Backström, Nature **290**, 322 (1981)

[264] M.W.C Dharma-Wardana, J. Phys. Chem. **87**, 4185 (1983)

[265] G.S. Nolas, J.M. Ward, J. Gryko, L. Qiu, M.-A. White, Phys. Rev. B **64**, 153201 (2001)

[266] V.L. Kuznetsov, L.A. Kuznetsova, A.E. Kaliazin, D.M. Rowe, J. Appl. Phys. **87**, 7871 (2000)

[267] B.C. Chakoumakos, B.C. Sales, D.G. Mandrus, G.S. Nolas, J. Alloys and Comp. **296**, 80 (2000)

[268] J.F. Meng, N.V. Charda Shekar, J.V. Badding, G.S. Nolas, J. Appl. Phys. **89**, 1730 (2001)

[269] B. Iversen, A. Bentien, A. E.C. Palmqvist, J.D. Bryan, G.D. Stucky, 19th International Conference on Thermoelectrics, Conf. Proc. (2000)

[270] N.P. Blake, L. Mollnitz, G. Kresse, H. Metiu, J. Chem. Phys. **111**, 3133 (1999)

[271] S.B. Schujman, G.S. Nolas, R.A. Young, C. Ling, A.P. Wilkinson, G.A. Slack, R. Patschke, M.G. Kanatzidis, M. Ulutagay, S.-J. Hwu, J. Appl. Phys. **87**, 1529 (2000)

[272] D.C. Mattis, *Theory of Magnetism*, Springer-Verlag, Berlin (1985)

[273] G.S. Nolas, J.L.Cohn, J.S.Dyck, C. Uher, J. Yang, Phys. Rev. B **65**, 165201 (2002)

[274] G.S. Nolas, G.A. Slack, J.L. Cohn, S.B. Schujman, 18th International Conference on Thermoelectrics, Conf. Proc., p. 40 (1999)

[275] G.S. Nolas, T.J.R. Weakley, J.L. Cohn, Chem. Mater. **11**, 2470 (1999)

List of publications

1. E. Bauer, St. Berger, A. Galatanu, M. Galli, G. Hilscher, H. Michor, Ch. Paul, A. Grytsiv, P. Rogl, V.H. Tran, D. Kaczorowski, ICT 2000 Cardiff, Conf. Proc. (2000)

   Large magnetoresistance and thermoelectric properties of Eu-filled skutterudites

2. Ch. Paul, St. Berger, E. Bauer, A. Grytsiv, P. Rogl, D. Kaczorowski, A. Saccone, R. Ferro, C. Godart, ICT 2001 Beijing, Conf. Proc., 77 (2001)

   Physical Properties of Novel Thermoelectric Skutterudites: $Eu_yFe_{4-x}Co_xSb_{12}$ and $Eu_yFe_{4-x}Ni_xSb_{12}$

3. T. Takabatake, T. Suemitsu, T. Sasakawa, Y. Bando, T. Takagi, Y. Echizen, T. Yoshino, K. Umeo, F. Iga, M. Sera, Ch. Paul, St. Berger and E. Bauer, ICT 2001 Beijing, Conf. Proc., 266 (2001)

   Kondo Semiconductors as a Novel Thermoelectric-Cooling Material

4. St. Berger, Ch. Paul, M. Della Mea, E. Bauer, A. Grytsiv, P. Rogl, ETS 2001 Freiburg, Conf. Proc. (2001)

   Correlations between the thermopower and the pressure response of the electrical resistivity of p- and n-type skutterudites

5. E. Bauer, Ch. Paul, St. Berger, S. Majumdar, H. Michor, M. Govannini, A. Saccone, A. Bianconi, J. Phys.: Cond. Matter **13**, 487 (2001)

   Thermal conductivity of superconducting MgB_2

6. St. Berger, A. Galatanu, G. Hilscher, H. Michor, Ch. Paul, E. Bauer, P. Rogl, M. Gomez-Berisso, P. Pedrazzini, J. G. Sereni, J. P. Kappler, A. Rogalev, S. Matar, F. Weill, B. Chevalier, J. Etourneau, Phys. Rev. B **64**, 134404 (2001)

   Experimental study of physical properties in the complex magnetic phase diagram of $Ce(Rh_{1-x}Ru_x)_3B_2$

7. E. Bauer, St. Berger, A. Galatanu, M. Galli, H. Michor, G. Hilscher, Ch. Paul, B. Ni, M. M. Abd-Elmeguid, V. H. Tran, A. Grytsiv, P. Rogl, Phys. Rev. B **63**, 224414 (2001)

   Crystal structure and physical properties of $Eu_{0.83}Fe_4Sb_{12}$

8. E. Bauer, St. Berger, A. Galatanu, H. Michor, Ch. Paul, G. Hilscher, V. H. Tran, A. Grytsiv, P. Rogl, J. Magn. Magn. Mat. **226**, 674 (2001)

   Magnetic and thermodynamic properties of Eu-filled skutterudites

9. E. Bauer, St. Berger, A. Galatanu, Ch. Paul, M. Della Mea, H. Michor, G. Hilscher, A. Grytsiv, P. Rogl, D. Kaczorowski, L. Keller, T. Hermannsdörfer, P. Fischer, Physica B **312-313**, 840 (2002)

   Magnetic behaviour of $PrFe_4Sb_{12}$ and $NdFe_4Sb_{12}$ skutterudites

10. A. Grytsiv, P. Rogl, St. Berger, Ch. Paul, E. Bauer, C. Godart, A. Saccone, R. Ferro, D. Kaczorowski, Mat. Res. Soc. Symp. Proc **691**, G8.36.1 (2002)

    Formation, Crystal Sructure and Physical Properties of Novel Thermoelectric Skutterudites: $Eu_yFe_{4-x}Ni_xSb_{12}$

11. A. Grytsiv, P. Rogl, St. Berger, Ch. Paul, H. Michor, E. Bauer, G. Hilscher, C. Godart, P. Knoll, M. Musso, W. Lottermoser, A. Saccone, R. Ferro, T. Roisnel, H. Noël, J. Phys.: Cond. Matter **14**, 7071 (2002)

    A novel skutterudite phase in the Ni-Sb-Sn system: phase equilibria and thermoelectric properties

12. T. Sasakawa, T. Suemitsu, T. Takabatake, Y. Bando, K. Umeo, M. H. Jung, M. Sera, T. Suzuki, T. Fujita, M. Nakajima, K. Iwasa, M. Kohgi, Ch. Paul, St. Berger, E. Bauer, Phys. Rev. B **66**, 411031 (2002)

    Successive phase transitions and energy-gap formation in CeRhAs

13. Ya. Mudryk, P. Rogl, C. Paul, S. Berger, E. Bauer, G. Hilscher, C. Godart, H. Noël, J. Phys.: Cond. Matter **14**, 7991 (2002)

    Thermoelectricity of Clathrate I Si and Ge Phases

14. St. Berger, Ch. Paul, H. Michor, E. Bauer, G. Hilscher, A.Grytsiv, P.Rogl, ICT 2002 Long Beach, Conf. Proc., 48 (2002)

    Crystal structure and thermoelectric properties of novel skutterudites $Ep_yNi_4Sb_{12-x}Sn_x$ with Ep=Sn, Eu and Yb

15. Ch. Paul, St. Berger, E. Bauer, A. Grytsiv, P. Rogl, ETS 2002 Pamplona, Conf. Proc. (2002)

Physical Properties and Thermoelectric Performance of $PrFe_{4-x}TM_xSb_{12}$ (TM = Co, Ni)

16. Y. Mudryk, P. Rogl, C. Paul, S. Berger, E. Bauer, G. Hilscher, C. Godart, H. Noël, A. Saccone, R. Ferro, ETS 2002 Pamplona, Conf. Proc. (2002)

Crystal Chemistry and Thermoelectric Properties of Type I Clathrates Partially Substituted by Europium

17. P. C. Ho, V. S. Zapf, E. D. Bauer, N. A. Frederick, M. B. Maple, G. Giester, P. Rogl, St. Berger, Ch. Paul, E. Bauer, Intern. J. of Mod. Phys. B **16**, 3008 (2002)

Superconducting and normal state properties of the heavy fermion compound $PrOs_4Sb_{12}$

18. A. Grytsiv, P. Rogl, St. Berger, Ch. Paul, E. Bauer, C. Godart, B. Ni, M. M. Abd-Elmeguid, A. Saccone, R. Ferro, D. Kaczorowski, Phys. Rev. B **66**, 94411 (2002)

Structure and physical properties of the thermoelectric skutterudites $Eu_yFe_{4-x}Co_xSb_{12}$

19. E. Bauer, St. Berger, Ch. Paul, H. Michor, A. Grytsiv and P. Rogl, Physica B **328**, 49 (2002)

Effect of ionic valence and electronic correlations on the thermoelectric power in some filled skutterudites

20. A. Grytsiv, P. Rogl, St. Berger, Ch. Paul, H. Michor, E. Bauer, G. Hilscher, W. Lottermoser, A. Saccone, R. Ferro, H. Noël, Physica B **328**, 71 (2002)

Novel thermoelectric skutterudites $Sn_yNi_4Sb_{12-x}Sn_x$

21. Ya. Mudryk, P. Rogl, C. Paul, St. Berger, E. Bauer, G. Hilscher, C. Godart, H. Noël, A. Saccone, R. Ferro, Physica B **328**, 44 (2002)

Crystal chemistry and thermoelectric properties of clathrates with rare-earth substitution

22. E. Bauer, St. Berger, Ch. Paul, M. Della Mea, G. Hilscher, H. Michor, M. Reissner, W. Steiner, A. Grytsiv, P. Rogl, E.W. Scheidt, Phys. Rev. B **66**, 214421 (2002)

Crystal field effects and thermoelectric properties of $PrFe_4Sb_{12}$

23. S. Gabani, E. Bauer, S. Berger, K. Flachbart, Y. Paderno, C. Paul, V. Pavlik, N. Shitsevalova, Phys. Rev. Lett. (2003) in press

    Pressure Induced Quantum Critical Point and Non-Fermi-Liquid Behavior in hexaboride SmB_6

24. H. Michor, St. Berger, M. El-Hagary, C. Paul, E. Bauer, G. Hilscher, P. Rogl, G. Giester, Phys. Rev. B **67**, 224428 (2003)

    Crystal structure and Kondo lattice behaviour of $CeNi_9Si_4$

25. A. Grytsiv, E. Bauer, St. Berger, G. Hilscher, H. Michor, Ch. Paul, P. Rogl, A. Daoud-Aladine, L. Keller, T. Roisnel, H. Noël, J. Phys.: Cond. Matter **15**, 3053 (2003)

    Novel Zn_9-cluster compounds $RE_2Zn_6Ge_3$ (RE: La, Ce, Pr, Nd, Sm, Gd): crystal structure and physical properties

26. E. Bauer, St. Berger, S. Gabani, G. Hilscher, H. Michor, Ch. Paul, M. Giovannini, A. Saccone, C. Godart, P. Bonville, Y.Aoki, H. Sato, Acta Physica Polonica B **34**, 367 (2003)

    Non-Fermi-liquid features of novel Yb_2Pd_2In

27. E. Bauer, St. Berger, M. Della Mea, G. Hilscher, H. Michor, Ch. Paul, A. Grytsiv, P. Rogl, E.W. Scheidt, C. Godart, M. Abd Elmeguid, Acta Physica Polonica B **34**, 595 (2003)

    Filled skutterudites: ground state properties and thermoelectric features

28. S. Gabani, E. Bauer, S. Berger, K. Flachbart, Y. Paderno, C. Paul, V. Pavlik, N. Shitsevalova, Phys. Rev. B **67**, 172406 (2003)

    Pressure-induced Fermi-liquid behavior in Kondo insulator SmB_6: Possible transition through a quantum critical point

29. E. Bauer, G. Hilscher, H. Michor, Ch. Paul, E.W. Scheidt, A. Gribanov, Yu. Seropegin, H. Noël, M. Sigrist, P. Rogl, Phys. Rev. Lett., in press (2003)

    Heavy fermion superconductivity and magnetic order in noncentrosymmetric $CePt_3Si$

30. Ch. Paul, E. Bauer, St. Berger, A. Grytsiv, G. Hilscher, H. Michor, P. Rogl, J. Magn. Magn. Mat., in press (2003)

    Magnetic and Thermoelectric Features of $Pr_yFe_{4-x}(Ni,Co)_xSb_{12}$

31. E. Bauer, G. Hilscher, H. Michor, Ch. Paul, Y. Aoki, H. Sato, M. Giovannini, A. Saccone, J. Magn. Magn. Mat., in press (2003)

    Evolution of ground state properties in novel $Yb_2Pd_2In_{1-x}Sn_x$

32. A.Vl. Andrianov, E. Bauer, Ch. Paul, O.A. Savel'evaa, J. Magn. Magn. Mat., in press (2003)

    Pressure-induced helical antiferromagnetism in ferromagnetic $Ho_{40}Gd_{60}$

33. E. Bauer, St. Berger, G. Hilscher, H. Michor, Ch. Paul, M. Reissner, W. Steiner, A. Grytsiv, P. Rogl, ICT 2003 La Grande-Motte, Conf. Proc., in press (2003)

    Ground state properties and thermoelectric behavior of $PrFe_{4-x}TM_xSb_{12-y}Sn_y$ (TM = Co, Ni)

34. P. Rogl, Y. Mudryk, Ch. Paul, St. Berger, E. Bauer, G. Hilscher, C. Godart, H. Noël, ICT 2003 La Grande-Motte, Conf. Proc., in press (2003)

    Structural chemistry, constitution and properties of clathrates

List of conference contributions

× **ICM 2000, International Conference on Magnetism, Aug. 6th to 11th 2000, Recife, Brazil**

Magnetic and thermodynamic properties of Eu-filled skutterudites

E. Bauer, St. Berger, A. Galatanu, H. Michor, Ch. Paul, G. Hilscher, V. H. Tran, A. Grytsiv, P. Rogl

× **19th International Conference on Thermoelectrics, Aug. 20th to 24th 2000, Cardiff, Wales, United Kingdom**

Large magnetoresistance and thermoelectric properties of Eu-filled skutterudites

E. Bauer, St. Berger, A. Galatanu, M. Galli, G. Hilscher, H. Michor, Ch. Paul, A. Grytsiv, P. Rogl, V.H. Tran, D. Kaczorowski

× **50. Jahrestagung der Österreichischen Physikalischen Gesellschaft, Sept. 25th to 29th 2000, Karl-Franzens Universität Graz, Austria**

Skutterudites: Novel thermoelectric materials

E. Bauer, St. Berger, M. Galli, H. Michor, C. Paul, G. Hilscher, A. Grytsiv and P. Rogl

× **16th Workshop on Novel Materials and superconductors, Feb. 11th to 17th 2001, Planneralm/Steiermark, Austria**

Magnetic and thermoelectric properties of Eu-filled skutterudites

E.Bauer, St.Berger, A.Galatanu, A.Grytsiv, H.Michor, C.Paul, G.Hilscher, P.Rogl

× **20th International Conference on Thermoelectrics, June 8th to 11th 2001, Beijing, P. R. China**

Physical Properties of Novel Thermoelectric Skutterudites: $Eu_yFe_{4-x}Co_xSb_{12}$ and $Eu_yFe_{4-x}Ni_xSb_{12}$

St. Berger, Ch. Paul, E. Bauer, A. Grytsiv, P. Rogl, D. Kaczorowski, A. Saccone, R. Ferro and C. Godart

Kondo Semiconductors as a Novel Thermoelectric-Cooling Material

T. Takabatake, T. Suemitsu, T. Sasakawa, Y. Bando, T. Takagi, Y. Echizen, T. Yoshino, K. Umeo, F. Iga, M. Sera, Ch. Paul, St. Berger, E. Bauer

× **SCES 2001, Strongly correlated electron systems, Aug. 6th to 10th 2001, Ann Arbor, Michigan, USA**

Magnetic behaviour of $PrFe_4Sb_{12}$ and $NdFe_4Sb_{12}$ skutterudites

E. Bauer, St. Berger, A. Galatanu, Ch. Paul, H. Michor, G. Hilscher, A. Grytsiv, P. Rogl, D. Kaczorowski, L. Keller, P. Fischer

× **6th European Workshop on Thermoelectrics of the European Thermoelectric Society, Sept. 21st to 22nd 2001, Freiburg im Breisgau, Germany**

Correlations between the thermopower and the pressure response of the electrical resistivity of p- and n-type skutterudites

St. Berger, Ch. Paul, M. Della Mea, E. Bauer, A. Grytsiv, P. Rogl

× **Physical Phenomena at High Magnetic Fields IV, Oct. 19th to 25th 2001, Santa Fe, New Mexico, USA**

Superconducting and normal state properties of the heavy fermion compound $PrOs_4Sb_{12}$

P.C. Ho, V.S. Zapf, E.D. Bauer, N.A. Frederick, M.B. Maple, G. Giester, P. Rogl, St. Berger, Ch. Paul, E. Bauer

× **MRS Fall Meeting, Nov. 26th to 30th 2001, Boston, Massachusetts, USA**

Formation, Crystal Sructure and Physical Properties of Novel Thermoelectric Skutterudites: $Eu_yFe_{4-x}Ni_xSb_{12}$

A. Grytsiv, P. Rogl, St. Berger, Ch. Paul, E. Bauer, C. Godart, A. Saccone, R. Ferro, D. Kaczorowski

× **6th Prague Colloquium on f-electron systems, July 6th to 9th 2002, Charles University Prague**

Heavy electron features of Pr-based skutterudites

E. Bauer, St. Berger, H. Michor, G. Hilscher, Ch. Paul, A. Grytsiv, P. Rogl

× **SCES 2002, Strongly correlated electron systems, July 10th to 13th 2002, Krakow, Poland**

Filled skutterudites: ground state properties and thermoelectric features

E. Bauer, St. Berger, G. Hilscher, H. Michor, Ch. Paul, A. Grytsiv, P. Rogl

Non-Fermi-liquid features of novel Yb_2Pd_2In

E. Bauer, St. Berger, S. Gabani, G. Hilscher, H. Michor, Ch. Paul, M. Giovannini, A. Saccone, C. Godart, P. Bonville, Y.Aoki, H. Sato

× **2nd Hiroshima Workshop - Transport and Thermal Properties of Advanced Materials, Aug. 16th to 19th 2002, Hiroshima, Japan**

Effect of ionic valence and electron correlations on the thermoelectric power in some filled skutterudites

E. Bauer, St. Berger, Ch. Paul, H. Michor, A. Grytsiv, P. Rogl

Novel thermoelectric skutterudites $Sn_yNi_4Sb_{12-x}Sn_x$

A. Grytsiv, P. Rogl, St. Berger, Ch. Paul, H. Michor, E. Bauer, G. Hilscher, W. Lottermoser, A. Saccone, R. Ferro, H. Noël

Crystal chemistry and thermoelectric properties of clathrates with rare-earth substitution

Ya. Mudryk, P. Rogl, C. Paul, St. Berger, E. Bauer, G. Hilscher, C. Godart, H. Noël, A. Saccone, R. Ferro

× **21st International Conference on Thermoelectrics, Aug. 25th to 29th 2002, Long Beach, California, USA**

Crystal structure and thermoelectric properties of novel skutterudites $Ep_yNi_4Sb_{12-x}Sn_x$ with $Ep=Sn$, Eu and Yb

St. Berger, Ch. Paul, H. Michor, E. Bauer, G. Hilscher, A.Grytsiv, P.Rogl

× **7th European Workshop on Thermoelectrics of the European Thermoelectric Society, Oct. 3rd to 4th 2002, Pamplona, Spain**

Physical Properties and Thermoelectric Performance of $PrFe_{4-x}TM_xSb_{12}$ $(TM = Co, Ni)$

Ch. Paul, St. Berger, E. Bauer, A. Grytsiv, P. Rogl

Crystal Chemistry and Thermoelectric Properties of Type I Clathrates Partially Substituted by Europium

Y. Mudryk, P. Rogl, C. Paul, S. Berger, E. Bauer, G. Hilscher, C. Godart, H. Noël, A. Saccone, R. Ferro

Thermoelectric Nickel-based Skutterudites, $(Sn, Eu, Yb)_yNi_4Sb_{12-x}Sn_x$

A. Grytsiv, P. Rogl, St. Berger, Ch. Paul, H. Michor, E.Bauer, G. Hilscher, C. Godart, W.Lottermoser, P.Knoll, M.Musso, R.Ferro, A.Saccone, H.Noël

× **2nd Hvar Workshop on Strongly Correlated Electrons, Oct. 3rd to 8th 2002, Hvar, Croatia**

Heavy electron behaviour and correlations in novel skutterudites $RETM_4X_{12}$ (RE=rare earth, TM=transition metal, X=pnicogen)

E. Bauer, St. Berger, H. Michor, G. Hilscher, Ch. Paul, A. Grytsiv, P. Rogl, E.-W. Scheidt

× **18th Workshop on Novel Materials and superconductors, Feb. 23rd to Mar. 1st 2003, Planneralm/Steiermark, Austria**

Crystal field effects and thermoelectric properties of $PrFe_4Sb_{12}$

M. Della Mea, E. Bauer, St. Berger, Ch. Paul, G. Hilscher, H. Michor, M. Reissner, W. Steiner, A. Grytsiv, P. Rogl, E.W. Scheidt

× **ICM 2003, International Conference on Magnetism, Jul. 27th to Aug. 1st 2003, Rome, Italy**

Magnetic and Thermoelectric Features of $Pr_yFe_{4-x}(Ni,Co)_xSb_{12}$

Ch. Paul, E. Bauer, St. Berger, A. Grytsiv, G. Hilscher, H. Michor, P. Rogl

Evolution of ground state properties in novel $Yb_2Pd_2In_{1-x}Sn_x$

E. Bauer, G. Hilscher, H. Michor, Ch. Paul, Y. Aoki, H. Sato, M. Giovannini, A. Saccone

Pressure-induced helical antiferromagnetism in ferromagnetic $Ho_{40}Gd_{60}$

A.Vl. Andrianov, E. Bauer, Ch. Paul, O.A. Savel'evaa

× **22nd International Conference on Thermoelectrics, Aug. 17th to 21st 2003, La Grande-Motte/Hérault, France**

Ground state properties and thermoelectric behavior of $PrFe_{4-x}TM_xSb_{12-y}Sn_y$ (TM = Co, Ni)

E. Bauer, St. Berger, G. Hilscher, H. Michor, Ch. Paul, M. Reissner, W. Steiner, A. Grytsiv, P. Rogl

Structural chemistry, constitution and properties of clathrates

P. Rogl, Y. Mudryk, Ch. Paul, St. Berger, E. Bauer, G. Hilscher, C. Godart, H. Noël

Curriculum Vitae

DI Christoph Paul
Vorgartenstraße 129-143/2/28
1020 Wien

12.9.1975	geboren in Wien, Eltern: Dr. Ernst Paul, Professor Elisabeth Paul, Volksschullehrerin
1982-1986	Volksschule der Pädagogischen Akademie, Wien Strebersdorf
1986-1994	BG und BRG Ödenburgerstraße, Wien 21
8.6.1994	Matura
1994-2000	Studium der Technischen Physik an der Technischen Universität Wien
1999-2000	Abfassung der Diplomarbeit *Formation, Kristall-struktur und thermoelektrische Eigenschaften der neuartigen Skutterudite* $Eu_x Fe_y Co_{4-y} Sb_{12}$
Nov. 2000	Beginn der Beschäftigung als Dissertant am Institut für Festkörperphysik der Technischen Universität Wien
17.1.2001	Ablegung der 2. Diplomprüfung mit ausgezeichnetem Erfolg
2002-2003	Lehrbeauftragter für Laborübungen aus Experimentalphysik